Design and Implementation of a Relative Localization System for Ground and Aerial Robotic Teams

by

©Oscar De Silva

A Thesis submitted to the School of Graduate Studies in partial fulfillment of the requirements for the degree of

PhD

Faculty of Engineering and Applied Science

Memorial University of Newfoundland

July, 2015

St. John's Newfoundland

Abstract

The main focus of this thesis is to address the relative localization problem of a heterogenous team which comprises of both ground and micro aerial vehicle robots. This team configuration allows to combine the advantages of increased accessibility and better perspective provided by aerial robots with the higher computational and sensory resources provided by the ground agents, to realize a cooperative multi robotic system suitable for hostile autonomous missions. However, in such a scenario, the strict constraints in flight time, sensor pay load, and computational capability of micro aerial vehicles limits the practical applicability of popular map-based localization schemes for GPS denied navigation. Therefore, the resource limited aerial platforms of this team demand simpler localization means for autonomous navigation.

Relative localization is the process of estimating the formation of a robot team using the acquired inter-robot relative measurements. This allows the team members to know their relative formation even without a global localization reference, such as GPS or a map. Thus a typical robot team would benefit from a relative localization service since it would allow the team to implement formation control, collision avoidance, and supervisory control tasks, independent of a global localization service. More importantly, a heterogenous team such as ground robots and computationally constrained aerial vehicles would benefit from a relative localization service since it provides the crucial localization information required for autonomous operation of the

weaker agents. This enables less capable robots to assume supportive roles and contribute to the more powerful robots executing the mission. Hence this study proposes a relative localization-based approach for ground and micro aerial vehicle cooperation, and develops inter-robot measurement, filtering, and distributed computing modules, necessary to realize the system.

The research study results in three significant contributions. First, the work designs and validates a novel inter-robot relative measurement hardware solution which has accuracy, range, and scalability characteristics, necessary for relative localization. Second, the research work performs an analysis and design of a novel nonlinear filtering method, which allows the implementation of relative localization modules and attitude reference filters on low cost devices with optimal tuning parameters. Third, this work designs and validates a novel distributed relative localization approach, which harnesses the distributed computing capability of the team to minimize communication requirements, achieve consistent estimation, and enable efficient data correspondence within the network. The work validates the complete relative localization-based system through multiple indoor experiments and numerical simulations.

The relative localization based navigation concept with its sensing, filtering, and distributed computing methods introduced in this thesis complements system limitations of a ground and micro aerial vehicle team, and also targets hostile environmental conditions. Thus the work constitutes an essential step towards realizing autonomous navigation of heterogenous teams in real world applications.

Table of Contents

Abstract ii

Table of Contents viii

List of Tables ix

List of Figures xvi

List of Abbreviations xvii

1 Introduction 1

1.1 Motivation - The Ground Aerial System 1

1.2 Background 4

1.2.1 Self-localization with SLAM 4

1.2.2 Drawbacks of SLAM for Heterogenous MRS 6

1.2.3 Relative localization for Heterogenous MRS 7

1.2.4 Issues related to relative localization 9

1.3 Thesis Problem statement 12

1.3.1 Problem I: Spatial inter-robot relative sensing 13

1.3.2 Problem II: Nonlinear filtering for relative localization 15

1.3.3 Problem III: Distributed relative localization 16

1.4 Objectives and expected contributions 18
1.5 Organization of the thesis 19

2 Relative Localization: Sensor Design **21**
2.1 Introduction 22
2.2 Background 24
2.2.1 RF based methods 24
2.2.2 Vision based methods 25
2.2.3 Ultrasonic based methods 27
2.2.4 IR based methods 28
2.3 Proposed Approach 29
2.3.1 Measurement principle 29
2.3.2 Sensor node design 30
2.3.3 Sensor calibration 32
2.3.4 Measurement configurations 38
2.3.5 Comparison with other IRRM solutions 42
2.4 Results 44
2.4.1 Static 3D positioning 44
2.4.2 Dynamic 3D positioning 45
2.4.3 Dynamic 3D positioning of an MAV 46
2.5 Conclusion 50

3 Relative Localization: Observability **53**
3.1 Introduction 54
3.2 Preliminaries 56
3.2.1 3D Rotation parameterization 56
3.2.2 Relative localization problem in 3D 59

3.2.3 Measurement availability . . . 60
3.3 Materials and Methods . . . 64
3.3.1 The system configurations . . . 64
3.3.2 Observability of non-linear systems . . . 65
3.3.3 Observability analysis - 3D Relative localization problem . . . 67
3.3.4 The 2.5D simplification of the problem . . . 68
3.3.5 Observability analysis - 2.5D Relative localization problem . . . 70
3.3.6 Implications on estimator design . . . 79
3.3.7 The EKF estimator . . . 81
3.4 Results . . . 83
3.4.1 Simulations - 3D analysis results . . . 83
3.4.2 Simulations - 2.5D analysis results . . . 84
3.4.3 Experimental validation - linear trajectory . . . 86
3.4.4 Experimental validation - circular trajectory . . . 88
3.5 Conclusion . . . 89

4 Relative Localization: Nonlinear Filtering 92
4.1 Introduction . . . 93
4.2 Background . . . 95
4.2.1 Symmetry preserving design . . . 96
4.2.2 Pose filtering . . . 97
4.2.3 Attitude filtering . . . 98
4.3 Materials and Methods . . . 99
4.3.1 Definitions . . . 100
4.3.2 IEKF design for relative localization . . . 102
4.3.3 Steady state IEKF design for relative localization . . . 109
4.3.4 IEKF design for attitude estimation . . . 118

4.3.5 Steady state IEKF design for attitude estimation 124
4.4 Results 129
4.4.1 Performance of the IEKF for relative localization 130
4.4.2 Performance of the steady state IEKF for relative localization 133
4.4.3 Performance of the RINCF 134
4.4.4 Experimental validation of the filters 137
4.5 Conclusion 141

5 Relative Localization: A Distributed Approach 144
5.1 Introduction 145
5.2 Preliminaries 148
5.3 Proposed Approach 152
5.3.1 Local Registration 154
5.3.2 Prediction 154
5.3.3 Correction 155
5.3.4 Pruning 156
5.3.5 Global Registration 156
5.3.6 Fusion 159
5.4 Results 161
5.4.1 Simulations - Global initialization 162
5.4.2 Simulations - Consistency study 163
5.4.3 Simulations - Repeatability study 165
5.4.4 Experimental data set 167
5.5 Conclusion 170

6 Relative Localization of Heterogeneous Multi-Robot Systems 172
6.1 Introduction 173

6.2 Material and Methods . . . 175
6.2.1 Integrating SLAM with DRL . . . 175
6.2.2 Data Correspondence module . . . 179
6.2.3 The Experimental Setup . . . 184
6.3 Results . . . 188
6.3.1 SLAM integration method validation - UTIAS dataset . . . 188
6.3.2 Data correspondence approach validation - simulated dataset . 191
6.3.3 System validation - Experimental multi robot system of IS Lab 195
6.4 Conclusion . . . 200

7 Conclusion and Outlook **202**
7.1 Research summary based on Objective I . . . 202
7.2 Research summary based on Objective II . . . 203
7.3 Research summary based on Objective III . . . 204
7.4 Contributions . . . 205
7.5 Future research directions . . . 208
7.5.1 Phase III design of the relative measurement sensor . . . 208
7.5.2 Design and implementation of estimators with dynamic constraints . . . 210
7.5.3 Multi robot exploration and mapping based on distributed relative localization . . . 211

Appendices **214**
A Relative localization in SE(3) using Invariant Extended Kalman Filtering 214

List of Tables

2.1 Summary of available IRRM solutions 25

2.2 Characteristics of the sensor network 43

2.3 Summary of available 3D IRRM solutions 43

2.4 Static positioning performance of the sensor network 45

3.1 All combinations relating to relative measurement and platform velocity measurement availability 64

3.2 Summary of the observability analysis for the 3D problem 68

3.3 Summary of the observability analysis for the 2.5D problem 79

4.1 Gain parameter fits for different system configurations 118

4.2 Summary of LIEKF* and RIEKF* 123

4.3 Gain parameter fits for the dominant gains for different system configurations 129

5.1 Summary of Monte Carlo average results 166

6.1 ROS nodes used in the experimental testbed 188

List of Figures

1.1 The heterogenous navigation framework targeted by this thesis. The powerful robots are identified as "Leaders" and the resource constrained robots are identified as "Pods". The leaders establish a relative positioning service, implement SLAM for global localization, and perform path planning for the pods. 3

1.2 (a) Single robot SLAM: the robot estimates its path and estimates a local map of the environment using the exteroceptive measurements. (b) Three robots implementing SLAM with navigation frames set to their respective mission start locations. (c) The global map generated by the robots after registration of the communicated individual local maps. Global map to robot transformation estimates can be used to calculate the multi-robot formation. 5

1.3 Overview of multi-robot localization strategies; (a) Single robot SLAM (b) Relative localization (c) Hierarchical localization 8

1.4 The control architecture of a powerful robot (top) and a less capable robot(bottom) implementing a relative localization based HNF 13

2.1 A relative localization based ground aerial system where range r and bearing b measurements are made within a robot network using attachable sensor nodes. 22

2.2 Relative positioning using (a)a marker array with known structure and a monocular camera [1], (b)a calibration tag and a monocular camera [2], (c)coloured markers and a stereo camera [3], (d)IR active marker array with known structure and an IR vision sensor [4]. 26
2.3 (a) 2D ultrasonic TOA and AOA based relative positioning sensor design [5]. (b) 3D ultrasonic TOA based range measurement sensor proposed by [6]. 27
2.4 (a) 2D IR transmitter/receiver array for RSS based relative position measurement proposed by [7]. (b) The 3D spherical array design proposed by [8]. 28
2.5 Inter-robot relative measurement principle and the designed sensor node 29
2.6 Sensor node hardware architecture 30
2.7 The experimental setup used for ultrasonic range and angle of arrival calibration 32
2.8 Ultrasonic range calibration plot and the error histogram of the linear measurement model 34
2.9 Ultrasonic range accuracy variation vs. separation between transmitter and receiver 34
2.10 The test bed arrangement used for infrared bearing measurement calibration 36
2.11 Pixel reprojection error of the calibrated vision sensor model. 39
2.12 IR bearing measurement accuracy variation vs separation between transmitter and receiver. 39
2.13 The scheduling of different tasks of the transmitter and receiver nodes: Rx- reception, Tx- transmission, US- Ultrasonic, COM- Xbee or serial communication 40

2.14 (a) Star measurement configuration. (b) Mesh measurement configuration. 41
2.15 TDMA scheduling between 3 nodes 42
2.16 Static positioning of the sensor network. 45
2.17 Actual and estimated path for a circular trajectory localization experiment 46
2.18 The circular trajectory of the robot and the measurements from the sensor 47
2.19 The measurement errors for the smooth circular trajectory of the robots 47
2.20 Actual and estimated path for an MAV following a random flight trajectory 48
2.21 The 3D trajectory of the flying MAV and the measurements from the sensor 48
2.22 The measurement errors for the 3D trajectory of the flying MAV . . . 49
2.23 Localization results for the random flight trajectory using an EKF . . 49

3.1 Relative localization frames of reference 59
3.2 Comparison between the sampled points and the first order approximation of noise figures related to a high noise relative portioning sensor and a low noise sensor. The standard deviation of Sensor 1 - $\sigma_r = 10cm,\ \sigma_\theta = 20°$, Sensor 2 - $\sigma_r = 3cm,\ \sigma_\theta = 1°$ 62
3.3 Trajectory of the local and target platforms used for the 3D EKF evaluation 84
3.4 Localization results for the 3D EKF for unknown v_{ix} 84
3.5 The Simulated path 85
3.6 Localization results for known input cases (S_1), of $Mesh$ and $Star$ configurations 86

3.7 Localization results for unknown input cases (S_2), of *Mesh* and *Star* configurations . . . 86
3.8 Localization results for unknown input cases (S_3), of *Mesh* and *Star* configurations . . . 87
3.9 The Experimental path . . . 87
3.10 Localization results for known input cases (S_1), of *Mesh* and *Star* configurations . . . 88
3.11 Localization results for unknown input cases (S_2), of *Mesh* and *Star* configurations . . . 89
3.12 Localization results for unknown input cases (S_3), of *Mesh* and *Star* configurations . . . 89
3.13 Actual and estimated path for a circular trajectory localization experiment . . . 90
3.14 Localization results for known input (S_1) and unknown input (S_2,S_3) with *Star* configuration (for the circular trajectory) . . . 90

4.1 The Lyapunov function and its level sets . . . 112
4.2 Results of gain parameter estimation for the gain matrix proposal. . . . 115
4.3 Results of gain parameter estimation for the modified gain matrix proposal. . . . 116
4.4 Gain adaptation for a smooth trajectory for (a) The EKF, (b) The LIEKF, (c) The RIEKF . . . 120
4.5 Gain evolution for a smooth trajectory for (a) The RIEKF*, (b) The LIEKF*, (c) The RINCF RINCF . . . 123
4.6 Gain evolution for a smooth trajectory for The RIEKF* (top), The RINCF (bottom), for $\omega_{max} = \pi/3$ (left), $\omega_{max} = 2\pi/3$ (middle), and $\omega_{max} = 5\pi/3$ (right) . . . 128

4.7 Gain parameter fits using the modified criteria for the dominant gain terms when $I_{\omega_z} = 0 rad/s$ 129
4.8 The simulated trajectory of the local and target robots used to validate the relative localization filter designs 130
4.9 State estimation achieved by EKF and the IEKF for case 2 131
4.10 State estimation accuracy achieved by EKF and the IEKF for case 2 131
4.11 Gain adaptation of the EKF and the IEKF for case 2 132
4.12 Summary of performance of the EKF vs the IEKF for all three cases 132
4.13 Position and heading estimation for case 2 using the IEKF and the ssIEKF 134
4.14 Gain evolution of the IEKF, steady state IEKF, and steady state IEKF with additional parameters, for Case 2 134
4.15 Summary of estimation errors for all 3 cases 135
4.16 The simulated trajectory of the platform and the estimation accuracy provided by the RINCF for *Case* 1 136
4.17 Comparative performance of the RINCF for *Case* 1 137
4.18 Comparative performance of the RINCF for all cases 137
4.19 Calibration of the magnetic compass of the ARDrone 2.0 138
4.20 Attitude heading estimate of the EKF and the RINCF 139
4.21 Attitude heading estimate of the different AHRS for the experimental data 140

5.1 The multi-robot system and a snapshot of individual fusers proposed in this work implemented on each robot 149
5.2 The proposed distributed localization framework. The prediction, correction and fusion operations are performed at different rates ($p < c < f$) 153

5.3 Robot configuration for the numerical tests. Left: Global initialization test, Middle: Consistency study, Right: Repeatability study 162
5.4 L01 Fuser delayed initialization by state communication and registration 163
5.5 Consistency analysis for a hierarchical fusion case 164
5.6 Consistency analysis for a multi-rate decentralized fusion case 165
5.7 Average results of 50 Monte Carlo runs. Only the average estimation results of the fuser on L01 areshown. 166
5.8 Robot trajectories and estimates for the experimental data set. Left: World frame, centralized estimates. Right: L01 frame, distributed estimates of fuser $L01$ 167
5.9 Consistency analysis using experimental data. Distributed estimates of fuser $L01$ compared with the centralized (shaded) estimates. 168
5.10 Mean and covariance of the states x, y, z and θ of the distributed fuser $L01$. 169

6.1 Estimates provided by SLAM running on robots and the proposed DRL approach running on robots 176
6.2 (a) Navigation frame initialization in track set $\mathcal{T}^{l*}$ (b) Navigation frame update in track set $\mathcal{T}^{l*}$ (c) Target frame update in track set $\mathcal{T}^{l}$ 178
6.3 Tracks generated by the multi hypothesis track management policy for different scenarios. 182
6.4 Multi hypothesis sensor registration example 183
6.5 ROS enabled multi robot system used for experimental validation . . 185
6.6 The path of the two robots and the locations of the landmarks 189
6.7 Errors of SLAM self localization of robots 190
6.8 The navigation frame register and the track list of each Fuser 191

6.9 Localization errors of the DRL approach with the SLAM integration module. (Without SLAM integration the tracks do not survive during the periods of measurement loss shown in figure) 192
6.10 Top: The path of three robots used for simulation 1. Bottom: Estimates of the paths given by the DRL approach together with the data correspondence scheme 193
6.11 The localization errors of tracks generated by Fuser 1 and Fuser 2 . . 194
6.12 Top: The path of five robots used for simulation 2. Bottom: estimates of the trajectories given by the DRL approach together with the data correspondence scheme running on two Fusers L01 and L02 196
6.13 The estimates of position and heading averaged for 25 Monte Carlo runs of simulation 2. 197
6.14 The path traversed by robots during the experiment and the estimated trajectory form the proposed DRL scheme. 198
6.15 The relative localization estimates generated by each Fuser 199
6.16 The path traversed by robots during the experiment and the estimated trajectory of the proposed DRL scheme. 199
6.17 The path traversed by robots during the experiment and the estimated trajectory of the proposed DRL scheme. 200

List of Abbreviations

AHRS	Attitude Heading Reference System
AOA	Angle of Arrival
CDMA	Code Division Multiple Access
CI	Covariance Intersection
CSMA	Carrier Select Multiple Access
CTR	Constant Turn Rate (model)
CV	Constant Velocity (model)
DARE	Discrete Algebraic Riccatti Equation
DRL	Distributed Relative Localization
EKF	Extended Kalman Filter
FIV	Field of View
GPS	Global Positioning System
HNF	Heterogenous Navigation Framework
IEKF	Invariant Extended Kalman Filter
IMU	Inertial Measurement Unit
IR	Infra Red
IRRM	Inter-Robot Relative Measurements
IRST	Infra Red Search and Track
JPDA	Joint Probabilistic Data Association

KF	Kalman Filter
LIEKF	Left Invariant Extended Kalman Filter
MAC	Media Access Control
MAV	Micro Aerial Vehicle
MEKF	Multiplicative Extended Kalman Filter
MEMS	Micro Electro Mechanical Systems
MHT	Multi-Hypothesis Tracking
MRS	Multi-Robot System
NCF	Nonlinear Complementary Filter
NCFRN	NSERC Canada Field Robotics Network
RANSAC	RANdom SAmple Consensus
RIEKF	Right Invariant Extended Kalman Filter
ROS	Robot Operating System
SDF	State De-correlation Filter
SLAM	Simultaneous Localization and Mapping
SMC	Sequential Monte Carlo
TDMA	Time Division Multiple Access
TOA	Time of Arrival
UGV	Unmanned Ground Vehicle
UKF	Unscented Kalman Filter
US	Ultra-Sonic
VTR	Variable Turn Rate

Chapter 1

Introduction

1.1 Motivation - The Ground Aerial System

In the past few decades, mobile robots have emerged as one of the highly reliable systems available for application in extreme settings where human presence is challenged. Disaster relief and associated activities such as bomb neutralization and threat surveillance are some application domains in which mobile robots tend to dominate. In recent years, the combined ground and aerial robotic system has emerged as a new combination equipped to effectively undertake these disaster relief tasks [9]. As an example, work reported in [10] performs a complete autonomous mapping of an earthquake damaged building using a similar system which includes a quadrotor Micro Aerial Vehicle (**MAV**) and an Unmanned Ground Vehicle (**UGV**).

The ground aerial multi-robot configuration has gained popularity in the robotics community mainly due to the complementary characteristics that are inherent to MAVs and UGVs. The MAV platforms offer aerial surveillance capability and the ability to quickly maneuver through multi-floor buildings [11, 12, 13] which are of high utility for the discussed application domains. However, the MAVs have low

endurance for many practical missions with reported flight times limited to 15-25 min and payload capacity limited 500-1000 g in typical platforms [14, Table 1.1]. In contrast, the unmanned ground vehicles exhibit higher payload capacity allowing them to operate for longer periods of time and to be equipped with powerful sensing and actuation devices essential for interacting with the environment.

The evolution of this ground aerial configuration is a product of the significant effort by different research groups to push towards a world of heterogenous multi-robot teams. The NSERC Canada Field Robotics Network (**NCFRN**) is a prominent example, where many researchers across Canada work towards developing heterogenous robot teams for outdoor missions. Another noteworthy example is the Robot Operating System (**ROS**) developer community, where close to 50,000 active developers and users [16, pp.17] contribute to realize a framework where almost any robot can unify and which has now become a standard tool catering to multi-robot research. A central theme of this movement is combining robots operating in different domains, varying capabilities, and different vendors, in an efficient and scalable team architecture. Achieving this calls for incrementally involved designs and methods to solve the core navigation functions of localization, planning, and control of multiple robots.

This research considers the localization problem of a heterogeneous Multi-Robot System (**MRS**) consisting of ground mobile robots, and micro aerial vehicles, operating in environments with poor Global Positioning System (**GPS**) reception. Conditions of poor or no GPS reception are often encountered by mobile robots operating in indoor environments, underground mines, and urban canyons. An evolutionary approach for localization of these devices in a GPS denied setting can be achieved by empowering each agent with the ability to self localize using a map based localization approach e.g.,[17]. However, this functionality is of high resource utilization and is more suited for implementation among the powerful agents of a heterogenous system.

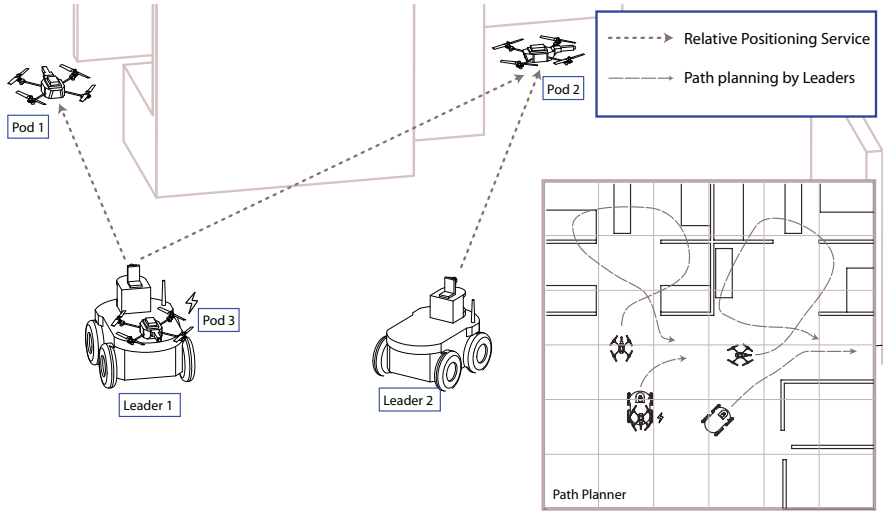

Figure 1.1: The heterogenous navigation framework targeted by this thesis. The powerful robots are identified as "Leaders" and the resource constrained robots are identified as "Pods". The leaders establish a relative positioning service, implement SLAM for global localization, and perform path planning for the pods.

MAVs in particular have to dedicate a considerable portion of their sensor payload and computational capability only for self-localization purposes, e.g.,[18, 19]. In a heterogenous team setting, a more efficient revolutionary approach is to allow a subset of powerful robots to perform map based localization and establish a relative positioning service to assist the operation of the weaker robots. The relative positioning service would contribute to the improvement of localization estimates of the overall team, in addition to acting as an enabler for autonomous navigation of the weaker agents.

In a ground aerial team where such efficient localization is achieved, the power limitation of the MAVs can be circumvented by allowing them to land on UGVs to save and recharge power. The mapping and exploration operation of the UGVs can be assisted by the information rich multiple aerial perceptions and fast searching provided by the aerial agents. The aerial agents can operate in the vicinity of powerful robots while utilizing the relative positioning service. The UGVs can act as computational power houses which perform complex mapping and planning operations of the mission,

which overall achieves an efficient Heterogenous Navigation Framework (**HNF**) as illustrated in Figure 1.1.

The overall system is mainly intended for mapping operations of GPS denied environments using an efficient heterogenous team structure. The mapping capability would cater many specific practical applications which include disaster assessment, asset integrity inspection, or surveying applications such as radio signal strength map generation of a given workspace.

1.2 Background

In general, the localization problem of a multi-robot system can be discussed along two avenues. First is self localization, which refers to localization of each robot individually using solely its onboard sensors. Second is relative localization, which is the process of estimating the formation of a robot team using measurements related to each other's relative location. These measurements are identified as Inter-Robot Relative Measurements(**IRRM**) in this thesis.

1.2.1 Self-localization with SLAM

In GPS denied environments, self localization of a mobile robot is achieved using a method called Simultaneous Localization and Mapping (**SLAM**) [20]. In fact, SLAM is the preferred approach even in outdoor environments due to poor accuracies of GPS and unavailability of the service when travelling through urban canyons, tunnels, and canopies. As illustrated in Figure 1.2, SLAM performs the estimation of both the location of the robot, and the location of environmental features (a map) with respect to a predefined navigation frame. Although dead reckoning is an easy alternative for self localization in an ideal world; noise, inaccuracies in modeling and

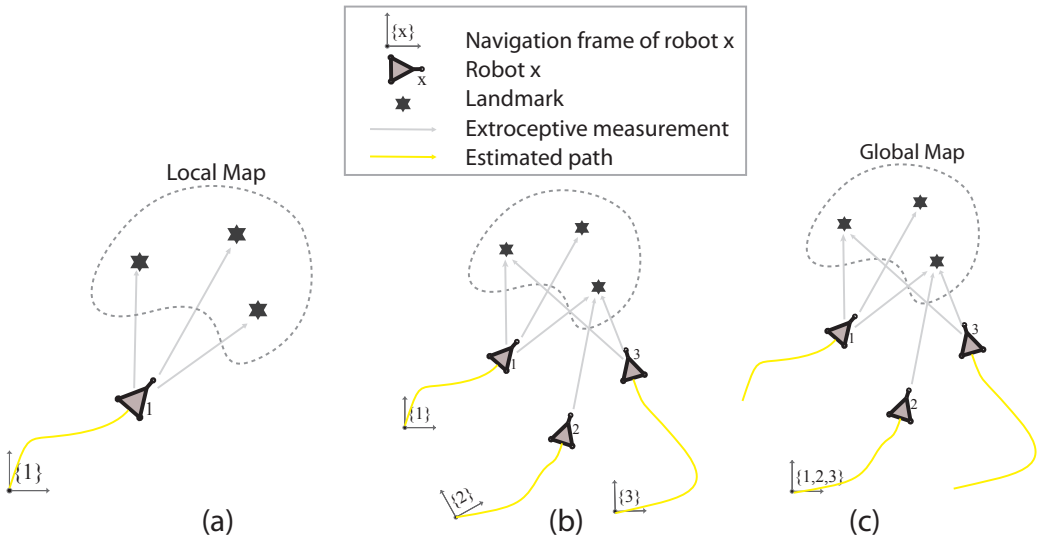

Figure 1.2: (a) Single robot SLAM: the robot estimates its path and estimates a local map of the environment using the exteroceptive measurements. (b) Three robots implementing SLAM with navigation frames set to their respective mission start locations. (c) The global map generated by the robots after registration of the communicated individual local maps. Global map to robot transformation estimates can be used to calculate the multi-robot formation.

numerical schemes cause unbounded drifting of these estimates, limiting the reliability to short periods of time. In order to overcome this drawback SLAM methods employ exteroceptive measurement sensors or sensing of the environment to arrive at a pose estimate which drifts slower and automatically corrects its drift during subsequent encounters of previously seen locations of a map.

Application of SLAM methods is more involved in MAVs than UGVs due to the higher order state space and fast dynamics of the platforms. In MAV localization it is reasonable to consider that roll and pitch rotations of the vehicles' pose are reliably estimated using an attitude heading reference system (**AHRS**) . The magnetic reference is often biased by the external magnetic fields present in indoor environments. Thus it is common to consider both the position and the heading (yaw) states of an MAV for localization purposes [21, 11, 22]. MAV self-localization using laser-based SLAM

implementations are widely reported with successful studies in multi-floor buildings [11, 18, 12]. Laser-based SLAM algorithms are generally fast to operate on a robot's onboard computers. In [18], a flight computer equipped with 1.6 GHz processing and 1 GB RAM was capable of performing laser scan matching-based self-localization of an MAV. Recent studies report the development of laser-based localization for aggressive indoor maneuvers for fast operation with obstacle avoidance [13]. Due to the high payload requirement and cost of onboard laser scanners, many researchers have attempted to develop vision-based techniques for self-localization. Stereo vision [19], monocular vision [23], and appearance-based implementations [24] are some of the reported methods where successful operation in a limited space is achieved. Monocular vision based SLAM methods have been successfully applied even in controlling recreational quadrotor platforms such as the ArDrone [25].

1.2.2 Drawbacks of SLAM for Heterogenous MRS

Laser and vision-based SLAM methods are valuable capabilities for MAVs which warrant further research. However, SLAM methods alone do not serve as an efficient tool to solve the localization problem faced by a heterogenous multi-robot system. This is mainly due to three reasons.

- First, SLAM has considerably high system resource utilization [26, Fig.6]. This has direct affects on the cost, computational budget, and the payload of a system. Although technological advances have enabled SLAM implementations to be realizable in single board computers equipped with vision or laser scanners, the utility of the methods in resource limited platforms of a heterogenous team is up to debate.

- Second, SLAM is not robust for environments with dynamic features and a

limited number of features. The features of an environment can change due to changing lighting conditions, seasonal changes, or due to moving objects. Robots operating in long hallways, and under limited lighting conditions experience deprivation of unique environmental features to support SLAM implementations. Addressing these scenarios would require additional incremental resource utilization in terms of perception capability and computational effort.

- The third problem is that using SLAM would only perform an implicit formation estimate. This is illustrated in Figure 1.2(c), where the robots in the team perform a registration of their individual local maps in order to estimate a global map with their relative formation. Thus the confidence of this formation estimate is quite low and is of questionable reliability to use for formation control of the team.

It is important to note that SLAM is essential for global localization of robots. However, for the task of estimating the formation of robots and more importantly to realize a relative positioning service in the team as desired in this thesis, it is intuitive to utilize more direct perception means which are available for robots in the form of inter robot relative measurements.

1.2.3 Relative localization for Heterogenous MRS

Relative localization is the process of estimating each robot's location with respect to the other robots in the team by utilizing inter-robot relative measurements.. This constitutes an efficient solution to establish a relative positioning service in the team. Figure 1.3(b) illustrates the process of relative localization. Since relative localization estimates the formation of the team using more direct means than those of SLAM (Figure 1.3(a)), it remains computationally tractable

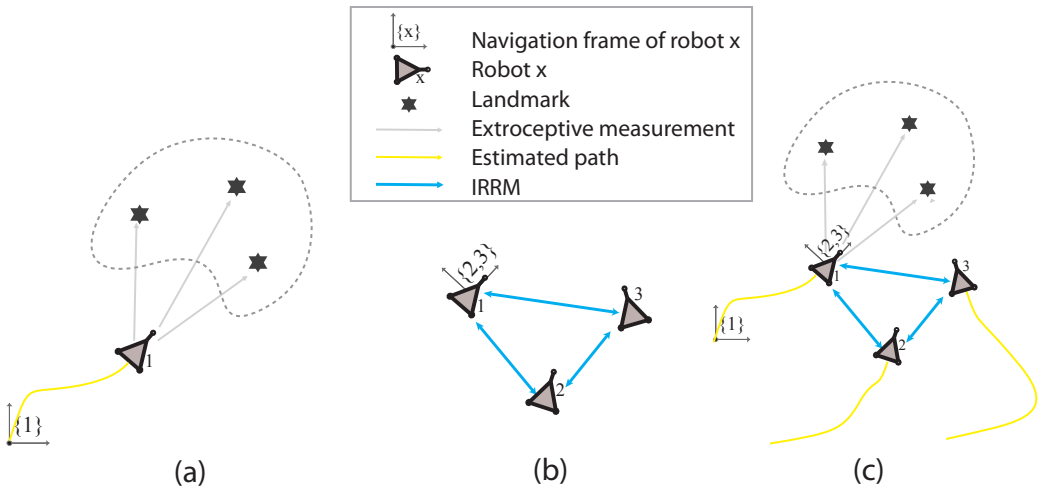

Figure 1.3: Overview of multi-robot localization strategies; (a) Single robot SLAM (b) Relative localization (c) Hierarchical localization

by even the most basic robots in a team. This further enables the implementation of a combined hierarchical localization approach as illustrated in Figure 1.3(c) where weaker robots utilize a relative positioning service established by the more powerful robots which implement SLAM.

The term *Relative Localization* first appeared in the works of [27, 28] and the term was later adopted by many researchers which include [29, 30, 31, 32, 33]. Following are similar terms used in literature relevant to the relative localization problem.

Cooperative Localization[34] In general cooperative localization refers to the sharing of information for localization purposes without any specific regard to the choice of the navigation frame. Relative localization specifically performs location estimation with respect to a moving coordinate frame fixed on a robot, hence can be considered as a branch of the more general problem of cooperative localization. However, most reported work on cooperative localization adopts a navigation frame which is stationary and which is common to all robots as illustrated in Figure 1.2(c).

Network Localization[35] refers to the relative localization problem in relation to a stationary set of robots/ sensor nodes. The term is widely popular in research related to wireless sensor networks.

Relative Mutual Localization[31] is a term adopted by *Franchi et al.*, which refers to the problem of relative localization under the conditions of unknown data correspondence [31, 32, 33].

1.2.4 Issues related to relative localization

Relative localization has been less investigated in the context of mobile robots as compared to other popular research problems such as SLAM and cooperative localization. Therefore, relative localization faces a number of unaddressed issues which require significant research effort, some of which are relevant to localization in general. A brief insight into these issues follows.

Measurement availability **:** Relative localization requires the availability of relative measurements. This is realized in most studies through environmental perception sensors on the robots. In [31], laser scanners are used for inter-robot measurement, while in [27, 36] and [37], the robots' cameras are used for inter-robot measurements. These studies rely on exteroceptive sensors that are not designed for the specific purpose which results in overhead computational tasks such as feature recognition and data correspondence. The unavailability of suitable IRRM sensors for robots has forced many researchers to use synthetic measurements generated using ground truth validation systems for experiments related to localization, e.g.,[22, 34].

Non line of sight conditions**:** The ability to perform relative localization becomes impossible when robots go beyond the IRRM sensing range of each other. This

cripples its applicability in a general setting as a dependable system for localization. However, for heterogenous robot teams considered in this thesis, the weaker robots are expected to operate in the vicinity of the powerful robots. Thus in the context of heterogenous systems, more relevant problems are the path planning of robots for maintaining line of sight, and the design of estimators to handle short periods of non-line of sight operation.

Measurement filtering **:** The relative measurements are affected by sensor noise and disturbances which necessitates the requirement for uncertainty handling mechanisms. Probabilistic approaches use the system and measurement stochastic models for estimation of the required states [17, 38]. For cooperative localization purposes Kalman filter (**KF**) based methods are used for their recursive state estimation capability and computational efficiency compared to the numerically exhaustive sequential Monte Carlo (**SMC**) filters [34, 39]. Measurement filtering additionally realizes state prediction capability which supports non-line of sight operation for short periods of time.

Nonlinearity **:** Physical system models and measurement equations of a maneuvering robotic system formulates a nonlinear system. This necessitates the use of linearized filters such as the Extended Kalman Filter (**EKF**) which does not guarantee convergence [40]. Filters specifically designed to handle the nonlinearity of a system attempts to address this non-ideal conditions by improving its domain of convergence [41, 42].

Observability **:** Observability of a system measures the solvability of the required set of states using the available sensor measurements and the system inputs. Therefore, a relative localization filter for a given system should remain fully observable for full state observation. Linearized and nonlinear observability rank

conditions [43] allow analysis of the robotic system to design sensor combinations and filters for full state observability.

Initialization **:** In order to achieve robust performance of recursive filters it is beneficial to establish accurate state initialization schemes. Localization using inter-robot measurements is addressed as a static case in network localization of wireless sensor networks [44]. The positions of the sensor nodes are solved on a snapshot basis without considering the temporal correlation of measurements. Deterministic initialization from all measurements in a multi-robot system system [45] and pairwise initialization using time series measurements [46] are also reported for initialization purposes of filters. These methods constitute effective means for state initialization.

Data correspondence **:** In addition to IRRM perception, an essential requirement for relative localization is knowing the identity of the robot perceived. Due to inherent limitations of some IRRM sensors, the output of the sensor remains invariant for different robots in the team. This problem is referred to as "unknown measurement correspondence" or "anonymity of measurements" as identified in [47]. Additionally, it is required to identify measurements as outliers or as clutter due to numerous disturbances affecting IRRM sensors. These can be caused by multi-path effects, diffraction, or signal interference.

Distributed computing **:** The relative localization process becomes efficient and scalable only when it is performed in a distributed fashion among a set of powerful robots in a team. This is mainly because of the robustness it brings to the overall system and the reduction in overall communication that distributed computing allows in comparison to a strictly centralized implementation. Preliminary work by researchers assesses delayed state information filters[48], and

distributed EKF[39] implementations for the task. However the area is not as developed as the multi radar target tracking methods[49], which can be considered as the closest comparable body of work from the more established field of target tracking.

All of the aspects outlined above should be effectively addressed to realize an efficient relative localization based HNF.

1.3 Thesis Problem statement

The main focus of this research study is to address the localization problem of a heterogenous system, using a relative localization-based navigation framework. The target heterogenous system consists of UGVs and MAVs.

Although relative localization based approaches have been discussed by a number of authors [37] [28] [50], a viable relative localization based system design suitable for real world applications has not been fully developed. This thesis targets a relative localization based HNF as illustrated in the system block diagram shown in Figure 1.4.

The robots with self localization capability are identified as “Leader” robots and ones which lack resources for implementation of map based localization schemes are identified as “Pod” robots in the figure. The three main modules related to achieving relative localization are identified as the “IRRM sensor”, “Relative localization filter” and the “Distributed relative localization module” in the illustrated HNF. In relation to these modules, this thesis investigates the following three key problems.

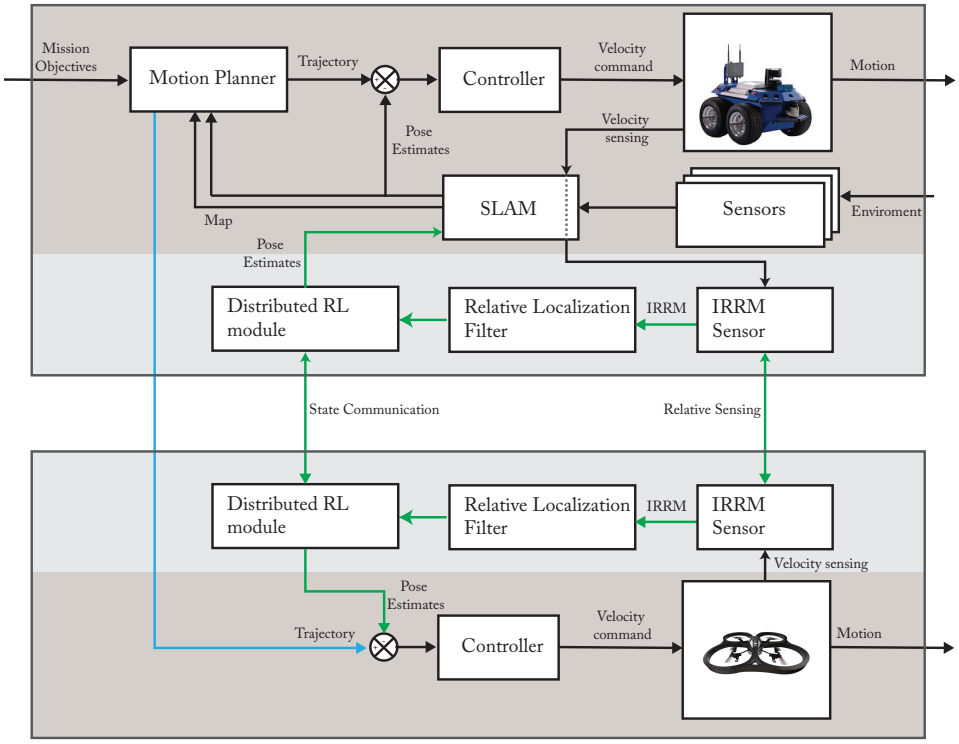

Figure 1.4: The control architecture of a powerful robot (top) and a less capable robot(bottom) implementing a relative localization based HNF

1.3.1 Problem I: Spatial inter-robot relative sensing

Perception devices which can measure relative range and bearing between platforms are essential for relative localization. For ground aerial systems, IRRM sensors should additionally feature spatial sensing capability. Conventional approaches to enable perception employ exteroceptive sensing devices such as laser scanners and vision sensors which are not designed for the specific purpose. These devices demand additional feature recognition and data correspondence steps to extract IRRMs from countless environmental features perceived, e.g.,[27, 36, 31]. Therefore, designing a spatial IRRM technology specifically for the purpose is required in order to achieve relative localization in a robust manner.

Enabling spatial IRRM capability faces the following key challenges. The first

challenge is achieving sufficient accuracy for indoor operations. Although strict standards are not available for the purpose, authors in [14] point out that errors must not exceed ± 15cm for the purpose of indoor navigation of these platforms, based on a typical platform size of 70 cm and a standard doorway size of 100cm [14, Fig. 1.3]. The second challenge is achieving a solution which has low cost, low power, and low payload so that it is applicable to weak agents of a heterogenous system, i.e., the perception devices remain economically and computationally feasible for the resource constrained platforms of a heterogenous system. The third challenge is making the method scalable beyond a pair of robots, since the perception devices are intended to service multi-robot team implementations. Therefore, multiple access methods or robust data correspondence mechanisms should be established.

IRRM base technologies for ground and aerial localization mainly utilize vision-based approaches. Stereo vision-based visual 3D tracking solutions in [3] and monocular vision-based approaches in [37] track the robot's specific features for identifying robots in the perceived image. Application of vision-based measurement methods in muti-robot scenarios faces difficulties mainly in solving the correspondence problem, FOV limitations, and robustness to changing lighting conditions. Ultrasonic and IR-based approaches solve the correspondence issue at the hardware level by incorporating multiple access methods. In [51], an ultrasonic signal-based approach is used for IRRM which possess the relative ranging capability in 3D. The method uses time of arrival of emitted ultrasonic signals for range measurement in a network of robots. Use of ultrasonic devices for relative measurement achieves centimeter level accuracies and favourable scalability characteristics as seen in indoor positioning systems reported in [52]. Work in [8] proposes an Infra-Red (**IR**) receiver array for received signal strength based range and bearing estimation. The method can be considered as state of the art among IRRM technologies which are accurate, robust, and scalable.

However, the array design takes a considerable volume of space and also demands higher power for IR emission. The accuracies achieved by the design are not comparable to ultrasonic only range estimation methods and vision based bearing estimation methods.

This thesis specifically investigates the feasibility of ultrasonic and vision based measurements as IRRM sources, in an attempt to design scalable sensor nodes which are attachable to "Pod" agents of a heterogenous system. Priority is given to realizing scalable and low resource demanding means of achieving relative measurements.

1.3.2 Problem II: Nonlinear filtering for relative localization

Nonlinear filtering specifically attempts to address nonlinearity of the relative localization problem. Relative localization is traditionally addressed with a classical treatment using an EKF. However the EKF performs linearization of the system dynamics which leads to divergence and instability of estimates. A nonlinear treatment of the problem attempts to circumvent the pitfalls associated with EKF based linearized treatments.

Nonlinear filtering for relative localization faces the following additional challenges. The first challenge is system observability. This is a theoretical limitation for the success or failure of an estimator for a given estimation problem. Thus observability limitations should be established for the problem of relative localization prior to any attempts of estimator design. The second challenge is achieving low-cost filtering. This is to reduce the computational demand of filters as much as possible since most of the relative localization filtering modules would eventually be implemented in low cost embedded systems. In terms of computational demand, deterministic filters tend to consume the least. However, deterministic filtering should be complemented with an optimal gain tuning procedure since the filtering approaches lose the optimal

estimation capability as a result of not considering the noise parameters of a system.

Nonlinear observability analysis methods are available for detailed observability evaluation of a given problem[43]. In [53], the 2D relative localization problem is analyzed and in [46], the 3D relative localization problem is evaluated. However, the studies lack investigation into the effect of platform velocities on system observability. This analysis is important since the availability of platform velocities of robots is not guaranteed under conditions of communication drops and lack of sufficient velocity sensing means. Thus observability constraints under limited platform input velocities should be further investigated to gain insight into the problem of relative localization.

In order to achieve low cost filtering, deterministic nonlinear filter designs are proposed for many comparable problems such as attitude filtering and localization [54, 42]. However, they lack systematic design procedures which can be followed easily for a different problem such as relative localization. Recent developments in geometric nonlinear filtering allow systematic filter design for problems having symmetries[41]. The method allows filter implementation in stochastic forms[55] or implementation in a more computationally efficient deterministic form[56]. However, establishing tuning procedures to achieve near optimal performance is not discussed in these studies.

This thesis investigates the problem of low cost nonlinear filter design for relative localization using the recently developed symmetry preserving approach, and attempts to establish optimal tuning procedures for the filters. Additionally, the thesis investigates the observability constraints of the system specifically in relation to input velocities of the platforms.

1.3.3 Problem III: Distributed relative localization

The problem of distributed relative localization relates to the scalability of relative localization to more than two robots. The problem is well studied for centralized

implementations where EKF estimators are shown to produce reliable consistent results [34]. As the centralized EKF is computationally intractable with an increasing number of robots and is prone to single point of system failure, a Distributed Relative Localization (**DRL**) approach is preferred for implementation.

The key challenges faced by distributed relative localization are as follows. The approach inherently demands high bandwidth communication channels to communicate measurements of robots among the team for filtering purposes. Therefore, achieving multi-robot relative localization with efficient communication means remains a key challenge. Additionally, when information is shared among platforms, successive reuse of the same information tends to develop false confidence in results. Therefore, achieving consistency of estimation is challenging for distributed implementations. Furthermore, the existence of multiple robots complicates the data correspondence effort when IRRM sources like lasers and cameras are incorporated in the estimation framework.

In order to limit the communication requirement in multi-robot relative localization, recent studies propose maintaining the history of measurements in an optimal manner[57]. Studies in [48] propose the use of a delayed state information form as a convenient statistic to establish such a framework. However, keeping a history of data is seen as a brute force approach which does not scale well compared to distributed methods used in target tracking literature [58]. In target tracking methods the strategy is to maintain a state vector which acts as a single statistic incorporating all past data. Target tracking approaches are equipped with well developed tools for handling data correspondence such as Joint Probabilistic Data Association (**JPDA**) [59], and Multi-Hypothesis Tracking (**MHT**) [60]. However, target tracking methods are not well exploited to address the challenges related to communication bandwidth and data correspondence issues encountered specifically in multi-robot relative localization.

This thesis investigates the applicability of target tracking methods in order to realize distributed relative localization. To this end the thesis attempts to identify required modification for distributed multi-target tracker implementations for mobile robots in order to achieve efficient communication, consistency in estimates, and data correspondence.

In order to address these three identified problems related to relative localization, the thesis assumes the following as the main objectives of this work.

1.4 Objectives and expected contributions

Objective 1 Design a scalable inter-robot relative measurement sensor for ground and MAV localization.

- Contribution 1 : Hardware design of a novel scalable IRRM sensor network with sufficient accuracy and range suitable for ground aerial systems operating in indoor environments.
- Contribution 2 : Experimental evaluation and optimization of the novel IRRM sensor design for UGV and MAV systems.

Objective 2 Design a geometric nonlinear filter for relative localization which is capable of implementing in low cost hardware.

- Contribution 3 : An observability analysis of the relative localization problem considering unknown platform velocities.
- Contribution 4 : A geometric nonlinear filter module design for relative localization.
- Contribution 5 : An optimal gain tuning approach for deterministic nonlinear filter designs related to relative localization.

Objective 3 Design of an efficient Distributed Relative Localization (**DRL**) method.

- Contribution 6 : A target tracking inspired distributed design for relative localization which supports asynchronous data communication and consistent estimation.
- Contribution 7 : A distributed data correspondence approach for multi-robot relative localization.
- Contribution 8 : A method of incorporating self localization estimates in the proposed DRL scheme.

1.5 Organization of the thesis

Since this thesis considers three different problem areas related to relative localization of robots, the background work related to each problem is discussed in detail in each corresponding chapter (2,3,4, and 5). Following is a brief outline of each chapter.

Chapter 1 - Introduction Introduces the research topic and the main objectives of this study.

Chapter 2 - Relative Localization: Sensor Design This chapter relates to objective 1 of the thesis. A hardware design of a novel IRRM sensor for relative localization is presented detailing experimental evaluation of the device. The chapter concludes discussing design evolutions targeted towards combined UGV and MAV implementations.

Chapter 3 - Relative Localization: Observability This chapter relates to objective 2 of the thesis. The chapter details an observability analysis for relative localization with an introduction to the system models, measurement models, and associated notations used throughout the thesis.

Chapter 4 - Relative Localization: Nonlinear Filtering This chapter relates to objective 2 of the thesis. The chapter details a nonlinear filter design and an optimal gain tuning approach for the relative localization problem.

Chapter 5 - Relative Localization: A Distributed Approach This chapter relates to objective 3 of the thesis. A target tracking inspired design for distributed relative localization is presented which features efficient communication and consistent estimation.

Chapter 6 - Relative Localization of Heterogenous Multi-Robot Systems This chapter develops the necessary axillary modules required for application of the proposed methods in a heterogenous team of robots. The overall system is validated using multiple numerical studies and experimental studies.

Chapter 7 - Conclusion This chapter concludes the thesis discussing the practicality of the proposed method, its drawbacks, and topics that require further research. The resulting publications of this work are outlined along with a summary related to each research objective.

Chapter 2

Relative Localization: Sensor Design

In order to realize relative localization between ground and aerial systems, first it is necessary to establish reliable perception means for 3D relative position measurement. This chapter[1] develops a novel sensor applicable for 3D relative position sensing, based on a combined vision and ultrasonic based approach. The sensor is low-power, light-weight, low-cost, and designed to be applicable across many robotic platforms including MAVs. The proposed sensor achieves a measurement accuracy of 0.96 cm RMSE for range, and 0.3° RMSE for bearing with a maximum of 10 Hz update rate over a detection range of 9 m. Correspondence between multiple robots is resolved using time division multiple access methods. These features are verified by multiple experimental evaluations on a multi-robot team with both ground and aerial agents. The chapter concludes with a detailed review of the sensor discussing ongoing research

[1]This chapter is based on the following publications of the author [61, 62]: [61] O. De Silva, G. K. I. Mann and R. G. Gosine, "Development of a relative localization scheme for ground-aerial multi-robot systems," in *IEEE/RSJ International Conference on Intelligent Robots and Systems*, 2012, pp. 870-875. [62] O. De Silva, G. K. I. Mann, and R. G. Gosine, "An Ultrasonic and Vision-Based Relative Positioning Sensor for Multirobot Localization," *IEEE Sensors Journal*, vol. 15, no. 3, pp. 1716-1726, 2015.

efforts targeting improved performance of the device.

2.1 Introduction

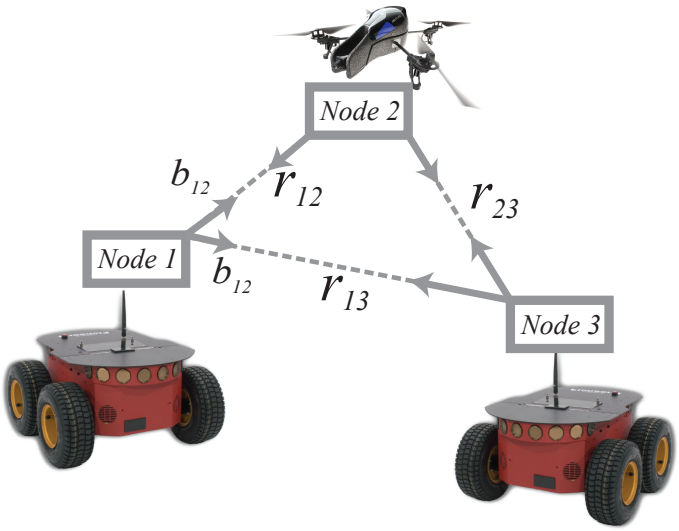

Figure 2.1: A relative localization based ground aerial system where range r and bearing b measurements are made within a robot network using attachable sensor nodes.

Relative 3D position sensing among ground and aerial platforms is a difficult task facing numerous challenges. Chapter 1 established a set of key specifications required for a candidate sensor design in order to realize effective relative positioning. These are as follows:

- Spatial sensing capability between any pair of robots in a team. The spatial sensing range should be sufficient at least for operation in a typical room of a building (5 m).
- Minimum positioning accuracy of 15 cm or below. As identified in Chapter 1, these minimum error bounds are necessary for a typical MAV platform with a width of 70 cm to navigate through a standard doorway of 100 cm [14, Fig. 1.3].

- Low payload, cost, and power consumption suitable for typical MAV and ground robotic platforms. Upper bounds for these specifications can be justified considering a low cost MAV platform such as the ARDrone 2.0. The drone has a $200g$ payload, a cost of $400, and a power consumption of $100W$. These can be considered as absolute upper bounds for the purposes of sensor design.
- Scalable design with measurement correspondence mechanisms to handle multi-robot teams.

Available sensor designs to address the problem of 3D relative positioning employ a multitude of sensing technologies. A detailed review of these methods is discussed in the next section. Among them, the vision based solutions report the best bearing measurement accuracies [63]. The main drawback of vision based approaches is that they require increased computational effort for robust data correspondence and experience limited depth perception for multi-robot applications. The best range measurement accuracies are achieved by acoustic and ultrasonic based means [6]. However, these solutions are prone to environmental disturbances and report poor accuracies when used for relative bearing measurement between two platforms [6]. The method proposed by [8] which is based on IR received signal strength, is widely accepted as state of the art in terms of relative positioning. Yet the current state of IR received signal strength based sensors has several drawbacks which include high power consumption, difficulty in miniaturizing the sensor, and poor accuracies in comparison to vision based or acoustic based solutions.

This work proposes a solution based on both vision and ultrasonic sensors. An ultrasonic sensor is used to measure the range and an infrared (**IR**) vision sensor is integrated to measure the bearing of IR active markers on the robots. This brings heightened accuracies in a small package which is capable of establishing time domain multiple access based measurement correspondence among sensors. The pro-

posed sensor is designed to be scalable and attachable to ground and aerial systems. Additionally, it is capable of operating alongside ultrasonic proximity sensors which are used by mobile robots for obstacle avoidance, and height measurement purposes.

2.2 Background

In general, relative measurements among platforms are established using transmitter and receiver pairs or arrays, which measure signal parameters related to Time Of Arrival (**TOA**), Received Signal Strength (**RSS**), or frequency [35]. Depending on the type of signal employed, the available relative measurement methods which are applicable to indoor mobile robots can be classified into four different groups: (a)RF transmitters and receivers, (b)image sensors and target features, (c)IR emitters and receivers, and (d)ultrasonic transmitters and receivers. Table 2.3 reports the main performance indicators relevant to available relative position measurement sensors. A detailed discussion of each type of sensor follows according to the type of signal used.

2.2.1 RF based methods

Most reported work utilizing RF transmitters and receivers performs TOA-based range measurement [64, 35] or RSS-based range measurement [30, 67] for localization. These methods are capable of using modulated signals and separate channels for data correspondence purposes [64], which allows easy scalability for multi-robot applications. The reported RF-based methods measure only range information. As a result, RF based methods require multiple and distinct measurements in order to achieve lateration based range only localization. The reported RF range measurement accuracies are in the order of meters [30] . This challenges the applicability of RF based techniques for spatial localization purposes of MAVs since the applications

Table 2.1: Summary of available IRRM solutions

Author	Method	Range/X error[1]	Bearing/Y error	Operating range	Corrrespondance (Update rate)
Range only					
Zickler et al, [30]	2D, RF, RSS	250.0cm	-	-	FDMA (-)
Wymeersch et al, [64]	2D, RF UWB, RTT	60cm	-	20m	FDMA (-)
Marziani et al. [65]	3D, Ultrasonic, CDMA RTT	1.0cm	-	6.7m	CDMA (-)
Range and Bearing 2D					
Rivard et al. [5]	2D, Ultrasonic, TOA/AOA	5.0cm	10.0^o	6.7m	TDMA (10 Hz)
Pugh et al. [7]	2D, IR, RSS	20.0cm	15.1^o	3.3m	CSMA (30 Hz)
Range and Bearing 3D					
Achtelik et al.[3]	3D, Stereo vision (known structure)	4.2cm (X)	12cm(Y)	4m FOV	Color markers (15 Hz)
Wenzel et al. [4]	3D, Monocular vision (known structure)	18cm(X)	23cm(Y)	5m FOV	- (25 Hz)
Breitenmoser et al. [1]	3D, Monocular vision (known structure)	1.7cm(X)	1.7cm(Y)	2m FOV	Color markers (n/a)
Eckert et al. [66]	3D, Ultrasonic, TOA/AOA	2.0cm	45^o	5.6m	TDMA (<35Hz)[3]
Roberts et al. [8]	3D, IR, RSS/AOA	45.4cm	3^o	12m	CSMA (1 KHz)

1 RMSE accuracies or max accuracies reported at a range of 6m. If the operating range of sensor is less than 6m the accuracy at full range is reported
2 Although both position and bearing are measured by the IRRM, due to the large error in bearing estimation range only localization is performed using multiple robots. The accuracies and range of reported localization are given in brackets.
3 The authors do not provide an update rate, but a localization computation time of 10 ms for 4 nodes is reported. This is combined with the ultrasonic propagation time for the operation range to calculate a feasible best case update rate figure.

require accuracies in the order of a few centimeters.

2.2.2 Vision based methods

Image sensors are used to measure the pixel locations of target features in a recorded image. They also allow 3D reconstruction of features using multiple cameras or using observations of known geometric structures. Commercial motion capture systems like Vicon® have been used for indoor localization of MAVs, with 50μm level 3D reconstruction accuracies and up to 375Hz update rates [68]. Motion capture systems can only be used in a fixed indoor work space, hence they are mainly reported as ground truth validation systems for various robotic experiments [68]. A motion cap-

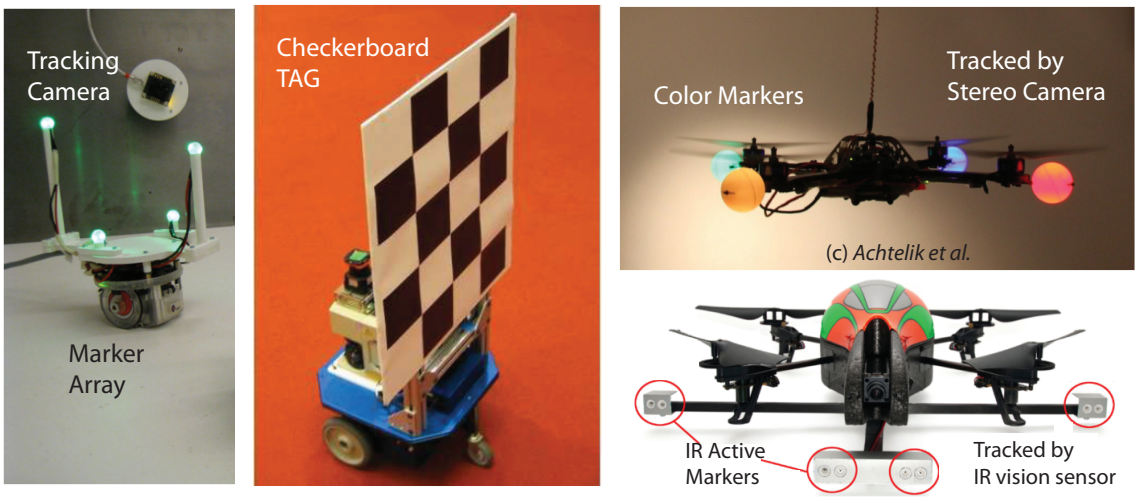

Figure 2.2: Relative positioning using (a)a marker array with known structure and a monocular camera [1], (b)a calibration tag and a monocular camera [2], (c)coloured markers and a stereo camera [3], (d)IR active marker array with known structure and an IR vision sensor [4].

ture system is not designed as a mobile system since the whole system would require a recalibration process even if one of the cameras of the system is repositioned. Therefore a motion capture system is not readily applicable as a network of IRRM sensors attached to robots.

Depth perception on mobile robot platforms is commonly performed using stereo vision [3, 19] or monocular vision-based measurements of known structures [69, 4, 1]. Stereo vision tracking of an MAV fixed with coloured marker balls obtains accuracies of 5 to 10 cm at a 4 m range [3]. Known marker structure and monocular vision-based tracking reports a maximum error of 12 cm at a 2 m range [1]. Another popular visual feature to use is calibration tags such as checker board tags [2] and April tags [70] which allow accurate tracking and correspondence. However this feature is rather difficult to incorporate on a robot to achieve accurate omnidirectional positioning, e.g. Figure 2.2(b). IR active markers and mono-vision tracking achieves 14 cm maximum error at a 1 m range [69, 4]. It is known that the depth perception accuracy of vision-

based approaches generally degrades with increasing range. Feature identification and data correspondence in vision based methods demand significant computational processing power. Moreover, in these methods the scalability of the team is limited to the number of uniquely identifiable features that can be attached to the robots.

2.2.3 Ultrasonic based methods

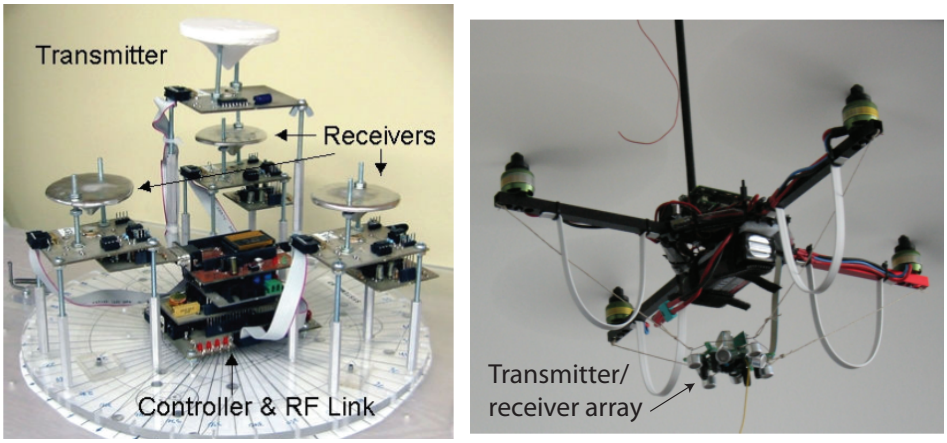

(a) *Rivard et al.* (b) *Eckert et al.*

Figure 2.3: (a) 2D ultrasonic TOA and AOA based relative positioning sensor design [5]. (b) 3D ultrasonic TOA based range measurement sensor proposed by [6].

Ultrasonic based relative measurement methods for robots are based on the well developed indoor positioning systems which include Cricket [71], Active BAT [72], 3D-LOCUS [73], and various other beacon-based acoustic localization networks [74, 75, 76]. Direct sequence spread spectrum signals and array signal processing as reported in [75], achieve sub-centimeter range measurement accuracies and 1-2° bearing measurement accuracies. Application of spread spectrum methods for mobile platforms is limited mainly due to the unavailability of commercial wide-band ultrasonic transmitters [77]. Moreover, they also demand fast hardware signal processors, e.g., [74]. Therefore, the reported studies on robotic systems have employed narrow-band

ultrasonic tones. As a result, the reported measurement errors for ground robotic systems are 6 cm in range and 17° in bearing [5]. Accuracies of 2 cm in range and 22° in azimuth bearing are reported for 3D robotic systems [6]. Due to the poor performance in bearing measurements, the range-based localization method as presented in [6] requires lateration techniques for accurate localization. Additionally, the sensors shown in Figure 2.3 [5, 6, 66] have failed to accommodate the strong narrow-band ultrasonic disturbance sources that generally occur due to the height measurement sensors of aerial robots and obstacle measurement sensors of ground platforms.

2.2.4 IR based methods

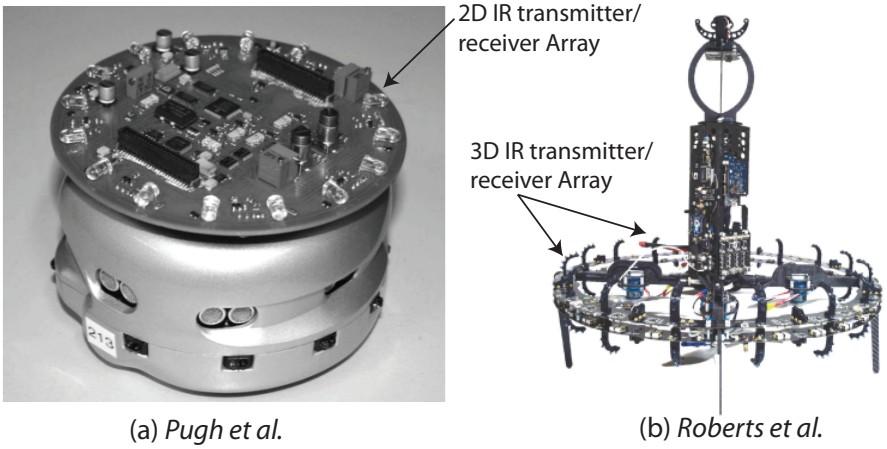

Figure 2.4: (a) 2D IR transmitter/receiver array for RSS based relative position measurement proposed by [7]. (b) The 3D spherical array design proposed by [8].

IR emitters and receivers employ modulated IR signals for RSS-based range and bearing measurement. The 2D design presented in [7] achieves accuracies of 35 cm for range and 15° for bearing over a 4 m range. The extension to 3D is reported in [8], where a 14 cm range and 3° bearing accuracies are achieved at a 6m range. This increased 3D detection field was realized by using spherical array designs and cascaded filtering [8]. The method facilitates fast refresh rates and robust measurement

correspondence over acoustic and vision-based approaches. The main drawbacks of the approach is its high power consumption and poor accuracies as compared to vision and ultrasonic systems. Additionally the large construction size of the sensor, as illustrated in Figure 2.4, complicates the integration of the sensor to many MAVs and ground robot platforms.

2.3 Proposed Approach

2.3.1 Measurement principle

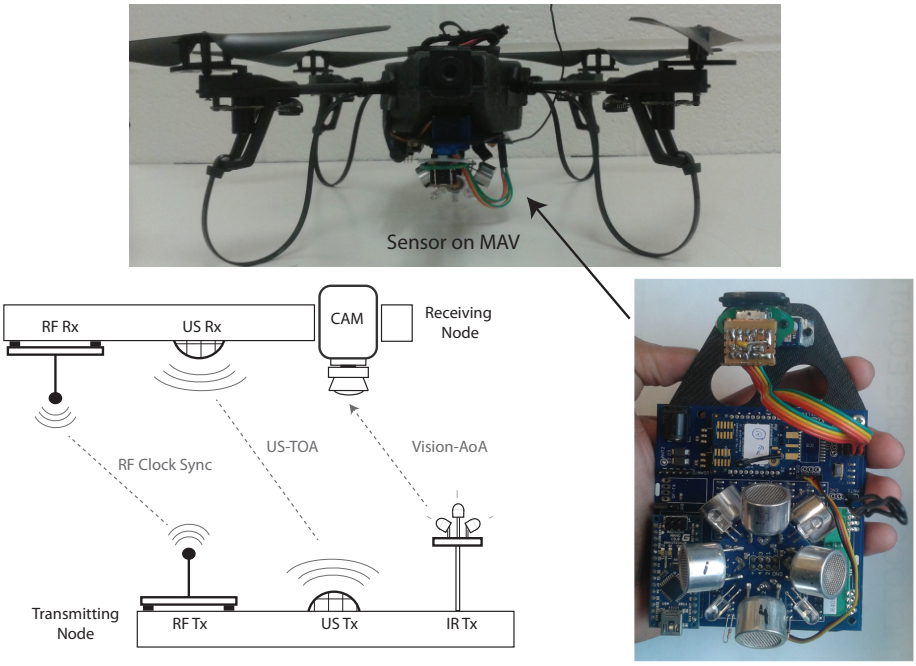

Figure 2.5: Inter-robot relative measurement principle and the designed sensor node

Figure 2.5 illustrates the proposed combined ultrasonic and vision-based relative measurement method. The ultrasonic range measurement module measures the TOA and the Angle Of Arrival (**AOA**) of an ultrasonic signal emitting from a transmitting node. An RF module is integrated for clock synchronization between the two nodes.

The receiving node can measure the time of acoustic signal reception. By knowing the signal transmission time from the transmitting node, the receiver can measure the TOA and the corresponding propagation distance of the signal. The difference in TOA among an array of receivers provides an estimate of the direction of arrival. A separate vision-based bearing measurement module measures the azimuth and the elevation of an IR active marker located at the transmitting node.

The sensor node which is performing the measurements is identified as the "Local node" while the sensor node which is being measured is identified as the "Target node". Similarly, the attaching robots of these sensors are termed as the "Local robot" and the "Target robot" respectively.

2.3.2 Sensor node design

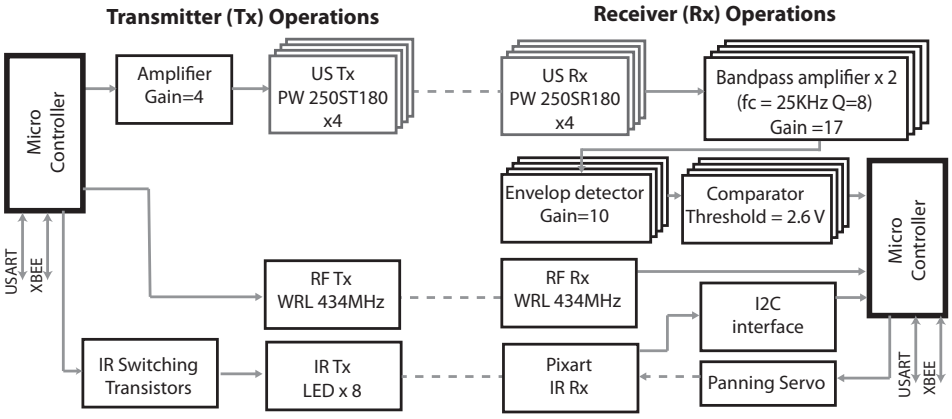

Figure 2.6: Sensor node hardware architecture

Figure 2.6 illustrates a functional block diagram representing various signal processing modules of transmitting and receiving nodes. The hardware has been designed in such a way that all modules are embedded in a single node and the user has the flexibility to choose the mode of operation (i.e. transmission or reception) using software. The range measurement sensor design uses an array of directional ultrasonic

transmitters (Prowave 250ST160) and an array of receivers (Prowave 250SR160). The transmitter bursts an ultrasonic tone of 25 kHz with 20 Vpp amplitude. The received signal undergoes an amplification, bandpass filtering, and envelope edge detection process to generate a digital pulse corresponding to the received 25 kHz ultrasonic tone. An RF transceiver pair ensures a clock synchronization of $\pm$ 5 μs, which only contributes to the range measurement error by less than 4 mm. A micro-controller measures the time between the RF synchronization pulse and the received processed ultrasonic pulse for TOA measurement. It is necessary to introduce bandpass filtering stages to filter out strong 40 kHz signals emitting from robots. These signals are generated from the sonar-based obstacle avoidance sensors and height measurement sensors attached to the robots which operate in close proximity to the 25 kHz receivers of the proposed module. Subsequent fine tuning of the receiver gains was necessary to remove the noise generated from the rotors of the MAVs.

The vision sensor used in the study is a PixArt computer vision IR target tracking sensor, which is commonly used for bearing estimation purposes of MAVs [69, 4]. The embedded processor of the sensor has the ability to perform image analysis and target detection tasks in order to provide the pixel positions of perceived IR sources. The image sensor has a limitation of recognizing only four targets. This limitation is effectively surpassed by using synchronized illumination of the IR markers on the robots, which in turn solves the measurement correspondence problem. An omnidirectional IR source was employed using a circular array of pulsed IR LEDs as the tracked target. A panning motor assembly performs IR Search and Track (**IRST**) tasks to extend the field of view of the sensor. The IR target tracking sensor has low computational overhead as compared to using a regular camera, mainly due to the fact that it does not require additional feature detection tasks for bearing measurement. Work in [8] reports modulation of IR signals with carrier frequencies of 455

KHz, to improve detection and enable robust correspondence. However, the update rate of the PixArt sensor is limited to a 100 Hz range, which makes it difficult to implement IR signal modulation schemes to improve the signal detection capability of the receiver.

The proposed sensor uses a dedicated Zigbee network for measurement communication. Additionally, each node is capable of establishing serial communication with the attaching robot and this allows the system to use the Wifi network and other resources of the attaching robot. The experimental system used for this study consists of a centralized host running the Robot Operating System (**ROS**). ROS nodes were used to communicate with each robot and each sensor node using the available Wifi or Zigbee network. This allows measurement calibration, analysis, and filtering operations to be performed at a centralized location for experimental purposes.

2.3.3 Sensor calibration

2.3.3.1 Ultrasonic range measurement calibration

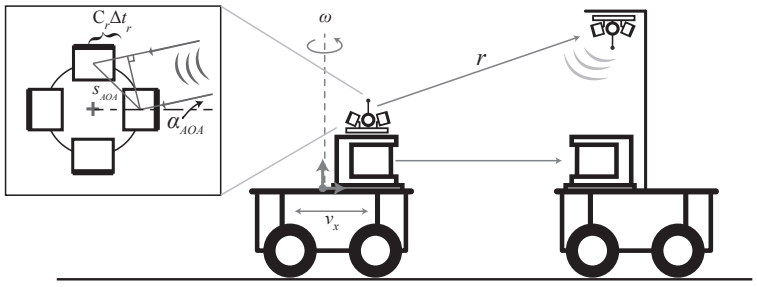

Figure 2.7: The experimental setup used for ultrasonic range and angle of arrival calibration

The measurement model selected for range measurement is given by

$$r = C_{air} t_r + b_r + \nu_r \tag{2.1}$$

where r is the range between the two nodes, C_{air} is the sound propagation speed in air, t_r is the TOA of the ultrasonic signal, b_r is a measurement bias term, and ν_r denotes the measurement noise term. The measurement noise is assumed to be drawn from a zero mean Gaussian distribution with standard deviation σ_r. In order to identify the parameters of the model given by (2.1), a calibration data set is required. For this purpose, a mobile robot with a receiver node fixed at a known height was maneuvered relative to another robot having a transmitter node. The measurements t_r were recorded from the receiver node along with a known set of range values r, which were derived from laser measurements taken from the robots.

In order to identify the model parameters, a nonlinear least-squares optimization process was performed using the Matlab Optimization Toolbox^{TM}. For this purpose, a cost function was defined as the sum of errors between the known range r, and the measured range given by (2.1). An identical optimization process was used for all parameter estimation tasks of this sensor. The values for parameter uncertainties were found by a first order propagation of the error covariance. The identified model parameters are given as follows.

Model parameters- Range measurement model (2.1)	
C_{air}	0.34 mm/μs ($\pm$ 4.7e-05)
b_r	-384.23 mm ($\pm$ 0.77)
$E(\nu_r)$	-0.098736 mm
σ_r	9.6978 mm
Optimization	Data size: 18000
	Outliers: 0.70 %

Figure 2.8 illustrates the error characteristics of the sensor and the results indicate good agreement with the linear model (2.1). Figure 2.9 illustrates the error variation with increasing distance between the transmitter and the receiver, where consistent performance is observed within the measurable range.

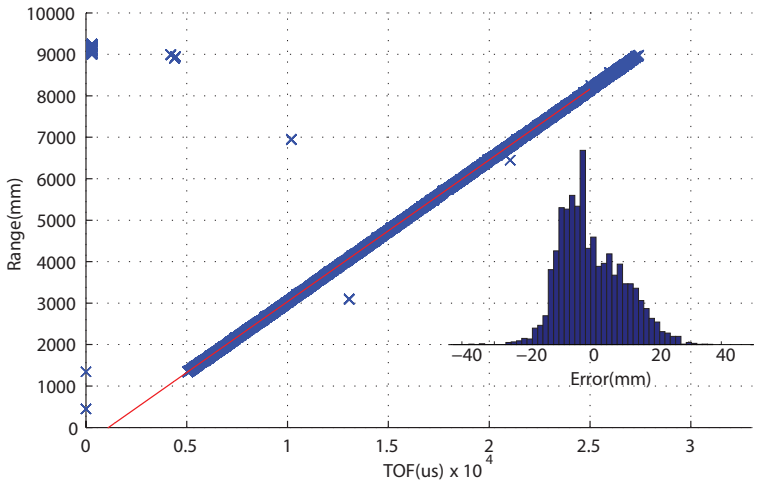

Figure 2.8: Ultrasonic range calibration plot and the error histogram of the linear measurement model

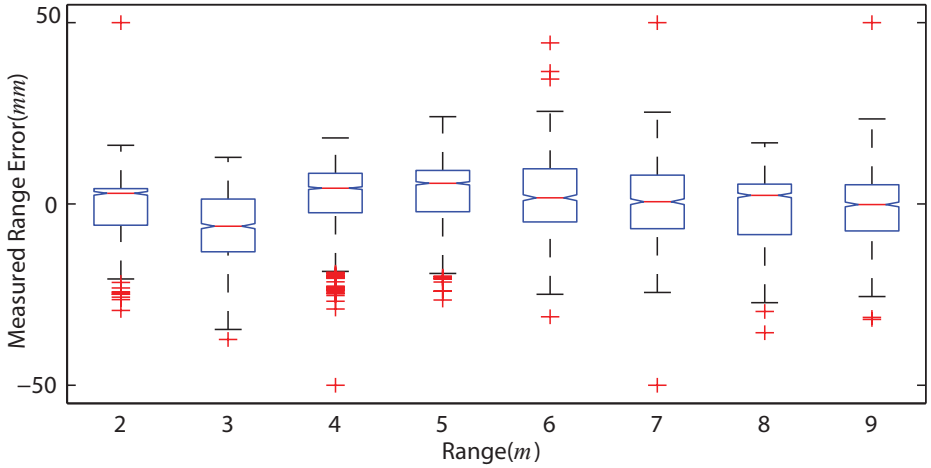

Figure 2.9: Ultrasonic range accuracy variation vs. separation between transmitter and receiver

2.3.3.2 Ultrasonic angle of arrival measurement calibration

The AOA estimation is performed using the TOA measurements of different receivers of the array. Due to the use of an array with four receivers, the receiver with minimum TOA provides a coarse estimate of the signal's direction of arrival with an accuracy of $\pm$ 45°. In order to improve this estimate the difference in TOA between receivers is used. The mathematical model for angle of arrival of a far field acoustic source is

given by

$$\alpha_{\text{AOA}} = \cos^{-1}\left(\frac{C_{air}\Delta t_r}{s_{\text{AOA}}}\right) + \lambda_{\text{AOA}} + \nu_{\text{AOA}} \tag{2.2}$$

where s_{AOA} is the separation between a pair of receivers, λ_{AOA} is a bias term, and Δt_r is the difference in TOA between the receivers. The receivers that are not facing the signal direction are prone to multi-path detection due to their directional sensitivity. To avoid this situation, α_{AOA} estimation is performed while considering only the minimum difference in TOA (Δt_r) between all receiver pairs of the array. This allows the nonlinear model given by (2.2) to be simplified into a linear model as given by

$$\begin{aligned} \alpha_{\text{AOA}} &= \tfrac{\pi}{2} + \lambda_{\text{AOA}} - \tfrac{C_{air}}{s_{\text{AOA}}}\Delta t_r \\ \alpha_{\text{AOA}} &= m_{\text{AOA}}\Delta t_r + b_{\text{AOA}} + \nu_{\text{AOA}} \end{aligned} \tag{2.3}$$

where, the parameters m_{AOA} and b_{AOA} are the gradient and bias terms for each sensor pair. The measurement noise is denoted by ν_{AOA} which is assumed to be a Gaussian random variable with standard deviation σ_{AOA}.

For AOA calibration the sensor node shown in Figure 2.7 was rotated 360° to record the TOA measurements of different receivers. The gyro corrected heading of the attaching robot was used as a reference value for α_{AOA}. The parameters of the AOA measurement model were identified through an optimization process.

Model parameters- Linear difference in TOA model (2.3)	
$\mathbf{m}_{\text{AOA}}$	$\begin{bmatrix}-492 & -385 & -540 & -348\end{bmatrix} \pm \begin{bmatrix}12.73 & 8.89 & 8.07 & 7.16\end{bmatrix}^{\circ}/ms$
$\mathbf{b}_{\text{AOA}}$	$\begin{bmatrix}64.24 & 153.70 & -51.25 & -148.39\end{bmatrix} \pm \begin{bmatrix}0.81 & 0.54 & 0.56 & 0.46\end{bmatrix}^{\circ}$
$E(\nu_{\text{AOA}})$	0.8423 °
σ_{AOA}	5.8005 ° (0.2 - 5 m)
Optimization	Data size: 18000
	Outliers: 2.11 %

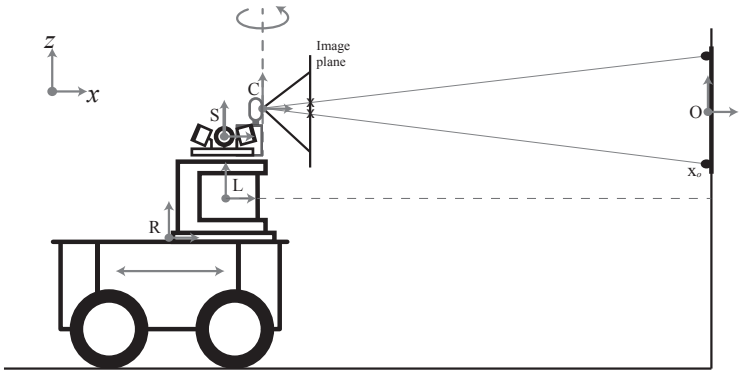

Figure 2.10: The test bed arrangement used for infrared bearing measurement calibration

2.3.3.3 Infrared bearing measurement calibration

The transformation frames associated with a robot which are relevant to the vision based bearing sensor calibration are introduced here. As illustrated in Figure 2.10, let $\{S\}$ be the transformation frame attached to the ultrasonic array, $\{C\}$ be the frame attached to the IR image sensor, $\{R\}$ be the frame attached to the robot, $\{L\}$ be the frame attached to the laser and $\{O\}$ denote the frame attached to the calibration rig. For a given set of transformation frames $\{S\}$ and $\{C\}$, let ${}^{s}\mathbf{p}_{c}$ denote the position of frame $\{S\}$ with respect to frame $\{C\}$, and ${}^{s}\mathbf{R}_{c}$ denote the rotation matrix that projects vectors expressed in frame $\{S\}$ to frame $\{C\}$.

A pinhole camera model is selected for the image sensor as given by equation (2.4). This is due to the low levels of nonlinear lens distortion reported for the image sensor [78] and due to the computational simplicity the model provides.

$$\mathbf{b}_{\text{px}} \quad = \quad \mathbf{K}_{c}[{}^{c}\mathbf{R}_{o} \; {}^{c}\mathbf{p}_{o}]\mathbf{x}_{o} + \boldsymbol{\nu}_{\text{px}} \tag{2.4}$$

For a given set of target points $\mathbf{x}_o$ attached to a calibration rig, the model finds its projection $\mathbf{b}_{\text{px}} = [1, \; x_{\text{px}}, \; y_{\text{px}}]^{T}$ on the image plane. First, the points $\mathbf{x}_o$ that are

expressed in frame $\{O\}$, are transformed into the camera fixed frame $\mathbf{C}$ using the matrix transformation $[{}^{c}\mathbf{R}_{o}\ {}^{c}\mathbf{p}_{o}]$. The transformed points are then projected to the image plane using a camera matrix $\mathbf{K}_{c}$ given by

$$\mathbf{K}_{c} = \begin{bmatrix} 1 & 0 & 0 \\ cc_{x} & f_{x} & 0 \\ cc_{y} & 0 & f_{y} \end{bmatrix}$$

where $[f_{x},\ f_{y}]$ denotes the focal lengths and $[cc_{x},\ cc_{y}]$ denotes the image centre. The measurement noise $\boldsymbol{\nu}_{\text{px}}$ is assumed to be a random variable drawn from a zero mean Gaussian distribution with covariance $\boldsymbol{\Sigma}_{\text{px}}$.

Calibration of the PixArt vision sensor is reported in different sources [78]. The methods require pixel measurements of a known four-point 2D structure fixed on frame $\{O\}$ placed randomly at different poses. Therefore, each new image introduces six unknown extrinsic parameters, to be estimated by using four projected measurements. Due to the limited number of available measurements per image, the resulting calibration has higher uncertainty.

This study performs calibration by using laser scan measurements to estimate the changing extrinsic parameters, i.e., the transformation from frame $\{S\}$ to frame $\{O\}$. As a result, the effective number of parameters that should be optimized is reduced to ten, which include the four intrinsic parameters of the camera and the six common extrinsic parameters describing the transformation $[{}^{c}\mathbf{R}_{s}\ {}^{c}\mathbf{p}_{s}]$ between frames $\{C\}$ and $\{S\}$.

The calibration rig was fabricated using four IR targets (LEDs) located at positions $\mathbf{x}_{o}$, which are expressed in frame $\{O\}$. In order to generate a calibration data set, the calibration rig was fixed onto a vertical surface and the robot equipped with the sensor was maneuvered on a horizontal plane as illustrated in Figure 2.10. The image

sensor panning motor was set to incremental rotation during the calibration process to capture errors generated by the sensor movement. For optimization, the parameters were initialized using nominal values and measurements. The optimization was performed to minimize the cost function given by

$$\underset{\mathbf{K}_c,\, {}^c\mathbf{R}_s,\, {}^c\mathbf{p}_s}{\operatorname{argmin}} \quad \sum^{\forall k} \left| \mathbf{b}_{\text{px}}^{(k)} - \mathbf{K}_c [{}^c\mathbf{R}_s \;\; {}^c\mathbf{p}_s] (\mathbf{x}_o + {}^s\mathbf{p}_o^{(k)}) \right|$$

where the superscript (k) was used to index the measurements $\mathbf{b}_{\text{px}}^{(k)}$ and transformations $[{}^c\mathbf{R}_o^{(k)} \;\; {}^c\mathbf{p}_o^{(k)}]$ related to each image k. The vector ${}^s\mathbf{p}_o^{(k)}$ was taken as a known quantity, which is derived from the measurements of the laser scanner. The optimized parameters of the bearing estimation model are as follows.

Model Parameters- Bearing measurement model (2.4)	
$\mathbf{f}_c$	$\begin{bmatrix}1345.0 & -1346.1\end{bmatrix} \pm \begin{bmatrix}18.5 & 13.6\end{bmatrix}$ px
$\mathbf{cc}$	$\begin{bmatrix}650.0 & 401.6\end{bmatrix} \pm \begin{bmatrix}66.7 & 44.8\end{bmatrix}$ px
${}^c\mathbf{R}_s$	$\begin{bmatrix}1.4 & 7.0 & 4.8\end{bmatrix} \pm \begin{bmatrix}0.1 & 2.9 & 1.9\end{bmatrix}^\circ$ (roll, pitch, yaw)
${}^c\mathbf{p}_s$	$\begin{bmatrix}0.07 & -20.4 & 21.50\end{bmatrix} \pm \begin{bmatrix}0.40 & 0.40 & 4.70\end{bmatrix}$ mm
$E(\boldsymbol{\nu}_{px})$	$\begin{bmatrix}-4.6e^{-05} & 3.91e^{-06}\end{bmatrix}$ px
$\boldsymbol{\Sigma}_{px}$	$\text{diag}(\begin{bmatrix}5.17^2 & 3.71^2\end{bmatrix})$ px^2
Optimization	Data size (features): 4000, Outliers ≈0.0%

Figure 2.11 illustrates the pixel reprojection error of all images after the optimization process. Figure 2.12 presents the bearing error measurement characteristics against the range between the transmitter and the receiver. The calibrated bearing measurement module was able to achieve sub-degree level consistent accuracy across the measurement range.

2.3.4 Measurement configurations

The proposed sensor node is designed with the capability to attach to both ground and aerial platforms. The nodes can be configured either to be a transmitter or a

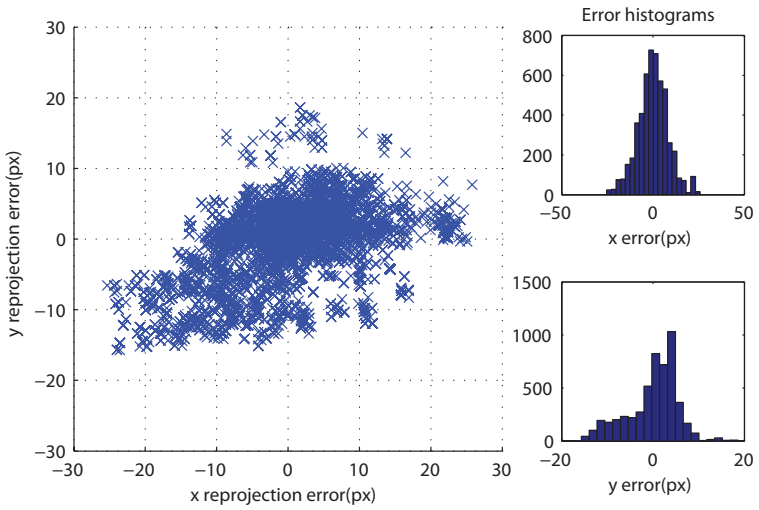

Figure 2.11: Pixel reprojection error of the calibrated vision sensor model.

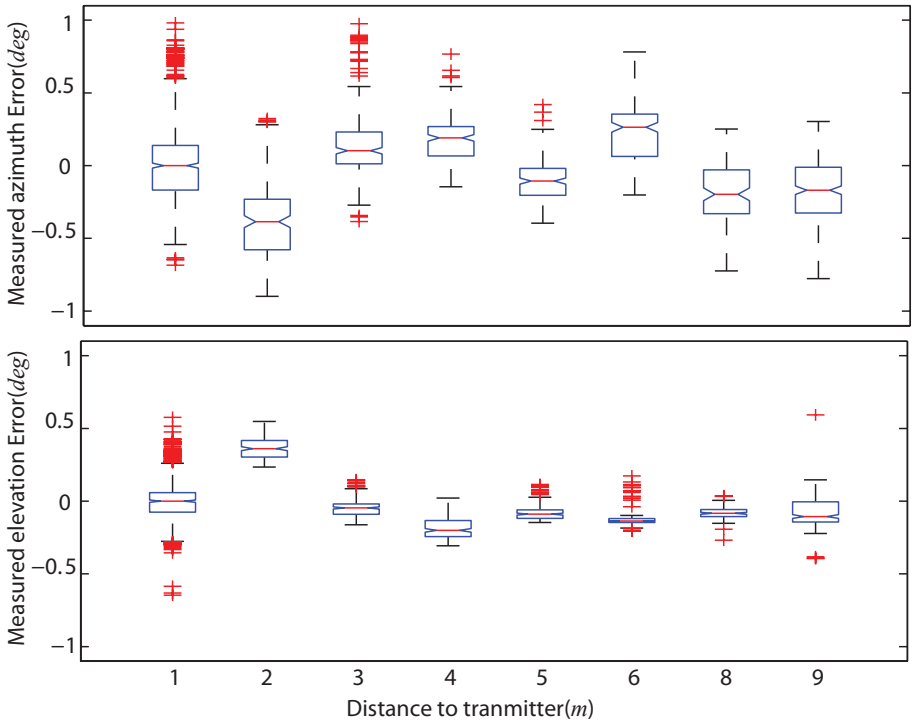

Figure 2.12: IR bearing measurement accuracy variation vs separation between transmitter and receiver.

receiver dynamically using a network coordinator. A full sensor module performs the ultrasonic processing, IR processing, motor control, communication, and computation tasks in one measurement cycle. In order to accurately initialize each cycle, a network

coordinator transmits RF timing synchronization pulses along with the information describing the role each node should assume. Upon receiving this information, the receiving sensor node executes the scheduled tasks corresponding to the role it is assigned for that particular cycle. The scheduling of the tasks corresponding to the different roles of the transmitters and receivers is illustrated in Figure 2.13. The assignment of the roles establishes the network measurement configuration of the multi-robot system.

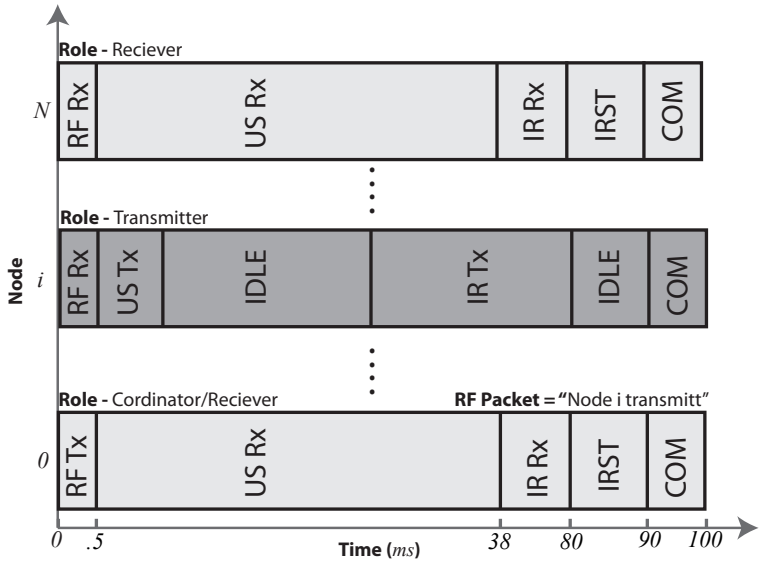

Figure 2.13: The scheduling of different tasks of the transmitter and receiver nodes: Rx- reception, Tx- transmission, US- Ultrasonic, COM- Xbee or serial communication

This study discusses two measurement configurations of the sensor network. The simplest is a static measurement configuration, with a single transmitting node and multiple receiving nodes performing simultaneous range and bearing measurements of the transmitter. This approach is termed as the *Star* measurement configuration (Figure 2.14a). The time taken to complete one set of measurements in this configuration is denoted by T (=100 ms).

Simultaneous measurement of multiple transmitters is possible using either code division multiple access or frequency division multiple access methods. These meth-

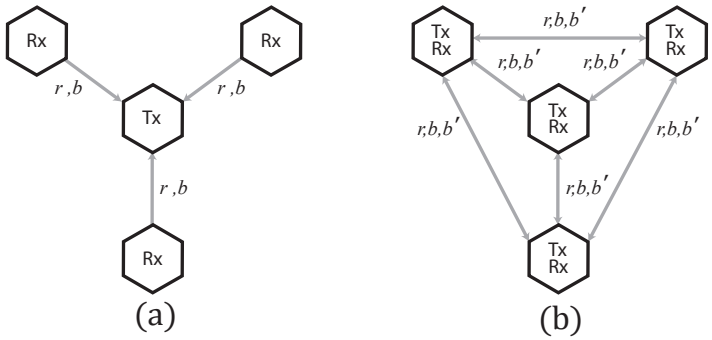

Figure 2.14: (a) Star measurement configuration. (b) Mesh measurement configuration.

ods have limited applicability for the proposed design due to the limited bandwidth of the receivers used. Therefore, scaling beyond one transmitting node in the proposed design is only realizable through Time Division Multiple Access (**TDMA**) methods, where different time slots are used by each transmitting node in the system. The *Mesh* measurement configuration (Figure 2.14b) uses TDMA to cycle the transmitting role throughout the network while limiting signal transmission to only one node during one cycle. The protocol takes nT total time to complete a full set of measurements in a network of n nodes. Figure 2.15 illustrates the scheduling of different tasks between the nodes in the case where three nodes are assuming a *Mesh* measurement configuration. Table 2.2 summarizes the characteristics of the sensor node and resource demand for each measurement configuration. Therefore, a *Star* configuration is necessary for fastest update speeds, while a full *Mesh* network provides the maximum information for filtering purposes.

The scheduling of tasks presented in Figure 2.13 is designed for sequential processing. It is possible to achieve faster update rates by parallel implementation of IR reception operations and Ultrasonic reception operations. Thus an optimized design would allow the cycle times to be as low as 40 ms. This can only be achieved by employing fast micro-controller units with enough hardware resources to simultaneously

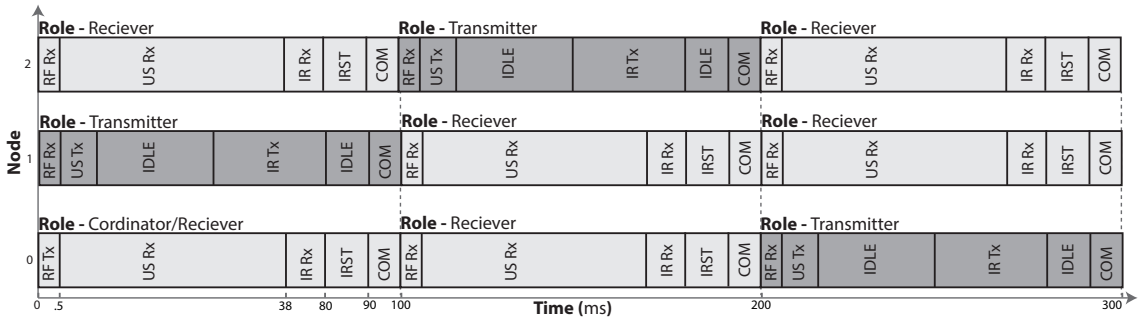

Figure 2.15: TDMA scheduling between 3 nodes

process multiple threads.

The designed sensor does not utilize a standard clock synchronization approach such as the network time protocol. Alternatively, the proposed method uses a basic RF transmitter with direct physical layer access, to send a synchronization pulse to initiate measurement cycles at each node. This is found to be simple and standard in many similar applications [71, 6]. The worst case error contribution of this method was calculated to be 3.0 mm for range measurement, and 0.015% for cycle time error. These low error statistics can be considered insignificant for this particular application. However, it is important to note that these errors can be minimized by opting for clock synchronization methods such as [76], which provides a clock drift compensation strategy applicable to ZigBee channels with Media Access Control (**MAC**) layer time stamping capability.

The presented sensor nodes are capable of relative measurement in a network of nodes independent of the attaching platforms and therefore are suitable for implementation in a wide class of robots.

2.3.5 Comparison with other IRRM solutions

Table 2.3 summarizes the main IRRM approaches reported in the literature for localization of ground and aerial systems. Accordingly, the proposed approach introduces

Table 2.2: Characteristics of the sensor network

Range Accuracy	$\sigma_r = 1.0$ cm	
Azimuth Accuracy	$\sigma_\alpha = 0.3°$	
Elevation Accuracy	$\sigma_\beta = 0.2°$	
Measurement Range	9 m	
Power Consumption	RX : 0.6 W TX : 6 W	
Weight	120 g (with attach brackets)	
Dimensions	140 x 85 x 45 mm (with attach brackets)	
Configurations	$Mesh$	$Star$
Measurements / Cycle	4^nC_2	$2(n-1)$
Cycle Time	nT	T=100 ms
Measurement Rate	$\frac{4^nC_2}{nT}$	$\frac{2(n-1)}{T}$

Table 2.3: Summary of available 3D IRRM solutions

Author /Method	Range error cm RMSE (Max) 3 m	6 m	Azimuth error RMSE (Max) 3 m	6 m	Elevation error RMSE (Max) 3 m	6 m	Operating range	Update rate /robot
Eckert et al. [66] US-TOA/AOA	<1(<1)	1.5(2)	10.2°	22.6°	-	-	5.6 m	30 Hz
Roberts et al.[8] IR-RSS/AOA	10(14.2)	30(45)	<3.1(4.3)°	3.1(13.9)°	-	4.4(9.4)°	**12** m	**1** kHz
Proposed method US+Vision	**1.0**(3.7)	**0.8**(4.4)	**0.2(1.0)**°	**0.3(1.3)**°	**0.2(0.1)**°	**0.2(0.1)**°	9 m	10 Hz
Achtelik et al.[3] Stereo vision	Localization error: X 4.2 cm Y 12 cm θ 2°						4 m FOV	15 Hz

significant improvements of combined range and bearing measurement accuracies. The signal filter designs and signal modulation in the proposed approach effectively handles the common 40 kHz ultrasonic disturbance sources evident in robot networks. This was a necessary improvement over the reported ultrasonic-only IRRM methods [5, 6, 66] for practical implementation. The correspondence problem faced by vision-only approaches [3, 1] was addressed effectively in this design via synchronized illumination of IR visual targets. Compared to the state-of-the-art system in [8], the proposed approach focuses on multi-platform attachable, low-power and payload design with higher accuracy. It should be noted that the higher accuracies are achieved at lower update rates when compared to [8]. However, the sensor networking protocols are designed so that multiple robots can simultaneously localize at a modest

frequency of 10 Hz, which is sufficient for relative localization purposes.

2.4 Results

The experimental results validate three main features of the proposed sensor network. The first experiment validates the capability of the sensor network to perform spatial measurements while being scalable using TDMA methods. For this purpose a static pose estimation case was considered where three sensor nodes performed measurements using the *Mesh* protocol. The second experiment validates the ability of the sensor to address acoustic disturbances from height sensors and obstacle avoidance sensors under dynamic conditions. The third experiment validates the capability of the sensor to operate onboard a flying MAV and analyzes the robustness of the system to acoustic disturbances generated from rotors of an MAV.

2.4.1 Static 3D positioning

The experimental sensor network used for this localization exercise consisted of two ground robots and one aerial robot. The relative measurements were captured at a centralized location, where system performance was evaluated. The aerial robot was fixed at an elevated location for this experiment. The height measurement sensors and the ultrasonic obstacle avoidance sensors of the robot platforms were operating at their nominal rates during this experiment. The laser scanners attached with the ground robots were used for ground truth validation purposes. Figure 2.16 illustrates the formation of the robot team and the real-time ROS visualization of the generated measurements. Table 2.4 summarizes the positioning performance of the sensor network, where a static localization accuracy in the order of centimeters was achieved among all pairs of sensors in the network.

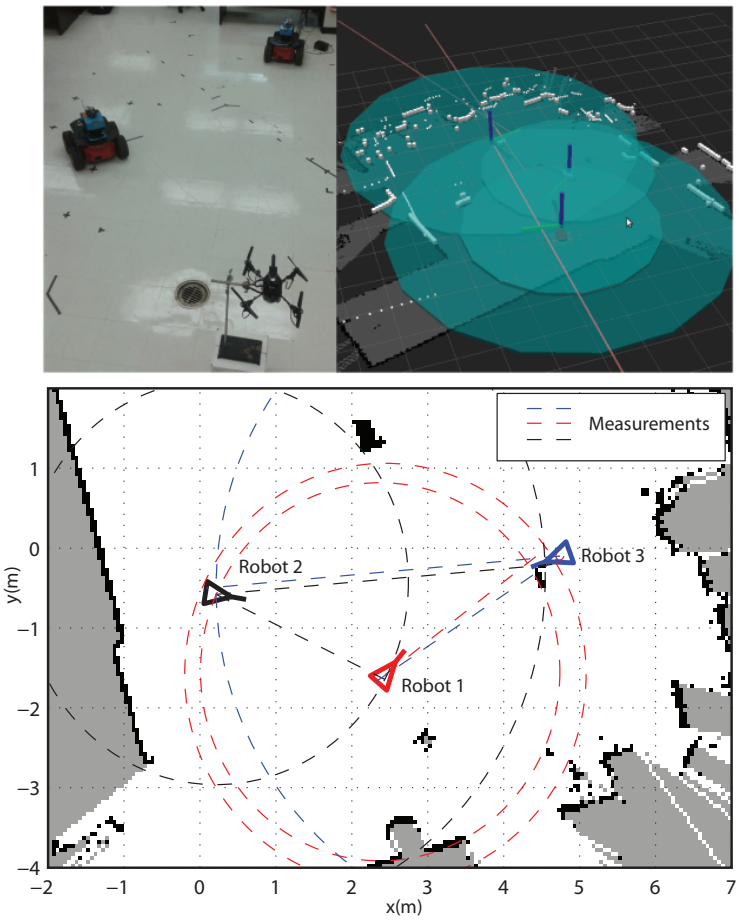

Figure 2.16: Static positioning of the sensor network.

Table 2.4: Static positioning performance of the sensor network

Measuring Node	**Measured Node**	x error (m)		y error (m)		z error (m)	
		RMSE	Max	RMSE	Max	RMSE	Max
1	3	0.0136	0.0503	0.0031	0.0114	0.0006	0.0020
2	1	0.0099	0.0233	0.0023	0.0054	0.0008	0.0017
3	2	0.0197	0.1013	0.0058	0.0296	0.0008	0.0043
3	1	0.0620	0.1629	0.0153	0.0404	0.0035	0.0091

2.4.2 Dynamic 3D positioning

For the purpose of dynamic 3D positioning error validation, the MAV was mounted on a ground robot which allowed the MAV to be maneuvered along a smooth trajectory and the position of the MAV to be derived from the laser-based localization capability

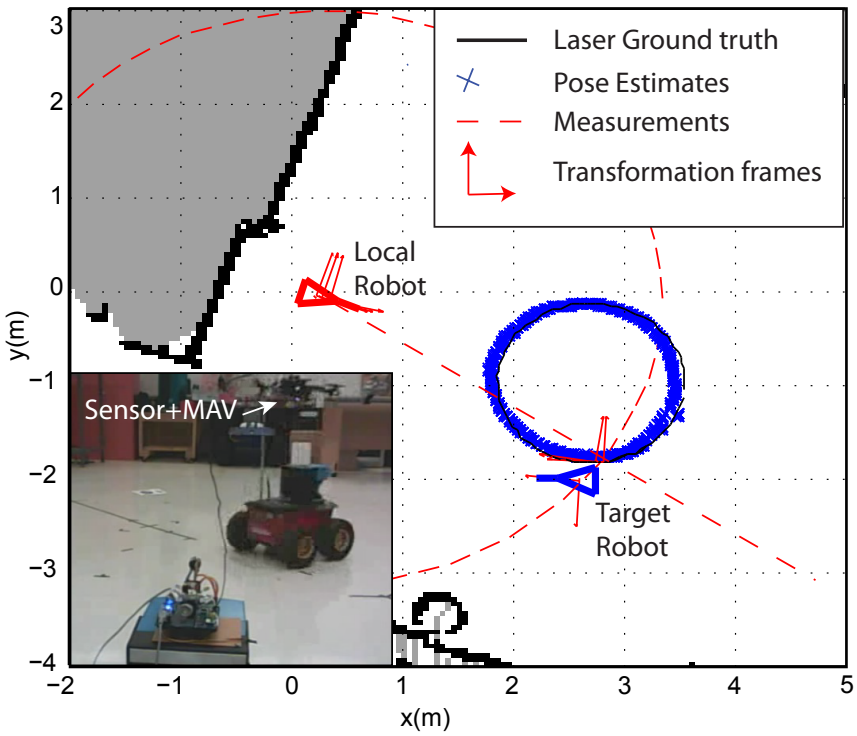

Figure 2.17: Actual and estimated path for a circular trajectory localization experiment

of the ground platform. Figure 3.13 illustrates the trajectory the MAV followed while mounted on the robot, and Figure 2.18 and Figure 2.19 illustrate the performance of the relative 3D positioning sensor. There were minimal occlusions and outliers during this experiment. The sensor successfully performed accurate measurements under these dynamic conditions while suppressing the disturbances introduced by the height and obstacle avoidance sensors.

2.4.3 Dynamic 3D positioning of an MAV

In order to validate the applicability of the sensor for MAVs, the sensor was attached and interfaced to a flying MAV and the measurements were sent to ROS through a WiFi link for validation. An April Tag based ground truth system [70] was established for ground truth validation. The MAV was maneuvered along a random trajectory

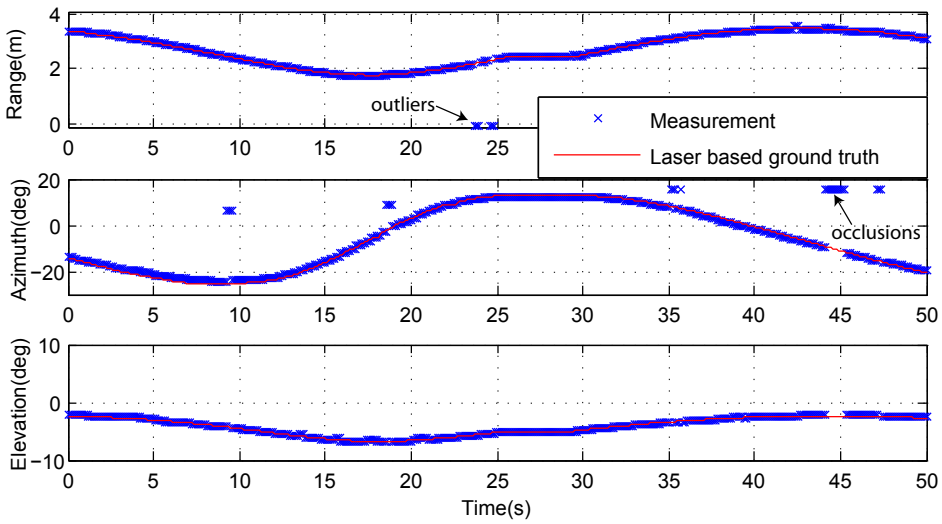

Figure 2.18: The circular trajectory of the robot and the measurements from the sensor

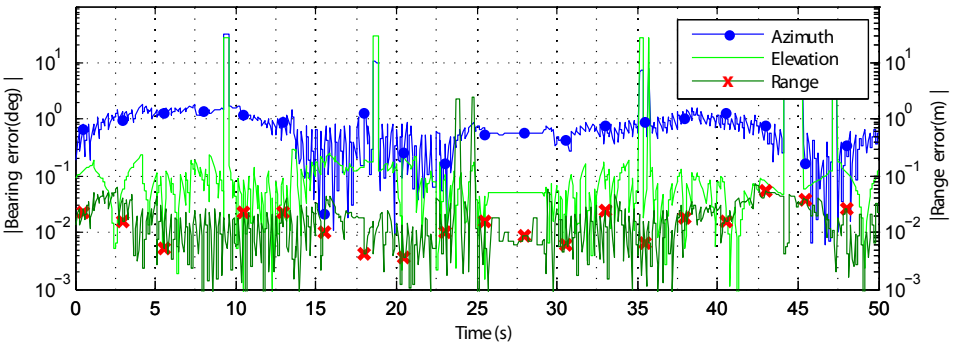

Figure 2.19: The measurement errors for the smooth circular trajectory of the robots

while the attached sensors on robots successfully positioned its flight path (Figure 2.20, Figure 2.21).

This particular experiment produced many outliers which are filtered in the results given in Figure 2.21 and Figure 2.22. The effect of the outliers and the sensor noise can be filtered using an EKF in order to estimate a continuous trajectory from the corrupted measurements. The results of an EKF applied to the measurements are presented in Figure 2.23 and the estimated trajectory is superimposed on the actual path of the MAV illustrated in Figure 2.20. Details relating to the EKF design for

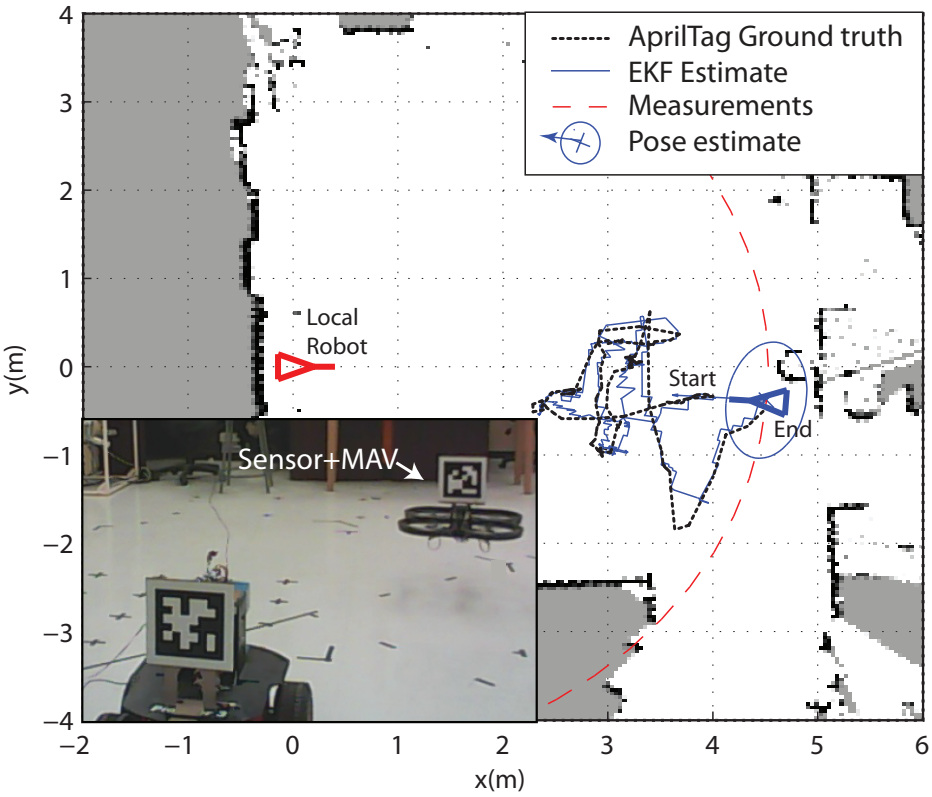

Figure 2.20: Actual and estimated path for an MAV following a random flight trajectory

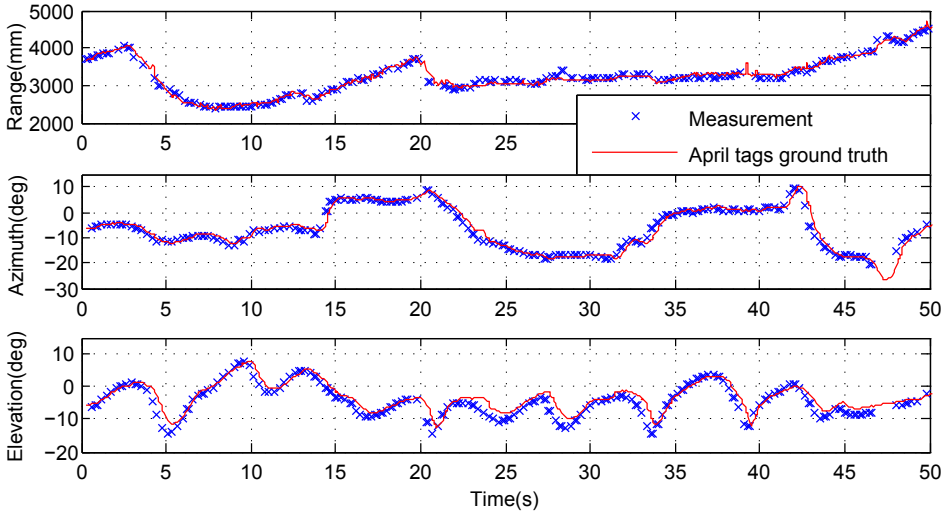

Figure 2.21: The 3D trajectory of the flying MAV and the measurements from the sensor

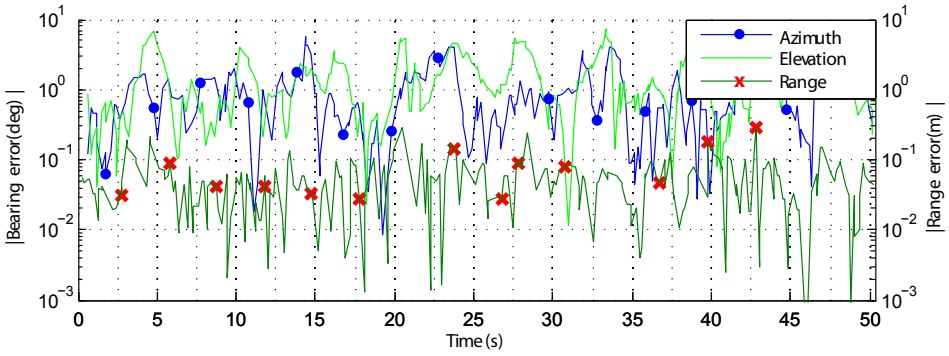

Figure 2.22: The measurement errors for the 3D trajectory of the flying MAV

the problem are discussed in later chapters.

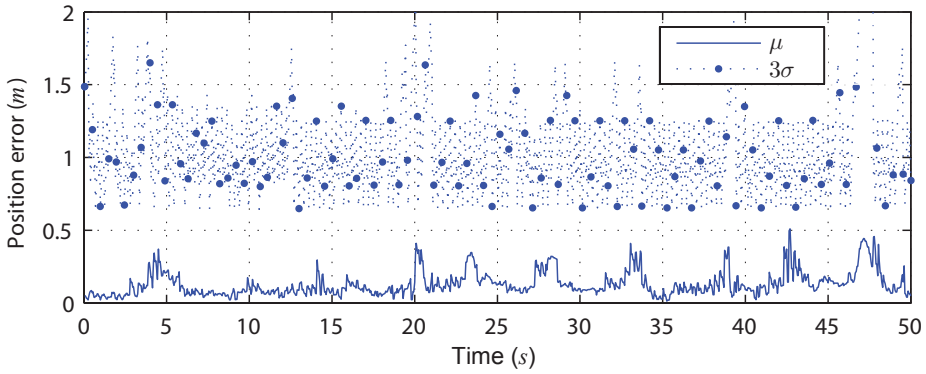

Figure 2.23: Localization results for the random flight trajectory using an EKF

The discrepancies between the trajectories of the AprilTags ground truth system and the proposed sensor system, as seen in Figure 2.20, originated from two main sources. The first is the accuracy limitation of the AprilTags system. The error statistics of the AprilTags system were found to be $\sigma_r = 2.8$cm, $\sigma_\alpha = 0.05°$, and , $\sigma_\beta = 0.05°$, by using the calibration parameters of the camera used for the ground truth system, and using a laser based range performance benchmarking of the AprilTags estimates. These error statistics signify poor range estimation capability of the ground truth reference system as compared to the proposed sensor. The second error source is the reduced measurement detection rate that occurs when the sensor operates on

a flying MAV. This decreased measurement rate causes the EKF updates to perform sudden corrections when the platform is performing high velocity maneuvers as seen in Figure 2.20. The effective measurement rate decreased mainly due to disturbances caused by the rotors, power source noises generated by the running motors, and visual occlusion of the IR emitters.

2.5 Conclusion

This chapter presented an innovative sensor network for spatial relative positioning of indoor ground and aerial robots. The method requires a minimum of two robots performing relative measurements of each other and achieves measurement accuracies of 0.97 cm RMSE for range and 0.3° RMSE for bearing. The sensor nodes are scalable with *Star* or *Mesh* protocols with a maximum of 10 Hz update rates over a detection range of 9 m. The nodes are applicable across many ground and aerial robotic platforms with their ability to reject disturbance sources of acoustic obstacle detection sensors, the low weight of 120 g, and a low mean power requirement. The outlined features were successfully validated by multiple experiments on a ground and aerial robotic system.

Although the proposed approach constitutes a working system, the design is not optimized for measurement range, power consumption, and speed. Additionally, the current iteration of the design suffers from the following main drawbacks:

- The vision based bearing measurement method has a limited field of view in comparison to the omnidirectional reception capability of the acoustic modules. Although a panning servo mechanism is implemented for improved field of view, this has poor performance in terms of speed and increases the power consumption of the sensor. In order to address the field of view limitation of the design,

one possible improvement is to use an omnidirectional lens setup. Another approach would be to establish better ultrasonic based bearing measurement capability and use a vision sensor only for improvement of the estimates in its field of view.

- In the current form the sensor is not applicable in outdoor settings. This is mainly due to the inability of the vision sensor to operate under direct sunlight. A solution for this is not to rely on IR features for bearing measurement and use passive visual feature detection by a standard CMOS camera for bearing measurement. However, the feature detection method employed should be kept elementary to meet the computational constraints of the sensor. Improving the ultrasonic bearing measurement capability would also contribute to enabling the system in outdoor settings, since ultrasonic modules are equally applicable for indoor and outdoor environments.

- The IR emitters consume a considerable amount of power in comparison to the acoustic modules. This issue can also be addressed using passive features in place of active features for bearing measurement.

- The ultrasonic sensors experience signal disturbances when running onboard an MAV. Although the disturbances generated from obstacle measurement sensors are effectively handled by bandpass filtering, the noise generated from the rotors remains a dominant disturbance source for the ultrasonic modules. A possible solution for this is to use encoded signals and better signal processing for disturbance suppression.

The next major version of the sensor, which effectively addresses the said drawbacks of the current design, is under development. The developed sensor uses ultrasonic modules with improved bearing measurement capability and keeps vision based

passive feature detection as an auxiliary source for measurement improvement. This is further inspired and enabled by recent developments in omni-directional MEMS microphones [79] and surface mount ultrasonic sensors [80]. It is expected that an optimized design of this sensor would constitute an integral part of a heterogenous multi-robot system, allowing team-based localization without heavy resource demand on the attaching platforms.

Chapter 3

Relative Localization: Observability

Prior to the design of filters for a relative localization task, it is necessary to establish theoretical limitations related to the problem. Nonlinear observability analysis tools [43] allow to gain the necessary insight required for filter design. Although numerous studies are reported for relative localization [81, 46], these studies do not investigate the relative localization problem under constraints related to platform velocity sensing capabilities. This chapter[1] analyzes observability of relative localization in detail for practical scenarios where there's limited availability of platform velocities. The analysis deduces the necessary conditions and design requirements relevant to a relative localization filter design, which are validated through multiple numerical and experimental studies.

[1] This chapter is based on the following publications of the author:

* O. De Silva, G. K. I. Mann, and R. G. Gosine, *"Pairwise Observable Relative Localization in Ground Aerial Multi-Robot Networks,"* in European Control Conference, 2014, pp. 324-329.

3.1 Introduction

In a multi-robot team, observability refers to the ability of a robot to estimate the relative formation of neighbouring team members using available measurements. When relative positions are measured among all robots, the problem can be solved in a deterministic manner by considering the constraints introduced by the polygonal connectivity between robots [32]. However, for robustness of a relative localization system, it is desirable to have full observability between each pair of robots in the team. This would allow the two robots to localize each other without relying on measurements gathered by other robots in the network. This pairwise approach imposes a loose set of constraints in terms of network connectivity for localization purposes. This property enables a team to execute critical behaviours such as sense and avoidance and formation maintenance with a minimum of two robots, provided that they are in the measurable vicinity of each other.

Several factors affect the observability between a pair of robots. The first important factor is the availability of sufficient measurements for estimation. For the relative localization problem, available measurements may include platform velocities, IRRMs, and inertial sensors. The second factor is the complexity of the estimated model. i.e, the number of states of the estimated model. For the relative localization problem the states of a system may include relative position, relative orientation, and unknown platform velocities. As the order of the estimated state increases, the estimation task becomes mathematically complex and may even result in the system losing its observability due to unavailability of sufficient measurements. The third factor relates to the dynamic constraints that are inherent to the system. The dynamics of a platform introduce constraints in terms of the trajectory the system can assume, hence provides more information to solve the observability problem. A nonlinear observability analysis provides the necessary insight into these factors and establishes the

theoretical limits governing estimators such as EKFs used for the relative localization task.

Observability analysis relevant to relative localization of 2D multi-robot systems is presented in [81], and extensions to 3D are presented in [46]. Both the studies derive necessary conditions for observability assuming a scenario where platform velocity inputs are known. However, most aerial platforms do not have reliable platform velocity measurement systems, mainly due to the unavailability of sensors and the drifting nature of MAVs. In the case where platform velocities are available, these measurements would be only communicated intermittently at a low rate between the robots to meet communication bandwidth limitations. Therefore it is necessary to analyze the observability of multi robot systems for cases where platform velocity measurements are unavailable, which allows gaining the necessary insight for the purpose of implementing estimation frameworks.

This chapter performs a nonlinear observability analysis of a ground aerial system considering the cases of unknown velocity inputs, along with the cases of different relative measurement availability between the pair of robots. The IRRM sensing modality selected for this study is a sensor which measures the relative position which corresponds to main relative measurement methods proposed in literature for ground and aerial systems [3, 8, 61] and the relative measurement sensor proposed in this thesis. The chapter validates the theoretical constraints identified by the observability analysis using numerical simulations and experimental studies. The chapter concludes discussing the implications of this study in designing and deploying relative localization based robotic systems.

3.2 Preliminaries

This section introduces quaternion parameterizations, general notational definitions, and operators used throughout the thesis.

3.2.1 3D Rotation parameterization

The parameterization and development of system models presented in this thesis are primarily motivated by work in [85] and related standard text on classical mechanics. Quaternion parametrization is preferred over Euler angles (roll, pitch, yaw) for its singularity free representation of the rotation group [82]. A quaternion is denoted by $\bar{\mathbf{q}} = (q_0 \; q_1 \; q_2 \; q_3)^\mathsf{T} = (q_0 \; \mathbf{q}^\mathsf{T})^\mathsf{T}$ where for a unit quaternion $||\bar{\mathbf{q}}|| = 1$. A unit quaternion can be used to represent a rotation from a local frame $\{L\}$ to a target frame $\{I\}$ about an axis represented by a unit vector $\mathbf{a}$ with an angle of θ.

$$\bar{\mathbf{q}} \;\; = (\cos\theta/2 \quad \mathbf{a}^\mathsf{T} \sin\theta/2)^\mathsf{T} \tag{3.1}$$

The inversion and multiplication($*$) operations related to a quaternion are defined as follows.

$$\begin{aligned} \bar{\mathbf{q}}^{-1} \quad &= (q_0 \;\; -\mathbf{q}^\mathsf{T})^\mathsf{T} \\ \bar{\mathbf{q}} * \bar{\mathbf{p}} \;\; &= \begin{pmatrix} p_0q_0 - p_1q_1 - p_2q_2 - p_3q_3 \\ p_0q_1 + p_1q_0 - p_2q_3 + p_3q_2 \\ p_0q_2 + p_2q_0 + p_1q_3 - p_3q_1 \\ p_0q_3 - p_1q_2 + p_2q_1 + p_3q_0 \end{pmatrix} \end{aligned} \tag{3.2}$$

A vector $\mathbf{v}$ is expressed as $\bar{\mathbf{v}} = (0 \; \mathbf{v}^\mathsf{T})^\mathsf{T}$ when evaluating a quaternion expression. Therefore, a quaternion multiplication between two vectors corresponds to the standard cross product between them. Using the rotation quaternion between two frames, a vector $\mathbf{v}_i$ in frame $\{I\}$ can be expressed in frame $\{L\}$, i.e, $(\mathbf{v}_i)^l$ as $(\bar{\mathbf{v}}_i)^l = \bar{\mathbf{q}} * \bar{\mathbf{v}}_i * \bar{\mathbf{q}}^{-1}$.

A matrix representation of the rotation operation from frame $\{L\}$ to frame $\{I\}$ can be established using rotation matrices $\mathbf{R}_{l,i}$, in which case the vector rotation between the frames can be expressed as $(\mathbf{v}_i)^l = \mathbf{R}_{l,i}\mathbf{v}_i$. Both parameterizations allow global non singular representation of the rotation group . The unit quaternions make it easier to represent rotations as a state vector since it only has a dimensionality of 4, while the rotation matrices provide familiar matrix operations which are preferred in deriving filters. Rotation kinematics between two frames can be expressed in both quaternion and rotation matrix parameterizations as follows.

$$\dot{\bar{\mathbf{q}}} = \tfrac{1}{2}\bar{\mathbf{q}} * \bar{\omega} \quad \dot{\mathbf{R}} = \mathbf{R}\Omega \tag{3.3}$$

where $\Omega = [\boldsymbol{\omega}]_\times$ is the relative angular velocity between the frames expressed in the target frame ($\{I\}$). The operator $[\cdot]_\times$ is used to represent a vector $\mathbf{v}$ in its skew symmetric form.

$$[\mathbf{v}]_\times := \begin{pmatrix} 0 & -v_z & v_y \\ v_z & 0 & -v_x \\ -v_y & v_x & 0 \end{pmatrix} \tag{3.4}$$

The left and right matrix equivalents of quaternion multiplication are defined in (3.5).

$$\begin{aligned} Q^+ &= q_0\mathbf{I} + \begin{pmatrix} 0 & -\mathbf{q}^\mathsf{T} \\ \mathbf{q} & [\mathbf{q}]_\times \end{pmatrix} \\ Q^- &= q_0\mathbf{I} + \begin{pmatrix} 0 & -\mathbf{q}^\mathsf{T} \\ \mathbf{q} & -[\mathbf{q}]_\times \end{pmatrix} \\ \bar{\mathbf{q}}_1 * \bar{\mathbf{q}}_2 &= Q_1^+\bar{\mathbf{q}}_2 = Q_2^-\bar{\mathbf{q}}_1 \\ \bar{\mathbf{q}}_1^{-1} * \bar{\mathbf{q}}_2^{-1} &= {Q_1^+}^\mathsf{T}\bar{\mathbf{q}}_2^{-1} = {Q_2^-}^\mathsf{T}\bar{\mathbf{q}}_1^{-1} \end{aligned} \tag{3.5}$$

Using these relations a rotation matrix can be expressed using a quaternion as follows.

$$\begin{aligned} (\bar{\mathbf{v}}_i)^l = \quad & \bar{\mathbf{q}} * \bar{\mathbf{v}}_i * \bar{\mathbf{q}}^{-1} && = Q^+ Q^{-\mathsf{T}} \bar{\mathbf{v}}_i \\ \Rightarrow \quad & \mathbf{R} && = I_{34} Q^+ Q^{-\mathsf{T}} I_{34}^{\mathsf{T}} \\ \text{where} \quad & I_{34} && = \begin{pmatrix} 0 & 1 & 0 & 0 \\ 0 & 0 & 1 & 0 \\ 0 & 0 & 0 & 1 \end{pmatrix} \end{aligned} \tag{3.6}$$

The axis angle representation of a rotation matrix takes the following form

$$\mathbf{R} \quad = e^{\theta[\mathbf{a}]_\times} \quad = I_3 + \sin\theta[\mathbf{a}]_\times + (1 - \cos\theta)[\mathbf{a}]_\times^2 \tag{3.7}$$

where $\mathbf{a}$ is the axis of revolution and θ is the rotation angle. The Euler representation of a rotation matrix takes the following form.

$$\begin{aligned} \mathbf{R} \; &= \; \mathbf{R}_{\theta_z} \mathbf{R}_{\theta_y} \mathbf{R}_{\theta_x} \\ &= \begin{pmatrix} \cos\theta_y \cos\theta_z & \cos\theta_z \sin\theta_x \sin\theta_y - \cos\theta_x \sin\theta_z & \sin\theta_x \sin\theta_z + \cos\theta_x \cos\theta_z \sin\theta_y \\ \cos\theta_y \sin\theta_z & \cos\theta_x \cos\theta_z + \sin\theta_x \sin\theta_y \sin\theta_z & \cos\theta_x \sin\theta_y \sin\theta_z - \cos\theta_z \sin\theta_x \\ -\sin\theta_y & \cos\theta_y \sin\theta_x & \cos\theta_x \cos\theta_y \end{pmatrix} \end{aligned} \tag{3.8}$$

In (3.8) the Euler angles corresponding to roll (θ_x), pitch (θ_y), and yaw (θ_z) are applied in the ZYX rotation sequence to arrive at the rotated frame.

The following relations are used throughout the text for differentiation of expressions related to a quaternion $\bar{\mathbf{q}}$ and a vector $\mathbf{v}$.

$$\begin{aligned} \tfrac{\partial}{\partial \bar{\mathbf{q}}} \bar{\mathbf{q}} * \bar{\mathbf{v}} * \bar{\mathbf{q}}^{-1} \; &= 2 Q^{-\mathsf{T}} V^- & \tfrac{\partial}{\partial \bar{\mathbf{q}}} \bar{\mathbf{q}}^{-1} * \bar{\mathbf{v}} * \bar{\mathbf{q}} \; &= 2 Q^{+\mathsf{T}} V^+ \\ \tfrac{\partial}{\partial \mathbf{v}} I_{34} \bar{\mathbf{q}} * \bar{\mathbf{v}} * \bar{\mathbf{q}}^{-1} \; &= \mathbf{R} & \tfrac{\partial}{\partial \mathbf{v}} I_{34} \bar{\mathbf{q}}^{-1} * \bar{\mathbf{v}} * \bar{\mathbf{q}} \; &= \mathbf{R}^{\mathsf{T}} \end{aligned} \tag{3.9}$$

3.2.2 Relative localization problem in 3D

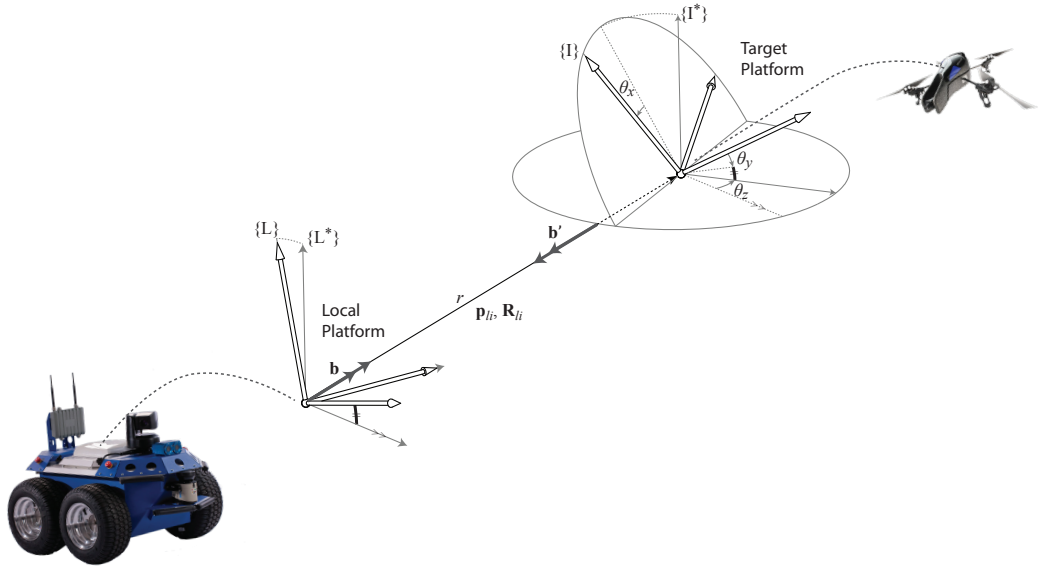

Figure 3.1: Relative localization frames of reference

Figure 3.1 illustrates the vector quantities of the frames $\{L\}$ and $\{I\}$ attached to two robots. The frames $\{L^*\}$ and $\{I^*\}$ illustrated in Figure 3.1 are zero-roll-pitch frames of robots, which are used in subsequent simplifications introduced in Section 3.3.4. As introduced in chapter 2 the term "target platform" is used to represent robot i and the term "local platform" is used to represent robot l. The position vector $\mathbf{p}_{l,i} = (x,\ y,\ z)^\mathsf{T}$ carries the relative coordinates of the target platform. The rotation matrix $\mathbf{R}_{l,i}$ carries the relative orientation which corresponds to roll (θ_x), pitch (θ_y), and yaw (θ_z), angles of platform $\{I\}$ relative to robot $\{L\}$. The double subscripts li denote that the variable is a relative quantity of frame $\{L\}$ with respect to frame $\{I\}$, and is expressed in frame $\{L\}$. The double subscripts are only used where necessary for clarity of presentation. Using quaternion parametrization the rotation matrix $\mathbf{R}_{l,i}$ is denoted as $\mathbf{R}_q$ and the rotation kinematics are expressed in quaternion form. The system model related to the two robots is captured using equation (3.10)

which constitutes a 3D variable turn rate (**VTR**) model.

$$\begin{aligned} \dot{\mathbf{x}} &= f(\mathbf{x}, \mathbf{u}, \mathbf{w}) \\ \begin{pmatrix} \dot{\mathbf{p}} \\ \dot{\bar{\mathbf{q}}} \end{pmatrix} &= \begin{pmatrix} \mathbf{R}_q \mathbf{v}_i - \mathbf{v}_l - \boldsymbol{\omega}_l \times \mathbf{p} + \mathbf{w}_v \\ \frac{1}{2}\bar{\mathbf{q}} * I_{43}(\boldsymbol{\omega}_i - \mathbf{R}_q^{\mathsf{T}} \boldsymbol{\omega}_l + \mathbf{w}_\omega) \end{pmatrix} \end{aligned} \tag{3.10}$$

The set of inputs $\mathbf{u} = (\ \mathbf{v}_l^{\mathsf{T}},\ \boldsymbol{\omega}_l^{\mathsf{T}},\ \mathbf{v}_i^{\mathsf{T}},\ \boldsymbol{\omega}_i^{\mathsf{T}})^{\mathsf{T}}$ captures the absolute velocities $\mathbf{v}_l = (v_{lx},\ v_{ly},\ v_{lz})^{\mathsf{T}}$, $\mathbf{v}_i = (v_{ix},\ v_{iy},\ v_{iz})^{\mathsf{T}}$, and absolute angular speeds $\boldsymbol{\omega}_l = (\omega_{lx},\ \omega_{ly},\ \omega_{lz})^{\mathsf{T}}$, $\boldsymbol{\omega}_i = (\omega_{ix},\ \omega_{iy},\ \omega_{iz})^{\mathsf{T}}$ of robot $\{L\}$ and robot $\{I\}$ respectively. The single subscript denotes that the vector is an absolute quantity relative to an inertial frame and is expressed in the body fixed frame of the platform. The state vector $\mathbf{x}$ includes the relative position $\mathbf{p}$ and the relative orientation $\bar{\mathbf{q}}$. The random variable $\mathbf{w}$ captures the process noise which is assumed to be zero mean Gaussian with covariance $E(\mathbf{w}\mathbf{w}^T) = Q$.

3.2.3 Measurement availability

This analysis considers three types of measurement sensors applicable for each platform. These include relative positioning sensors, velocity sensors, and attitude reference sensors. The following is a discussion of each type of sensor. The sensor model for each sensor is captured using a nonlinear measurement model as given in (3.11). The random variable $\boldsymbol{\nu}$ captures the process noise which is assumed to be zero mean Gaussian with covariance $E(\boldsymbol{\nu}\boldsymbol{\nu}^{\mathsf{T}}) = \acute{R}$.

3.2.3.1 Relative positioning sensor-$\mathbf{y}_p,\ \mathbf{y}_{p'}$

The local platform is assumed to be equipped with a sensor which can measure the relative range r, and bearing $\mathbf{b}$ of a target platform. Similarly the target platform can measure the range r' and bearing $\mathbf{b}'$ of the local platform, due to transformational

invariance of range $r = r'$. Therefore the distinct quantities r, b, and b' of these measurements can be captured in a sensor model as follows.

$$\mathbf{y} = h(\mathbf{x}, \boldsymbol{\nu})$$
$$\begin{pmatrix} r \\ \mathbf{b} \\ \mathbf{b}' \end{pmatrix} = \begin{pmatrix} ||\mathbf{p}|| \\ \mathbf{p}||\mathbf{p}||^{-1} \\ -\mathbf{R}_q^{\mathsf{T}}\mathbf{p}||\mathbf{p}||^{-1} \end{pmatrix} + \begin{pmatrix} \nu_r \\ \boldsymbol{\nu}_b \\ \boldsymbol{\nu}_{b'} \end{pmatrix} \tag{3.11}$$

The corresponding noise figures of the sensors are denoted by ν_r, $\boldsymbol{\nu}_b$, and $\boldsymbol{\nu}_{b'}$. In multi robot research it is advantageous to convert this model to a cartesian form given by

$$\mathbf{y} = h(\mathbf{x}, \boldsymbol{\nu})$$
$$\begin{pmatrix} \mathbf{y}_p \\ \mathbf{y}_{p'} \end{pmatrix} = \begin{pmatrix} \mathbf{p} \\ -\mathbf{R}_q^{\mathsf{T}}\mathbf{p} \end{pmatrix} + \begin{pmatrix} \boldsymbol{\nu}_p \\ \boldsymbol{\nu}_{p'} \end{pmatrix} \tag{3.12}$$

where the measurements $\mathbf{y}_p$, and $\mathbf{y}_{p'}$ denotes the relative position measurements with respect to local and target platforms respectively. The noise figures are captured in a cartesian form as additive white noise through first order transformation of the original noise parameters. However this is only valid if the noise parameters are considerably small, which allows a cartesian sensor model to be a good approximation of the polar noise distributions. This phenomenon is better illustrated by Figure 3.2 where the first order approximation of measurement covariance under low noise statistics exhibits good approximation of the underlying noise distribution. In this text we opt for a cartesian model for relative positioning assuming a sensor with low noise statistics as presented in Chapter 2.

Depending on the measurement configuration assumed, two cases of relative measurement availability can be considered.

Star **configuration:** In *Star* measurement configuration, only $\mathbf{y}_p$ is measured. For

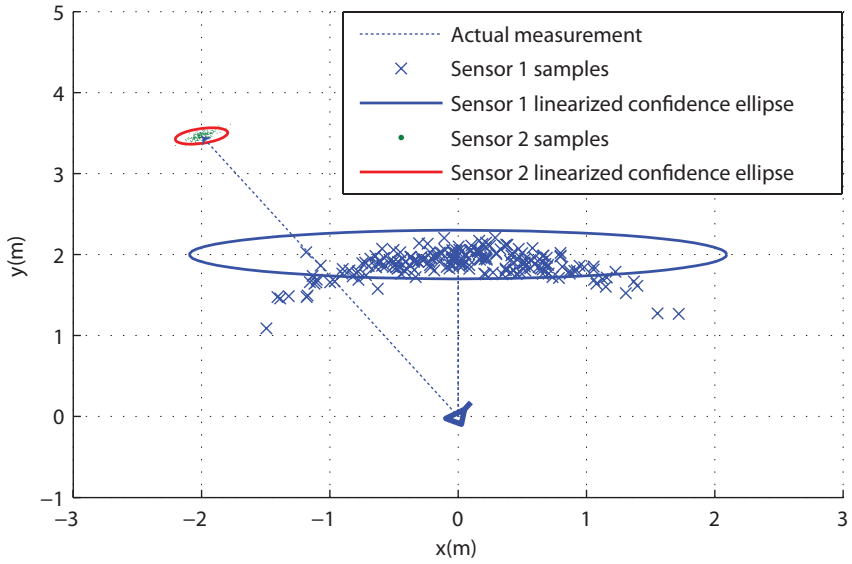

Figure 3.2: Comparison between the sampled points and the first order approximation of noise figures related to a high noise relative portioning sensor and a low noise sensor. The standard deviation of Sensor 1 - $\sigma_r = 10cm,\ \sigma_\theta = 20°$, Sensor 2 - $\sigma_r = 3cm,\ \sigma_\theta = 1°$

the purposes of this observability study, the *Star* configuration relates to the general case where the measurement $y_{p'}$ is unavailable. This can occur due to reasons ranging from measurement unavailability, communication constraints, or field of view constraints.

Mesh **configuration:** In *Mesh* measurement configuration, both $\mathbf{y}_p$ and $\mathbf{y}_{p'}$ are measured.

3.2.3.2 Platform velocity sensor-$\mathbf{y}_v,\ \mathbf{y}_\omega$

Platforms can measure their velocities using numerous methods which include wheel encoders, optical flow sensors, doppler velocity logs etc.. For the purpose of analysis it is advantageous to consider these velocities as inputs of the model when available. Hence this study considers the following three cases for analysis.

Case S_1**:** All velocities of the local and target platforms are available. Thus $\mathbf{v}_i, \boldsymbol{\omega}_i, \mathbf{v}_l, \boldsymbol{\omega}_l$

act as inputs to the model as given in equation (3.10).

Case S_2: All velocities related to the local platform are available. For this case only $\mathbf{v}_l,\ \boldsymbol{\omega}_l$ are inputs while $\mathbf{v}_i,\ \boldsymbol{\omega}_i$ are introduced as states with random walk processes for estimation purposes. Hence the system model given by (3.10) is concatenated with additional rows given below.

$$\begin{pmatrix} \dot{\mathbf{v}}_i \\ \dot{\boldsymbol{\omega}}_i \end{pmatrix} = \begin{pmatrix} \mathbf{0} \\ \mathbf{0} \end{pmatrix} + \begin{pmatrix} \mathbf{w}_{v_i} \\ \mathbf{w}_{\omega_i} \end{pmatrix}$$

Case S_3: All velocities related to the target platform are available. For this case only $\mathbf{v}_i,\ \boldsymbol{\omega}_i$ are inputs and $\mathbf{v}_l,\ \boldsymbol{\omega}_l$ are introduced as states with random walk processes for estimation purposes. Hence the system model given by(3.10) is concatenated with additional rows given below for Case S_3.

$$\begin{pmatrix} \dot{\mathbf{v}}_l \\ \dot{\boldsymbol{\omega}}_l \end{pmatrix} = \begin{pmatrix} \mathbf{0} \\ \mathbf{0} \end{pmatrix} + \begin{pmatrix} \mathbf{w}_{v_l} \\ \mathbf{w}_{\omega_l} \end{pmatrix}$$

The special case where all velocities are unknown is well studied in target tracking literature where a linear model such as the Constant Velocity(**CV**) model or the Constant Turn Rate (**CTR**) model is used for estimation purposes.

3.2.3.3 Attitude reference sensors-$\mathbf{y}_{gi}$

These measurements are not explicitly considered in this thesis for relative localization purposes. The attitude reference measurements are only used in subsequent simplifications of the problem introduced in Section 3.3.4. Attitude reference sensing is enabled through Inertial Measurement Units (**IMU**) attached to robots. Attitude estimation using an IMU can be easily implemented by a nonlinear complimentary

filter [54] with intuitive gain tuning approaches as proposed in Chapter 4. The attitude reference systems implicitly estimate the rotations of the body fixed frames $\{I\}$ and $\{L\}$ of platforms relative to the zero roll pitch frames $\{I^*\}$ and $\{L^*\}$. The heading reference provided by digital compasses are biased due to disturbance caused by power lines, fero-magnetic structures, and robotic motors, hence are not preferred as reliable heading measurement systems in indoor settings. This fact is reported in many studies [83, 84] and as a result most indoor multi-robot research considers heading as an unknown quantity that require estimation through localization filters.

3.3 Materials and Methods

3.3.1 The system configurations

Table 3.1: All combinations relating to relative measurement and platform velocity measurement availability

✓- available ✗- unavailable - Dont care entry

Configuration	**Measurement availability**			
	p_{li}	p_{il}	v_i, ω_i	v_l, ω_l
$S_1 - Mesh$	✓	✓	✓	✓
$S_1 - Star$	✓	✗	✓	✓
$S_2 - Mesh$	✓	✓	✗	✓
$S_2 - Star$	✓	✗	✗	✓
$S_3 - Mesh$	✓	✓	✓	✗
$S_4 - Star$	✓	✗	✓	✗
Dual Configurations	✗	✓	-	-
Target tracking	-	-	✗	✗
Odometer	✗	✗	-	-

Table 3.3.1 tabulates all possible configurations with regard to the availability of relative measurements and platform velocities. The unique identifier which is used to identify each configuration is given in the first column of Table 3.3.1. This work analyzes the observability characteristics of the first six cases given in the table. The

reasons for not explicitly considering the remaining three cases are as follows.

- The *Dual configurations* given in the table relate to all the configurations derived simply by interchanging the local and target platforms of the first six configurations. Hence the observability characteristics of the first six configurations hold equally for its dual problems. For example, the filter estimating w.r.t. the local platform for the $S_1 - Star$ configuration, can be used for its dual configuration as well, by implementing the filter w.r.t. the target platform.

- The *Target Tracking* configuration given in the table relates to the case where all platform velocities are unknown. This is the general approach taken in target tracking methods which uses a constant velocity model. The states of the constant velocity model only include the position and linear velocities of the origin of $\{I\}$. This model is known to be fully observable when relative position is measured, and the proof is rather straightforward [49].

- The class of configurations termed as *Odometer* given in Table 3.3.1 relates to the cases where there are no relative measurements. Thus the model acts as an odometer which predicts the location of the platform by integrating the velocity estimates. As a result, the model experiences an unbounded increase of the localization error for this case. I.e., the model is unobservable.

3.3.2 Observability of non-linear systems

Equation (3.13) gives the control affine form of a general nonlinear system.

$$\begin{aligned} \dot{\mathbf{x}} &= f_0(\mathbf{x}) + \sum_{\forall k=1:l} f_k(\mathbf{x})\mathbf{u}_k \\ \mathbf{y} &= h(\mathbf{x}) \end{aligned} \tag{3.13}$$

The system model related to each configuration considered in this study as given in (3.10) constitutes a nonlinear system which requires a nonlinear observability analysis. The following classes of observability are introduced by [43] in relation to observability of nonlinear systems.

Indistinguishable A pair of states $\mathbf{x}_0$ and $\mathbf{x}_1$ in state space $\mathcal{X}$ are indistinguishable if the system (3.13) produces the same input output map for every admissible input trajectory $\mathbf{u}$.

Observable A system is observable if indistinguishability I of each state $\mathbf{x} \in \mathcal{X}$ only includes $\mathbf{x}$. This is denoted as $I(\mathbf{x}) = \{\mathbf{x}\}$. I.e., each state $\mathbf{x}$ is distinguishable from all other states in the state space $\mathcal{X}$.

Locally Observable A system is locally observable if each state $\mathbf{x} \in \mathcal{X}$ is distinguishable within any open neighbourhood $U \subseteq \mathcal{X}$. This is denoted as $I_U(\mathbf{x}) = \{\mathbf{x}\}$. I.e., the system does not need to travel a considerable amount of time for the state to be distinguishable from others.

Weakly Observable A system is weakly observable if each state $\mathbf{x} \in \mathcal{X}$ is only distinguishable in a subset $V \subseteq \mathcal{X}$. This is denoted as $I(\mathbf{x}) \cap V = \{\mathbf{x}\}$. This implies the existence of multiple indistinguishable states in the state space.

Locally Weakly Observable If each state $\mathbf{x} \in \mathcal{X}$ is only distinguishable within a subset $V \in X$ and it is distinguishable in any open subset (neighbourhood) $U \in V$, the system is locally weakly observable. $(I_U(\mathbf{x}) \cap V = \{\mathbf{x}\})$

The relationship between various forms of observability discussed for nonlinear systems can be captured as follows. For linear systems all of these observability classes

are equivalent.

$$\begin{array}{ccc} \text{Locally observable} & \Rightarrow & \text{Observable} \\ \Downarrow & & \Downarrow \\ \text{Locally weakly observable} & \Rightarrow & \text{Weakly observable} \end{array}$$

Hermman *et al.* have introduced the necessary and sufficient conditions under which the nonlinear system shown in (3.13) can be locally weakly observable [43]. Following the notation of [46], an observability matrix is defined as in (3.14), using all Lie derivatives of the function $h(\mathbf{x})$, with respect to $\mathbf{f}_k(\mathbf{x})$. The system given by (3.13) is said to be locally weakly observable, if matrix $\mathcal{O}$ satisfies the observability rank conditions, i.e., $rank(\mathcal{O}) = n$.

$$\mathcal{O} = \{\Delta \mathfrak{L}^l_{f_a,\dots f_b} h(\mathbf{x}) | a, b = 0 \dots k; l \in \mathbb{N}\} \tag{3.14}$$

3.3.3 Observability analysis - 3D Relative localization problem

The 3D analysis is not incorporated in the final design process of localization filters and the distributed computing modules, and is presented only for completeness of the observability study. Therefore only the summary of the results are presented in Table 3.3.3 which is generated through evaluating the rank of the observability matrix using the Matlab Symbolic toolbox. For this purpose the system equations given by (3.15) were used which corresponds to different configurations related to relative localization.

System Model	Measurement Model
Case S_1 $\dot{\mathbf{x}} = f_1(\mathbf{x})\mathbf{v}_i + f_2(\mathbf{x})\omega_i + f_3(\mathbf{x})\mathbf{v}_l + f_4(\mathbf{x})\omega_l$ $\begin{pmatrix}\dot{\mathbf{p}}\\ \dot{\bar{\mathbf{q}}}\end{pmatrix} = \begin{pmatrix}\mathbf{R}_q\\ 0\end{pmatrix}\mathbf{v}_i + \begin{pmatrix}\mathbf{0}_{3\times1}\\ \frac{1}{2}Q^+\end{pmatrix}\boldsymbol{\omega}_i + \begin{pmatrix}-\mathbf{I}_{3\times3}\\ 0\end{pmatrix}\mathbf{v}_l + \begin{pmatrix}\mathbf{p}\times\\ -\frac{1}{2}Q^-\end{pmatrix}\boldsymbol{\omega}_l$ *Case* S_2 $\dot{\mathbf{x}} = f_0(\mathbf{x}) + f_1(\mathbf{x})\mathbf{v}_l + f_2(\mathbf{x})\boldsymbol{\omega}_l$ $\begin{pmatrix}\dot{\mathbf{p}}\\ \dot{\bar{\mathbf{q}}}\\ \dot{\mathbf{v}}_i\\ \dot{\boldsymbol{\omega}}_i\end{pmatrix} = \begin{pmatrix}\mathbf{R}_q\mathbf{v}_i\\ \frac{1}{2}Q^+\boldsymbol{\omega}_i\\ \mathbf{0}_{3\times1}\\ \mathbf{0}_{3\times1}\end{pmatrix} + \begin{pmatrix}-\mathbf{I}_{3\times3}\\ \mathbf{0}_{4\times3}\\ \mathbf{0}_{3\times3}\\ \mathbf{0}_{3\times3}\end{pmatrix}\mathbf{v}_l + \begin{pmatrix}\mathbf{p}\times\\ -\frac{1}{2}Q^-\\ \mathbf{0}_{3\times3}\\ \mathbf{0}_{3\times3}\end{pmatrix}\boldsymbol{\omega}_l$ *Case* S_3 $\dot{\mathbf{x}} = f_0(\mathbf{x}) + f_1(\mathbf{x})\mathbf{v}_i + f_2(\mathbf{x})\boldsymbol{\omega}_i$ $\begin{pmatrix}\dot{\mathbf{p}}\\ \dot{\bar{\mathbf{q}}}\\ \dot{\mathbf{v}}_i\\ \dot{\boldsymbol{\omega}}_i\end{pmatrix} = \begin{pmatrix}-\mathbf{v}_l + \mathbf{p}\times\boldsymbol{\omega}_l\\ -\frac{1}{2}Q^-\boldsymbol{\omega}_l\\ \mathbf{0}_{3\times1}\\ \mathbf{0}_{3\times1}\end{pmatrix} + \begin{pmatrix}\mathbf{R}_q\\ \mathbf{0}_{4\times3}\\ \mathbf{0}_{3\times3}\\ \mathbf{0}_{3\times3}\end{pmatrix}\mathbf{v}_i + \begin{pmatrix}\mathbf{0}_{3\times3}\\ \frac{1}{2}Q^+\\ \mathbf{0}_{3\times3}\\ \mathbf{0}_{3\times3}\end{pmatrix}\boldsymbol{\omega}_i$	*Star Configuration* $\mathbf{y} = h(\mathbf{x},\mathbf{u})$ $\begin{pmatrix}\mathbf{y}_p\end{pmatrix} = \begin{pmatrix}\mathbf{p}\end{pmatrix}$ *Mesh Configuration* $\mathbf{y} = h(\mathbf{x},\mathbf{u})$ $\begin{pmatrix}\mathbf{y}_p\\ \mathbf{y}_{p'}\end{pmatrix} = \begin{pmatrix}\mathbf{p}\\ -\mathbf{R}_q^\mathsf{T}\mathbf{p}\end{pmatrix}$ (3.15)

Table 3.2: Summary of the observability analysis for the 3D problem
✓- Locally weakly observable ✗- Unobservable

Configuration	Rank($\mathcal{O}$)	Full state observability
$S_1 - Mesh$	7	✓
$S_1 - Star$	7	✓
$S_2 - Mesh$	13	✓
$S_2 - Star$	9	✗
$S_3 - Mesh$	13	✓
$S_3 - Star$	12	✗

3.3.4 The 2.5D simplification of the problem

3D systems can be approximated to 2.5D under the assumptions of low roll and pitch dynamics. This is a common strategy used in research related to MAV localization [22]. The 2.5D system considers the zero-roll-pitch frames of reference $\{L^*\}$ and $\{I^*\}$ attached to the robots. The attitude reference systems attached to each platform estimate the rotation between frames $\{L\}$ and $\{L^*\}$ denoted by $\mathbf{R}_{l^*,l}$, and the rotation between frames $\{I\}$ and $\{I^*\}$ denoted by $\mathbf{R}_{i^*,i}$. Using these quantities the following

simplifications are performed to the 3D system model given in (3.10) and the related measurement equations.

- The rotation estimate $\mathbf{R}_{l^*,l}$ is used to express the measured vector quantities $\mathbf{v}_l, \boldsymbol{\omega}_l, \mathbf{y}_p$ in the frame of reference $\{L^*\}$. I.e., $\mathbf{v}_l^* = \mathbf{R}_{l^*,l}\mathbf{v}_l$ and $\omega_l^* = \mathbf{R}_{l^*,l}\boldsymbol{\omega}_l$ $\mathbf{y}_p^* = \mathbf{R}_{l^*,l}\mathbf{y}_p$.

- Similarly, the rotation estimate $\mathbf{R}_{i^*,i}$ is used to express vector quantities $\mathbf{v}_i, \boldsymbol{\omega}_i,\ \mathbf{y}_{p'}$ in the frame of reference $\{I^*\}$. I.e., $\mathbf{v}_i^* = \mathbf{R}_{i^*,i}\mathbf{v}_i$ and $\omega_i^* = \mathbf{R}_{i^*,i}\boldsymbol{\omega}_i$ $\mathbf{y}_{p'}^* = \mathbf{R}_{i^*,i}\mathbf{y}_{p'}$.

- Simplify the system model by assuming negligible roll and pitch dynamics. Therefore the angular speeds would only include the yaw rate, i.e. $\boldsymbol{\omega_i} = (0, 0, \omega_{iz}^*)^\mathsf{T}, \boldsymbol{\omega_l} = (0, 0, \omega_{lz}^*)^\mathsf{T}$. The rotational kinematics can be simplified to a one degree of freedom system which only considers the heading θ_z dynamics.

$$\bar{\mathbf{q}} = \tfrac{1}{2}\bar{\mathbf{q}} * \bar{\boldsymbol{\omega}} \quad \rightarrow \quad \theta_z = \omega_z \tag{3.16}$$

The following notational simplifications are incorporated when refering to 2.5D problems which assume zero-roll-pitch frames of references of each platform. $\theta_z \rightarrow \theta$, $\mathbf{R}_q \rightarrow \mathbf{R}_\theta$, $\mathbf{v}_l^* \rightarrow \mathbf{v}_l$, $\mathbf{v}_i^* \rightarrow \mathbf{v}_i$, $\omega_{lz}^* \rightarrow \omega_l$, $\omega_{iz}^* \rightarrow \omega_i$. After assuming these simplifications and associated notation, the system and measurement models related to different cases can be summarized by (3.17) .

Here $\mathbf{e}$ denotes the unit basis vectors of $\mathbb{R}^3$. I.e., $[\mathbf{e}_1\ \mathbf{e}_2\ \mathbf{e}_3] = I_{3\times 3}$. For the purpose of the analysis we define $\frac{d}{d\theta}^n\ \mathbf{R}_\theta := \ \mathbf{J}_\theta^{(n)}$.

System Model	Measurement Model
$\underline{Case\ S_1}$ $\dot{\mathbf{x}} = f_1(\mathbf{x})\mathbf{v}_i + f_2(\mathbf{x})\omega_i + f_3(\mathbf{x})\mathbf{v}_l + f_4(\mathbf{x})\omega_l$ $\begin{pmatrix}\dot{\mathbf{p}}\\ \dot{\theta}\end{pmatrix} = \begin{pmatrix}\mathbf{R}_\theta\\ 0\end{pmatrix}\mathbf{v}_i + \begin{pmatrix}\mathbf{0}_{3\times1}\\ 1\end{pmatrix}\omega_i + \begin{pmatrix}-\mathbf{I}_{3\times3}\\ 0\end{pmatrix}\mathbf{v}_l + \begin{pmatrix}\mathbf{p}\times\mathbf{e}_3\\ -1\end{pmatrix}\omega_l$ $\underline{Case\ S_2}$ $\dot{\mathbf{x}} = f_0(\mathbf{x}) + f_1(\mathbf{x})\mathbf{v}_l + f_2(\mathbf{x})\boldsymbol{\omega}_l$ $\begin{pmatrix}\dot{\mathbf{p}}\\ \dot{\theta}\\ \dot{\mathbf{v}}_i\\ \dot{\omega}_i\end{pmatrix} = \begin{pmatrix}\mathbf{R}_\theta\mathbf{v}_i\\ \omega_i\\ \mathbf{0}_{3\times1}\\ 0\end{pmatrix} + \begin{pmatrix}-\mathbf{I}_{3\times3}\\ 0\\ \mathbf{0}_{3\times3}\\ 0\end{pmatrix}\mathbf{v}_l + \begin{pmatrix}\mathbf{p}\times\mathbf{e}_3\\ -1\\ \mathbf{0}_{3\times1}\\ 0\end{pmatrix}\omega_l$ $\underline{Case\ S_3}$ $\dot{\mathbf{x}} = f_0(\mathbf{x}) + f_1(\mathbf{x})\mathbf{v}_i + f_2(\mathbf{x})\boldsymbol{\omega}_i$ $\begin{pmatrix}\dot{\mathbf{p}}\\ \dot{\theta}\\ \dot{\mathbf{v}}_i\\ \dot{\omega}_i\end{pmatrix} = \begin{pmatrix}-\mathbf{v}_l + \mathbf{p}\times\mathbf{e}_3\omega_l\\ -\omega_l\\ \mathbf{0}_{3\times1}\\ 0\end{pmatrix} + \begin{pmatrix}\mathbf{R}_\theta\\ 0\\ \mathbf{0}_{3\times3}\\ 0\end{pmatrix}\mathbf{v}_i + \begin{pmatrix}\mathbf{0}_{3\times1}\\ 1\\ \mathbf{0}_{3\times1}\\ 0\end{pmatrix}\omega_i$	$\underline{Star\ Configuration}$ $\mathbf{y} = h(\mathbf{x},\mathbf{u})$ $\begin{pmatrix}\mathbf{y}_p\end{pmatrix} = \begin{pmatrix}\mathbf{p}\end{pmatrix}$ $\underline{Mesh\ Configuration}$ $\mathbf{y} = h(\mathbf{x},\mathbf{u})$ $\begin{pmatrix}\mathbf{y}_p\\ \mathbf{y}_{p'}\end{pmatrix} = \begin{pmatrix}\mathbf{p}\\ -\mathbf{R}_\theta^\mathsf{T}\mathbf{p}\end{pmatrix}$ (3.17)

3.3.5 Observability analysis - 2.5D Relative localization problem

$\underline{Case\ S_1 - Mesh}$ **configuration observability**

In this configuration, all platform velocities are known and both relative position measurements with respect to the local and target platforms are available. An observability matrix can be formed by evaluating the Lie derivatives as follows.

$$\mathcal{L}^0 h = h, \qquad \nabla\mathcal{L}^0 h = \begin{bmatrix}\mathbf{I}_{3\times3} & \mathbf{0}_{3\times1}\\ -\mathbf{R}_\theta^\mathsf{T} & -\mathbf{J}_\theta^{(1)^\mathsf{T}}\mathbf{p}\end{bmatrix}$$

$$\mathcal{L}^1_{f_1} h = \nabla\mathcal{L}^0 h f_1 = \begin{bmatrix}\mathbf{R}_\theta\mathbf{e}_j\\ -\mathbf{e}_j\end{bmatrix},\ \forall\mathbf{e}_j = \{\mathbf{e}_1,\ \mathbf{e}_2,\ \mathbf{e}_3\} \quad \nabla\mathcal{L}^1_{f_1} h = \begin{bmatrix}\mathbf{0}_{3\times3} & \mathbf{J}_\theta^{(1)}\mathbf{e}_j\\ \mathbf{0}_{3\times3} & \mathbf{0}_{3\times1}\end{bmatrix}$$

$$\mathcal{L}^1_{f_3} h = \nabla\mathcal{L}^0 h f_3 = \begin{bmatrix}-\mathbf{e}_j\\ \mathbf{R}_\theta^\mathsf{T}\mathbf{e}_j\end{bmatrix}, \qquad \nabla\mathcal{L}^1_{f_3} h = \begin{bmatrix}\mathbf{0}_{3\times3} & \mathbf{0}_{3\times1}\\ \mathbf{0}_{3\times3} & \mathbf{J}_\theta^{(1)^\mathsf{T}}\mathbf{e}_j\end{bmatrix}$$

$$O = \begin{bmatrix}\nabla\mathcal{L}^0 h^\mathsf{T} & \nabla\mathcal{L}^1_{f_1} h^\mathsf{T} & \nabla\mathcal{L}^1_{f_3} h^\mathsf{T}\end{bmatrix}^\mathsf{T}$$

The term $-\mathbf{J}_{\theta}^{(1)^{\mathsf{T}}}\mathbf{p}$ of $\mathcal{O}$ is zero when $x = y = 0$. This occurs when the target robot is directly on top of or below the local platform. The terms $\nabla\mathcal{L}_{f_1}^1 h,\ \nabla\mathcal{L}_{f_3}^1 h$ vanish when the input velocities $\mathbf{v}_l = \mathbf{v}_i = \mathbf{0}$. Additionally, $\mathbf{J}_{\theta}^{(1)}\mathbf{e}_3$ of $\nabla\mathcal{L}_{f_1}^1 h$ is always zero which implies that the observability of θ is independent of the vertical velocity v_{lz}. Similarly, $\mathbf{J}_{\theta}^{(1)^{\mathsf{T}}}\mathbf{e}_3$ of $\nabla\mathcal{L}_{f_3}^1 h$ is always zero which implies that the observability of θ is independent of the target's vertical velocity v_{iz}. For all other conditions the matrix $\mathcal{O}$ has a column rank of 4 which satisfies the observability rank conditions required for the system to be locally weakly observable (*Theorem* 3.1 in [43]). Therefore the system is locally weakly observable for all cases except when $x = y = v_{ix} = v_{iy} = v_{lx} = v_{ly} = 0$. I.e., the system is only unobservable for an $S_1 - Mesh$ configuration when the target robot is directly on top of or below the local platform, and both robots are stationary on a horizontal plane.

Case $S_1 - Star$ **configuration observability**

$$\mathcal{L}^0 h = h = \mathbf{p}, \qquad \nabla\mathcal{L}^0 h \begin{bmatrix} \mathbf{I}_{3\times 3} & \mathbf{0}_{3\times 1} \end{bmatrix}$$

$$\mathcal{L}_{f_1}^1 h = \nabla\mathcal{L}^0 h f_1 = \mathbf{R}_{\theta}\mathbf{e}_j,\ \forall \mathbf{e}_j = \{\mathbf{e}_1,\ \mathbf{e}_2,\ \mathbf{e}_3\} \quad \nabla\mathcal{L}_{f_1}^1 h \begin{bmatrix} \mathbf{0}_{3\times 3} & \mathbf{J}_{\theta}\mathbf{e}_j \end{bmatrix}$$

$$\mathcal{O} = \begin{bmatrix} \nabla\mathcal{L}^0 h^{\mathsf{T}} & \nabla\mathcal{L}_{f_1}^1 h^{\mathsf{T}} \end{bmatrix}^{\mathsf{T}}$$

The non zero terms of $\nabla\mathcal{L}_{f_1}^1 h^{\mathsf{T}}$ vanish when $\mathbf{v}_i = \mathbf{0}$. The term $\mathbf{J}_{\theta}\mathbf{e}_3$ of $\nabla\mathcal{L}_{f_1}^1 h^{\mathsf{T}}$ is always zero which implies that the observability of θ does not depend on the vertical velocity v_{iz}. Therefore matrix $\mathcal{O}$ has a column rank of 4 which satisfies the observability rank conditions $\forall v_{ix}$ *or* $v_{iy} \neq 0$. I.e., the system is unobservable for an $S_1 - Star$ configuration when the target robot is stationary on a horizontal plane.

Case $S_2 - Mesh$ **configuration observability**

$$\mathcal{L}^0 h = h, \qquad \nabla\mathcal{L}^0 h = \begin{bmatrix} \mathbf{I}_{3\times3} & \mathbf{0}_{3\times1} & \mathbf{0}_{3\times3} & \mathbf{0}_{3\times1} \\ -\mathbf{R}_\theta^\mathsf{T} & -\mathbf{J}_\theta^{(1)^\mathsf{T}}\mathbf{p} & \mathbf{0}_{3\times3} & \mathbf{0}_{3\times1} \end{bmatrix}$$

$$\mathcal{L}^1_{f_0} h = \nabla\mathcal{L}^0 h f_0 = \begin{bmatrix} \mathbf{R}_\theta \mathbf{v}_i \\ -\mathbf{v}_i - \omega_i \mathbf{J}_\theta^{(1)^\mathsf{T}}\mathbf{p} \end{bmatrix},$$

$$\nabla\mathcal{L}^1_{f_0} h = \begin{bmatrix} \mathbf{0}_{3\times3} & \mathbf{J}_\theta^{(1)}\mathbf{v}_i & \mathbf{R}_\theta & \mathbf{0}_{3\times1} \\ -\omega_i \mathbf{J}_\theta^{(1)^\mathsf{T}} & -\omega_i \mathbf{J}_\theta^{(2)^\mathsf{T}}\mathbf{p} & -\mathbf{I}_{3\times3} & -\mathbf{J}_\theta^{(1)^\mathsf{T}}\mathbf{p} \end{bmatrix}$$

$$\mathcal{L}^1_{f_1} h = \nabla\mathcal{L}^0 h f_1 = \begin{bmatrix} -\mathbf{e}_j \\ \mathbf{R}_\theta^\mathsf{T}\mathbf{e}_j \end{bmatrix},\ \forall j \qquad \nabla\mathcal{L}^1_{f_1} h = \begin{bmatrix} \mathbf{0}_{3\times3} & \mathbf{0}_{3\times1} & \mathbf{0}_{3\times3} & \mathbf{0}_{3\times1} \\ \mathbf{0}_{3\times3} & \mathbf{J}_\theta^{(1)^\mathsf{T}}\mathbf{e}_j & \mathbf{0}_{3\times3} & \mathbf{0}_{3\times1} \end{bmatrix}$$

$$\mathcal{L}^2_{f_1,f_0} h = \nabla\mathcal{L}^1_{f_1} h f_0 = \omega_i \mathbf{J}_\theta^{(1)^\mathsf{T}}\mathbf{e}_j,\ \forall j \qquad \nabla\mathcal{L}^2_{f_1,f_0} h = \begin{bmatrix} \mathbf{0}_{3\times3} & \omega_i \mathbf{J}_\theta^{(2)^\mathsf{T}}\mathbf{e}_j & \mathbf{0}_{3\times3} & \mathbf{J}_\theta^{(1)^\mathsf{T}}\mathbf{e}_j \end{bmatrix}$$

$$\mathcal{O} = \begin{bmatrix} \nabla\mathcal{L}^0 h^\mathsf{T} & \nabla\mathcal{L}^1_{f_0} h^\mathsf{T} & \nabla\mathcal{L}^1_{f_1} h & \nabla\mathcal{L}^2_{f_1,f_0} h \end{bmatrix}^\mathsf{T}$$

The matrix $\mathcal{O}$ loses the column rank of 8 when the term $-\mathbf{J}_\theta^{(1)^\mathsf{T}}\mathbf{p}$ is zero and the terms $\nabla\mathcal{L}^1_{f_1} h, \nabla\mathcal{L}^2_{f_1,f_0} h$ vanish ($\mathbf{v}_l = 0$). $\mathbf{J}_\theta^{(1)^\mathsf{T}}\mathbf{e}_3$ of $\nabla\mathcal{L}^1_{f_1} h$ is always zero since observability of θ is independent of the vertical velocity v_{lz}. Therefore the system is locally weakly observable for all cases except when $x = y = v_{lx} = v_{ly} = 0$. I.e., the system is unobservable for an $S_2 - Mesh$ configuration when the target robot is directly on top of or below the local platform and the local robot is stationary on a horizontal plane.

Case $S_2 - Star$ **configuration observability**

$$\mathcal{L}^0 h = h = \mathbf{p}, \quad \nabla\mathcal{L}^0 h = \begin{bmatrix} \mathbf{I}_{3\times3} & \mathbf{0}_{3\times1} & \mathbf{0}_{3\times3} & \mathbf{0}_{3\times1} \end{bmatrix}$$

The rank 3 matrix $\nabla\mathbf{L}^0 h$, has a column space that spans the 3-dimensional vector space $\mathbf{p}$. Therefore, states $\mathbf{p}$ can be fully determined. Now higher-order Lie derivatives with gradients along $[\theta\ \mathbf{v}_i\ \omega_i]$, i.e., $\nabla_{[\theta,\mathbf{v}_i,\omega_i]}\mathcal{L}^n_{f_0,f_1,f_2} h$, which spans the vector space $[\theta\ \mathbf{v}_i\ \omega_i]$, should be found to satisfy observability rank conditions.

$$\nabla\mathcal{L}^1_{f_1}h = \nabla\mathcal{L}^2_{f_0,f_1} = \nabla\mathcal{L}^2_{f_2,f1} = \mathbf{0}$$
$$\mathcal{L}^1_{f_2}h = [\mathbf{e}_3]^\mathsf{T}_\times\mathbf{p}$$
$$\nabla_{[\theta,\mathbf{v}_j,\omega_j]}\mathcal{L}^1_{f_2} = \mathbf{0}$$

All remaining higher-order non-zero Lie derivatives are along vector combinations of the set $\{f_0, f_2\}$, which can be summarized using equations (3.18).

$$\mathcal{L}^n_{\{f_0,f_2,..\}}h = \omega_i^{(m-1)}(-1)^{(n-m)}[-\mathbf{e}_3]^s_\times\ \mathbf{J}_\theta^{(n-1)}\ \mathbf{v}_i$$

$$\nabla_{[\theta,\mathbf{v}_i,\omega_i]}\mathcal{L}^n_{\{f_0,f_2,..\}}h \quad = \omega_i^{m-1}(-1)^{n-m}[-\mathbf{e}_3]^s_\times\left[\mathbf{J}_\theta^{(n)}\mathbf{v}_i \quad \mathbf{J}_\theta^{(n-1)} \quad \tfrac{m-1}{\omega_i}\mathbf{J}_\theta^{(n-1)}\mathbf{v}_i\right] \tag{3.18}$$

In (3.18), n is the degree of the Lie derivative, m is the number of times it is evaluated along f_0, and s is the number of times the derivative is initially evaluated along f_2. In this general expression $J_\theta^{(0)}$ is equivalent to R_θ. However, the rank of (3.18) is found to be 4 (but should be 5 for full rank). This is because $Col_\theta = -Col_{v_{ix}}v_{iy} + Col_{v_{iy}}v_{ix}$. Here the column vector of a particular state variable θ in $\mathcal{O}$, is defined as Col_θ. Full rank is only observed for all $v_i \neq 0$, when the transverse velocity state is constrained (known to be zero), i.e., $v_{iy} = 0$. This is also valid for ground differential drive robots where lateral velocities are not experienced.

Case $S_3 - Mesh$ **configuration observability**

$$\mathcal{L}^0 h = h, \qquad \nabla\mathcal{L}^0 h = \begin{bmatrix} \mathbf{I}_{3\times3} & \mathbf{0}_{3\times1} & \mathbf{0}_{3\times3} & \mathbf{0}_{3\times1} \\ -\mathbf{R}_\theta^\mathsf{T} & -\mathbf{J}_\theta^{(1)^\mathsf{T}}\mathbf{p} & \mathbf{0}_{3\times3} & \mathbf{0}_{3\times1} \end{bmatrix}$$

$$\mathcal{L}^1_{f_0} h = \nabla\mathcal{L}^0 h f_0 = \begin{bmatrix} -\mathbf{v}_l + \omega_l \mathbf{p} \times \mathbf{e}_3 \\ -\mathbf{R}_\theta^\mathsf{T}(-\mathbf{v}_l + \omega_l \mathbf{p} \times \mathbf{e}_3) + \omega_l \mathbf{J}_\theta^{(1)^\mathsf{T}}\mathbf{p} \end{bmatrix},$$

$$\nabla\mathcal{L}^1_{f_0} h = \begin{bmatrix} -\omega_l[\mathbf{e}_3]_\times & \mathbf{0}_{3\times1} & -\mathbf{I}_{3\times3} & \mathbf{p}[\mathbf{e}_3]_\times \\ - & - & \mathbf{R}_\theta^\mathsf{T} & \mathbf{R}_\theta^T[\mathbf{e}_3]_\times \mathbf{p} + \mathbf{J}_\theta^{(1)^\mathsf{T}}\mathbf{p} \end{bmatrix}$$

$$\mathcal{L}^1_{f_1} h = \nabla\mathcal{L}^0 h f_1 = \begin{bmatrix} \mathbf{R}_\theta \mathbf{e}_j \\ -\mathbf{e}_j \end{bmatrix}, \ \forall j \qquad \nabla\mathcal{L}^1_{f_1} h = \begin{bmatrix} \mathbf{0}_{3\times3} & \mathbf{J}_\theta^{(1)}\mathbf{e}_j & \mathbf{0}_{3\times3} & \mathbf{0}_{3\times1} \\ \mathbf{0}_{3\times3} & \mathbf{0}_{3\times1} & \mathbf{0}_{3\times3} & \mathbf{0}_{3\times1} \end{bmatrix}$$

$$\mathcal{L}^2_{f_1,f_0} h = \nabla\mathcal{L}^1_{f_1} h f_0 = -\omega_l \mathbf{J}_\theta^{(1)}\mathbf{e}_j, \ \forall j \quad \nabla\mathcal{L}^2_{f_1,f_0} h = \begin{bmatrix} \mathbf{0}_{3\times3} & -\omega_l \mathbf{J}_\theta^{(2)}\mathbf{e}_j & \mathbf{0}_{3\times3} & -\mathbf{J}_\theta^{(1)}\mathbf{e}_j \end{bmatrix}$$

$$\mathcal{O} = \begin{bmatrix} \nabla\mathcal{L}^0 h^\mathsf{T} & \nabla\mathcal{L}^1_{f_0} h^\mathsf{T} & \nabla\mathcal{L}^1_{f_1} h^\mathsf{T} & \nabla\mathcal{L}^2_{f_1,f_0} h^\mathsf{T} \end{bmatrix}^\mathsf{T}$$

Matrix $\mathcal{O}$ loses the column rank of 8 when the term $-\mathbf{J}_\theta^{(1)^\mathsf{T}}\mathbf{p}$ is zero and the terms $\nabla\mathcal{L}^1_{f_1} h, \nabla\mathcal{L}^2_{f_1,f_0} h$ vanish ($\mathbf{v}_i = 0$). $\mathbf{J}_\theta^{(1)}\mathbf{e}_3$ of $\nabla\mathcal{L}^1_{f_1} h$ is always zero since observability of θ is independent of the vertical velocity v_{iz}. Therefore the system is locally weakly observable for all cases except when $x = y = v_{ix} = v_{iy} = 0$. I.e., the system is unobservable for an $S_3 - Mesh$ configuration when the target robot is directly on top of or below the local platform and the target robot is stationary on a horizontal plane.

Case $S_3 - Star$ **configuration observability**

$$\mathcal{L}^0 h = h, \qquad \nabla\mathcal{L}^0 h = \begin{bmatrix} \mathbf{I}_{3\times3} & \mathbf{0}_{3\times1} & \mathbf{0}_{3\times3} & \mathbf{0}_{3\times1} \end{bmatrix}$$

$$\mathcal{L}^1_{f_1} h = \nabla\mathcal{L}^0 h f_1 = \begin{bmatrix} \mathbf{R}_\theta \mathbf{e}_j \end{bmatrix} \ \forall j, \quad \nabla\mathcal{L}^1_{f_1} h = \begin{bmatrix} \mathbf{0}_{3\times3} & \mathbf{J}_\theta^{(1)}\mathbf{e}_j & \mathbf{0}_{3\times3} & \mathbf{0}_{3\times1} \end{bmatrix}$$

$$\mathcal{L}^1_{f_0} h = \begin{bmatrix} -\mathbf{v}_l + \omega_l \mathbf{p} \times \mathbf{e}_3 \end{bmatrix}, \qquad \nabla\mathcal{L}^1_{f_0} h = \begin{bmatrix} -\omega_l[\mathbf{e}_3]_\times & \mathbf{0}_{3\times1} & -\mathbf{I}_{3\times3} & -[\mathbf{e}_3]_\times \mathbf{p} \end{bmatrix}$$

$$\mathcal{L}^2_{f_1,f_0} h = \begin{bmatrix} -\omega_l \mathbf{J}_\theta^{(1)}\mathbf{e}_j \end{bmatrix}, \qquad \nabla\mathcal{L}^2_{f_1,f_0} h = \begin{bmatrix} \mathbf{0}_{3\times3} & -\omega_l \mathbf{J}_\theta^{(2)}\mathbf{e}_j & \mathbf{0}_{3\times3} & -\mathbf{J}_\theta^{(1)}\mathbf{e}_j \end{bmatrix}$$

$$\mathcal{O} = \begin{bmatrix} \nabla\mathcal{L}^0 h^\mathsf{T} & \nabla\mathcal{L}^1_{f_1} h^\mathsf{T} & \nabla\mathcal{L}^1_{f_0} h^\mathsf{T} & \nabla\mathcal{L}^2_{f_1,f_0} h^\mathsf{T} \end{bmatrix}^\mathsf{T}$$

Matrix $\mathcal{O}$ loses the column rank of 8 when the terms $\mathcal{L}^1_{f_0} h$, $\nabla\mathcal{L}^2_{f_1,f_0} h$ vanish

($\mathbf{v}_i = 0$). The term $\mathbf{J}_\theta^{(1)}\mathbf{e}_3$ is always zero since observability of θ is independent of the vertical velocity v_{iz}. Therefore the system is locally weakly observable for all cases except when $v_{ix} = v_{iy} = 0$. I.e., when the target robot is stationary on a horizontal plane its states are unobservable for an $S_3 - Star$ configuration.

Global uniqueness

The analysis given above establishes whether a system is "*locally weakly observable*". For a system to be "*locally observable*" it should be solvable for a unique global solution instantaneously; i.e., all states $\mathbf{x}$ should be distinguishable using the inputs and measurement quantities for any neighbourhood around $\mathbf{x} \in \mathcal{X}$. The following four Lemmas complete the analysis by establishing global uniqueness of the solution for each case.

Lemma 1. *The system of equations related to all Mesh measurement configurations has a globally unique solution for the relative pose between the platforms when $x \neq 0$ and $y \neq 0$.*

Proof. Consider the two relative measurements $\mathbf{y}_p$ and $\mathbf{y}_{p'}$. The position can be directly read from $\mathbf{y}_p$. To find orientation θ, first modify the vectors by removing their z components which do not have any coupling with rotation in a 2.5D analysis.

$$\mathbf{y}_p \leftarrow \begin{bmatrix} \mathbf{e}_1^\mathsf{T}\mathbf{y}_p & \mathbf{e}_2^\mathsf{T}\mathbf{y}_p & 0 \end{bmatrix}^\mathsf{T}, \quad \mathbf{y}_{p'} \leftarrow \begin{bmatrix} \mathbf{e}_1^\mathsf{T}\mathbf{y}_{p'} & \mathbf{e}_2^\mathsf{T}\mathbf{y}_{p'} & 0 \end{bmatrix}^\mathsf{T}$$

Using the relations $\mathbf{y}_p = \mathbf{p}$ and $\mathbf{y}_{p'} = -\mathbf{R}_\theta^\mathbf{T}\mathsf{p}$ where $p = [x \ y \ 0]^\mathsf{T}$, the cross product and the dot product can be found as follows:

$$\mathbf{y}_{p'} \times \mathbf{y}_p = \begin{bmatrix} 0 & 0 & -(x^2+y^2)\sin\theta \end{bmatrix}^\mathsf{T}, \quad \mathbf{y}_{p'}^\mathsf{T}\mathbf{y}_p = -(x^2+y^2)\cos\theta$$

Therefore when $x^2 + y^2 \neq 0$ a globally unique solution for θ can be found.

$$\hat{\theta} \quad = \arctan 2(-(\mathbf{y}_{p'} \times \mathbf{y}_p)^\mathsf{T}\mathbf{e}_3, -\mathbf{y}_{p'}^\mathsf{T}\mathbf{y}_p)$$

□

Lemma 2. *The system of equations given by $S1 - Star$ measurement configuration has a globally unique solution for the relative pose between the platforms when $v_{ix} \neq 0$ and $v_{iy} \neq 0$.*

Proof. Consider the known measurements and their dynamics at any time instant k.

$$\mathbf{y}_p = \mathbf{p}, \quad \dot{\mathbf{y}}_p = \mathbf{R}_\theta \mathbf{v}_i - \mathbf{v}_l + \mathbf{y}_p \times \mathbf{e}_3 \omega_l \tag{3.19}$$

For S_1 configurations the vector of unknowns is $(\mathbf{p}^\mathsf{T},\ \theta)^\mathsf{T}$. The position $\mathbf{p}$ can be read directly from the first equation ($\hat{\mathbf{p}} = y$). The second equation is modified by taking all known quantities to R.H.S. and redefining them as $\boldsymbol{\gamma}$.

$$\begin{aligned} \mathbf{R}_\theta \mathbf{v}_i \ &= \boldsymbol{\gamma} \\ \boldsymbol{\gamma} := \dot{\mathbf{y}} + \mathbf{v}_l - \mathbf{y}_p \times \mathbf{e}_3 \boldsymbol{\omega}_l \end{aligned}$$

By expanding this vector equation, the following trigonometric equation can be found.

$$\begin{aligned} \cos\theta v_{ix} - \sin\theta v_{iy} \ &= \mathbf{e}_1^\mathsf{T}\boldsymbol{\gamma} \\ \sin\theta v_{ix} + \cos\theta v_{iy} \ &= \mathbf{e}_2^\mathsf{T}\boldsymbol{\gamma} \\ v_{iz} \qquad\qquad\ &= \mathbf{e}_3^\mathsf{T}\boldsymbol{\gamma} \end{aligned}$$

This can be solved to find the solution for θ.

$$\hat{\theta} := \theta \quad = \arctan 2(\mathbf{e}_2^\mathsf{T}\boldsymbol{\gamma}, \mathbf{e}_1^\mathsf{T}\boldsymbol{\gamma}) - \arctan 2\left(\frac{v_{iy}}{\sqrt{v_{ix}^2+v_{iy}^2}}, \frac{v_{ix}}{\sqrt{v_{ix}^2+v_{iy}^2}}\right)$$

Therefore the $S_1 - Star$ configuration has a globally unique solution given by $(\hat{\mathbf{p}}^\mathsf{T},\ \hat{\theta})^\mathsf{T}$ which is valid for all $\mathbf{x}$ when $v_{ix}^2 + v_{iy}^2 \neq= 0$. □

Lemma 3. *The system of equations given by the $S2-Star$ measurement configuration where the transverse velocities are constrained ($v_{iy} = 0$), has two globally distinct solutions for the relative pose between the platforms when $v_{ix} \neq 0$.*

Proof. Following the same steps as above one arrives at the following set of equations:

$$\begin{aligned} \cos\theta v_{ix} - \sin\theta v_{iy} &= \mathbf{e}_1^\mathsf{T}\boldsymbol{\gamma} \\ \sin\theta v_{ix} + \cos\theta v_{iy} &= \mathbf{e}_2^\mathsf{T}\boldsymbol{\gamma} \\ v_{iz} &= \mathbf{e}_3^\mathsf{T}\boldsymbol{\gamma} \end{aligned}$$

For the S_2 configurations the vector of unknowns is $(\mathbf{p}^\mathsf{T},\ \theta,\ \mathbf{v}_i^\mathsf{T},\ \omega_i)^\mathsf{T}$. As required by observability conditions $v_{iy,}$ is forced to be zero. v_{iz} is directly found by the third equations. The resulting trigonometric equations can be solved for two distinct solutions by using the relation $\cos\theta^2 + \sin\theta^2 = 1$.

$$\begin{aligned} \hat{v}_{ix} &= \pm\sqrt{\mathbf{e}_1^\mathsf{T}\boldsymbol{\gamma}^2 + \mathbf{e}_2^\mathsf{T}\boldsymbol{\gamma}^2} \\ \theta &= \arctan 2\left(\tfrac{\mathbf{e}_2^\mathsf{T}\gamma}{v_{ix}}, \tfrac{\mathbf{e}_1^\mathsf{T}\gamma}{v_{ix,k}}\right),\ \forall v_{ix} \neq 0 \end{aligned}$$

ω_i can be found as follows using $\ddot{\mathbf{y}}$.

$$\begin{aligned} \boldsymbol{\gamma}' := \ddot{\mathbf{y}}_p + \dot{\mathbf{v}}_l - \dot{\mathbf{y}}_p \times \mathbf{e}_3\omega_l - \mathbf{y}_p \times \mathbf{e}_3\dot{\omega}_l &= \mathbf{J}_\theta(\omega_i - \omega_l)\mathbf{v}_i \\ \omega_i &= \omega_l + \tfrac{\mathbf{e}_2^\mathsf{T}\boldsymbol{\gamma}' - \mathbf{e}_1^\mathsf{T}\boldsymbol{\gamma}'}{2\sin\theta} \end{aligned}$$

Therefore the $S_2 - Star$ configuration has two globally distinct solutions. The solutions for the unknown quantities $(\mathbf{p},\ \theta,\ \mathbf{v}_i,\ \omega_i)$ can be summarized as follows:

$$\begin{aligned} &(\hat{\mathbf{p}},\ \hat{\theta},\ \hat{\mathbf{v}}_i,\ \hat{\omega}_i + \omega_l) \\ &(\hat{\mathbf{p}},\ \pi + \hat{\theta},\ [\ -v_{ix},\ -v_{iy},\ v_{iz}]^\mathsf{T},\ -\hat{\omega}_i + \omega_l),\ \forall v_{ix} \neq 0 \end{aligned}$$

□

Lemma 4. *The system of equations given by $S3-Star$ measurement configuration has two globally distinct solutions for the relative pose between the platforms when $v_{ix} \neq 0$ and $v_{iy} \neq 0$.*

Proof. Consider the known measurement and its dynamics at a time instant k. We assume that the target is moving at a trajectory where $\dot{\mathbf{v}}_i = \dot{\omega}_i = 0$.

$$\begin{aligned} \mathbf{y}_p &= \mathbf{p}, \\ \dot{\mathbf{y}}_p &= \mathbf{R}_\theta \mathbf{v}_i - \mathbf{v}_l + \mathbf{y}_p \times \mathbf{e}_3 \omega_l \\ \ddot{\mathbf{y}}_p &= \mathbf{J}_\theta \mathbf{v}_i (\omega_i - \omega_l) + \dot{\mathbf{y}}_p \times \mathbf{e}_3 \omega_l \end{aligned} \tag{3.20}$$

By expanding this vector equation, the following trigonometric equation can be found.

$$\begin{aligned} (-\sin\theta v_{ix} - \cos\theta v_{iy})(\omega_i - \omega_l) + \dot{y}_2 \omega_l &= \ddot{y}_1 \\ (\cos\theta v_{ix} - \sin\theta v_{iy})(\omega_i - \omega_l) - \dot{y}_1 \omega_l &= \ddot{y}_2 \end{aligned}$$

The equations produce the following quadratic equation for ω_l, which can be solved for two distinct solutions.

$$(\omega_i - \omega_l)^2 = (\dot{y}_2 \omega_l - \ddot{y}_1)^2 + (-\dot{y}_1 \omega_l - \ddot{y}_2)^2$$
$$\hat{\omega}_l = \{\omega_{l_1}, \omega_{l_2}\}$$

θ and $\mathbf{v}_l$ is found using the equation related to $\dot{\mathbf{y}}$ and $\ddot{\mathbf{y}}$

$$\begin{aligned} \hat{\theta} &= ATan2(\dot{y}_2 \hat{\omega}_l - \ddot{y}_1, -\dot{y}_1 \hat{\omega}_l - \ddot{y}_2) - ATan2(v_{iy}, v_{ix}),\ \forall v_{ix} \wedge v_{iy} \neq 0 \\ \hat{\mathbf{v}}_l &= \mathbf{R}_{\hat{\theta}} - \dot{y} + \mathbf{y}_p \times \mathbf{e}_3 \hat{\omega}_l \end{aligned}$$

It is evident from the solutions that the $S_3 - Star$ configuration produces a globally distinct solution $\forall v_{ix}$ & $v_{iy} \neq 0$, if the local robot does not assume a turn rate ($\omega_l = 0$). Otherwise the system produces two globally distinct solutions. □

The summary of analysis - 2.5D problem

The results of the observability analysis are summarized in Table 3.3.5.

Table 3.3: Summary of the observability analysis for the 2.5D problem
✓- Locally observable ✗- Unobservable

Configuration	Observability	Unobservable conditions
$S_1 - Mesh$	✓	$x = y = v_{ix} = v_{iy} = v_{lx} = v_{ly} = 0$
$S_1 - Star$	✓	$v_{ix} = v_{iy} = 0$
$S_2 - Mesh$	✓	$x = y = v_{lx} = v_{ly} = 0$
$S_2 - Star$	✗	See note[1]
$S_3 - Mesh$	✓	$x = y = v_{ix} = v_{iy} = 0$
$S_3 - Star$	✓	$v_{ix} = v_{iy} = 0$ See note[2]

[1] - The $S_2 - Star$ configuration can be modified to be locally weakly observable by, 1)sensing at least one horizontal velocity component of target, 2) constraining the target trajectory; i.e, make v_{iy} known to be zero, 3) assuming platforms with constrained movement, e.g, differential drive robots where $v_{iy} = 0$.

[2] - This configuration is only locally observable for $\omega_l = 0$. Otherwise the configuration is locally weakly observable.

3.3.6 Implications on estimator design

The observability study results in the following implications in the subsequent filter design and the distributed estimation framework design.

- For full state observability communication must be established between platforms. The measurement quantities which require communication to the local platform are $y_{p'}$, $\mathbf{v}_i$ and ω_i. All observable configurations presented have utilized at least one of these quantities. Therefore when the measurements $y_{p'}$ or $(\mathbf{v}_i,\ \omega_i)$ are communicated between platforms the overall system becomes an observable configuration.

- The third column of Table 3.3.5, reports the unobservable conditions of the system as identified by the observability study. These results can be explained in a

practical standpoint as follows. The $S_1 - Mesh$ configuration is only unobservable when both the local and the target robots are stationary and the two robots align on top of each other. Under this condition the relative orientation of the robots are unobservable, hence the orientation results of any estimator under this configuration should be treated with low confidence. Similarly, $S_2 - Mesh$ configuration is only unobservable when the local robot is stationary and the two robots align on top of each other. $S_3 - Mesh$ configuration is only unobservable when the target robot is stationary and the two robots align on top of each other. $S_1 - Star$ and $S_3 - Star$ configurations are only unobservable when the target robot is stationary. $S_2 - Star$ configuration is an unobservable system.

- In the absence of communicated $y_{p'}$, $\mathbf{v}_i$ and ω_i measurements ($S_2 - Star$ configuration), the system is unobservable. The study shows that in order to establish an observable system under these conditions, one should either use platforms which cannot produce transverse velocities (such as differential drive robots) or assume trajectories which constrain the platform to have zero transverse velocities.

- Although $S_1 - Star$, $S_3 - Star$ and the constrained $S_2 - Star$ configurations are observable under non stationary conditions, only the $S_1 - Star$ configuration has a globally unique solution. $S_2 - Star$ and $S_3 - Star$ produce multiple global solutions depending on the velocities assumed by the robots. This necessitates robust initialization schemes to find a correct solution, or multiple hypothesis estimation schemes to keep track of possible solutions.

- To incorporate this simplified 2.5D model studied in the localization filters, an attitude reference system must be attached to each platform which allows

the transformation of the measurement quantities to a zero-roll-pitch frame of reference.

3.3.7 The EKF estimator

The EKF is a standard nonlinear stochastic estimator which can be used for the relative localization task. In this section EKFs are derived for the different system configurations considered, in order to use them as filters to validate the findings of the observability study. An EKF for a given system model $f(\mathbf{x}, \mathbf{u})$ and a measurement model $h(\mathbf{x})$, takes the form (3.21). It has a prediction term $f(\hat{\mathbf{x}}, \mathbf{u})$, and a correction term KE, where $\hat{\mathbf{x}}$ is the state estimate and E is a linear output error term, i.e., $E(\hat{\mathbf{x}}, \mathbf{y}, \boldsymbol{\nu}) = \mathbf{y} - h(\hat{\mathbf{x}}, \mathbf{u})$.

$$\dot{\hat{\mathbf{x}}} = f(\hat{\mathbf{x}}, \mathbf{u}) + K(\mathbf{y} - h(\hat{\mathbf{x}}, \mathbf{u})) \tag{3.21}$$

The EKF performs a first order Taylor series expansion of the system dynamics (3.10) about the current state estimate ($\mathbf{x} = \hat{\mathbf{x}}$, $\mathbf{w} = 0$, $\boldsymbol{\nu} = 0$).

$$\begin{aligned} \dot{\mathbf{x}} &= f(\hat{\mathbf{x}}, \mathbf{u}) + \frac{\partial f}{\partial \mathbf{x}}(\mathbf{x} - \hat{\mathbf{x}}) + \frac{\partial f}{\partial \mathbf{w}}(\mathbf{w} - 0) \\ \mathbf{y} &= h(\hat{\mathbf{x}}, \mathbf{u}) + \frac{\partial h}{\partial \mathbf{x}}(\mathbf{x} - \hat{\mathbf{x}}) + \frac{\partial h}{\partial \boldsymbol{\nu}}(\boldsymbol{\nu} - 0) \end{aligned} \tag{3.22}$$

The state error $\tilde{\mathbf{x}}$ is defined as $\hat{\mathbf{x}} - \mathbf{x}$. The dynamics of the state error are found by subtracting (3.22) from (3.21) to deduce a linear system.

$$\begin{gathered} \dot{\tilde{\mathbf{x}}} = (A - KC)\tilde{\mathbf{x}} - M\mathbf{w} + KN\boldsymbol{\nu} \\ \left[A = \frac{\partial f}{\partial \mathbf{x}},\ C = \frac{\partial E}{\partial \mathbf{x}},\ M = \frac{\partial f}{\partial \mathbf{w}},\ N = \frac{\partial E}{\partial \boldsymbol{\nu}}\right]\Bigg|_{(\hat{\mathbf{x}},0,0)} \end{gathered}$$

The state transition jacobian A, output jacobian C, process noise jacobian M, and the measurement noise jacobian N are used to perform Kalman gain computation

and covariance propagation in its standard linear form as follows:

$$\dot{P} = AP + PA^T + MQM^T$$
$$K = PC^T(CPC^T + NRN^T)^{-1}$$
$$P = (I - KC)P$$

Following this procedure the EKF derivation for the 3D $S_2 - Star$ configuration is presented as an example.

Initialization

$$\hat{\mathbf{x}} = \begin{bmatrix} \mathbf{y}_p & 1 & \mathbf{0} & \mathbf{0} & \mathbf{0} \end{bmatrix}^T_{1\times 13} \quad P = \mathrm{E}(\tilde{\mathbf{x}}\tilde{\mathbf{x}}^T) = \mathbf{I} \quad Q = \mathrm{E}(\mathbf{w}\mathbf{w}^T) \quad R = \mathrm{E}(\boldsymbol{\nu}\boldsymbol{\nu}^T)$$

3D Observer

$$\begin{pmatrix} \dot{\hat{\mathbf{p}}} \\ \dot{\hat{\mathbf{q}}} \\ \dot{\hat{\mathbf{v}}}_i \\ \dot{\hat{\omega}}_i \end{pmatrix} = \underbrace{\begin{pmatrix} \mathbf{R}_{\hat{\mathbf{q}}}\hat{\mathbf{v}}_i - \mathbf{v}_l - \boldsymbol{\omega}_l \times \hat{\mathbf{p}} \\ \frac{1}{2}(\hat{\mathbf{q}} * \hat{\bar{\boldsymbol{\omega}}}_i - \bar{\boldsymbol{\omega}}_l * \hat{\mathbf{q}}) \\ \mathbf{0} \\ \mathbf{0} \end{pmatrix}}_{State\ Prediction} + \underbrace{\begin{pmatrix} K_p E \\ K_\theta E \\ K_v E \\ K_\omega E \end{pmatrix}}_{State\ Correction} \qquad E = \underbrace{\begin{pmatrix} \mathbf{y}_p - \hat{\mathbf{p}} \\ \mathbf{y}_{v_i} - \hat{\mathbf{v}}_\mathbf{i} \\ \mathbf{y}_{\omega_i} - \hat{\boldsymbol{\omega}}_\mathbf{i} \end{pmatrix}}_{Innovation}$$

$$Gain\ Matrix \quad K = \begin{bmatrix} K_p & K_\theta & K_{vi} & K_\omega \end{bmatrix}^T$$

Covariance Prediction

$$A = \begin{bmatrix} [-\hat{\boldsymbol{\omega}}_i]_\times & 2Q^{+\intercal}V_i^+ & Q^+Q^{-T} & [\mathbf{p}]_\times \\ \mathbf{0} & \frac{1}{2}(\hat{\Omega}_i^- - \hat{\Omega}_l^+) & \mathbf{0} & \frac{1}{2}\hat{\Omega}_i^+ \\ \mathbf{0} & \mathbf{0} & \mathbf{0} & \mathbf{0} \\ \mathbf{0} & \mathbf{0} & \mathbf{0} & \mathbf{0} \end{bmatrix} \quad M = \mathbf{I}$$

$$\dot{P} = AP + PA^T + MQM^T$$

Covariance Correction

$$C = \begin{bmatrix} \mathbf{I} & \mathbf{0} & \mathbf{0} & \mathbf{0} \\ \mathbf{0} & \mathbf{0} & \mathbf{I} & \mathbf{0} \\ \mathbf{0} & \mathbf{0} & \mathbf{0} & \mathbf{I} \end{bmatrix} \quad N = \mathbf{I}$$

$$K = PC^T(CPC^T + NRN^T)^{-1} \quad P = (I - KC)P$$

Similarly the filter derivation for the 2.5D relative localization problem reads:

2.5D Observer

$$\dot{\hat{\mathbf{x}}} = \begin{pmatrix} \dot{\hat{\mathbf{p}}} \\ \dot{\hat{\theta}} \\ \mathbf{v}_i \\ \omega_i \end{pmatrix} = \begin{pmatrix} \mathbf{R}_{\hat{\theta}}\mathbf{v}_i - \mathbf{v}_l - \boldsymbol{\omega}_l \times \hat{\mathbf{p}} \\ \omega_i - \omega_l \\ \mathbf{0} \\ 0 \end{pmatrix} + \begin{pmatrix} K_p E \\ K_\theta E \end{pmatrix} \qquad E = \left(\mathbf{y}_p - \hat{\mathbf{p}}\right)$$

EKF Matrices

$$A = \begin{bmatrix} -[\boldsymbol{\omega}_l]_\times & \mathbf{J}_{\hat{\theta}}\mathbf{v}_i & \mathbf{R}_{\hat{\theta}} & \mathbf{e}_3^T[\mathbf{p}]_\times \\ \mathbf{0} & 0 & \mathbf{0} & 0 \\ \mathbf{0} & 0 & \mathbf{0} & 0 \end{bmatrix} \quad C = \begin{bmatrix} \mathbf{I}_3 & \mathbf{0} & \mathbf{0} & \mathbf{0} \end{bmatrix}$$

$$M = \mathbf{I}_4 \qquad N = \mathbf{I}_3 \qquad K = \begin{bmatrix} K_p & K_\theta \end{bmatrix}^T$$

This standard EKF design procedure was used to derive filters for all other configurations in a similar manner.

3.4 Results

The EKF estimator is used to validate the observability results derived in this chapter. Numerical simulations are used to validate the different observability limitations identified in this analysis for 2.5D simplifications. An experimental system is used to reproduce these characteristics using real measurements logged by robots following a simple linear trajectory and a 2.5D circular trajectory.

3.4.1 Simulations - 3D analysis results

This is a numerical simulation designed to demonstrate the capability of the EKF to perform estimation of unknown states including unknown velocities as identified by the observability analysis related to the full 3D system. Figure 3.3 illustrates a trajectory that is assumed by two platforms. Figure 3.4 illustrates the position and orientation estimation of an EKF and the ability of the EKF to estimate the unknown

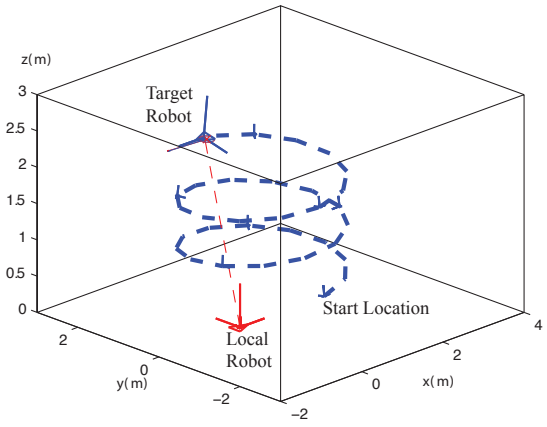

Figure 3.3: Trajectory of the local and target platforms used for the 3D EKF evaluation

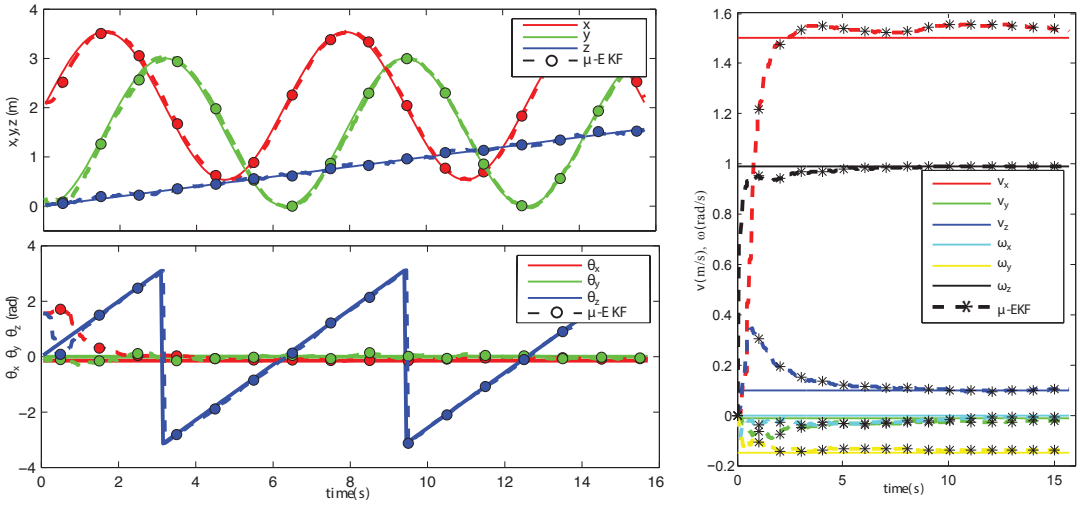

Figure 3.4: Localization results for the 3D EKF for unknown v_{ix}

forward velocity of the platform.

3.4.2 Simulations - 2.5D analysis results

This is a numerical simulation designed to validate the observability requirements established for the 2.5D system. The different configurations were numerically simulated with noise figures relevant to the selected sensor presented in chapter 2. This

allows the numerical validation of the localization performance and observability for each case. A pair of robots was simulated along a trajectory as illustrated in Figure 3.5.

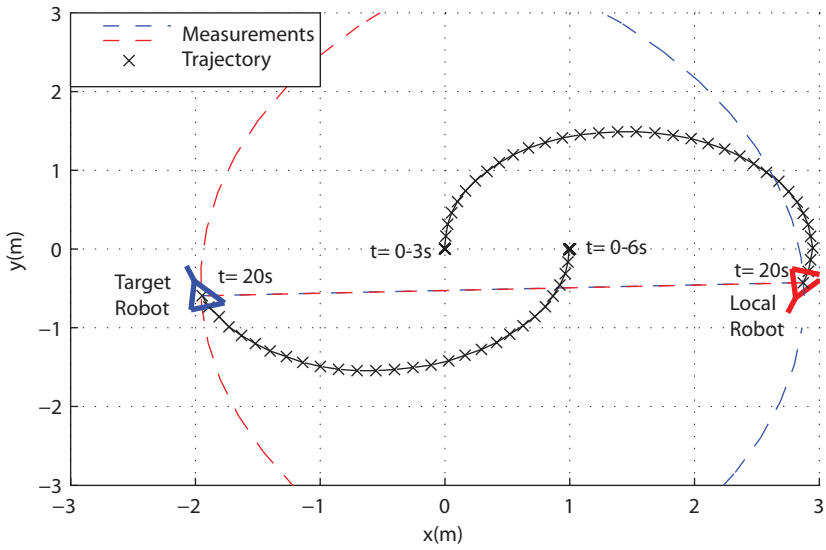

Figure 3.5: The Simulated path

Both the local and target robots only start movement at $t = 6s$, thereby allowing the analysis of the localization capability for cases where input velocities are zero (Figure 3.5). Figure 3.7 illustrates localization results for cases where input velocities of the target platform are unknown. Figure 3.8 illustrates localization results for cases where input velocities of the local platform are unknown. As identified in the observability study, all $Mesh$ configurations are observable irrespective of input availability or zero inputs to the system. The S_2-Star configuration is only observable in scenarios where the target robot is moving and the transverse velocities of the robot are constrained while the $S_3 - Star$ configuration is observable when $\mathbf{v}_i \neq 0$. The filters for the $S_2 - Star$ configuration specifically demonstrate random stabilization to one of the two global solutions. The results present a run which stabilized to the correct global solution, thus necessitating the requirement of multi-hypothesis

estimate propagation to handle incorrect initializations.

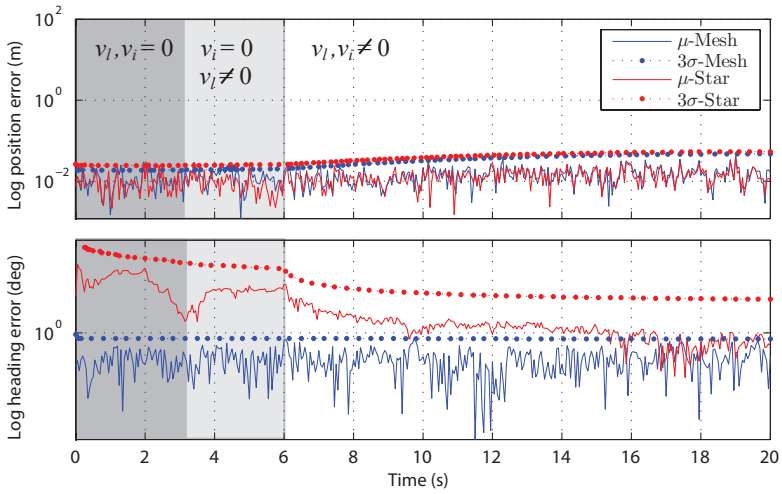

Figure 3.6: Localization results for known input cases (S_1), of *Mesh* and *Star* configurations

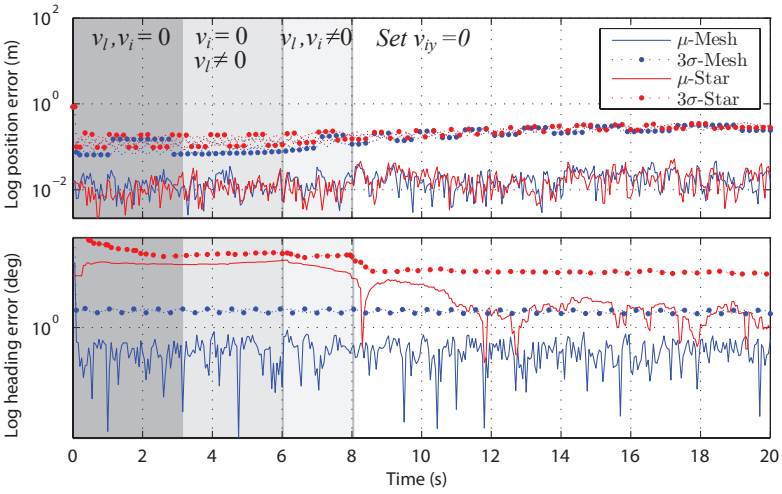

Figure 3.7: Localization results for unknown input cases (S_2), of *Mesh* and *Star* configurations

3.4.3 Experimental validation - linear trajectory

Observability between two robots was evaluated similar to the simulations by moving a pair of robots equipped with ultrasonic and vision based sensor nodes. Figure 3.9

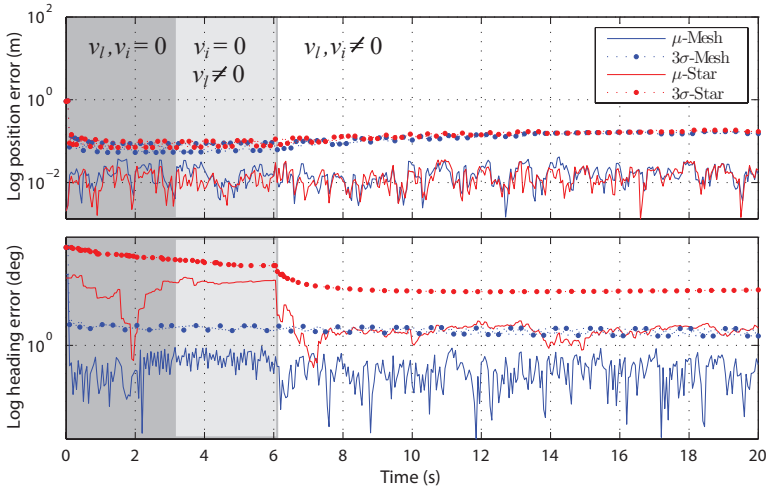

Figure 3.8: Localization results for unknown input cases (S_3), of *Mesh* and *Star* configurations

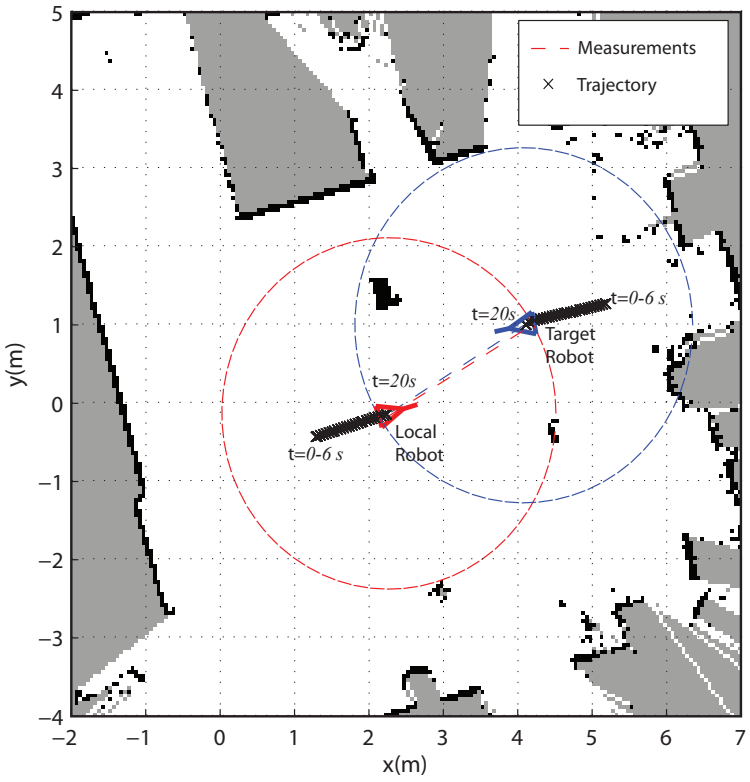

Figure 3.9: The Experimental path

illustrates the trajectory of the robots while Figure 3.10 illustrates the localization performance. Due to inaccuracies in laser localization of ground robots, the mean position error figures exhibit a small bias in ground truth validation. However, the error variance figures exhibit good congruence with the numerical simulations. As identified in the observability study, the *Star* configurations required platform movement for the states of the system to be observable.

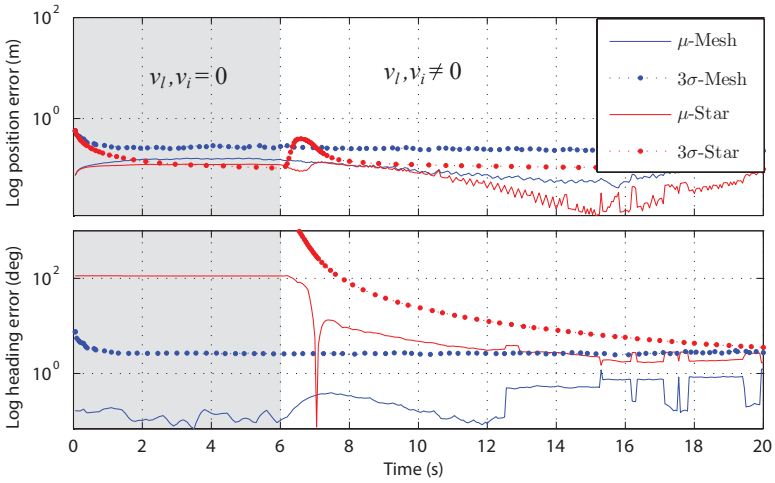

Figure 3.10: Localization results for known input cases (S_1), of *Mesh* and *Star* configurations

3.4.4 Experimental validation - circular trajectory

This experiment performs EKF relative localization for the elevated circular trajectory between robots presented in chapter 2. Figure 3.13 illustrates the experimental system and the trajectory it assumed, while Figure 3.14 presents the convergence of filters. Here a Mesh configuration was not used due to field of view limitations experienced by the sensor attached to the MAV. Results related to $S_1 - Star$ and $S_2 - Star$ with constrained transverse velocity and $S_3 - Star$ configuration are presented which exhibits correct estimation.

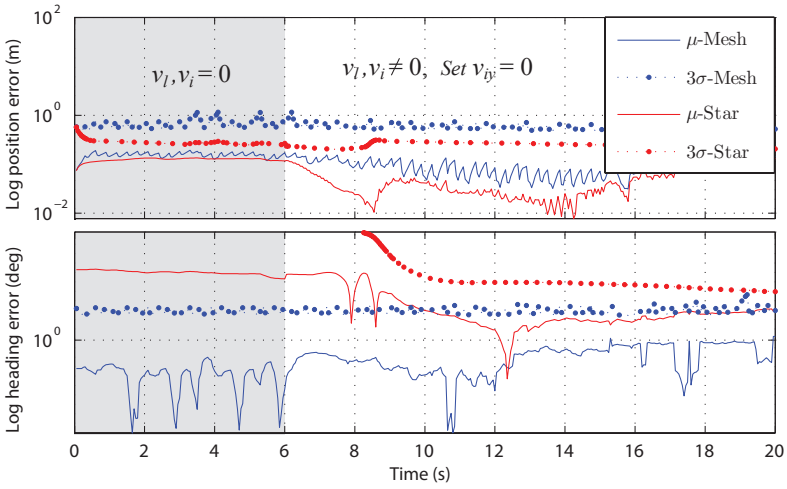

Figure 3.11: Localization results for unknown input cases (S_2), of *Mesh* and *Star* configurations

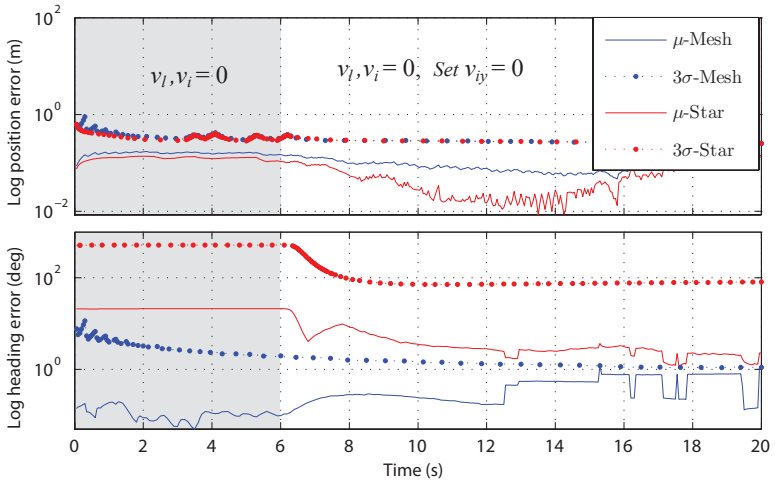

Figure 3.12: Localization results for unknown input cases (S_3), of *Mesh* and *Star* configurations

3.5 Conclusion

This chapter presented an exhaustive observability analysis of the relative localization problem. Configurations considering different availability of relative measurements and input velocities were considered. Conditions required for full system observability were identified, and validated through both numerical studies and an implementation

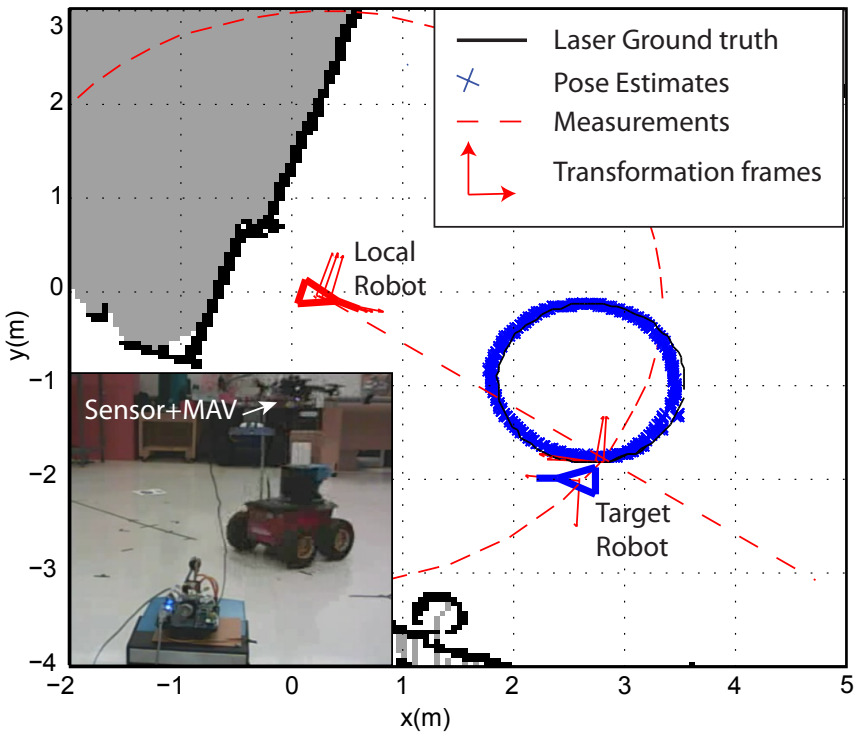

Figure 3.13: Actual and estimated path for a circular trajectory localization experiment

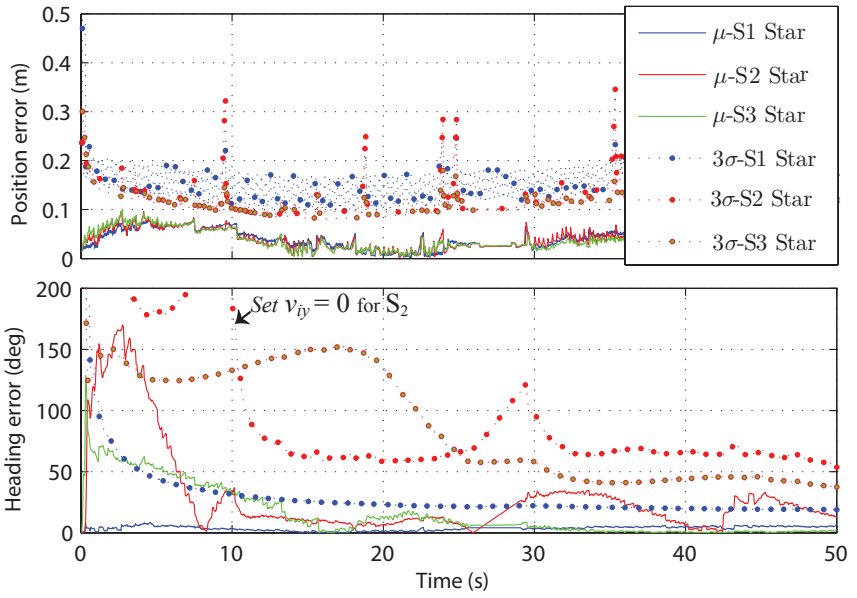

Figure 3.14: Localization results for known input (S_1) and unknown input (S_2,S_3) with *Star* configuration (for the circular trajectory)

of a multi-robot system equipped with relative positioning sensors.

Although the analysis is general in terms of input availability and measurement availability, it provides valuable insight into the specific relative localization designs considered in subsequent chapters of the thesis. Chapter 4 develops the $S_2 - Star$ configuration to design nonlinear filters to be used with the proposed distributed filtering framework, along with the attitude reference systems necessary for 2.5D simplification of the problem. Chapter 5 establishes specific modules to communicate measurement quantities at low rates, and handle uncertain initialization of the filters using multi-hypothesis estimation. This is to propagate the globally distinct solutions resulting from observability limitations of the $S_2 - Star$ configuration.

The work presented in this chapter completes the observability analysis for the relative localization problem under input constraints. However the work identifies the requirement of additional analysis relevant to relative localization. The main remaining work is the 3D observability problem considering the full sensor suit consisting of an IMU attached to each sensor. Since inertial sensing measures accelerations and angular velocities of platforms, this analysis would point to interesting sensor design strategies and path planning strategies to realize observable sensor networks.

Chapter 4

Relative Localization: Nonlinear Filtering

The previous chapter identified the requirement of a relative pose filter and an attitude estimator to support 2.5D relative localization pursued in this thesis. In a 2.5D setting the relative pose filter's task is to find the relative position and heading of the platform while the attitude estimator finds the roll and pitch of the platform. The previous chapter also introduced the EKF as an estimator for these filtering tasks which can be considered as the most popular solution used for relative pose filtering [39], and attitude estimation of robots [85]. However, the EKF constitutes a linear formulation of the inherently nonlinear problem faced by robotic platforms. As a result, the EKF does not extend well to low cost deterministic designs. This work designs both relative pose and attitude estimation modules with particular attention given to the nonlinearity of the problem, and low-cost implementation of the filters. The chapter [1] presents a novel steady-state invariant extended Kalman filter design

[1] This chapter is based on the following publications of the author:

* O. De Silva, G. K. I. Mann, and R. G. Gosine, "Relative Localization of Robots with Steady State Invariant Extended Kalman Filtering," *IEEE Transactions on Control System Technology*, (Under Review), 2015.

approach applied to the attitude filtering and pose filtering modules. The proposed approach incorporates a symmetry preserving observer design method proposed by [41] to derive the filters for the attitude and relative pose filtering tasks. Then these nonlinear filter designs are extended to low cost applications by identifying gain tuning procedures which are based on process and measurement noise parameters of a system. The chapter concludes with numerical and experimental validation of the proposed filter designs along with a detailed discussion of its limitations.

4.1 Introduction

Estimating the pose (position and heading) and the attitude (roll and pitch) of robots using available measurements is traditionally addressed using Extended Kalman Filters [39, 85]. In fact, EKF dominates as a popular filter in many nonlinear estimation problems. Notable applications related to robotics are landmark localization [86], SLAM [86], target tracking [49], AHRS [85], and inertial navigation systems [85] etc. However, the use of the EKF has two main drawbacks when considering nonlinear system models with additive white Gaussian noise figures.

The first problem of the EKF is associated with the fact that it considers a first order approximation of the system model used for filtering. This causes the filter to be unstable and even diverge in cases where the linearization is performed about an inaccurately estimated trajectory. The linearized approximation additionally gives an inaccurate representation of the covariance estimate which eventually leads to

* O. De Silva, G. K. I. Mann, and R. G. Gosine, “Relative Localization with Symmetry Preserving Observers," in *IEEE Canadian Conference on Electrical and Computer Engineering (CCECE)*, 2014, pp. 1-6.

* O. De Silva, G. K. I. Mann, and R. G. Gosine, “Automated Tuning of the Nonlinear Complementary Filter for an Attitude Heading Reference Observer," in *IEEE Workshop on Robot Vision*, 2013, pp. 171-176.

inconsistent updates. The effect of this problem is reduced at the expense of more computational resources in Unscented Kalman Filters(**UKF**) [87], and particle filters [86] where better nonlinear propagation of state covariances is performed.

A second problem of the EKF is that it assumes a linear state error and a linear output error in its formulation. This error representation is inaccurate in many practical applications because the EKF formulation tends to overlook the underlying geometry of the system in consideration. This is common to even UKF solutions if applied directly without changing the linear error state assumptions. This problem has been well addressed by nonlinear filters which results in solutions with similar or reduced computation demand in comparison to an EKF, but with increased difficulty in systematic design for a general system. Attitude heading reference systems are prime examples where exploiting the geometry of the rotation group $SO(3)$ results in commercial grade solutions such as, the multiplicative extended Kalman filter [82], and the nonlinear complimentary filter [54], that exhibit similar and reduced computational demand respectively.

Correspondingly, multi-robot systems operate in the special Euclidean group $SE(3)$, i.e., the group of translations and rotations. Different nonlinear filter derivations are reported in literature where the solutions are deterministic formulations and are not applicable in a systematic manner for a general nonlinear problem [42]. However, a recent breakthrough in nonlinear filter design reported in [41] proposes a constructive method to derive nonlinear filters for systems possessing symmetries. Combining this approach with error state Kalman filtering for gain stabilization [55] allows one to systematically design localization filters for robots which explicitly considers the nonlinearity of the problem.

This chapter considers the attitude reference and relative localization filter design problems relevant to the HNF presented in Figure 1.4, and designs efficient nonlinear

filters for the application. First a nonlinear symmetry preserving design approach is followed to derive the filters. Then a novel approach is proposed to extended these filters to deterministic forms preserving a Kalman like gain tuning procedure which uses the process and measurement noise figures of the system. The resulting filters require similar computational power as an EKF in its stochastic forms, and require significantly low computational demand in its deterministic forms. The deterministic designs additionally feature system noise based tuning capability. The proposed filters are compared with generic filter designs for the problem, with comparative performance analysis on estimation errors and gain convergence. The chapter concludes with an experimental validation of the proposed attitude filters applied on an experimental robotic system for validation of the proposed design methodology.

4.2 Background

Recall the EKF formulation introduced in Section 3.3.7. An EKF for a given system model $f(\mathbf{x}, \mathbf{u})$ and a measurement model $h(\mathbf{x}, \mathbf{u})$, is represented by (4.1).

$$\dot{\hat{\mathbf{x}}} = f(\hat{\mathbf{x}}, \mathbf{u}) + K(\mathbf{y} - h(\hat{\mathbf{x}}, \mathbf{u})) \tag{4.1}$$

It consists of a linear output error term $E(\hat{\mathbf{x}}, \mathbf{y}, \boldsymbol{\nu}) = \mathbf{y} - h(\hat{\mathbf{x}}, \mathbf{u})$ and a linear error state $\tilde{\mathbf{x}} = \hat{\mathbf{x}} - \mathbf{x}$. The dynamics of $\tilde{\mathbf{x}}$ was found by first order Taylor linearization of the system model, from which the Kalman gain K was computed.

The EKF formulation inherently violates the geometry of SE(3) because it considers a linear error state and a linear output error. From intuition, for SE(3), the error between the estimator frame and the actual frame should be $\hat{T}^{-1}T$ if a homogenous transformation matrix parametrization T is assumed. Therefore, for the filter to be consistent with the geometry of the state space, one should introduce the respective

modifications for error state, output error, and the filter structure. The symmetry preserving design approach presented in [41, 55], proposes a systematic method to deduce a filter for systems which possess symmetries similar to the ones considered in this chapter.

4.2.1 Symmetry preserving design

The symmetry preserving observer structure proposed by [41] takes the following form.

$$\dot{\hat{\mathbf{x}}} = f(\hat{\mathbf{x}}, \mathbf{u}) + WL\mathcal{E}$$

This structure has the usual prediction term $f(\hat{\mathbf{x}}, \mathbf{u})$ with a modified correction term $WL\mathcal{E}$, compared to the usual Kalman observer structure given in (3.21). This modified form includes a gain L, and a nonlinear output error term $\mathcal{E}$ in place of the usual linear output error E. The term W does the necessary transformation of the correction term $L\mathcal{E}$ to the observer reference frame. The symmetry preserving filter design methodology proposed in [41, 55] presents a systematic approach to identify the terms W, $\mathcal{E}$, and the nonlinear error state dynamics, used to design the gains L of the observer.

Two main strategies can be followed to design the gains L using this method. The first is to design a deterministic form of the filter [56, 41, 88]. This is enabled by the nonlinear observer design procedure, which allows the identification of a simplified nonlinear error state dynamic system for the problem. This is seldom achieved by conventional direct linearization of the system dynamics. As a result, one can identify constant gain designs for L or nonlinear gain functions for L which stabilize the filter, by analyzing the simplified set of error state dynamic equations.

The second approach is to adopt an Invariant Extended Kalman Filter (**IEKF**)

form of the observer. Here the gains are found using an error state Kalman filter applied to the simplified set of nonlinear error state dynamic equations identified by following the symmetry preserving design approach [55, 89, 88, 55]. The symmetry preserving design approach is applied to pose filtering and attitude filtering problems in both deterministic and stochastic forms. A review of pose filtering and attitude filtering solutions is presented in the following sections.

4.2.2 Pose filtering

The filters reported for pose estimation in robotic applications are primarily EKF based. The application of the symmetry preserving design approach has resulted in stochastic filters for the full SE(3) inertial navigation problem [90]. Work in [88] proposes a stochastic form applicable for the EKF SLAM problem with characteristic gain stabilization capability under permanent trajectories. Work in [56] proposes a deterministic filter derived on Lie groups for localization which exhibits compact simple notation, and [41] proposes a deterministic derivation of the filter for landmark localization. However, the relative localization problem differs form the landmark localization, inertial navigation, and SLAM problems discussed, due to the consideration of a non-inertial body fixed reference coordinate frame.

This thesis specifically investigates a first application of the IEKF design approach for the problem of relative localization. The work focuses on a design which only considers the locally available measurements to the platforms. This is to be compatible with the overall filtering framework targeted in this thesis. The proposed stochastic filter design for relative localization is intended for application in the proposed HNF which provides more geometrically sound implementation than the traditional EKF for the problem.

The proposed work then extends this design to a steady state formulation for

low cost implementation with intuitive gain tuning capability that is based on the system noise parameters. However, in the current state the deterministic design is targeted for sensor networks where velocity sensing is available through fast inter sensor communication networks. The case where the velocity is not available for the low cost deterministic filter is not pursued in this thesis.

4.2.3 Attitude filtering

This section discusses the state of the art in attitude filtering for robotic applications. The objective of an AHRS is to estimate the orientation of a platform using multiple measurement sources which typically include accelerometers, magnetometers, gyroscopes, and velocity sensors. Lower end applications do not possess platform velocity estimators and thus assume gravity as the only dominating signal of the accelerometers. In more accurate applications it is assumed that velocity sensing of the platform is present and the accelerometers experience significant accelerations with drift and scale factor errors [85].

The conventional EKF is the de facto standard for attitude filtering reported in many commercial grade IMUs [91]. The departure from considering the classical linear error terms, to more geometrically accurate error definitions in EKF based AHRS is introduced in [82, 85]. Here the more accurate multiplicative error term between two rotated frames is considered; hence, the filter is termed the Multiplicative Extended Kalman filter (**MEKF**). Further generalization of the MEKF is achieved recently with the development of the IEKF for attitude filtering purposes. Specifically, the right invariant extended Kalman filter (**RIEKF**) has demonstrated interesting results where the gains stabilize to steady state values when following a particular class of trajectories termed “permanent trajectories”.

Deterministic nonlinear filter formulations for the AHRS problem are also re-

ported using a symmetry preserving design approach [41]. The nonlinear complimentary filter (**NCF**) reported in [54] dominates as the deterministic solution for the AHRS problem due to its simple set of equations, with global stability implications, and low cost implementation capability on elementary embedded devices. However, the tuning of gain parameters of these filters follows an ad-hoc trial and error approach which would benefit from a systematic intuitive tuning procedure based on system noise figures similar to an EKF.

Since NCF is the preferred deterministic form for an AHRS, this work modifies an IEKF for the problem to match with an NCF structure in order to identify a stochastic error state system for tuning purposes. Then a steady state gain design is identified which ultimately allows tuning of the gains of the NCF directly using the system noise figures which achieve steady state optimal performance of the resulting filter.

4.3 Materials and Methods

The IEKF designs derived in this work are based on the symmetry preserving design approach proposed by Bonnabel et al. [41]. This work further extends the filter designs to steady state deterministic implementations which are capable of incorporating system noise parameters for tuning purposes. The IEKF design procedure follows a differential geometric formulation. The following is a summary of important definitions and necessary notation which are useful in deriving IEKFs, as discussed in the original work on symmetry preserving design theory of Bonnabel et al. [41].

4.3.1 Definitions

Definition 1: A set G is a *Group*, if for all $g \in G$, we can define a *Group operation* (multiplication) $\diamond$ with a corresponding identity element e, and an inverse element g^{-1}, which satisfies the conditions of closure and associativity.

As an example, the set of translations and rotations $(\mathbf{p}, \theta) = g \in SE(2) \times \mathbb{R}^1$ in which the robots operate can be identified as a group with the group operation for $g_0, g \in G$ defined as (4.2), which satisfies closure $g_0 \diamond g \in G$, and associativity $(g_0 \diamond g) \diamond g = g_0 \diamond (g \diamond g)$. An identity element $e = (0,\ 0,\ 0,\ 0) \in G$ and an inverse element $g^{-1} = (-\mathbf{R}_\theta^T \mathbf{p},\ -\theta) \in G$ can be identified such that $g \diamond g^{-1} = e$.

$$g_0 \diamond g = \begin{pmatrix} \mathbf{p}_0 \\ \theta_0 \end{pmatrix} \diamond \begin{pmatrix} \mathbf{p} \\ \theta \end{pmatrix} = \begin{pmatrix} \mathbf{R}_{\theta_0}\mathbf{p} + \mathbf{p}_0 \\ \theta + \theta_0 \end{pmatrix} \tag{4.2}$$

More specifically $g_0 \diamond g$ is termed the left group operation. Similarly, the corresponding right group operation $g \diamond g_0$ for the group $(\mathbf{p}, \theta) = g \in SE(2) \times \mathbb{R}^1$ can be identified as follows.

$$g \diamond g_= \begin{pmatrix} \mathbf{p} \\ \theta \end{pmatrix} \diamond \begin{pmatrix} \mathbf{p}_0 \\ \theta_0 \end{pmatrix} = \begin{pmatrix} \mathbf{R}_{\theta}\mathbf{p}_0 + \mathbf{p} \\ \theta + \theta_0 \end{pmatrix}$$

Definition 2: A smooth map ϕ_g is a *Group action* on a set (more generally a manifold) $\mathcal{M}$, if $(g, m) \in G \times \mathcal{M} \Rightarrow \phi_g(m) \in \mathcal{M}$, s.t. $\phi_e(m) = m$ and $\phi_{g_1}(\phi_{g_2}(m)) = \phi_{g_1 \diamond g_2}(m)$.

As an example consider transformation of linear velocity $\mathbf{v} \in \mathbb{R}^3$ using a transformation $(\mathbf{p}, \theta) = g \in SE(2) \times \mathbb{R}^1$. The mapping is defined as $\phi_g(\mathbf{v}) = \mathbf{R}_\theta \mathbf{v} \in \mathbb{R}^3$. Consider group elements $g_1, g_2, e \in SE(2) \times \mathbb{R}^1$ where $g_1 = (\mathbf{p}_1, \theta_1)$, $g_2 = (\mathbf{p}_2, \theta_2)$, and $e = \mathbf{0}$. ϕ_g can easily be identified as a smooth map according to definition 2 since $\phi_e(\mathbf{v}) = \mathbf{v}$, and $\phi_{g_1}(\phi_{g_2}(\mathbf{v})) = \mathbf{R}_{\theta_1}\mathbf{R}_{\theta_2}\mathbf{v} = \phi_{g_1 \diamond g_2}(\mathbf{v})$.

Definition 3: The system $\dot{\mathbf{x}} = f(\mathbf{x}, \mathbf{u})$ is *G-invariant* if $f(\varphi_g(\mathbf{x}), \psi(\mathbf{u})) = D\varphi_g(\mathbf{x}) \circ$

$f(\mathbf{x}, \mathbf{u})$, for group actions $\varphi_g(\mathbf{x})$ on states $\mathbf{x} \in X$, and $\psi_g(\mathbf{u})$ on inputs $\mathbf{u} \in U$.

Definition 4: The output $y = h(\mathbf{x}, \mathbf{u})$ is *G-equivariant* if $h(\varphi_g(\mathbf{x}), \psi_g(\mathbf{u})) = \rho_g(\mathbf{y})$, for group action $\rho_g(\mathbf{y})$ on outputs $\mathbf{y} \in Y$.

Definitions 3 and 4 state the conditions to satisfy for the system and output models to be considered as invariant, when subjected to smooth maps $\varphi_g,\ \psi_g,\ \rho_g$. A symmetry is an operation that one can perform on a system (i.e. smooth maps) which results in certain features (i.e. invariants) of the system to remain unchanged. Therefore, one can find the symmetries of a system, by identifying the smooth maps which satisfy definitions 3 and 4. Application of these definitions for identification of symmetries for relative localization is presented in the filter derivations that follow.

Definition 5: A function $\lambda(X, Y, U)$ is an *Invariant* quantity if $\phi_g(\lambda) := \lambda(\varphi_g(X), \rho_g(Y), \psi_g(U)) = \lambda(X, Y, U)$.

As an example, consider the quantity $\lambda = \mathbf{R}_\theta^T \boldsymbol{\omega}_l$. This quantity remains unchanged under the group actions $\varphi_{g_0}(\mathbf{R}_\theta) = \mathbf{R}_{\theta_0}\mathbf{R}_\theta$ and $\psi_{g_0}(\boldsymbol{\omega}_l) = \mathbf{R}_{\theta_0}\boldsymbol{\omega}_l$ for group element $g_0 = (\mathbf{p}_0, \theta_0)$. i.e., $\phi_g(\lambda) \ = (\mathbf{R}_{\theta_0}\mathbf{R}_\theta)^T(\mathbf{R}_{\theta_0}\boldsymbol{\omega}_l) \ = \mathbf{R}_\theta^T\boldsymbol{\omega}_l \ = \lambda$

The process of deriving the IEKF is separated into four main steps for clarity. The steps are a) Identify system symmetries, b) Identify invariants of the system, c) Identify the error state dynamics, and d) Perform error state Kalman filtering. This work extends the procedure with the following steps. e) Identify a candidate steady state deterministic form, f) find optimal steady state gains. First an IEKF is designed for the relative localization problem followed by a steady state optimal design for the problem. Then an IEKF is designed for the attitude estimation problem followed by a steady state optimal AHRS design.

4.3.2 IEKF design for relative localization

Recall the 2.5D relative localization problem which only uses the locally available measurements.

$$\dot{\mathbf{x}} = f(\mathbf{x}, \mathbf{u}, \mathbf{w}) \qquad \mathbf{y} = h(\mathbf{x}, \mathbf{u}, \boldsymbol{\nu})$$

$$\begin{pmatrix} \dot{\mathbf{p}} \\ \dot{\theta} \\ \dot{\mathbf{v}}_i \\ \dot{\omega}_i \end{pmatrix} = \begin{pmatrix} \mathbf{R}_\theta \mathbf{v}_i - \mathbf{v}_l - \boldsymbol{\omega}_l \times \mathbf{p} + \mathbf{w}_p \\ \omega_i - \omega_l + \mathbf{w}_\theta \\ \mathbf{0} + \mathbf{w}_{v_i} \\ 0 + \mathbf{w}_{\omega_i} \end{pmatrix} \qquad \begin{pmatrix} \mathbf{y}_p \\ \mathbf{y}_{v_i} \\ y_{\omega_i} \end{pmatrix} = \begin{pmatrix} \mathbf{p} & +\boldsymbol{\nu}_p \\ \mathbf{v}_i & +\boldsymbol{\nu}_{v_i} \\ \omega_i & +\nu_{\omega_i} \end{pmatrix} \tag{4.3}$$

Notice the inclusion of the target platform velocities as measurements. This is so that platform velocities and constraints can be incorporated to the estimate, at the low rates at which velocity communication occurs. The filter minimally requires availability of y_p and $y_{viy} = 0$ for system observability as identified in Chapter 4. Therefore these minimal conditions are assumed when validating the proposed filter designs in the results section. What follows is a first application of the symmetry preserving observer design procedure [41] for the relative localization problem given by (4.3).

Step 1: Identify System Symmetries

Identifying symmetries of the system is the process of finding the actions on the states $\mathbf{x}$, inputs $\mathbf{u}$, and outputs $\mathbf{y}$, such that the system is *G-invariant*. Consider the system given by (4.3) with noises removed i.e. $\boldsymbol{\nu} = 0$, $\mathbf{w} = 0$. For group $G = SE(2) \times \mathbb{R}^1$, define the group actions on states $\varphi_g : G \times X \to X$, on input $\psi_g : G \times U \to U$, and on measurements $\rho_g : G \times Y \to Y$ as follows.

$$\varphi_g \begin{pmatrix} \mathbf{p} \\ \theta \\ \mathbf{v}_i \\ \omega_i \end{pmatrix} = \begin{pmatrix} \mathbf{R}_{\theta_0}\mathbf{p} + \mathbf{p}_0 \\ \theta_0 + \theta \\ \mathbf{v}_i \\ \omega_i \end{pmatrix} \quad \psi_g \begin{pmatrix} \mathbf{v}_l \\ \omega_l \end{pmatrix} = \begin{pmatrix} \mathbf{R}_{\theta_0}\mathbf{v}_l - [\boldsymbol{\omega}_l]_\times \mathbf{p}_0 \\ \boldsymbol{\omega}_l \end{pmatrix} \quad \rho_g \begin{pmatrix} \mathbf{y}_\mathbf{p} \\ \mathbf{y}_{v_i} \\ y_{\omega_i} \end{pmatrix} = \begin{pmatrix} \mathbf{R}_{\theta_0}\mathbf{y}_p + \mathbf{p}_0 \\ \mathbf{y}_{v_i} \\ y_{\omega_i} \end{pmatrix} \tag{4.4}$$

Consider a group element $g_0 = (\mathbf{p}_0,\ \theta_0) \in G$. Equation set (4.5) verifies that the system given by (4.3) is *G-invariant* under the group actions φ_g and ψ_g, i.e., $D\varphi_g \circ f(\mathbf{x}, \mathbf{u}) = f(\varphi_g(\mathbf{x}), \psi_g(\mathbf{u}))$.

$$\begin{aligned} D\varphi_g \circ f(\mathbf{x}, \mathbf{u}) = \tfrac{d}{dt}\varphi_g \begin{pmatrix} \mathbf{p} \\ \theta \\ \mathbf{v}_i \\ \omega_i \end{pmatrix} &= \begin{pmatrix} \mathbf{R}_{\theta_0}\dot{\mathbf{p}} \\ \dot{\theta} \\ \mathbf{0} \\ 0 \end{pmatrix} \\ = \begin{pmatrix} \mathbf{R}_{\theta_0}(\mathbf{R}_\theta v_i - v_l) - \mathbf{R}_{\theta_0}\omega_l \times p \\ \omega_i - \omega_l \\ \mathbf{0} \\ 0 \end{pmatrix} &= f(\varphi_g(\mathbf{x}), \psi_g(\mathbf{u})) \end{aligned} \tag{4.5}$$

The measurement model given in (4.3) is found to be *G-equivariant* under the group actions ρ_g, φ_g, ψ_g. i.e., $\rho_g(\mathbf{y}) = h(\varphi_g(\mathbf{x}), \psi_g(\mathbf{u}))$.

$$h(\varphi_g(\mathbf{x}), \psi_g(\mathbf{u})) = \begin{pmatrix} \mathbf{R}_{\theta_0}\mathbf{p} + \mathbf{p}_0 \\ \mathbf{v}_i \\ \omega_i \end{pmatrix} = \begin{pmatrix} \mathbf{R}_{\theta_0}\mathbf{y}_\mathbf{p} + \mathbf{p}_0 \\ \mathbf{y}_{vi} \\ y_{\omega i} \end{pmatrix} = \rho_g(\mathbf{y}) \tag{4.6}$$

The particular group action φ_g acting on the state space relates to translation and rotation of the reference coordinate system to a different location attached to

the robot. The mappings of inputs $\mathbf{u}$ and outputs $\mathbf{y}$ to this new frame of reference are defined by the group actions ψ_g, ρ_g. Thus, the group actions do not change the intrinsic dynamics of the system; rather, they are transformed to a new coordinate representation.

Step 2: Identify Invariants

To identify the complete set of invariants, the moving frame method is applied [41]. The moving frame is identified by solving the equation $\phi_g(\mathbf{x}) = \mathbf{e}$ for $g := \gamma(\mathbf{x})$, where $\mathbf{e}$ is the group identity element.

$$\varphi_g \begin{pmatrix} \mathbf{p} \\ \theta \end{pmatrix} = \begin{pmatrix} \mathbf{R}_{\theta_0}\mathbf{p} + \mathbf{p}_0 \\ \theta_0 + \theta \end{pmatrix} = \begin{pmatrix} \mathbf{0} \\ \mathbf{I} \end{pmatrix} \Rightarrow \gamma(\mathbf{x}) = (-\mathbf{R}_\theta^T\mathbf{p}, -\theta)$$

Then the set of invariants $\mathcal{I}(\hat{\mathbf{x}}, \mathbf{u})$ is found by operating $\gamma(\hat{\mathbf{x}})$ on U and Y.

$$\mathcal{I}(\hat{\mathbf{x}}, \mathbf{u}) := \begin{pmatrix} \mathcal{I}_{v_l} \\ \mathcal{I}_{\omega_l} \end{pmatrix} = \psi_{\gamma(\hat{\mathbf{x}})} \begin{pmatrix} \mathbf{v}_l \\ \omega_l \end{pmatrix} = \begin{pmatrix} \mathbf{R}_{\hat{\theta}}^T\mathbf{v}_l + \omega_l \times \mathbf{R}_{\hat{\theta}}^T\hat{\mathbf{p}} \\ \omega_l \end{pmatrix}$$

$$\mathcal{J}(\hat{\mathbf{x}}, \mathbf{u}) := \begin{pmatrix} \mathcal{J}_{y_p} \\ \mathcal{J}_{y_{v_i}} \\ \mathcal{J}_{y_{\omega_i}} \end{pmatrix} = \rho_{\gamma(\hat{\mathbf{x}})} \begin{pmatrix} \mathbf{y}_p \\ \mathbf{y}_{v_i} \\ y_{\omega_i} \end{pmatrix} = \begin{pmatrix} \mathbf{R}_{\hat{\theta}}^T\mathbf{y}_p - \mathbf{R}_{\hat{\theta}}^T\hat{\mathbf{p}} \\ \mathbf{y}_{v_i} \\ y_{\omega_i} \end{pmatrix}$$

The trajectories in which the invariants $\mathcal{I}$,$\mathcal{J}$ are constant are termed permanent trajectories. The invariant frame W is defined as the mapping of basis vectors ν_i of the tangent space $\mathcal{T}X$, by the smooth map $D\varphi_g$. The basis vectors $\nu_i = e_i$ for $T\mathbb{R}^3$, where e_i denoted the standard basis of $\mathbb{R}^3$. The invariant frame is found as follows.

$$W \;= \frac{d}{d\tau}\left(\varphi_{\gamma(\hat{x})^{-1}}(\nu_i \tau)\right)|_{\tau=0} \;= \begin{pmatrix} \mathbf{R}_{\hat{\theta}} e_i \\ 1 \\ e_i \\ 1 \end{pmatrix}$$

Step 3: Identify Invariant Error State Dynamics

An invariant observer for a general *G-invariant* system $\dot{\mathbf{x}} = f(\mathbf{x}, \mathbf{u})$, and a *G-equivariant* output $\mathbf{y} = h(\mathbf{x}, \mathbf{u})$, is given by *Theorem* 1 in reference [41]. It takes the following general form.

$$F(\hat{\mathbf{x}}, \mathbf{u}, \mathbf{y}) = f(\hat{\mathbf{x}}, \mathbf{u}) + W(\hat{\mathbf{x}}) L(\mathcal{I}, \mathcal{E}) \mathcal{E}(\hat{\mathbf{x}}, \mathbf{u}, \mathbf{y}) \tag{4.7}$$

The term $f(\hat{\mathbf{x}}, \mathbf{u})$ is the usual forward prediction as seen in extended Kalman filters and the term $W.L.\mathcal{E}$ is the correction term with gain L, output error $\mathcal{E}$, and invariant frame W. The output error $\mathcal{E}$ is not the usual linear innovation term $h(\hat{\mathbf{x}}, \mathbf{u}) - \mathbf{y}$ in EKFs; rather, it is a nonlinear invariant error term. This error is defined as $\mathcal{E} = \mathcal{J}(\hat{\mathbf{x}}, \mathbf{y}) - \mathcal{J}(\hat{\mathbf{x}}, h(\hat{\mathbf{x}}, \mathbf{u}))$ and is found as follows.

$$\mathcal{E}(\hat{\mathbf{x}}, \mathbf{u}, \mathbf{y}) \;= \rho_{\gamma(\hat{\mathbf{x}})}(h(\hat{\mathbf{x}})) - \rho_{\gamma(\hat{\mathbf{x}})}(\mathbf{y}) = \begin{pmatrix} \mathbf{R}_{\hat{\theta}}^T(\hat{\mathbf{p}} - \mathbf{y}_p) \\ \hat{\mathbf{v}}_\mathbf{i} - \mathbf{y}_{v_i} \\ \hat{\omega}_i - y_{\omega_i} \end{pmatrix}$$

The invariant observer for the problem is obtained by substituting the invariant output

error and the invariant frame in (4.7).

$$\begin{pmatrix} \dot{\hat{\mathbf{p}}} \\ \dot{\hat{\theta}} \\ \dot{\hat{\mathbf{v}}}_i \\ \dot{\hat{\omega}}_i \end{pmatrix} = \begin{pmatrix} \mathbf{R}_{\hat{\theta}}\hat{\mathbf{v}}_i - \mathbf{v}_l - \boldsymbol{\omega}_l \times \hat{\mathbf{p}} \\ \hat{\omega}_i - \omega_l \\ \mathbf{0} \\ 0 \end{pmatrix} + \begin{pmatrix} \mathbf{R}_{\hat{\theta}}(L_p\mathcal{E}) \\ L_\theta\mathcal{E} \\ L_v\mathcal{E} \\ L_\omega\mathcal{E} \end{pmatrix} \tag{4.8}$$

The invariant estimation error $\boldsymbol{\eta}$ of the observer is defined as $\boldsymbol{\eta} = \varphi_{\gamma(\hat{\mathbf{x}})}(\hat{\mathbf{x}}) - \varphi_{\gamma(\hat{\mathbf{x}})}(\mathbf{x})$. Notice that this is different from the usual linear estimation error term $(\hat{\mathbf{x}} - \mathbf{x})$ seen in EKFs. The invariant estimation error reads as

$$\boldsymbol{\eta} \quad = \varphi_{\gamma(\hat{\mathbf{x}})}(\hat{\mathbf{x}}) - \varphi_{\gamma(\hat{\mathbf{x}})}(\mathbf{x}) \quad = \begin{pmatrix} \mathbf{R}_{\hat{\theta}}^T(\hat{\mathbf{p}} - \mathbf{p}) \\ \hat{\theta} - \theta \\ \hat{\mathbf{v}}_i - \mathbf{v}_i \\ \hat{\omega}_i - \omega_i \end{pmatrix} =: \begin{pmatrix} \boldsymbol{\eta}_p \\ \eta_\theta \\ \boldsymbol{\eta}_{vi} \\ \eta_{\omega i} \end{pmatrix}$$

One can verify the invariance of the invariant quantities $\mathcal{I},\ \boldsymbol{\eta},\ \mathcal{E}$ under transformations $\varphi_g,\ \phi_g,\ \rho_g$, using *Definition 5*.

In order to perform error state Kalman filtering, a stochastic model of the system should be deduced. The new stochastic model should also preserve the stochastic versions of *G-invariant* and *G-equivariant* definitions given by the following equations.

$$\begin{aligned} D\varphi_g \circ f(\mathbf{x}, \mathbf{u}, M(x)\mathbf{w}) &= f\Big(\varphi_g(\mathbf{x}), \psi_g(\mathbf{u}), M(\varphi_g(x))\mathbf{w}\Big) \\ \rho_g\Big(h(\mathbf{x}, \mathbf{u}, N(x)\boldsymbol{\nu})\Big) &= h\Big(\varphi_g(\mathbf{x}), \psi_g(\mathbf{u}), N(\phi_g(x))\boldsymbol{\nu}\Big) \end{aligned} \tag{4.9}$$

Here, the usual process noise $\mathbf{w}$ and measurement noise $\boldsymbol{\nu}$ terms as seen in (4.3) are replaced by invariant noises $M(x)\mathbf{w}$ and $N(x)\boldsymbol{\nu}$ respectively. The definitions given by (4.9) are satisfied when $M(x) = \mathbf{R}_\theta$ and $N(x) = \mathbf{R}_\theta$ for $\mathbf{w}_p$ and $\boldsymbol{\nu}_p$ respectively.

All other noise terms remain unchanged. I.e., $M(x), N(x)$ are identity mappings for $\mathbf{w}_\theta, \mathbf{w}_{vi}, w_{\omega i}, \boldsymbol{\nu}_{vi}$, and $\nu_{\omega i}$.

Now the error state dynamics of the system are derived as a function of $\boldsymbol{\eta}$. The invariant output error $\mathcal{E}$ in terms of $\boldsymbol{\eta}$ reads

$$\mathcal{E}(\hat{\mathbf{x}}, \mathbf{u}, \mathbf{y}) \quad = \mathbf{R}_{\hat{\theta}}^T(\hat{\mathbf{p}} - \mathbf{y}_p) = \mathbf{R}_{\hat{\theta}}^T(\hat{\mathbf{p}} - \mathbf{p} - \mathbf{R}_\theta \boldsymbol{\nu}_p) \Rightarrow \mathcal{E}(\eta, \boldsymbol{\nu}) = \boldsymbol{\eta}_p - \mathbf{R}_{\eta\theta}^T \boldsymbol{\nu}_p$$

The other output error terms corresponding to $\mathbf{y}_{v_i}$, $\mathbf{y}_{\omega_i}$, remain trivial. By differentiating the estimation error state, we have

$$\begin{pmatrix} \dot{\boldsymbol{\eta}}_p \\ \dot{\eta}_\theta \\ \dot{\boldsymbol{\eta}}_{vi} \\ \dot{\eta}_{\omega i} \end{pmatrix} = \begin{pmatrix} \dot{\mathbf{R}}_{\hat{\theta}}^T(\hat{\mathbf{p}} - \mathbf{p}) + \mathbf{R}_{\hat{\theta}}^T(\dot{\hat{\mathbf{p}}} - \dot{\mathbf{p}}) \\ \dot{\hat{\theta}} - \dot{\theta} \\ \dot{\hat{\mathbf{v}}}_i - \dot{\mathbf{v}}_i \\ \dot{\hat{\omega}}_i - \dot{\omega}_i \end{pmatrix}$$

By substituting the derivative terms from equations (4.3) and (4.8), and identifying $\dot{\mathbf{R}}_\theta^T = [\boldsymbol{\omega}_l - \boldsymbol{\omega}_i - \mathbf{w}_\omega]_\times \mathbf{R}_\theta^T$ we can derive the error state dynamics of the observer.

$$\begin{pmatrix} \dot{\boldsymbol{\eta}}_p \\ \dot{\eta}_\theta \\ \dot{\boldsymbol{\eta}}_{vi} \\ \dot{\eta}_{\omega i} \end{pmatrix} = \begin{pmatrix} [-\hat{\boldsymbol{\omega}}_i + \boldsymbol{\eta}_{\omega i}]_\times \boldsymbol{\eta}_p + (I_3 - \mathbf{R}_{\eta\theta}^T)(\hat{\mathbf{v}}_i - \boldsymbol{\eta}_{vi}) - [L_\theta \mathcal{E}]_\times \boldsymbol{\eta}_p - \mathbf{R}_{\eta\theta}^T \mathbf{w}_v + L_p \mathcal{E} \\ L_\theta \mathcal{E} - w_{\omega_i} + \eta_{\omega_i} \\ L_{vi} \mathcal{E} - \mathbf{w}_{vi} \\ L_{\omega i} \mathcal{E} - w_{\omega i} \end{pmatrix} \tag{4.10}$$

The symmetry preserving observer for the system is (4.8). The gains L should be designed so that the invariant error state dynamic system given by (4.10) is stable.

Step 4: Perform Error State Kalman Filtering

The gain design of the observer can be achieved using many methods. A de-

terministic approach would consider the noiseless version of (4.10), and use stability analysis tools such as Lyapunov, for gain design. For stabilization of (4.10), many other standard stochastic filtering approaches are applicable which include error state versions of Kalman filters, sigma point filters, and moving horizon methods. Here we use an error state extended Kalman filtering approach as proposed by [55].

The error state EKF approach differs from the standard EKF formulation given in Section 4.2. The standard EKF formulation first linearizes the system dynamics before deducing the error state dynamics of the observer. In the error state Kalman filter formulation, first the dynamics of the error state system is deduced without any linearized approximations. Then it is linearized about the nominal value of the error state to obtain the familiar Kalman structure given in (4.1).

The nonlinear error state dynamics for the system are already found by equation (4.10). Next, a linearization of the error states $\eta_p,\ \eta_\theta,\ \eta_{vi},\ \eta_{\omega i}$, is performed by applying the small signal assumption, and removing the resulting second order error terms. This results in a linear Kalman like filter structure.

$$\begin{pmatrix} \delta\dot{\boldsymbol{\eta}}_p \\ \delta\dot{\eta}_\theta \\ \delta\dot{\boldsymbol{\eta}}_{vi} \\ \delta\dot{\eta}_{\omega i} \end{pmatrix} = (A - KC) \begin{pmatrix} \delta\boldsymbol{\eta}_p \\ \delta\eta_\theta \\ \delta\boldsymbol{\eta}_{vi} \\ \delta\eta_{\omega i} \end{pmatrix} - M \begin{pmatrix} \mathbf{w}_p \\ w_\theta \\ \mathbf{w}_{vi} \\ w_{\omega i} \end{pmatrix} + KN \begin{pmatrix} \boldsymbol{\nu}_p \\ \boldsymbol{\nu}_{v_i} \\ \nu_{\omega_i} \end{pmatrix}$$

The A,C,K,M,N matrices are identified from this linearized system. The resulting

filter can be summarized as follows.

Initialization

$$\hat{\mathbf{x}} = \begin{bmatrix} \mathbf{y}_p & 0 & \mathbf{0} & 0 \end{bmatrix}^T \quad P = \mathrm{E}(\boldsymbol{\eta}\boldsymbol{\eta}^T) = \mathbf{I} \quad Q = \mathrm{E}(\mathbf{w}\mathbf{w}^T) \quad R = \mathrm{E}(\boldsymbol{\nu}\boldsymbol{\nu}^T)$$

2.5D Observer

$$\begin{pmatrix} \dot{\hat{\mathbf{p}}} \\ \dot{\hat{\theta}} \\ \dot{\hat{\mathbf{v}}}_i \\ \dot{\hat{\omega}}_i \end{pmatrix} = \underbrace{\begin{pmatrix} \mathbf{R}_{\hat{\theta}}\hat{\mathbf{v}}_i - \mathbf{v}_l - \boldsymbol{\omega}_l \times \hat{\mathbf{p}} \\ \hat{\omega}_i - \omega_l \\ \mathbf{0} \\ \mathbf{0} \end{pmatrix}}_{\textit{State Prediction}} + \underbrace{\begin{pmatrix} \mathbf{R}_{\hat{\theta}}(L_p\mathcal{E}) \\ L_\theta\mathcal{E} \\ L_v\mathcal{E} \\ L_\omega\mathcal{E} \end{pmatrix}}_{\textit{State Correction}} \qquad \mathcal{E} = \underbrace{\begin{pmatrix} \mathbf{R}_{\hat{\theta}}^T(\hat{\mathbf{p}} - \mathbf{y}_p) \\ \hat{\mathbf{v}}_\mathbf{i} - \mathbf{y}_{v_i} \\ \hat{\omega}_i - y_{\omega_i} \end{pmatrix}}_{\textit{Innovation}}$$

$$\textit{Gain Matrix} \quad K = \begin{bmatrix} -L_p & -L_\theta & -L_v & -L_\omega \end{bmatrix}^T$$

Covariance Prediction

$$A = \begin{bmatrix} [-\hat{\boldsymbol{\omega}}_i]_\times & [-\hat{\mathbf{v}}_i]_\times \mathbf{e}_3^\mathsf{T} & \mathbf{I} & 0 \\ \mathbf{0} & 0 & \mathbf{0} & 1 \\ \mathbf{0} & \mathbf{0} & \mathbf{0} & \mathbf{0} \\ \mathbf{0} & 0 & \mathbf{0} & 0 \end{bmatrix}$$

$$M = \mathbf{I}$$

$$\dot{P} = AP + PA^T + MQM^T$$

Covariance Correction

$$C = \begin{bmatrix} \mathbf{I} & 0 & \mathbf{0} & \mathbf{0} \\ \mathbf{0} & 0 & \mathbf{I} & \mathbf{0} \\ \mathbf{0} & 0 & \mathbf{0} & 1 \end{bmatrix}$$

$$N = \mathbf{I}$$

$$K = PC^T(CPC^T + NRN^T)^{-1}$$

$$P = (I - KC)P$$

This completes the IEKF filter design for relative localization. The validation of this filter is presented in the results section. The formulation is equally applicable for the full 3D (SE(3)) scenario which is presented in Appendix A.

4.3.3 Steady state IEKF design for relative localization

The steady state gain design procedure attempts to identify a parameterized gain function for L which is tunable to produce comparable gains produced by the IEKF under permanent trajectories. This is termed as "steady state optimal gains" in the context of this work. For the steady state design it is assumed that the platform velocities are available and the filter is intended to be applied on the sensor node itself. I.e., $\boldsymbol{\eta}_{v_i} = 0$, $\hat{\mathbf{v}}_i = \mathbf{v}_i$, $\eta_{\omega_i} = 0$, $\hat{\omega}_i = \omega_i$. The case where velocities are unavailable is not pursued in this thesis in designing low cost nonlinear estimators.

$$\begin{pmatrix} \dot{\boldsymbol{\eta}}_p \\ \dot{\eta}_\theta \end{pmatrix} = \begin{pmatrix} [-\boldsymbol{\omega}_i + \boldsymbol{\eta}_{\omega i}]_\times \boldsymbol{\eta}_p + (I_3 - \mathbf{R}_{\eta_\theta}^T)\mathbf{v}_i - [L_\theta \mathcal{E}]_\times \boldsymbol{\eta}_p - \mathbf{R}_{\eta_\theta}^T \mathbf{w}_v + L_p \mathcal{E} \\ -\mathbf{w}_\omega + L_\theta \mathcal{E} \end{pmatrix} \tag{4.11}$$

Under these simplifications the IEKF design simplifies to a 4-state filter, which exhibits an important characteristic. i.e., the filter matrices are only dependant on the inputs. Therefore the resulting gains would also be functions of only the inputs and the noise parameters. As a result, it is possible to design a parameterized gain matrix which is a function of the inputs and the system noise parameters. This gain function design would enable low cost application of the filter to achieve comparable steady state performance without using error state Kalman filtering for gain adaptation. The gain function design is performed in two main steps. First, a steady state filter is identified for the noiseless error state system corresponding to the 2.5D filter. Next, a minimal set of parameters and a tuning approach is identified to incorporate the noise parameters of the system in identifying the observer gains.

Step 5: Identify deterministic design

Consider the noiseless version of the 2.5D error state dynamics given by equations (4.11). Note that this system has no approximations or small signal assumptions; thus, a gain design would be valid in a global sense. Consider the gain proposition given by

$$L = \begin{pmatrix} L_p \\ \\ L_\theta \end{pmatrix} = \begin{pmatrix} -a_0 + [\boldsymbol{\omega_i}]_\times - a_2'[\mathbf{v}_i]_\times I_{e_3}[\mathbf{v}_i]_\times^T \\ -a_1'[\boldsymbol{\omega}_i]_\times[\boldsymbol{\omega}_i]_\times^T + [L_\theta \mathcal{E}]_\times \\ -a_4' \mathbf{e}_3^T [\mathbf{v}_i]_\times \end{pmatrix}$$

where $I_{e_3} := diag(0,\ 0,\ 1)$. Substituting the gain L in (4.11) gives the following

system.

$$\begin{pmatrix} \dot{\eta}_p \\ \\ \\ \dot{\eta}_{\theta_z} \end{pmatrix} = \begin{pmatrix} (I_3 - \mathbf{R}_{\eta_\theta}^T)\mathbf{v}_i + -a_0\boldsymbol{\eta}_p \\ -a_2'[\mathbf{v}_i]_\times I_{e_3}[\mathbf{v}_i]_\times^T\boldsymbol{\eta}_p - a_1'[\boldsymbol{\omega}_i]_\times[\boldsymbol{\omega}_i]_\times^T\boldsymbol{\eta}_p \\ -a_4'(v_{ix}\eta_y - v_{iy}\eta_x) \end{pmatrix} \tag{4.12}$$

Global stability is analyzed assuming permanent trajectories where $\dot{\mathbf{v}}_i = 0$ and $\dot{\omega}_i = 0$, hence (4.12) is an autonomous system. The error state space $\boldsymbol{\eta} \in \mathcal{X} \equiv SE(2) \times \mathbb{R}^1$ has a unique equilibrium point at $(\boldsymbol{\eta}_p, \mathbf{R}_{\eta_\theta}) = (\mathbf{0}, I) \in \mathcal{X}$. Here the trajectory $\eta_x = {}^{vix}/_{v_{iy}}\eta_y \Rightarrow \dot{\eta}_\theta = 0$ is not an equilibrium since, $\eta_x = {}^{vix}/_{v_{iy}}\eta_y \Rightarrow \dot{\eta}_x = {}^{vix}/_{v_{iy}}\dot{\eta}_y \Rightarrow \dot{\eta}_x$, $\dot{\eta}_y \neq 0$ when $\eta_x, \eta_y \neq 0$. A similar 2D error state system corresponding to global localization of robots is considered in [41], where the authors reduce the error state system to a form comparable to the dynamics of a pendulum. Exploiting this result, a scalar function V is designed, which is comparable to a Lyapunov function used for stability analysis of a simple pendulum.

$$V(\boldsymbol{\eta}) = \frac{1}{2}\dot{\boldsymbol{\eta}}_\theta^2 + a_4'(v_{ix}^2 + v_{iy}^2)(1 - \cos\eta_\theta) + \frac{1}{2}\eta_z^2 \geq 0$$

The trajectory $\eta_x = {}^{v_{ix}}/_{v_{iy}}\eta_y$ is considered separately for clarity. Consider the space $\mathcal{X}' = \{\boldsymbol{\eta} \in \mathcal{X} | \eta_x \neq {}^{v_{ix}}/_{v_{iy}}\eta_y \vee (\eta_x,\ \eta_y) = \mathbf{0}\}$. When $\eta_x \neq {}^{v_{ix}}/_{v_{iy}}\eta_y$, the function $V(\boldsymbol{\eta})$ is positive definite. I.e., $V(0) = 0$ and $\boldsymbol{\eta} \neq \mathbf{0} \Rightarrow V > 0$. Differentiating the expression and substituting $\ddot{\eta}_\theta$, $\dot{\boldsymbol{\eta}}_p$, cancels the trigonometric nonlinearities of the expression which results in the following expression for $\dot{V}(\boldsymbol{\eta})$.

$$\dot{V}(\boldsymbol{\eta}) = -a_4'^2(v_{iy}\eta_x - v_{ix}\eta_y)^2\Big(a_0 + a_1'\omega_i^2 + a_2'|\mathbf{v}_i|^2\Big) - a_0\eta_z^2 \ \leq \ 0$$

The function $\dot{V}(\boldsymbol{\eta})$ is negative semi-definite in the space $\mathcal{X}'$. I.e., $\eta_\theta \neq 0,\ \boldsymbol{\eta}_p = 0 \Rightarrow \dot{V} = 0$. Consider a set $\Omega_{l'} = \{\boldsymbol{\eta} \in \mathcal{X}' | V(\boldsymbol{\eta}) \leq l',\ l' = 2a_4'(v_{ix}^2 + v_{iy}^2)\}$. Since the Lyapunov function $V(\boldsymbol{\eta}) > 0$ for all $\eta \neq 0 \in \Omega_{l'}$, and $\dot{V} \leq 0$, the states in $\Omega_{l'}$ are

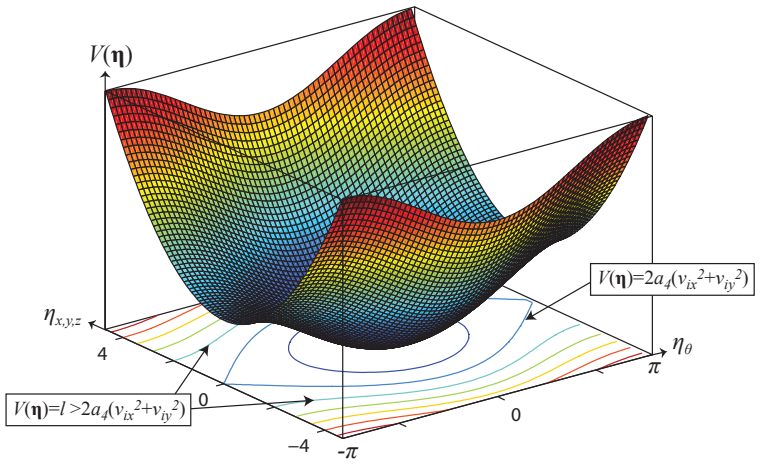

Figure 4.1: The Lyapunov function and its level sets

Lyapunov stable, hence bounded. Consider the set $\mathcal{S} = \{\boldsymbol{\eta} \in \Omega_{l'} | \dot{V}(\boldsymbol{\eta}) = 0\}$. The set $\mathcal{S}$ additionally includes the trajectories $\eta_\theta \neq 0$ apart from the origin $(\boldsymbol{\eta}_p, \mathbf{R}_{\eta_\theta}) = (\mathbf{0}, I)$. Observing the filter dynamics (4.12) one can verify that $\eta_\theta \neq 0 \Rightarrow \dot{\eta}_p \neq 0 \Rightarrow \eta_p \notin \mathcal{S}$ when $v_{ix}, v_{iy} \neq 0$. I.e the trajectory $\eta_\theta \neq 0$ does not remain in $\mathcal{S}$ and the largest invariant set of $\mathcal{S}$ only includes the origin $(\boldsymbol{\eta}_p, \mathbf{R}_{\eta_\theta}) = (\mathbf{0}, I)$. From LaSalle's theorem the origin is asymptotically stable in the domain of convergence $\Omega_{l'}$.

In fact the domain of convergence shown here is much larger. Consider Figure 4.1. Although the level set Ω_l is hard to define as closed in $SE(2)$ when $l > l' = 2a'_4(v_{ix}^2 + v_{iy}^2)$, it is evident from the figure that set Ω_l for $l > l' = 2a'_4(v_{ix}^2 + v_{iy}^2)$ includes the space $(-2a_4'^2 v_{iy}^2 l - l' < \eta_x < 2a_4'^2 v_{iy}^2 l - l',\ -2a_4'^2 v_{ix}^2 l - l' < \eta_y < 2a_4'^2 v_{ix}^2 l - l',$ $-2l - l' < \eta_z < 2l - l',\ \mathbf{R}_{\eta_\theta} \in SO(2)) \in SE(2) \times \mathbb{R}^1$. Since l can be arbitrarily large the domain of convergence spans the whole space $\mathcal{X}'$ when $v_{ix}, v_{iy} \neq 0$.

Consider the trajectory $\eta_x = {}^{v_{ix}}/_{v_{iy}}\eta_y \in \mathcal{X}$. In this case the error state system

reduces to:

$$\begin{pmatrix} \dot{\eta}_x \\ \dot{\eta}_y \\ \dot{\eta}_z \\ \dot{\eta}_\theta \end{pmatrix} = \begin{pmatrix} (1-\cos\eta_\theta)v_{ix} - \sin\eta_\theta v_{iy} - (a_0 + a_1\omega_i^2)\frac{v_{ix}}{v_{iy}}\eta_y \\ \sin\eta_\theta v_{ix} + (1-\cos(\eta_\theta)v_{iy} - (a_0 + a_1\omega_i^2)\eta_y \\ -a_0\eta_z \\ 0 \end{pmatrix} \tag{4.13}$$

The solutions for the system to remain in the trajectory $\dot{\eta}_x = {}^{v_{ix}}/_{v_{iy}}\dot{\eta}_y$ can be found only when $\eta_\theta = 0$. I.e., when $\eta_\theta \neq 0$ the trajectory exits from $\eta_x = {}^{v_{ix}}/_{v_{iy}} \cdot \eta_y$ to space $\mathcal{X}'$ and the Lyapunov analysis shown above applies. When $\eta_\theta = 0$ the system 4.13 reduces to the form $\dot{\eta} = -a\eta$ which has a globally asymptotically convergent solution at the equilibrium. Thus all trajectories in $\mathcal{X}$ including $\{\eta \in \mathcal{X} | \eta_x = {}^{v_{ix}}/_{v_{iy}}\eta_y\}$ are asymptotically convergent to the origin.

This completes the global convergence proof. The proposed filter with gain function L where $a_0, a_1', a_2', a_4' > 0$ is asymptotically stable about any permanent trajectory when $v_{ix}, v_{iy} \neq 0$ with a global convergence domain spanning the whole error state space $\mathcal{X}$.

For local stability analysis consider the linearized noiseless error state system given by

$$\begin{pmatrix} \delta\dot{\boldsymbol{\eta}}_p \\ \delta\dot{\eta}_\theta \end{pmatrix} = \begin{pmatrix} -[\mathbf{v}_i]_\times \delta\boldsymbol{\eta}_\theta - a_0\delta\boldsymbol{\eta}_p - a_2'[\mathbf{v}_i]_\times[\mathbf{v}_i]_\times^T\delta\boldsymbol{\eta}_p - a_1'[\boldsymbol{\omega}_i]_\times[\boldsymbol{\omega}_i]_\times^T\delta\boldsymbol{\eta}_p \\ -a_4'[\mathbf{v}_i]_\times\delta\boldsymbol{\eta}_p \end{pmatrix} \tag{4.14}$$

where $\delta\boldsymbol{\eta}_\theta = (0\ 0\ \delta\eta_\theta)^\mathsf{T}$ and the second order error terms are removed for local analysis. Local stability is analyzed assuming any trajectory, hence (4.14) is a non-autonomous system. Consider the following candidate Lyapunov function $V(\eta, t)$, which is lower

bounded.

$$V(\boldsymbol{\eta}, t) = \frac{1}{2}\delta\boldsymbol{\eta}_p^{\mathsf{T}}\delta\boldsymbol{\eta}_p + \frac{1}{a_4'}\frac{1}{2}\delta\boldsymbol{\eta}_\theta^{\mathsf{T}}\delta\boldsymbol{\eta}_\theta \geq 0$$

The derivative $\dot{V}$ reads as follows.

$$\begin{aligned}\dot{V}(\boldsymbol{\eta}, t) &= -\delta\boldsymbol{\eta}_p^{\mathrm{T}}[\mathbf{v}_i]_\times\delta\boldsymbol{\eta}_\theta - a_0\delta\boldsymbol{\eta}_p^{\mathrm{T}}\delta\boldsymbol{\eta}_p - a_2'\delta\boldsymbol{\eta}_p^{\mathrm{T}}[\mathbf{v}_i]_\times[\mathbf{v}_i]_\times^T\delta\boldsymbol{\eta}_p \\ &\quad -a_1'\delta\boldsymbol{\eta}_p^{\mathrm{T}}a_1'[\boldsymbol{\omega}_i]_\times[\boldsymbol{\omega}_i]_\times^T\delta\boldsymbol{\eta}_p - \delta\boldsymbol{\eta}_\theta^{\mathrm{T}}[\mathbf{v}_i]_\times\delta\boldsymbol{\eta}_p \qquad \leq 0\end{aligned}$$

The $\delta\boldsymbol{\eta}_\theta^{\mathrm{T}}[\mathbf{v}_i]_\times\delta\boldsymbol{\eta}_p$ terms cancel each other. The matrices of form $[\cdot]_\times[\cdot]_\times^{\mathsf{T}}$ are positive definite. A time invariant negative semi-definite dominant term $-a_0\delta\boldsymbol{\eta}_p^{\mathrm{T}}\delta\boldsymbol{\eta}_p$ can be found implying Lyapunov stability. Therefore the state $\boldsymbol{\eta}_p$ and η_θ are bounded for a bounded set of inputs $(\mathbf{v}_i, \omega_i)$ and its derivatives $(\dot{\mathbf{v}}_i, \dot{\omega}_i)$. The function $\ddot{V}$ is a polynomial function of the terms $\delta\boldsymbol{\eta}_p$, $\delta\eta_\theta$, $(\mathbf{v}_i, \omega_i)$, and $(\dot{\mathbf{v}}_i, \dot{\omega}_i)$. Hence $\ddot{V}$ is bounded $\Rightarrow \dot{V}$ and is uniformly continuous. From Barbalat's lemma $\dot{V} \to 0$ as $t \to \infty$. I.e. $\delta\boldsymbol{\eta}_p \to 0$ as $t \to \infty$. Analyzing the local error state dynamics (4.14), $\dot{\delta\boldsymbol{\eta}_p}$ is bounded and $\ddot{\delta\boldsymbol{\eta}_p}$ is a polynomial function of $\delta\boldsymbol{\eta}_p$, $\delta\eta_\theta$, $(\mathbf{v}_i, \omega_i)$, and $(\dot{\mathbf{v}}_i, \dot{\omega}_i)$. Hence $\ddot{\delta\boldsymbol{\eta}_p}$ is bounded and $\dot{\delta\boldsymbol{\eta}_p}$ is uniformly continuous. From Barbalat's lemma $\dot{\delta\boldsymbol{\eta}_p} \to 0$ as $t \to \infty$. Since $\delta\boldsymbol{\eta}_p \to 0$ as $t \to \infty$, this means that $\delta\eta_\theta \to 0$ as $t \to \infty$. This completes the local stability analysis.

Therefore the proposed filter with gain function L where $a_0, a_1', a_2', a_4' > 0$ is locally asymptotically stable about any trajectory and globally asymptotically stable about any permanent trajectory when $v_{ix}, v_{iy} \neq 0$.

Step 6: Optimal gain design

The gain proposition above achieves a large domain of convergence (when v_{ix}, $v_{iy} \neq 0$ and v_{ix}, v_{iy} are constant for global convergence). However this gain matrix design is not unique. I.e., many other gain matrix proposals are available to stabilize this error state system [42][41]. The convergence of these filters heavily depends on

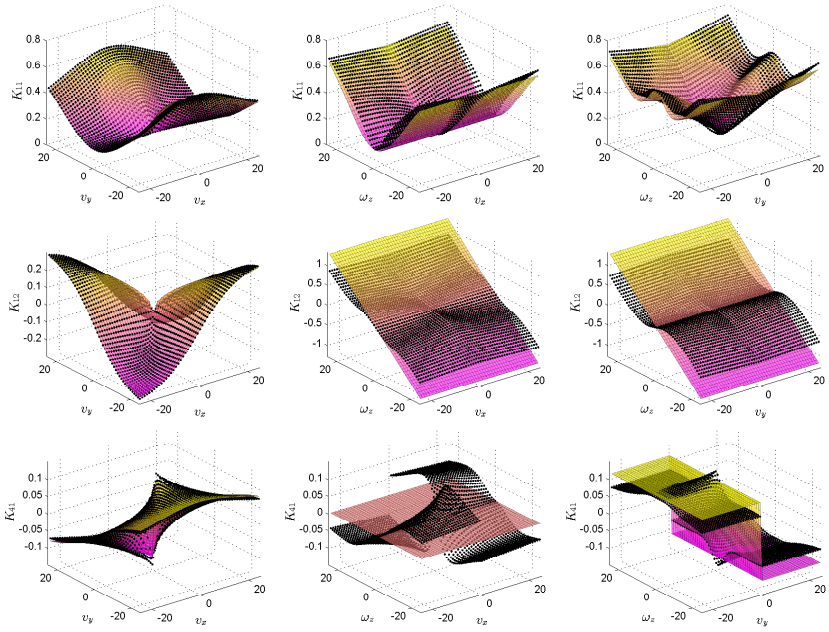

Figure 4.2: Results of gain parameter estimation for the gain matrix proposal.

the parameter selection of the gain matrix proposal, which however lacks a systematic specification in all reported studies.

Here we attempt to redesign the proposed gain matrix so that its performance is comparable to that of a steady state IEKF solution to the problem. This solution would be a highly favourable design for a low cost system due to its ability to tune parameters to achieve IEKF like performance at steady state while demanding significantly less computational processing during operation.

The linearized error state system given by (4.11) acts as a linear time invariant system under permanent trajectories. This allows the application of the Eigen structure decomposition method [92], to find the steady state Kalman gains. A suitable gain matrix proposal can be identified for a given Q and R matrix by analyzing the steady state Kalman gain corresponding to different inputs in the operating region. The identified gain matrix takes the following form.

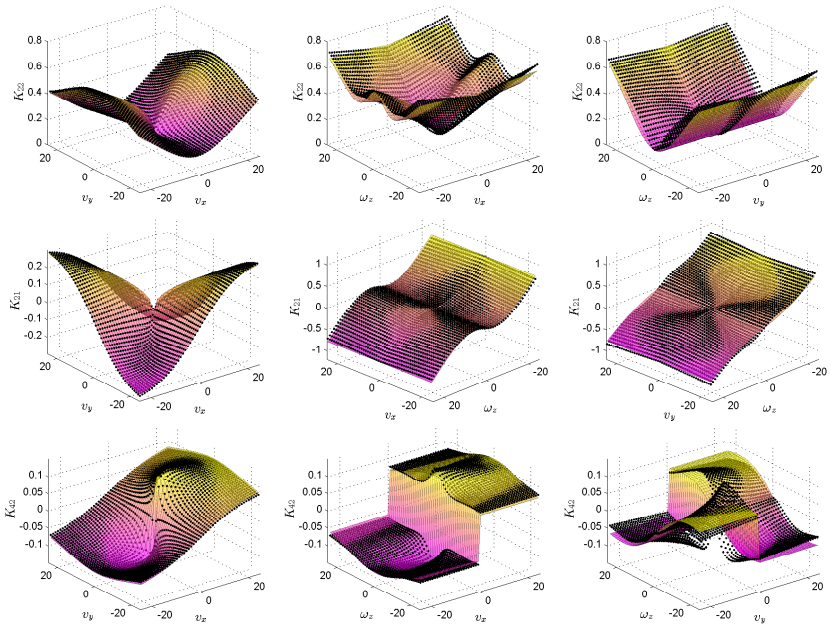

Figure 4.3: Results of gain parameter estimation for the modified gain matrix proposal.

$$
\begin{aligned}
L_p &= -a_0 + [\boldsymbol{\omega}_i]_\times dt - \tfrac{1}{|[a1\ \boldsymbol{\omega}_i^T]|^2}[\boldsymbol{\omega}_i]_\times[\boldsymbol{\omega}_i]_\times^T \\
&\quad - \tfrac{a_2 a_3^2}{|\mathbf{v}_i|^{3/2}\ |[a_3^2\ \omega_i^T]|^2}[\mathbf{v}_i]_\times I_{e_3}[\mathbf{v}_i]_\times^T + [L_\theta \mathcal{E}]_\times dt \\
L_\theta &= -\tfrac{a_4}{|\mathbf{v}_i|}\mathbf{e}_3^T[\mathbf{v}_i]_\times
\end{aligned}
$$

Notice that the modification only replaces a_1', a_2', a_4' with positive normalized terms. Therefore, it does not violate the stability conditions of the original gain matrix proposal. The sampling time dt appears in the gain matrix in discrete implementations of the filter. Parameter identification of the gain matrix is performed using a series of surface fits against the steady state optimal gain values which are computed for a range of operating velocity conditions $-25m/s < v_{ix}, v_{iy} < 25m/s$ and $-25rad/s < \omega_{iz} < 25rad/s$. Figure 4.2 illustrates the surface fits for the non-zero elements K_{11}, K_{12}, K_{41} of the gain matrix. The terms K_{22}, K_{21}, K_{42} produce similar results due to the symmetry of L. The black markers indicate the optimal gain corresponding to the target platform velocities $v_{ix}, v_{iy}, \omega_{iz}$. The coloured surface illustrates the least squared

fit surface using the identified parameterized gain function proposal. The sampling time, process noise, and measurement noise covariances used for the estimation were $dt = 0.05\text{s},\ Q = diag(0.3, 0.3, 0.3, 0.3)^2 dt^2,\ R = diag(0.1, 0.1, 0.1)^2$.

Additional terms can be introduced to the gain matrix to capture the higher order behaviour of the steady state optimal gain. These additional terms are captured in the gain function $L' = (L'_p,\ L'_\theta)^T$, which however does not carry any theoretical stability proofs. Thus L' is only applicable for verified system configurations and operating regions, whereas L possesses desirable local and global stability implications for any positive parameter selection.

$$
\begin{aligned}
L'_p &= L_p - \frac{a_7}{|\mathbf{v}_i|\ |[a_1\ \omega_i^T]|^3} \left(\left[\frac{a_7}{|[1\ a_7\omega_i^T]|^2} \right]_\times [\mathbf{v}_i]_\times^T [\mathbf{v}_i]_\times + [\mathbf{v}_i]_\times [\mathbf{v}_i]_\times^T \left[\frac{2a_7}{|[1\ 2a_7\omega_i^T]|^2} \right]_\times \right) \\
L'_\theta &= L_\theta - \frac{a_5}{|\mathbf{v}_i|\ |[a_1\ \omega_i^T]|^3} \mathbf{e}_3^T [\mathbf{v}_i]_\times [\omega_i]_\times - \frac{a_6}{|\mathbf{v}_i|\ |[a_1\ \omega_i^T]|^2} \mathbf{e}_3^T [\mathbf{v}_i]_\times [\omega_i]_\times [\omega_i]_\times
\end{aligned}
$$

Figure 4.3 illustrates the surface fits for the non-zero elements $K_{22},\ K_{21},\ K_{42}$ of the gain matrix with additional terms. Table 4.1 presents gain parameter estimates with increasing measurement noise conditions and different sampling times dt. The goodness of fit is also evaluated using a normalized mean squared error cost function. The results validate the tuning ability of the proposed gain function L to achieve steady state Kalman performance for a range of operating conditions. In implementation this parameter estimation process will be performed off-line or at startup and the identified gain matrix would allow deployment of the filter with low computational demand compared to that of an EKF or an IEKF.

This completes the steady state IEKF design process for relative localization. The next section designs the necessary attitude filters required for the implementation of the 2.5D forms of the relative localization filters.

Table 4.1: Gain parameter fits for different system configurations

dt	Sensor Noise Multiplier	Parameters $a = [\mathbf{a}_\alpha\ \mathbf{a}_\beta]$ $\mathbf{a}_\alpha = [a_0\ a_1\ a_2\ a_3\ a_4]$ $\mathbf{a}_\beta = [a_5\ a_6\ a_7]$	Goodness of fit $\mathcal{R}^2$
0.05	1	$\mathbf{a}_\alpha = [0.135\ 25.44\ 0.092\ 7.888\ 0.114]$	0.7867
		$\mathbf{a}_\beta = [124.5\ 0.101\ 0.030]$	0.9885
0.05	10^3	$\mathbf{a}_\alpha = [0.005\ 20.17\ 0.0208\ 1.181\ 0.005]$	0.7387
		$\mathbf{a}_\beta = [3.802\ 0.005\ 0.025]$	0.9730
0.05	10^{-2}	$\mathbf{a}_\alpha = [0.741\ 75.46\ 0.143\ 63.02\ 0.510]$	0.9836
		$\mathbf{a}_\beta = [2003\ -0.5\ 2]$	0.9830
0.1	1	$\mathbf{a}_\alpha = [0.253\ 19.88\ 0.171\ 13.38\ 0.173]$	0.9441
		$\mathbf{a}_\beta = [66.68\ 0.117\ 0.0457]$	0.9896
0.25	1	$\mathbf{a}_\alpha = [0.530\ 31.39\ 0.275\ 21.54\ 0.186]$	0.9945
		$\mathbf{a}_\beta = [64.85\ 0.225\ 0.1008]$	0.9943
0.5	1	$\mathbf{a}_\alpha = [0.788\ 61.92\ 0.262\ 34.67\ 0.122]$	0.9992
		$\mathbf{a}_\beta = [112.4\ 0.194\ 0.2647]$	0.9986

4.3.4 IEKF design for attitude estimation

The Attitude filtering problem faced by robotic platforms can be summarized as follows.

$$\dot{\mathbf{x}} = f(\mathbf{x}, \mathbf{u}, \mathbf{w})$$
$$\begin{pmatrix} \dot{\mathbf{q}} \\ \dot{\boldsymbol{\omega}}_b \end{pmatrix} = \begin{pmatrix} \frac{1}{2}\mathbf{q} * (\boldsymbol{\omega}_m - \boldsymbol{\omega}_b + \mathbf{w}_{\omega_m}) \\ \mathbf{w}_{\omega_b} \end{pmatrix} \tag{4.15}$$

$$\mathbf{y} = g(\mathbf{x}, \boldsymbol{\nu})$$
$$\begin{pmatrix} \mathbf{y}_a \\ \mathbf{y}_b \end{pmatrix} = \begin{pmatrix} -\mathbf{R}_q^\mathsf{T}\mathbf{g}_e + \boldsymbol{\nu}_a \\ \mathbf{R}_q^\mathsf{T}\mathbf{b}_e + \boldsymbol{\nu}_b \end{pmatrix} \tag{4.16}$$

where $\boldsymbol{\omega}_m$ denotes the gyroscope measurement which is corrupted by a bias term $\boldsymbol{\omega}_b$, and a measurement noise term $\mathbf{w}_{\omega_m}$. The gyroscopic bias follows a random walk process with noise $\mathbf{w}_{\omega_b}$. The measurement models $\mathbf{y}_a$ and $\mathbf{y}_b$ denote an accelerometer and a magnetometer attached to the platform. For low cost attitude estimation it is assumed that platform accelerations are absorbed in the accelerometer measurement noise term given by $\boldsymbol{\nu}_a$; as a result, accelerations due to the gravity $\mathbf{g}_e$ dominates

the accelerometer measurements. The magnetometer assumes low external magnetic disturbances and measures the magnetic reference vector $\mathbf{b}_e$ relative to the body fixed frame corrupted with a noise term $\boldsymbol{\nu}_b$. The magnetometer is given less confidence in indoor navigation considered in this work. Therefore the yaw estimates given by the attitude reference system are considered unreliable and heavily prone to errors due to local magnetic disturbances.

Standard EKF design can be followed for this problem and the resulting filtering equations are summarized below. IEKF designs for this problem are also well established in the work presented in [55]. It follows the symmetry preserving observer design procedure to derive two forms of the filter. The left invariant extended Kalman filter (LIEKF) and the right invariant extended Kalman filter (RIEKF). The difference between these two filters is with the consideration of the corresponding left group action and the right group action of the group. E.g. for group elements $g = \mathbf{q}$, $g_0 = \mathbf{q}_0 \in \mathrm{SO}(3)$, $g_0 \diamondsuit g = \mathbf{q}_0 * \mathbf{q}$ and $g_0 \diamondsuit g = \mathbf{q} * \mathbf{q}_0$ denotes the left and right group actions respectively. The summary of filtering equations of the EKF, LIEKF, and the RIEKF for the AHRS problem can be summarized as follows:

Filter Equations

	System model	*Measurement model*	*State Error*	*Output Error*
EKF :	$\begin{pmatrix} \dot{\hat{\mathbf{q}}} \\ \dot{\hat{\omega}}_b \end{pmatrix} = \begin{pmatrix} \frac{1}{2}\hat{\mathbf{q}} * (\boldsymbol{\omega}_m - \hat{\boldsymbol{\omega}}_b) \\ \mathbf{0} \end{pmatrix} + K\mathcal{E}$	$\begin{pmatrix} \hat{\mathbf{y}}_a \\ \hat{\mathbf{y}}_b \end{pmatrix} = \begin{pmatrix} -\hat{\mathbf{R}}_{\mathbf{q}}^T g_e \\ \hat{\mathbf{R}}_{\mathbf{q}}^T b_e \end{pmatrix}$	$\eta = \begin{pmatrix} \hat{q} - q \\ \hat{\omega}_b - \omega_b \end{pmatrix}$	$\mathcal{E} = \begin{pmatrix} \mathbf{y}_a - \hat{\mathbf{y}}_\mathbf{a} \\ \mathbf{y}_b - \hat{\mathbf{y}}_\mathbf{b} \end{pmatrix}$
LIEKF :	$\begin{pmatrix} \dot{\hat{\mathbf{q}}} \\ \dot{\hat{\omega}}_b \end{pmatrix} = \begin{pmatrix} \frac{1}{2}\hat{\mathbf{q}} * (\boldsymbol{\omega}_m - \hat{\boldsymbol{\omega}}_b) \\ \mathbf{0} \end{pmatrix} + \begin{pmatrix} \hat{\mathbf{q}} * L_q\mathcal{E} \\ L_{\omega_b}\mathcal{E} \end{pmatrix}$	$\begin{pmatrix} \hat{\mathbf{y}}_a \\ \hat{\mathbf{y}}_b \end{pmatrix} = \begin{pmatrix} -\hat{\mathbf{R}}_q^T g_e \\ \hat{\mathbf{R}}_q^T b_e \end{pmatrix}$	$\eta = \begin{pmatrix} q^{-1} * \hat{q} \\ \hat{\omega}_b - \omega_b \end{pmatrix}$	$\mathcal{E} = \begin{pmatrix} \hat{\mathbf{R}}_q^\intercal \hat{\mathbf{y}}_a - \mathbf{y}_a \\ \hat{\mathbf{R}}_q^\intercal \hat{\mathbf{y}}_b - \mathbf{y}_b \end{pmatrix}$
RIEKF :	$\begin{pmatrix} \dot{\hat{\mathbf{q}}} \\ \dot{\hat{\omega}}_b \end{pmatrix} = \begin{pmatrix} \frac{1}{2}\hat{\mathbf{q}} * (\boldsymbol{\omega}_m - \hat{\boldsymbol{\omega}}_b) \\ \mathbf{0} \end{pmatrix} + \begin{pmatrix} L_q\mathcal{E} * \hat{\mathbf{q}} \\ L_{\omega_b}\mathcal{E} \end{pmatrix}$	$\begin{pmatrix} \hat{\mathbf{y}}_a \\ \hat{\mathbf{y}}_b \end{pmatrix} = \begin{pmatrix} -\hat{\mathbf{R}}_q^T g_e \\ \hat{\mathbf{R}}_q^T b_e \end{pmatrix}$	$\eta = \begin{pmatrix} \hat{q} * q^{-1} \\ \mathbf{R}_q(\hat{\omega}_b - \omega_b) \end{pmatrix}$	$\mathcal{E} = \begin{pmatrix} -\mathbf{g}_e - \hat{\mathbf{R}}_q \mathbf{y}_a \\ \mathbf{b}_e - \hat{\mathbf{R}}_q \mathbf{y}_b \end{pmatrix}$

(4.17)

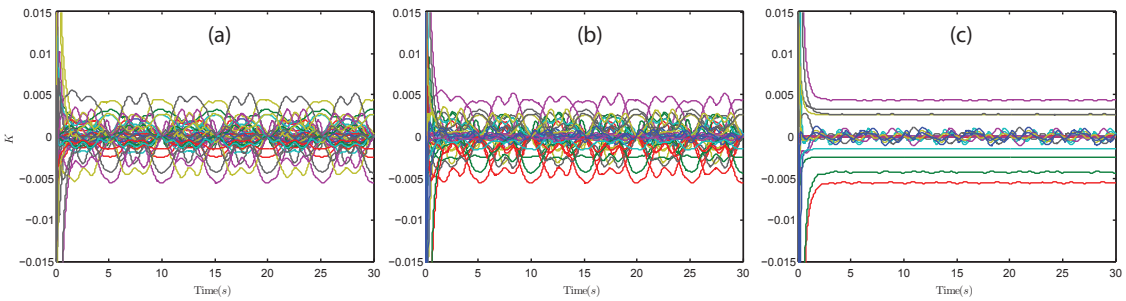

Figure 4.4: Gain adaptation for a smooth trajectory for (a) The EKF, (b) The LIEKF, (c) The RIEKF

Work in [55] presents detailed step by step derivation of these Invariant filters for the AHRS problem, which follows the same steps 1 through 4 followed in the previous section. Therefore the derivation related to these steps is not explained here.

Figure **??** illustrates the gain stabilization behaviour of the filters when the platforms are excited on a random smooth trajectory. All filters show good convergence. Out of the three filters, the RIEKF specifically exhibits steady state convergence of its dominant gains. This is an important characteristic which allows to exploit steady state behaviour of the filter in order to design low cost deterministic versions of the filter. Since this work targets a low cost design, we modify the IEKF designs to the form comparable to that of the NCF. This is because the NCF exhibits good convergence and wide acceptance as a deterministic, fixed gain, and low cost form, applicable to attitude filtering. The NCF for the attitude estimation problem can be summarized as follows.

Initialization : $\hat{\mathbf{x}} = \begin{bmatrix} 1 & \mathbf{0} & \mathbf{0} \end{bmatrix}^T$

Filter Equations

$$\begin{pmatrix} \dot{\hat{\mathbf{q}}} \\ \dot{\hat{\omega}}_b \end{pmatrix} = \begin{pmatrix} \frac{1}{2}\hat{\mathbf{q}} * (\boldsymbol{\omega}_m - \hat{\boldsymbol{\omega}}_b) \\ \mathbf{0} \end{pmatrix} + \begin{pmatrix} \hat{\mathbf{q}} * k_p \mathcal{E} \\ k_i \mathcal{E} \end{pmatrix} \qquad \begin{pmatrix} \hat{\mathbf{y}}_a \\ \hat{\mathbf{y}}_b \end{pmatrix} = \begin{pmatrix} -\hat{\mathbf{R}}_{\mathbf{q}}^T g_e \\ \hat{\mathbf{R}}_{\mathbf{q}}^T b_e \end{pmatrix}$$

Output Error $\mathcal{E} = k_1(\hat{\mathbf{y}}_\mathbf{a} \times \mathbf{y}_a) + k_2(\hat{\mathbf{y}}_\mathbf{b} \times \mathbf{y}_b)$ *Gains* $\begin{bmatrix} k_p & k_i & k_1 & k_2 \end{bmatrix}^T > 0$

This is directly comparable to the LIEKF given in 4.17 except for the output cross product error definition assumed in the NCF. Therefore we modify the output error definition of the LIEKF to take this cross product form.

$$\mathcal{E} = \begin{pmatrix} \mathbf{y}_\mathbf{a} \times \hat{\mathbf{y}}_a \\ \mathbf{y}_\mathbf{b} \times \hat{\mathbf{y}}_b \end{pmatrix}$$

The sign change of the error definitions is usual in Luenberger type observers, which cancels the effect by producing gains with the corresponding sign change. To be congruent with the symmetry preserving framework, this output error definition should satisfy conditions for invariance. The relevant symmetries of the LIEKF when operated by a group element $(\mathbf{q}_0,\ \boldsymbol{\omega}_{b0}) \in G = SO(3) \times \mathbb{R}^3$ can be summarized as follows, which is found by applying Definitions 3 and 4.

$$\varphi_g \begin{pmatrix} \mathbf{q} \\ \omega_b \end{pmatrix} = \begin{pmatrix} \mathbf{q}_0 * \mathbf{q} \\ \omega_b + \omega_{b0} \end{pmatrix} \quad \psi_g \begin{pmatrix} \omega_m \\ \mathbf{g}_e \\ \mathbf{b}_e \end{pmatrix} = \begin{pmatrix} \omega_m + \omega_{b0} \\ \mathbf{R}_{q_0}\mathbf{g}_e \\ \mathbf{R}_{q_0}\mathbf{b}_e \end{pmatrix} \quad \rho_g \begin{pmatrix} \mathbf{y}_a \\ \mathbf{y}_b \end{pmatrix} = \begin{pmatrix} \mathbf{y}_a \\ \mathbf{y}_b \end{pmatrix}$$

Using these mappings the cross product error term is found to be invariant using

Definition 5.

$$\phi_g(\mathcal{E}(x,u,y)) = \mathcal{E}(\varphi_g(x),\psi_g(u),\rho_g(y))$$
$$\phi_g\begin{pmatrix}\mathbf{y_a}\times -\hat{\mathbf{R}}_q^\mathsf{T}\mathbf{g}_e\\ \mathbf{y_b}\times \hat{\mathbf{R}}_q^\mathsf{T}\mathbf{b}_e\end{pmatrix} = \begin{pmatrix}\mathbf{y_a}\times -\hat{\mathbf{R}}_q^\mathsf{T}\mathbf{R}_{q0}^\mathsf{T}\mathbf{R}_{q0}\mathbf{g}_e\\ \mathbf{y_b}\times \hat{\mathbf{R}}_q^\mathsf{T}\mathbf{R}_{q0}^\mathsf{T}\mathbf{R}_{q0}\mathbf{b}_e\end{pmatrix} = \begin{pmatrix}\mathbf{y_a}\times -\hat{\mathbf{R}}_q^\mathsf{T}\mathbf{g}_e\\ \mathbf{y_b}\times \hat{\mathbf{R}}_q^\mathsf{T}\mathbf{b}_e\end{pmatrix} = \mathcal{E}(x,u,y)$$

By applying this cross product error modification, the modified LIEKF denoted as LIEKF* can be found following the IEKF design process. Similarly one can find the modified RIEKF form using a comparable invariant cross product error term applicable to right group actions.

$$\mathcal{E} = \begin{pmatrix}\hat{\mathbf{R}}_q(\mathbf{y_a}\times\hat{\mathbf{y}}_a)\\ \hat{\mathbf{R}}_q(\mathbf{y_b}\times\hat{\mathbf{y}}_b)\end{pmatrix}$$

The following set of equations verifies the invariance of $\mathcal{E}$ for symmetries relevant to right group actions.

$$\varphi_g\begin{pmatrix}\mathbf{q}\\ \omega_b\end{pmatrix} = \begin{pmatrix}\mathbf{q}*\mathbf{q}_0\\ \mathbf{R}_{q_0}^\mathsf{T}\omega_b+\omega_{b0}\end{pmatrix}\quad \psi_g\begin{pmatrix}\omega_m\\ \mathbf{g}_e\\ \mathbf{b}_e\end{pmatrix} = \begin{pmatrix}\mathbf{R}_{q_0}^\mathsf{T}\omega_m+\omega_{b0}\\ \mathbf{g}_e\\ \mathbf{b}_e\end{pmatrix}\quad \rho_g\begin{pmatrix}\mathbf{y}_a\\ \mathbf{y}_b\end{pmatrix} = \begin{pmatrix}\mathbf{R}_{q_0}^\mathsf{T}\mathbf{y}_a\\ \mathbf{R}_{q_0}^\mathsf{T}\mathbf{y}_b\end{pmatrix}$$

$$\phi_g(\mathcal{E}(x,u,y)) = \mathcal{E}(\varphi_g(x),\psi_g(u),\rho_g(y))$$
$$\phi_g\begin{pmatrix}\hat{\mathbf{R}}_q(\mathbf{y_a}\times -\hat{\mathbf{R}}_q^\mathsf{T}\mathbf{g}_e)\\ \hat{\mathbf{R}}_q(\mathbf{y_b}\times \hat{\mathbf{R}}_q^\mathsf{T}\mathbf{b}_e)\end{pmatrix} = \begin{pmatrix}\hat{\mathbf{R}}_q\mathbf{R}_{q_0}(\mathbf{R}_{q_0}^\mathsf{T}\mathbf{y_a}\times -\mathbf{R}_{q_0}^\mathsf{T}\hat{\mathbf{R}}_q^\mathsf{T}\mathbf{g}_e)\\ \hat{\mathbf{R}}_q\mathbf{R}_{q_0}(\mathbf{R}_{q_0}^\mathsf{T}\mathbf{y_b}\times \mathbf{R}_{q_0}^\mathsf{T}\hat{\mathbf{R}}_q^\mathsf{T}\mathbf{b}_e)\end{pmatrix} = \begin{pmatrix}\hat{\mathbf{R}}_q(\mathbf{y_a}\times -\hat{\mathbf{R}}_q^\mathsf{T}\mathbf{g}_e)\\ \hat{\mathbf{R}}_q(\mathbf{y_b}\times \hat{\mathbf{R}}_q^\mathsf{T}\mathbf{b}_e)\end{pmatrix}$$
$$= \mathcal{E}(x,u,y)$$

By applying this cross product error modification the modified RIEKF denoted as RIEKF* can be found by following the IEKF design process. The attitude observers

LIEKF* and RIEKF* are summarized in Table 4.2.

Table 4.2: Summary of LIEKF* and RIEKF*

LIEKF *	**RIEKF***
Initialization	
$\hat{\mathbf{x}} = \begin{bmatrix}1 & \mathbf{0} & \mathbf{0}\end{bmatrix}^T \quad P = \mathrm{E}(\boldsymbol{\eta}\boldsymbol{\eta}^T) = \mathbf{I} \quad Q = \mathrm{E}(\mathbf{w}\mathbf{w}^T) \quad R = \mathrm{E}(\boldsymbol{\nu}\boldsymbol{\nu}^T)$	
Filter Equations	
$\begin{pmatrix}\dot{\hat{\mathbf{q}}}\\ \dot{\hat{\omega}}_b\end{pmatrix} = \begin{pmatrix}\frac{1}{2}\hat{\mathbf{q}} * (\boldsymbol{\omega}_m - \hat{\omega}_b)\\ \mathbf{0}\end{pmatrix} + \begin{pmatrix}\hat{\mathbf{q}} * L_q\mathcal{E}\\ L_{\omega_b}\mathcal{E}\end{pmatrix}$	$\begin{pmatrix}\dot{\hat{\mathbf{q}}}\\ \dot{\hat{\omega}}_b\end{pmatrix} = \begin{pmatrix}\frac{1}{2}\hat{\mathbf{q}} * (\boldsymbol{\omega}_m - \hat{\omega}_b)\\ \mathbf{0}\end{pmatrix} + \begin{pmatrix}\hat{\mathbf{q}} * L_q\mathcal{E}\\ L_{\omega_b}\mathcal{E}\end{pmatrix}$
$\begin{pmatrix}\hat{\mathbf{y}}_a\\ \hat{\mathbf{y}}_b\end{pmatrix} = \begin{pmatrix}-\hat{\mathbf{R}}_{\mathbf{q}}^T\mathbf{g}_e\\ \hat{\mathbf{R}}_{\mathbf{q}}^T\mathbf{b}_e\end{pmatrix} \quad \mathcal{E} = \begin{pmatrix}\mathbf{y_a} \times \hat{\mathbf{y}}_a\\ \mathbf{y_b} \times \hat{\mathbf{y}}_b\end{pmatrix}$	$\begin{pmatrix}\hat{\mathbf{y}}_a\\ \hat{\mathbf{y}}_b\end{pmatrix} = \begin{pmatrix}-\hat{\mathbf{R}}_{\mathbf{q}}^T\mathbf{g}_e\\ \hat{\mathbf{R}}_{\mathbf{q}}^T\mathbf{b}_e\end{pmatrix} \quad \mathcal{E} = \begin{pmatrix}\hat{\mathbf{R}}_{\mathbf{q}}(\mathbf{y_a} \times \hat{\mathbf{y}}_a)\\ \hat{\mathbf{R}}_{\mathbf{q}}(\mathbf{y_b} \times \hat{\mathbf{y}}_b)\end{pmatrix}$
$K = \begin{bmatrix}-L_q & -L_{\omega_b}\end{bmatrix}^{\mathsf{T}}$	
Filter Matrices(used to compute Kalman Gain K)	
$A = \begin{bmatrix}[\omega_b - \omega_m]_\times & -\frac{1}{2}\mathbf{I}\\ \mathbf{0} & \mathbf{0}\end{bmatrix}$	$A = \begin{bmatrix}\mathbf{0} & -\frac{1}{2}\mathbf{I}\\ \mathbf{0} & \mathbf{R_q}(\omega_m - \omega_b)\end{bmatrix}$
$C = \begin{bmatrix}2[\mathbf{R_q}^T\mathbf{g}_e]_\times^2 & \mathbf{0}\\ 2[\mathbf{R_q}^T\mathbf{b}_e]_\times^2 & \mathbf{0}\end{bmatrix}$	$C = \begin{bmatrix}2[\mathbf{g}_e]_\times^2 & \mathbf{0}\\ 2[\mathbf{b}_e]_\times^2 & \mathbf{0}\end{bmatrix}$
$M = \begin{bmatrix}-0.5\mathbf{I} & \mathbf{0}\\ \mathbf{0} & -\mathbf{I}\end{bmatrix}$	$M = \begin{bmatrix}0.5\mathbf{I} & \mathbf{0}\\ \mathbf{0} & -\mathbf{I}\end{bmatrix}$
$N = \begin{bmatrix}\mathbf{I} + [\mathbf{R_q}^T\mathbf{g}_e]_\times & \mathbf{0}\\ \mathbf{0} & \mathbf{I} - [\mathbf{R_q}^T\mathbf{b}_e]_\times\end{bmatrix}$	$N = \begin{bmatrix}\mathbf{I} + [\mathbf{g}_e]_\times & \mathbf{0}\\ \mathbf{0} & \mathbf{I} - [\mathbf{b}_e]_\times\end{bmatrix}$

Notice that the cross product is a rank deficient operation which causes the noise Jacobians to lose their rank. Therefore the noise Jacobians are modified to $I + N$ to preserve full rank and allow application of Kalman gain computation equations.

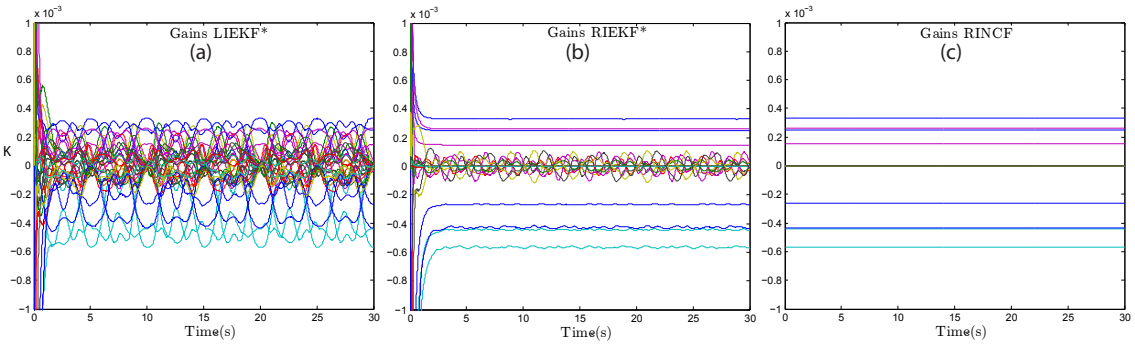

Figure 4.5: Gain evolution for a smooth trajectory for (a) The RIEKF*, (b) The LIEKF*, (c) The RINCF RINCF

Figures 4.5 (b) and (c) illustrate the gain stabilization of the LIEKF* and the RIEKF* respectively. It is evident that the RIEKF form exhibits good stabilizing

behaviour which allows the pursuit of a fixed gain design. Gain identification for the LIEKF form will be difficult due to the strong coupling the steady state gains exhibit with the system trajectory. Next we attempt to exploit particularly the RIEKF* to propose a method to modify the nonlinear complimentary filter to achieve easy system noise based tunability.

4.3.5 Steady state IEKF design for attitude estimation

Similar to the approach followed for relative localization, one can find a gain function L which mimics the dynamics of the gains produced by the RIEKF*. The nonlinear error state dynamics for RIEKF* with its modified output error definition is found to be

$$\begin{pmatrix}\dot{\boldsymbol{\mu}}\\ \dot{\boldsymbol{\beta}}\end{pmatrix} = \begin{pmatrix}-\frac{1}{2}\boldsymbol{\beta} * \boldsymbol{\mu} + L_\mu \mathcal{E}\\ \boldsymbol{\mu}^{-1} * \hat{I}_\omega * \boldsymbol{\mu} \times \boldsymbol{\beta} + \mu^{-1} * L_\beta \mathcal{E} * \boldsymbol{\mu}\end{pmatrix} \quad \mathcal{E} = \begin{pmatrix}\mathbf{e}_g\\ \mathbf{e}_b\end{pmatrix} = \begin{pmatrix}\boldsymbol{\mu} * \mathbf{g}_e * \boldsymbol{\mu}^{-1} \times \mathbf{g}_e\\ \boldsymbol{\mu} * \mathbf{b}_e * \boldsymbol{\mu}^{-1} \times \mathbf{b}_e\end{pmatrix}$$

where $\boldsymbol{\eta}$ is the error state defined by $\boldsymbol{\eta} = (\boldsymbol{\mu},\ \boldsymbol{\beta}) = (\hat{\mathbf{q}} * \mathbf{q}^{-1},\ \mathbf{q}(\hat{\boldsymbol{\omega}}_b - \boldsymbol{\omega}_b) * \mathbf{q}^{-1})$, and $\hat{I}_\omega$ is an invariant quantity defined as $\hat{I}_\omega = \hat{\mathbf{q}} * (\boldsymbol{\omega}_m - \hat{\boldsymbol{\omega}}_b) * \hat{\mathbf{q}}^{-1}$. The steps of the derivations above were omitted since they follow the standard IEKF design steps. We continue from step (e) of the filter derivation process in detail in order to identify an optimal steady state design for attitude estimation.

Step 5: Identify deterministic design

The characteristic steady state behaviour of the RIEKF* shown in Figure 4.5 implies that the optimal gain matrix mainly consists of a constant set of gains. Consider the following constant gain matrix proposal.

$$L = \begin{pmatrix} L_\mu \\ L_\beta \end{pmatrix} = \begin{pmatrix} \mathbf{I_a} & \mathbf{I_b} \\ -\mathbf{I_c} & -\mathbf{I_d} \end{pmatrix}, \begin{aligned} \mathbf{I_a} &= diag([a_1\ a_2\ a_3]) \\ \mathbf{I_b} &= diag([b_1\ b_2\ b_3]) \\ \mathbf{I_c} &= diag([c_1\ c_2\ c_3]) \\ \mathbf{I_d} &= diag([d_1\ d_2\ d_3]) \end{aligned}$$

By substituting L and linearizing the error state dynamics, the following set of error state equations can be found.

$$\begin{pmatrix} \dot{\delta\boldsymbol{\mu}} \\ \dot{\delta\boldsymbol{\beta}} \end{pmatrix} = \begin{pmatrix} -\frac{1}{2}\delta\boldsymbol{\beta} + A_\mu \delta\boldsymbol{\mu} \\ \hat{I}_\omega \times \delta\boldsymbol{\beta} + A_\beta \delta\boldsymbol{\mu} \end{pmatrix}, \quad A_\mu = \begin{pmatrix} -2g_e^2 a_1 & 0 & 0 \\ 0 & -2g_e^2 a_2 - 2b_e^2 b_2 & 0 \\ 0 & 0 & -2b_e^2 b_3 \end{pmatrix},$$
$$A_\beta = \begin{pmatrix} 2g_e^2 c_1 & 0 & 0 \\ 0 & 2g_e^2 c_2 + 2b_e^2 d_2 & 0 \\ 0 & 0 & 2b_e^2 d_3 \end{pmatrix} \tag{4.18}$$

This system is found to be locally asymptotically stable using a candidate Lyapunov function V as proposed in [93].

$$V = \delta\boldsymbol{\beta}^\mathsf{T}\delta\boldsymbol{\beta} + (2A_\beta\delta\boldsymbol{\mu})^\mathsf{T}\delta\boldsymbol{\mu} \geq 0$$

The derivative of the Lyapunov function is found to be:

$$\begin{aligned} \dot{V} &= (4A_\beta\delta\boldsymbol{\mu})^\mathsf{T} A_\mu \delta\boldsymbol{\mu} \\ &= -4\delta\mu_y^2(2b_2b_e^2 + 2a_2g_e^2)(2d_2b_e^2 + 2c_2g_e^2) - 16b_3b_e^4d_3\delta\mu_z^2 - 16a_1c_1g_e^4\delta\mu_x^2 \end{aligned}$$

Here $\dot{V}$ is negative semi-definite which implies Lyapunov stability. I.e. $\delta\boldsymbol{\mu}$ and $\delta\boldsymbol{\beta}$ are bounded. $\ddot{V}$ is a polynomial function of $\delta\boldsymbol{\mu}$, $\delta\boldsymbol{\beta}$, I_ω and $\dot{I}_\omega$. Hence $\ddot{V}$ is bounded and

$\dot{V}$ is uniformly continuous. From Barbalat's lemma $\dot{V} \to 0$ as $t \to \infty$, hence $\delta\boldsymbol{\mu} \to 0$ as $t \to \infty$. Analyzing the local error state dynamics (4.18), $\delta\dot{\boldsymbol{\mu}}$ is bounded and $\delta\ddot{\boldsymbol{\mu}}$ is a polynomial function of $\delta\boldsymbol{\mu}$, $\delta\boldsymbol{\beta}$, I_ω and $\dot{I}_\omega$. Hence $\delta\dddot{\boldsymbol{\mu}}$ is bounded and $\delta\ddot{\boldsymbol{\mu}}$ is uniformly continuous. From Barbalat's lemma $\delta\dot{\boldsymbol{\mu}} \to 0$ as $t \to \infty$. Since $\delta\boldsymbol{\mu} \to 0$ as $t \to \infty$, this means that $\delta\boldsymbol{\beta} \to 0$ as $t \to \infty$. Therefore the system is locally asymptotically convergent to the equilibrium for any positive parameter selection for $a_1,\ a_2,\ b_2,\ b_3,$ $c_1,\ c_2,\ d_2,\ d_3,$. Work in [54] includes global stability implications of the filter, which is not discussed in this text.

Step 6: Optimal gain design

The constant gain L can be found by applying the Eigen structure decomposition method using the matrices A, C, M, N relevant to the RIEKF*. The time varying components of the filter matrices are omitted in arriving at the steady state gain values. I.e., $\hat{I}_\omega = 0$. This cannot be performed on the LIEKF* which in its noiseless form is equivalent to the usual NCF proposed by [54]. It is evident that despite the popularity of the NCF, the right invariant form of the NCF exhibits better performance and tunability using system noise parameters, while a stochastic derivation of the generic NCF does not allow one to identify the optimal gains easily due to the dominant coupling the optimal gains exhibit with the system trajectory. Therefore this thesis proposes the steady state RIEKF* as a natural extension to the NCF, which by design inherits similar characteristics as the original NCF, but with added tuning capability, using system and measurement noise figures. We term this formulation the right invariant nonlinear complimentary filter (RINCF). The filter can be summarized as follows.

Initialization

$$\hat{\mathbf{x}} = \begin{bmatrix} 1 & \mathbf{0} & \mathbf{0} \end{bmatrix}^T \quad Q = \mathrm{E}(\mathbf{w}\mathbf{w}^T) \quad R = \mathrm{E}(\boldsymbol{\nu}\boldsymbol{\nu}^T)$$

Filter Equations

$$\begin{pmatrix} \dot{\hat{\mathbf{q}}} \\ \dot{\hat{\omega}}_b \end{pmatrix} = \underbrace{\begin{pmatrix} \frac{1}{2}\hat{\mathbf{q}} * (\boldsymbol{\omega}_m - \hat{\boldsymbol{\omega}}_b) \\ \mathbf{0} \end{pmatrix}}_{\textit{State Prediction}} + \underbrace{\begin{pmatrix} L_q \mathcal{E} * \hat{\mathbf{q}} \\ \hat{\mathbf{q}}^{-1} * L_{\omega_b} \mathcal{E} * \hat{\mathbf{q}} \end{pmatrix}}_{\textit{State Correction}} \underbrace{\begin{pmatrix} \hat{\mathbf{y}}_a \\ \hat{\mathbf{y}}_b \end{pmatrix} = \begin{pmatrix} -\hat{\mathbf{R}}_{\mathbf{q}}^T \mathbf{g}_e \\ \hat{\mathbf{R}}_{\mathbf{q}}^T \mathbf{b}_e \end{pmatrix}}_{\textit{Output Prediction}}$$

$$\textit{Output Error } \mathcal{E} = \begin{pmatrix} \hat{\mathbf{R}}_{\mathbf{q}}(\hat{\mathbf{y}}_{\mathbf{a}} \times \mathbf{y}_a) \\ \hat{\mathbf{R}}_{\mathbf{q}}(\hat{\mathbf{y}}_{\mathbf{b}} \times \mathbf{y}_b) \end{pmatrix} \quad \textit{Gain Matrix } K = \begin{bmatrix} -L_q & -L_{\omega_b} \end{bmatrix}^T$$

$$\textit{Gain Computation} \quad DARE(I + Adt,\ C,\ MQM^T dt^2,\ NRN^T)$$

Filtering Matrices

$$A = \begin{bmatrix} \mathbf{0} & -\frac{1}{2}\mathbf{I} \\ \mathbf{0} & \mathbf{0} \end{bmatrix} \quad C = \begin{bmatrix} 2[\mathbf{g}_e]_\times^2 & \mathbf{0} \\ 2[\mathbf{b}_e]_\times^2 & \mathbf{0} \end{bmatrix}$$

$$M = \begin{bmatrix} 0.5\mathbf{I} & \mathbf{0} \\ \mathbf{0} & -\mathbf{I} \end{bmatrix} \quad N = \begin{bmatrix} \mathbf{I} + [\mathbf{g}_e]_\times & \mathbf{0} \\ \mathbf{0} & \mathbf{I} - [\mathbf{b}_e]_\times \end{bmatrix}$$

The resulting filter has a low cost, and is easily tunable using the system noise parameters off line. I.e., one can easily find K by using Matlab's discrete algebraic Riccatti equation (**DARE**) solving function with the 4 matrices given above as parameters. The resulting steady state gains are illustrated in Figure 4.5, where the RINCF was capable of achieving the optimal steady state dominant gains achieved by the RIEKF*.

It is important to note that at high angular velocities the optimal gains produce coupling with the angular velocities. By analyzing the behaviour it was identified that the gain function approximates to the following form with 2 extra parameters.

$$L = \begin{pmatrix} L_\mu \\ L_\beta \end{pmatrix} = \begin{pmatrix} \mathbf{I_a} & \mathbf{I_b} \\ -\mathbf{I_c} + p_1[\hat{-\mathbf{I}}_\omega]_\times & -\mathbf{I_d} + p_2[\hat{-\mathbf{I}}_\omega]_\times \end{pmatrix}$$

The parameters p_1 and p_2 can be found by applying a DARE solving function with $\hat{\mathbf{I}}_\omega = (\omega_{max},\ 0,\ 0)$ and then reading of p_1 and p_2 from the gain matrix. I.e $p_1 = K_{62}/\omega_{max},\ p_2 = -K_{56}/\omega_{max}$. Figure 4.6 illustrates the gain adaptation achievable

with this modified form for three different angular velocities. Figure 4.7 illustrates the variation of the dominant gains over a wide range of angular velocities. The surface represents the gains predicted by the tuning method and the black markers denote the optimal steady state gain computed using the DARE solve function over a range of values for $\hat{\mathbf{I}}_{\omega}$.

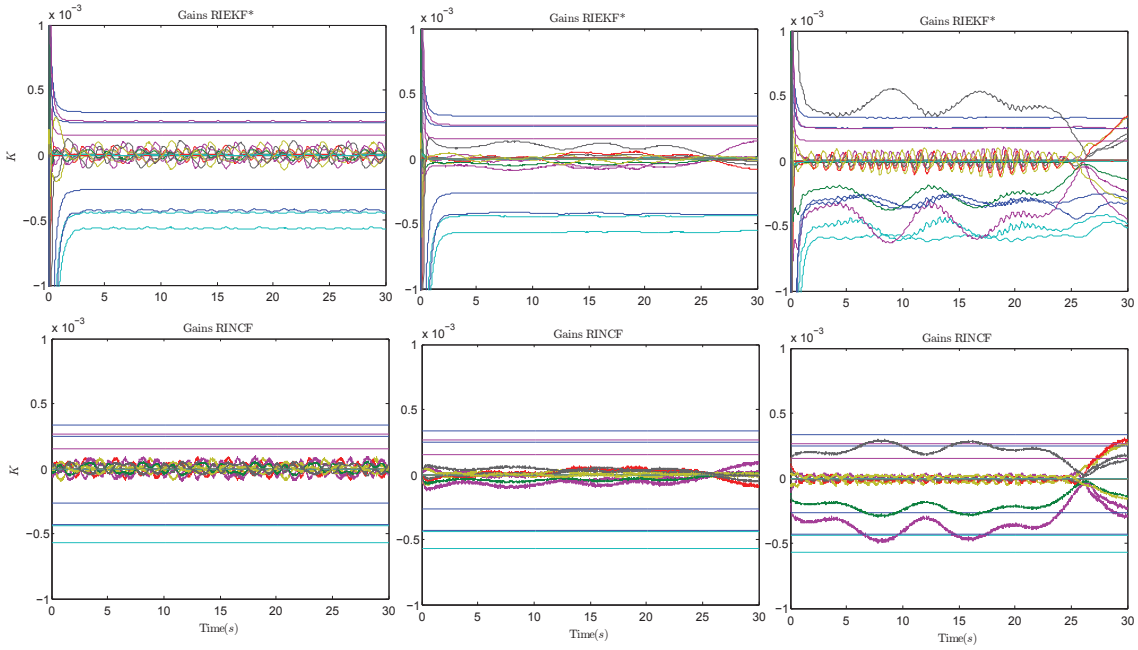

Figure 4.6: Gain evolution for a smooth trajectory for The RIEKF* (top), The RINCF (bottom), for $\omega_{max} = \pi/3$ (left), $\omega_{max} = 2\pi/3$ (middle), and $\omega_{max} = 5\pi/3$ (right)

Table 4.3 evaluates the goodness of fit of this modified form for different noise configurations. The gains were evaluated for ω ranging from -5 to 5rad/s. The noise parameters used were $Q = 0.1\mathbf{I}_6$, and $R = diag(0.3\mathbf{I}_6, 0.5\mathbf{I}_6)$.

The statistics suggest good approximation of the steady state optimal gains of the RINCF by the proposed tuning method in a wide range of operating conditions. This completes the low cost filter design procedure for relative localization. The results section evaluates the comparative performance of the designed filters.

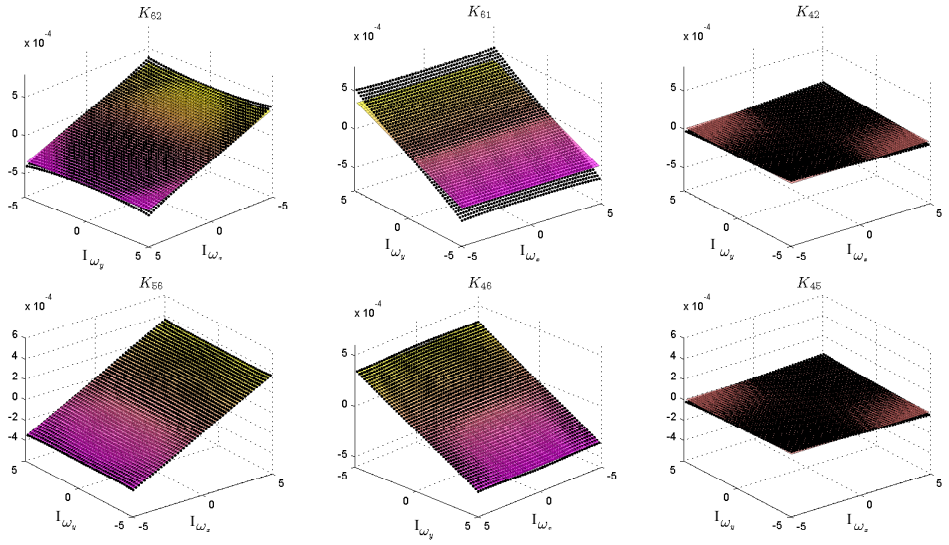

Figure 4.7: Gain parameter fits using the modified criteria for the dominant gain terms when $I_{\omega_z} = 0 rad/s$

Table 4.3: Gain parameter fits for the dominant gains for different system configurations

dt	Sensor Noise Multiplier	Parameters $a = [\mathbf{a}_\alpha \ \mathbf{a}_\beta]$ $\alpha = [p_1 \ p_2]$	Goodness of fit $\mathcal{R}^2$
0.01	1	$\alpha = [0.6643 \ 0.7083]e^{-4}$	0.9231
0.01	10	$\alpha = [0.4372 \ 0.3058]e^{-4}$	0.9582
0.01	10^{-1}	$\alpha = [0.0831 \ 0.1144]e^{-3}$	0.8762
0.05	1	$\alpha = [0.7068 \ 0.7392]e^{-3}$	0.8830
0.005	1	$\alpha = [0.2945 \ 0.3166]e^{-5}$	0.9196
0.1	100	$\alpha = [0.0019 \ 0.0013]$	0.8389

4.4 Results

The previous section derived three different filters relevant to relative localization. First is an IEKF for relative localization in 2.5D. This filter is applicable as an estimator in the overall HNF proposed in this thesis. Second is a low cost steady state IEKF for 2.5D relative localization. This filter is applicable in the embedded electronics of a communicating set of sensor nodes when velocities are available. The filter features low cost implementation and optimal steady state tunability. The third is

the RINCF for attitude estimation. This filter is also capable of residing in embedded electronics to support the 2.5D relative localization modules. The filter features low cost reliable attitude estimation comparable to an NCF, with the ability to tune the gain parameters to achieve optimal steady state performance. This section compares the performance of these three filters to generic solutions reported in literature.

Numerical simulations are presented evaluating the performance of the filters in terms of estimation accuracy and gain stabilization. Experimental validation of the RINCF is presented using an MAV as validation of the nonlinear steady state filter design procedure proposed in this work.

4.4.1 Performance of the IEKF for relative localization

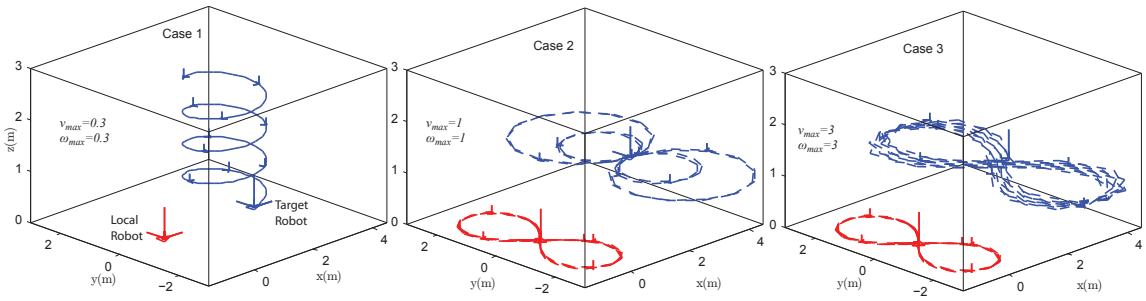

Figure 4.8: The simulated trajectory of the local and target robots used to validate the relative localization filter designs

The following three cases are considered in evaluating the performance of the proposed relative localization filters. Case 1 considers a low velocity permanent trajectory, Case 2 considers a medium velocity discrete non-permanent trajectory, and Case 3 considers a continuous non-permanent trajectory with high velocities.

Case 2 was used to analyze the filter's response, in which the target platform switches over eight permanent trajectories to follow a figure of eight. The relative positioning sensor was enabled for this experiment while the velocities were estimated

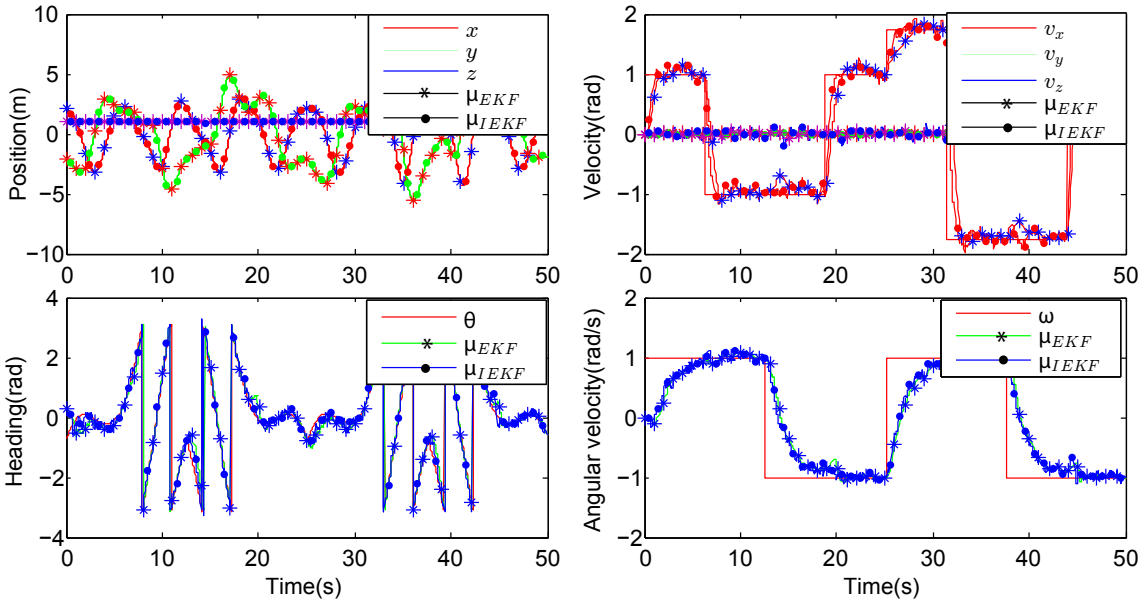

Figure 4.9: State estimation achieved by EKF and the IEKF for case 2

by the filter. As required by system observability conditions the transverse velocity was constrained to zero. The vector quantities were transformed to zero-roll-pitch frames of references as required by the 2.5D filter implementations.

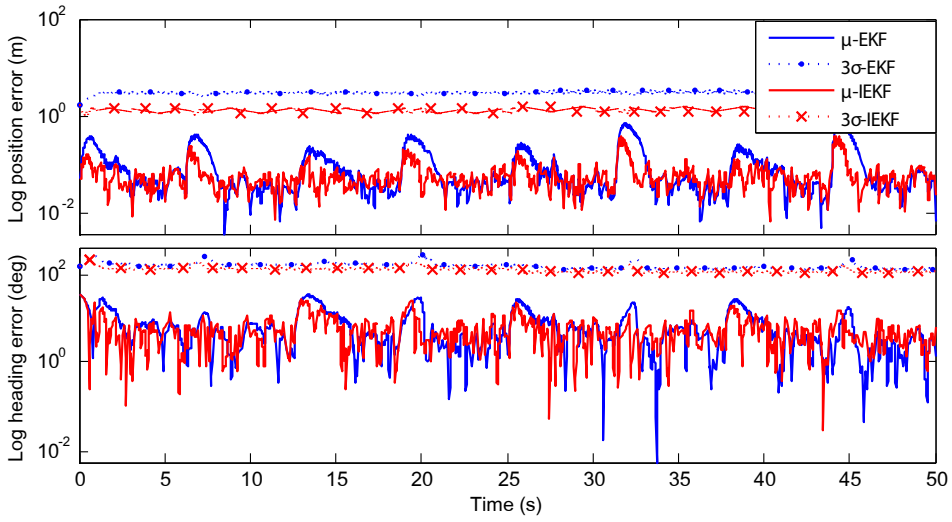

Figure 4.10: State estimation accuracy achieved by EKF and the IEKF for case 2

Figures 4.9 and 4.10 illustrate the performance of the state estimation and esti-

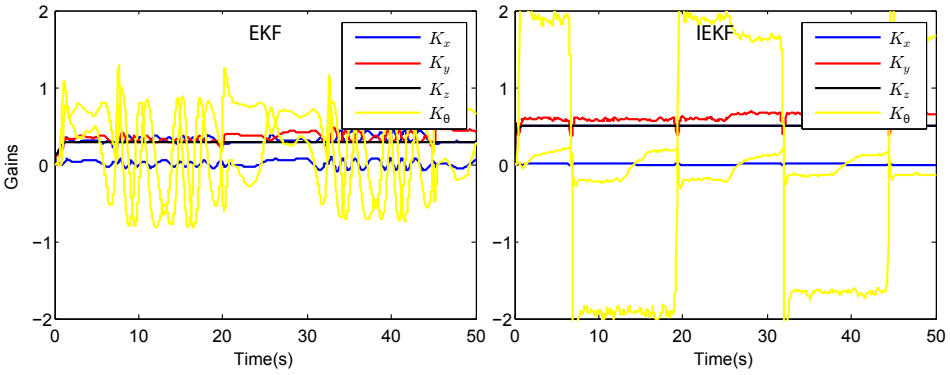

Figure 4.11: Gain adaptation of the EKF and the IEKF for case 2

mation error propagation of the IEKF for this case. Figure 4.11 illustrates the gain propagation which exhibits the characteristic steady state gain stabilization behaviour expected for IEKFs. Figure 4.12 illustrates the performance comparison of the EKF and the IEKF for relative localization for all three cases. The results validate the ability of the IEKF to achieve comparable performance to the EKF while estimating the unknown velocities.

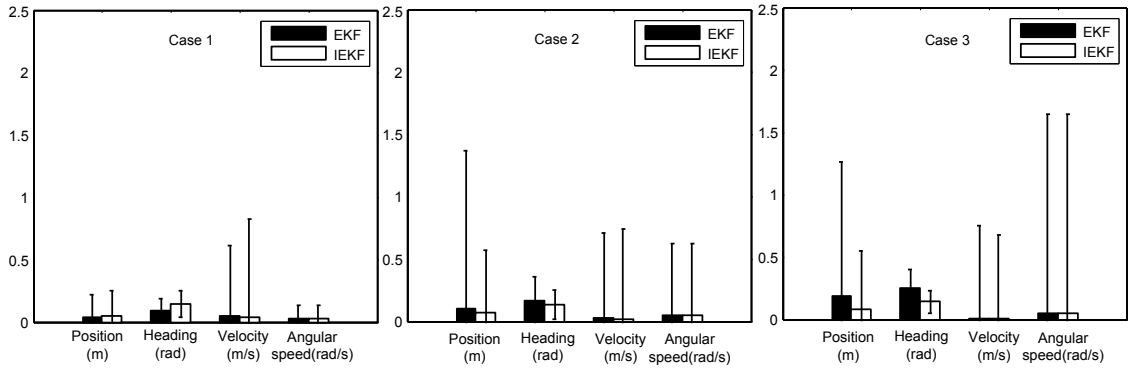

Figure 4.12: Summary of performance of the EKF vs the IEKF for all three cases

4.4.2 Performance of the steady state IEKF for relative localization

Case 2 was used as a scenario to validate the steady state IEKF designs. For the steady state IEKF (ssIEKF) it was assumed that the velocities which correspond to a sensor network are available through dedicated fast communicating channels. The ssIEKF was implemented using a discrete time single step EKF form [94]. This form produces identical steady state gains corresponding to the gain solution of the discrete time algebraic Riccati equation for the problem. The parameters of the gain matrix were estimated using the globally stable gain matrix proposal given in the previous section. These were found to be $\mathbf{a}_\alpha = [0.135\ 25.44\ 0.092\ 7.888\ 0.114]$ with $R^2 = 0.7867$. Figure 4.13 illustrates the tracking performance of this steady state form which is comparable to EKF and IEKF implementations to the problem. Figure 4.14 illustrates the values of the parameterized gain matrix for the steady state forms with both a_α and $[a_\alpha, a_\beta]$. The gain matrix with extra parameters closely compares to the steady state gains produced by the IEKF.

The error comparisons for all cases are presented in Figure 4.15. The ssIEKF was capable of successfully handling all different cases which correspond to different operating conditions. It was identified that the extra parameters did not significantly effect the estimation accuracy for the operating velocities considered in these simulations; thus, can be omitted depending on the application. The results validate the proposed ssIEKF design for relative localization and the tuning method which allows to achieve comparable steady state performance over a wide range of system configurations.

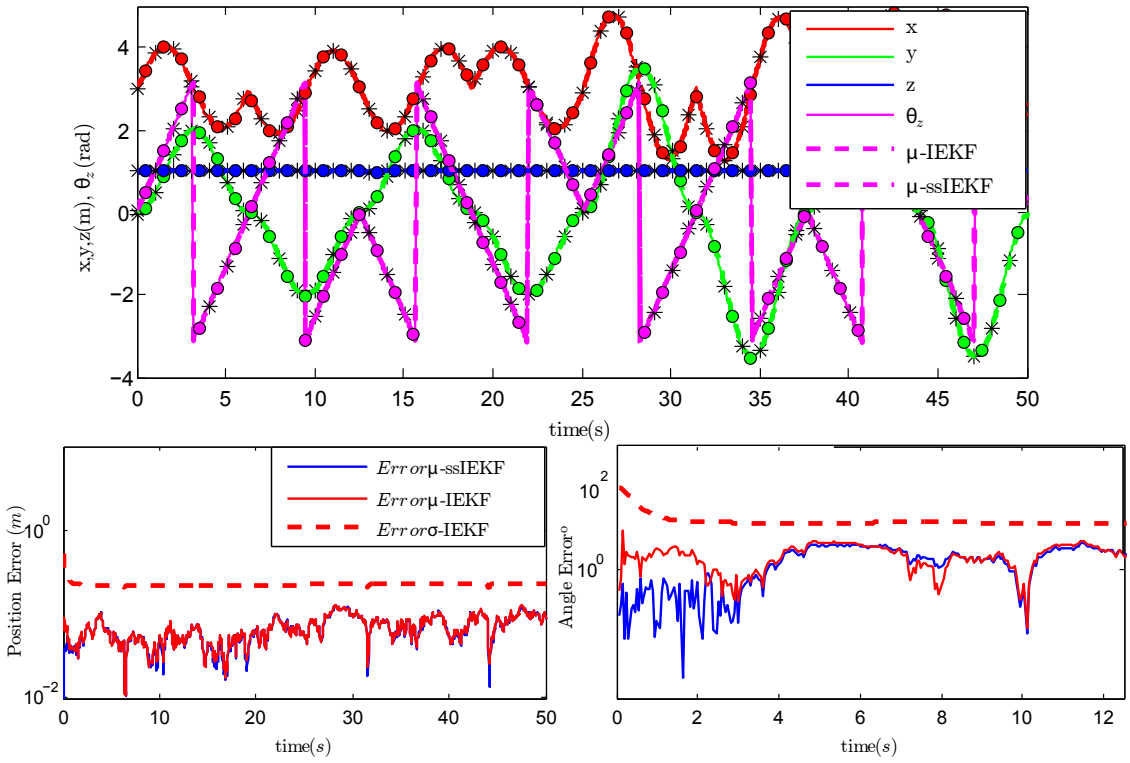

Figure 4.13: Position and heading estimation for case 2 using the IEKF and the ssIEKF

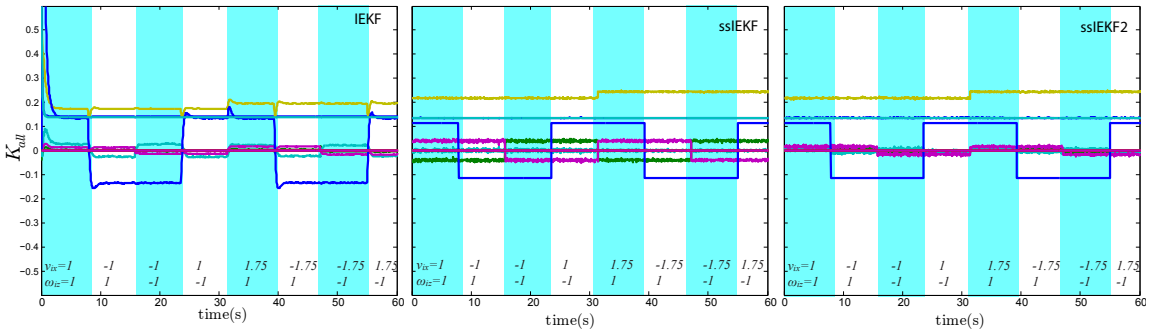

Figure 4.14: Gain evolution of the IEKF, steady state IEKF, and steady state IEKF with additional parameters, for Case 2

4.4.3 Performance of the RINCF

The following three trajectories are used for numerical evaluation of the proposed RINCF. The trajectories are randomly selected to evaluate the performance of the filter along with its tuning procedure for low, medium, and high angular velocity

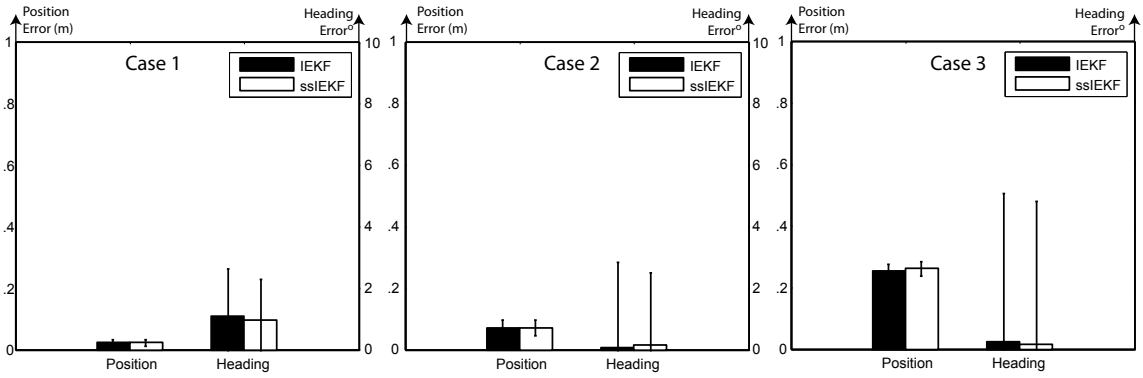

Figure 4.15: Summary of estimation errors for all 3 cases

trajectories.

Case 1	*Case* 2	*Case* 3
$\omega_x = \pi/3\sin(2\pi 0.7t + \pi/3)$	$\omega_x = \pi\sin(2\pi 0.7t)$	$\omega_x = 5\pi/3\sin(2\pi.07t + \pi/3)$
$\omega_y = \pi/3\sin(2\pi 0.2t + \pi)$	$\omega_y = \pi\sin(2\pi.02t + \pi)$	$\omega_y = 5\pi/3\sin(2\pi.02t + \pi)$
$\omega_z = \pi/3\sin(2\pi 0.4t)$	$\omega_z = \pi\sin(2\pi.04t + \pi/3)$	$\omega_z = 5\pi/3\sin(2\pi.04t)$

The system noise parameters were taken as $Q = 0.1\mathbf{I}_6$, and $R = diag(0.3\mathbf{I}_6, 0.5\mathbf{I}_6)$. The proposed RINCF was implemented and the parameters were found using 2 DARE runs in Matlab with ω_{max} taken as 5. The resulting tuning parameters were $(a_1,\ a_2,\ b_2,\ b_3,\ c_1,\ c_2,\ d_2,\ d_3) = (0.3326,\ 0.2517,\ 0.1511,\ 0.2630,\ 0.5666,\ 0.4412,\ 0.2648,\ 0.4332)e^{-3}$ and $(p_1,\ p_2) = (6.6430,\ 3.9873)e^{-5}$ which were used in all simulations presented. Figure 4.16 illustrates the estimation of roll, pitch, and yaw for *Case* 1. RINCF is capable of good convergence and tracking of the attitude using the proposed tuning approach which produces steady state optimal gains.

The results of the RINCF were compared against all other attitude estimators introduced in this text for *Case* 1, which corresponds to typical operating velocities of aerial platforms. Figure 4.17 illustrates the mean and standard deviation of the estimation error produced by the filters after 2.5 seconds. The filter denoted as WAB is

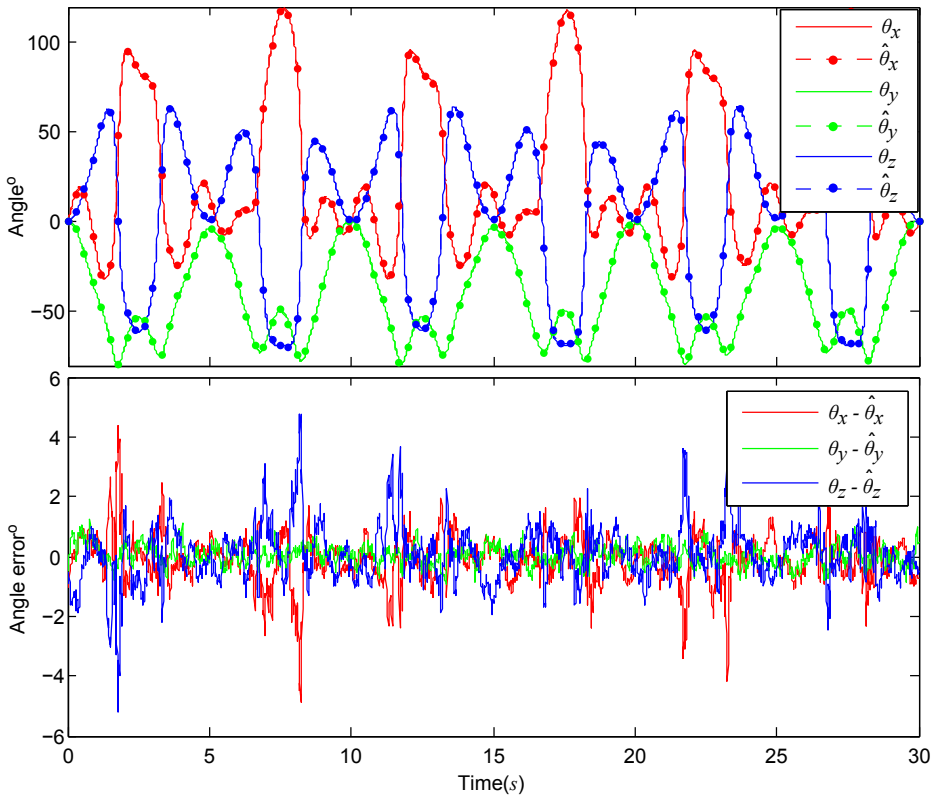

Figure 4.16: The simulated trajectory of the platform and the estimation accuracy provided by the RINCF for *Case* 1

the solution achieved by solving the Wahba's problem using singular value decomposition [95]. This denotes the attitude solution achievable using solely an accelerometer and a magnetometer; thus corresponds to the worst case performance expected from the attitude filters. RINCF1 and RINCF2 denotes the one with and without modifying terms (p_1, p_2) respectively. The RINCFs provide as good comparable results as all other estimators considered in this Chapter. Out of the filters presented in Figure 4.17, the NCF and the RINCFs are the only deterministic implementations applicable in low cost domains. The RINCF dominates as the only deterministic filter with system noise based gain tuning capability.

Figure 4.18 illustrates a comparison of the RIEKF* and the proposed RINCF for the three cases. It is evident that the RINCF achieves comparable performance

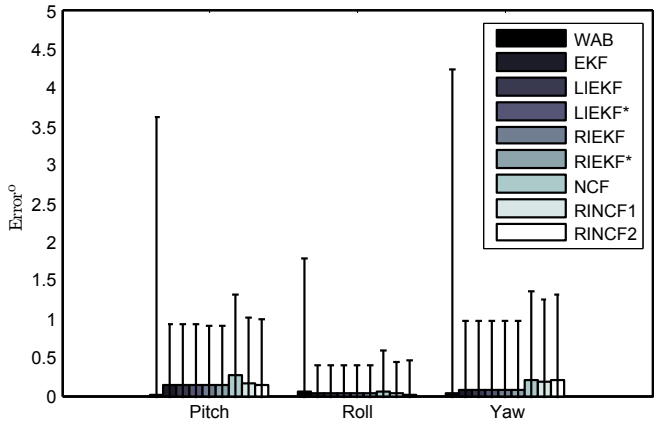

Figure 4.17: Comparative performance of the RINCF for *Case* 1

as the RIEKF* after convergence with increasing angular rates. The improvements introduced by the modifying terms are only significant at higher angular velocities (*Case* 3), thus can be neglected depending on the application. The results validate the proposed RINCF design for attitude reference and the proposed tuning method which allows to achieve comparable steady state performance over a wide range of system configurations and trajectories.

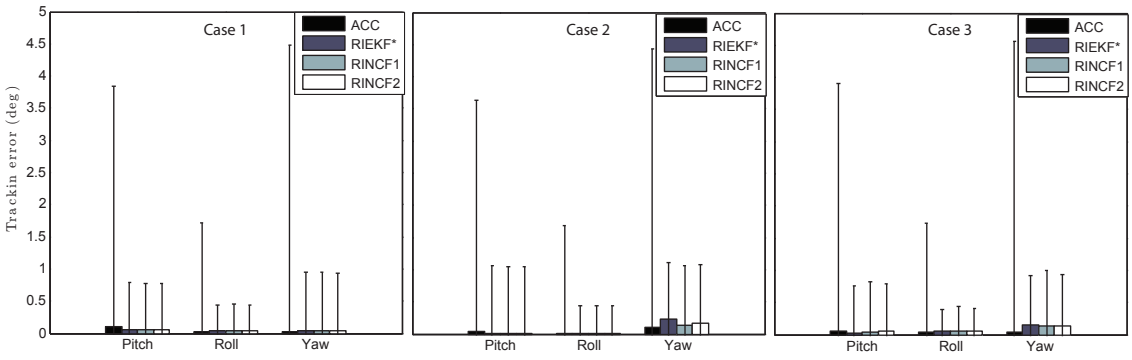

Figure 4.18: Comparative performance of the RINCF for all cases

4.4.4 Experimental validation of the filters

The experimental validation of the RINCF was performed using an ARDrone 2.0 platform. The platform was programmed with custom firmware which records the raw

measurements from the onboard accelerometers, gyroscopes, and magnetic compass. Scale factors and bias values related to these sensors were identified. The identification of the hard iron distortion effects of the magnetometer is presented in Figure 4.19 along with the validation of the measurements by converting them back to a zero roll pitch frame of reference. These calibrated measurements were used to validate each type of filter.

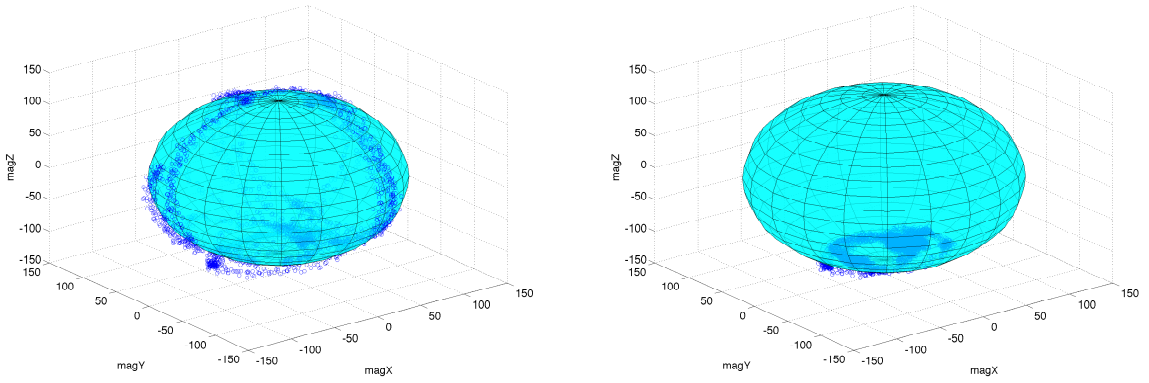

Figure 4.19: Calibration of the magnetic compass of the ARDrone 2.0

It is important to note that the magnetic heading is highly biased depending on the operating location of the drone. These errors were minimized by calibrating the compass to a particular test location. This is the case even when the drone's yaw is to be controlled in a closed loop using the factory firmware. In this case the factory software performs a 360^0 rotating data capture from the magnetic compass and identifies the hard iron distortion parameters in order to operate in the particular environment. However, these errors are not expected to affect the relative localization filters since the relative localization filters do not rely on the heading estimates of a compass due to the unknown biases that affect the measurements.

Figure 4.20 illustrates the performance of an EKF for measurements captured by the drone. Since a generic EKF with an additive noise assumption was used, the results exhibit poor estimation capability. This is mainly due to the linearized

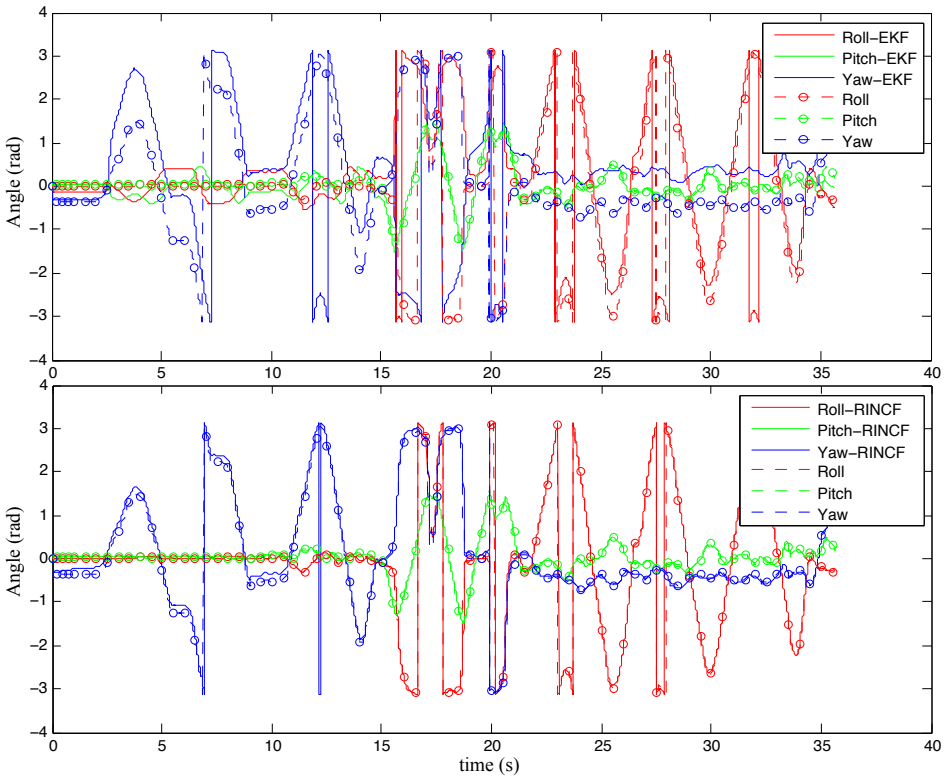

Figure 4.20: Attitude heading estimate of the EKF and the RINCF

formulation of the filter and the biases of the magnetic sensors which ultimately affect roll and pitch estimates due to coupling. In contrast the RINCF estimates (Figure 4.20) were found to perform better due to the selective updating capability of the filter, where the magnetic compass is forced only to update the yaw estimates and the accelerometers are forced to update only the roll and pitch estimates. This is possible due to the right invariant formulation of the filter which carries the error states of the system defined with respect to the filters' navigation frame of reference. I.e. the error states directly correspond to the errors in roll, pitch, and yaw. The following equation reports the gain values estimated using the noise parameters related to the sensors. In order to force the desired selective updating by the sensors, one simply requires to set the corresponding blocks of the gain matrix K_{RINCF} to zeros, which are highlighted in bold. All other values are calculated using the discrete algebraic

Ricatti solve function of Matlab. It was not necessary to introduce the additional p_1 and p_2 terms in calculating the gain matrix.

$$K_{RINCF} = 10^{-2} \begin{pmatrix} 0.0229 & 0 & 0 & \mathbf{0} & \mathbf{0} & \mathbf{0} \\ 0 & 0.0228 & 0 & \mathbf{0} & \mathbf{0} & \mathbf{0} \\ \mathbf{0} & \mathbf{0} & \mathbf{0} & -0.8837 & 0.5025 & 0.4929 \\ -0.0202 & 0 & 0 & \mathbf{0} & \mathbf{0} & \mathbf{0} \\ 0 & -0.0201 & 0 & \mathbf{0} & \mathbf{0} & \mathbf{0} \\ \mathbf{0} & \mathbf{0} & \mathbf{0} & 0.1741 & -0.0990 & -0.0971 \end{pmatrix}$$

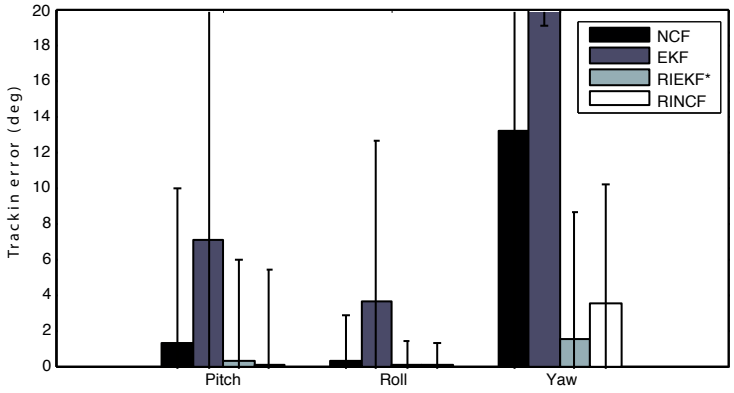

Figure 4.21: Attitude heading estimate of the different AHRS for the experimental data

Results related to an EKF, NCF, RIEKF, and an RINCF are presented in Figure 4.21. Only the RIEKF and RINCF allowed the convenience of incorporating the capability discussed above, where selective updating of estimates is achieved. The EKF and the NCF only allowed to manipulate the confidence between the accelerometer and the compass and did not allow the flexibility of forcing selective updating of states, which is a valuable capability in practical applications. Therefore RINCF constitutes an excellent innovative approach for the attitude filtering problem which

has the added capability of tuning the filter using an intuitive approach which is based on the system noise parameters, and the capability of deploying on devices with low computational demand for attitude and heading estimation.

4.5 Conclusion

This chapter presented three nonlinear filter designs relevant to relative localization. These include 1) a design of an IEKF for relative localization with unknown velocity estimation capability, 2) a steady state IEKF for relative localization which requires known platform velocities, and 3) a steady state IEKF for attitude estimation termed the RINCF. A novel gain tuning procedure was proposed with parameterized gain functions for low cost optimal implementation of the filters. The formulation is geometrically sound and enables deployment with favourable computational demand and a comparable performance to an EKF. The performance of these filters was evaluated using both numerical and experimental studies. The IEKF design for relative localization and the RINCF design for attitude estimation service the relative localization and attitude filtering modules of the proposed HNF. The steady state IEKF for relative localization is intended primarily for those applications where velocity communication between sensor nodes is established using reliable communication channels. What follows is a discussion of limitations and future work related to the three filter designs proposed in this thesis.

The IEKF for relative localization

It is important to note the following key limitations of the IEKF design. First, the filter has a limitation of not translating well to polar parameterizations and to associated range only and bearing only localization problems. This is due to the difficulty of identifying the symmetries when a polar form is used. However, cartesian

parametrization of a sensor model is a good approximation of the relative position sensing technologies used by robots. Second, the filter is a 2.5D design which is suited in applications where low roll and pitch dynamics can be assumed. A full SE(3) formulation as presented in the appendix would complement those applications where high velocity maneuvers are expected. Third, the presented IEKF design augments the noise parameters of the system by introducing mappings in order to force symmetry of the stochastic system. This would be inaccurate in some applications where the noise mechanisms are well established and known to follow a process model. This drawback can be surpassed by keeping the noise functions of the systems unchanged in such applications. The IEKF design process allows this flexibility in its formulation.

The ssIEKF for relative localization

The ssIEKF faces the following additional drawbacks over the ones discussed above. First, the filter in its current state is only applicable under known velocity conditions and assumes that the velocity measurements of the target platform are communicated for filtering purposes. Therefore, in practice the method is ideally suited for low update rates which support the bandwidth limitations of the available communication channels. Second, the filter does not posses global convergence guarantees under non-permanent trajectories. The filter guarantees local convergence about any trajectory and the filter produced desirable performance for non-permanent trajectories in experiments. However, further analysis and exhaustive experimentation is required to validate global convergence for non-permanent trajectories in order to improve robustness of the filter. Future work will nvestigate the steady state form for the unknown velocity cases with a detailed experimental validation of its stability under non-permanent trajectories.

The RINCF

The RINCF in its current form faces the following limitations. First, the RINCF

does not carry convergence guarantees for the additional p_1 and p_2 terms which are used to mimic optimal gains at higher angular velocity conditions. However, in typical applications as presented in experiments, the fixed gain form without the p_1 and p_2 terms constitutes a desirable solution with local convergence guarantees about any trajectory. For higher angular velocity excitations, it is desirable to establish theoretical guarantees regarding the extra p_1 and p_2 terms introduced to the gain matrix. Second, the RINCF formulation did not consider dynamics of the attaching platforms. Recent work reported in [96, 97], has demonstrated the ability to use the dynamic model of MAVs to achieve better attitude filtering and velocity estimation. However, this capability was not exploited in this work since the formulation targets a general 6DOF platform without considering any platform specific dynamic constraints.

Future work related to the RINCF design expects to investigate convergence guarantees for optimal gains at higher angular velocities. Additionally, filter developments where the dynamics of the platform and couplings with pose filtering modules present important research directions desirable for low cost application of attitude estimators.

Chapter 5

Relative Localization: A Distributed Approach

The previous chapter designed the necessary relative localization filters which allowed a single robot to find the relative poses of its neighbours. However, in a multi robot network many robots perform relative measurements within the team with respect to their corresponding body fixed frames. In order to address this scenario a multi-robot relative localization method should be in place. The main reported solutions for the problem of multi-robot relative localization require synchronous communication between robots, where the network should communicate each time a relative measurement is logged in the team. This chapter[1] proposes a localization method which can accommodate communication at a low predefined rate rather than forcing communication each time a measurement is logged. This is achieved without explicitly accumulating past measurements locally at each robot. This capability is necessary to

[1] This chapter is based on the following publications of the author:

* O. De Silva, G. K. I. Mann, and R. G. Gosine, "Efficient Distributed Multi-Robot Localization : A Target Tracking Inspired Design," in *IEEE International Conference on Robotics and Automation (ICRA)*, 2015, (Accepted).

support an increasing number of robots in a team, when operating within finite communication and computation resources. The design includes a novel fusion strategy, a consistent estimation method, and a state based initialization method, embedded in a distributed target tracking framework. The design is efficient in terms of computation demand, since it scales linearly with the number of robots. Additionally, the design is efficient in terms of communication demand, since communication is neither required to be synchronized with sensor readings, nor constrained to be in a specific topology. The proposed approach is validated for its initialization capability, consistency of estimates, and robustness of performance, through several numerical simulations and using a publicly available multi-robot data set.

5.1 Introduction

The traditional solution to the problem of relative localization is the centralized Extended Kalman Filter [39]. This is different from the local version of the EKF and its nonlinear derivation, the IEKF used for relative localization in Chapters 3,4. The centralized EKF for multi robot localization stacks all states of each robot in the team together to form a single state vector. At each time step all measurements are communicated to the centralized EKF to perform the Kalman update. The drawbacks of the EKF with regard to the nonlinearity of the localization problem were considered in detail in the previous chapter. In a multi-robot analysis, however, the more pressing concern is efficient distributed implementation of the filter in the robot network. Pioneering work which proposes centralized equivalent strategies to efficiently distribute the filtering operation among a set of agents are demonstrated in [39][57]. However, these centralized and equivalent forms have two main drawbacks that make it difficult for one to use them in practical situations.

The first main drawback is that the centralized equivalent approaches require ideal communication where each member is required to communicate its information within the team at each occurrence of a measurement in the network. As the number of robots in the team increases, this solution soon becomes less practical. To overcome this issue, one strategy is to intermittently communicate packets of accumulated raw data and incorporate this information to the filter in retrospect. The authors in [57] propose a past sensor data management method to store the optimal amount of data which allows the achievement of a centralized equivalent estimation at a fusion center after communication. Work in [48] proposes the delayed state information form to accumulate past data. This allows to exploit the additive property of the extended information filters to fuse delayed data in a convenient manner. However, explicitly accumulating past data has unbounded memory demand since the strategy assumes that the information will soon be incorporated into a state estimate via communication. Conversely, work presented in [98] and methods proposed in distributed tracking approaches [49] accumulate past data in the form of recursive states rather than explicitly maintaining a set of past raw measurements for each time step.

A second drawback in the centralized method is that the computation cost of the approach scales quadratically with the number of robots. This is because it considers the full cross correlation structure among all the robots to perform a centralized equivalent update. In order to address this problem, it is necessary to use approximate state correction schemes instead of maintaining the full cross correlation structure of the robot group. In naive implementations, the estimation is performed assuming that there is zero cross correlation between the states. This leads to overconfidence of the localization estimates in cases where the measurement model is coupled across multiple states. More intuitive implementations employ information matrix based state de-correlation schemes as seen in [58], and Covariance Intersection (**CI**) based

schemes as seen in [99], for approximate consistent fusion of the robots' states.

In order to solve both the problems discussed above, this work identifies that it is essential to implement a combination of an approximate state fusion scheme, and a past data accumulation scheme in the form of recursive states. This is inspired by the well established field of distributed multi-sensor multi-target tracking [49]. The underlying principles of target tracking have been well exploited in many robotic applications, such as simultaneous localization, mapping and moving object tracking [100], single leader multi-robot localization [33], and multi-object tracking in the RoboCup standard platform league [101]. Unlike these studies, the proposed work exploits methods in distributed target tracking in order to specifically address limitations of communication and computation demand encountered in the multi-robot relative localization problem.

The proposed approach results in a distributed multi-robot localization framework which has no constraints with regard to timing or the topology of communication among the robots. Additionally, the approach produces consistent estimates of the team formation with a computational complexity that scales linearly with the number of robots. Three main contributions originating from this design can be identified.

- A novel distributed fusion strategy with a complimentary set of statistics (states), which allows to perform communication between robots at a low predefined rate. This is a significant improvement over the conventional methods which communicate each time a measurement is logged in the network.

- A measurement registration method and a CI based fusion scheme, which incorporates communicated data to the current estimate of a robot in a consistent manner irrespective of the communication topology. This is an improvement over the conventional state de-correlation based fusion schemes.

- A dynamic global registration scheme which utilizes communicated states from other robots to initialize estimates. This is a necessary modification over the raw measurement based global registration schemes [32], in order to achieve robust initialization in the proposed distributed framework.

It is important to discuss the applicability of the nonlinear filtering methods proposed in the previous chapter for application in the proposed distributed relative localization framework. The right invariant nonlinear complimentary filter is applied for attitude estimation of aerial platforms to perform 2.5D simplification of the relative localization problem. I.e, transform all vector quantities to the zero roll pitch frame of reference. The IEKF designed for relative localization is applied in place of a Kalman filter in the DRL method which produces almost similar performance in the context of stochastic filtering. The steady state IEKF is not applicable in the proposed DRL since this is a deterministic filter which does not propagate the covariances required for application of the method.

5.2 Preliminaries

The notations introduced in chapter 3 are modified to support multi robot applications and filter designs as follows. In a multi robot scenario there are N number of robots in a team identified as $\{\mathcal{R}_1, ... \mathcal{R}_i \ , ...\mathcal{R}_N\}$. The body fixed frame of robot $\mathcal{R}_i$ is denoted by $\{I\}$, and the fixed inertial navigation frame of robot $\mathcal{R}_i$ is denoted as $\{I*\}$, i.e., the fixed frame attached to the ground at the starting location of each robot. Each robot takes measurements of its own linear velocities $\mathbf{v}_k^i$, and angular velocities $\boldsymbol{\omega}_k^i$. The single superscript i is used to denote that the vector is an absolute quantity (measured relative to an inertial navigation frame $\{I*\}$) and it is expressed in frame $\{I\}$. The relative measurements are denoted by $\mathbf{z}_k^{i,j}$ where double superscripts i, j are

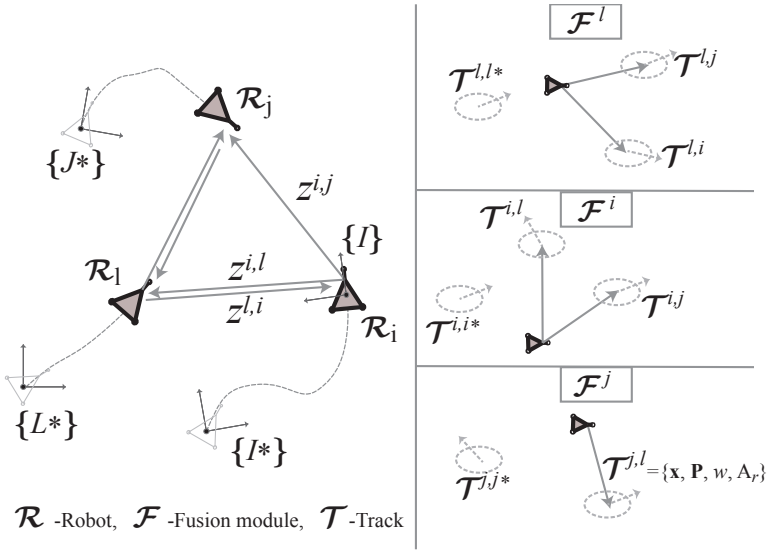

Figure 5.1: The multi-robot system and a snapshot of individual fusers proposed in this work implemented on each robot

used to denote that the vector of frame $\{J\}$ is measured relative to frame $\{I\}$, and it is expressed in frame $\{I\}$. The subscript k denotes the time index and is used only where necessary.

Assume that robot $\mathcal{R}_l$ performs a relative localization task. In this case, robot $\mathcal{R}_l$ is the "local robot" and all neighbours $\{\mathcal{R}_1, ... \mathcal{R}_i \ , ...\mathcal{R}_N\}\backslash\{\mathcal{R}_l\}$ are "target robots". The relative localization filter attempts to establish accurate pose estimates of target robots with respect to a local robot $\mathcal{R}_l$, as illustrated in Figure 5.1. Recall the 2.5D robot model introduced in Chapter 3. The system model of an arbitrary robot $\mathcal{R}_i$ relative to a reference frame $\{L\}$ can be expressed as follows.

$$\begin{aligned} \dot{\mathbf{x}}^{l,i} &= f_i(\mathbf{x}^{l,i}, \mathbf{u}^l, \mathbf{u}^i, \mathbf{w}) \\ \begin{bmatrix} \dot{\mathbf{p}}^{l,i} \\ \dot{\theta}^{l,i} \end{bmatrix} &= \begin{bmatrix} \mathbf{R}_\theta^{l,i} \ (\mathbf{v}^i + \mathbf{w}_{vi}) - (\mathbf{v}^l + \mathbf{w}_{vl}) - (\boldsymbol{\omega}^l + \mathbf{w}_{\omega l}) \times \mathbf{p}^{l,i} \\ (\omega^i + \mathbf{w}_{\omega i}) - (\omega^l + \mathbf{w}_{\omega l}) \end{bmatrix} \end{aligned} \tag{5.1}$$

The velocities are taken as inputs here to introduce the centralized multi robot filter. This assumption will be relaxed in the distributed design explained in Section 5.3.

The vector quantities $\mathbf{u}^i = (\mathbf{v}^{i\ \mathsf{T}},\ \omega^i)^\mathsf{T}$ and $\mathbf{u}^l = (\mathbf{v}^{l\ \mathsf{T}},\ \omega^l)^\mathsf{T}$ denote the system inputs, and $\mathbf{w} = (\mathbf{w}_{vl}^\mathsf{T},\ \mathbf{w}_{\omega l},\ \mathbf{w}_{vi}^\mathsf{T},\ \mathbf{w}_{\omega i})^\mathsf{T}$ denotes the process noise which is assumed to be drawn from a Gaussian distribution with covariance $Q_i = diag(\boldsymbol{\sigma}_{vl},\ \sigma_{\omega l},\ \boldsymbol{\sigma}_{vi},\ \sigma_{\omega i})^2$. This general expression given by (5.1) is valid for all frames $\{I\}$. Therefore, when the superscript $i = l*$, the resulting variables $\mathbf{v}^{l*},\ \mathbf{w}_{vl*},\ \omega^{l*},\ \mathbf{w}_{\omega l*}$ of the expression are set to $\mathbf{0}$.

The measurement model of the relative position measurement $\mathbf{z}^{i,j}$ is expressed by

$$\begin{aligned} \mathbf{y}^{i,j} &= h_{ij}(\mathbf{x}^{l,i}, \mathbf{x}^{l,j}, \boldsymbol{\nu}) \\ \mathbf{y}_p^{i,j} &= \mathbf{R}_\theta^{i,l}(\mathbf{p}^{l,j} - \mathbf{p}^{l,i}) \quad + \boldsymbol{\nu}_p \end{aligned} \tag{5.2}$$

where $\boldsymbol{\nu}$ denotes the measurement noise, which is assumed to be drawn from a zero mean Gaussian distribution with covariance $\acute{R} = diag(\sigma_p)^2$. This general expression is valid for all frames $\{I\}$ and $\{J\}$. Therefore, when the superscripts i or $j = l$, the resulting variables $\mathbf{p}^{l,l}$ and $\mathbf{R}_\theta^{l,l}$ in the expression (5.2) are $\mathbf{0}$ and $\mathbf{I}$ respectively. The measurements are assumed to be acquired with a detection probability of P_D and they are assumed to be corrupted by clutter, uniformly distributed in measurement space with clutter rate following a Poisson clutter model of spacial density λ.

In order to perform a centralized localization task relative to robot $\mathcal{R}_l$, the states of all robots in the network are stacked to form a single state vector $\mathbf{x}_k = (\mathbf{x}_k^{l,l*\mathsf{T}},\ \mathbf{x}_k^{l,1\mathsf{T}},\ \mathbf{x}_k^{l,2\mathsf{T}} \ldots\ \mathbf{x}_k^{l,i\mathsf{T}}, \ldots\ \mathbf{x}_k^{l,N\mathsf{T}})^\mathsf{T}$. This results in a state covariance matrix P with dimension $N \times N$. Correspondingly, the system model Jacobians F_i, process noise Jacobians G_i, and process noise covariances Q_i are also stacked to implement a centralized EKF for the problem.

The noiseless version of the system model given by (5.1) can be used to perform a mean prediction of the joint state. The covariance prediction of the joint state can

be performed using the following equations.

$$\begin{aligned} F &= \text{blkdiag}(F_{l*}, ...F_i, ...F_N) \quad & F_i &= \tfrac{\partial f_i}{\partial \mathbf{x}^{l,i}} \\ G &= \text{blkdiag}(G_{l*}, ...G_i, ...G_N) \quad & G_i &= [\tfrac{\partial f_i}{\partial \mathbf{w}_{ul}} \ \tfrac{\partial \mathbf{f}_i}{\partial \mathbf{w}_{ui}}] \\ Q &= \text{blkdiag}(Q_{l*}, ...Q_i, ...Q_N) \quad & \dot{P} &= FPF^{\mathsf{T}} + GQG^{\mathsf{T}} \end{aligned} \tag{5.3}$$

To perform the Kalman correction step the noiseless version of the measurement model given by (5.2) is used for measurement prediction. The Kalman correction step for each measurement $\mathbf{z}^{i,j}$ is given below.

$$\begin{aligned} H_{ij} &= \tfrac{\partial h_{ij}}{\partial \mathbf{x}} \quad & R_{ij} &= \text{diag}(\boldsymbol{\sigma}_y) \\ S_{ij} &= H_{ij} P H_{ij}^{\mathsf{T}} + R_{ij} \quad & K &= P H_{ij}^{\mathsf{T}} S_{ij}^{-1} \\ \mathbf{x} &= \mathbf{x} + K(\mathbf{z}^{i,j} - \mathbf{y}^{i,j}) \quad & P &= (I - K H_{ij}) P \end{aligned} \tag{5.4}$$

The matrix P and associated computations scale quadratically with the increasing number of robots. It is therefore advantageous to improve computation cost for better scalability of the solution. The prediction step as described in equation (5.1) requires the communication of input velocities of the target platforms $\mathbf{v}^i$, $\omega^i \ \forall i \neq l, l*$ to the centralized filter. Additionally, the correction step requires communication of all measurements which do not originate from the local platform, i.e., $\mathbf{z}^{i,j} \ \forall i \neq l, l*$. Such synchronous simultaneous communication between all robots cannot be supported in a network due to practical bandwidth limitations and channel limitations of communication mediums. Therefore, it is necessary to design a distributed approach which possesses better scalability in terms of computation, and which enables ad-hoc asynchronous communication to support realistic communication mediums.

5.3 Proposed Approach

The proposed approach assumes the following simplifications:

- The relative measurement modules measure the neighbouring robots with known data correspondence. This is valid for a variety of vision based, acoustic based, and IR based relative measurement modules including the measurement solution proposed in Chapter 2. Handling data correspondence using the proposed framework is addressed separately in Chapter 6.

- The communication cost between a pair of robots for a given payload is assumed constant. i.e., no routing of communication is considered.

Figure 5.1 illustrates a summarized version of the proposed distributed localization framework. A distributed fusing module $\mathcal{F}^i$, also termed a "Fuser", is implemented on each robot $\mathcal{R}_i$. The term "Track" is used to refer to an estimate of a robot (or more generally an estimate of the coordinate frame of a robot). An indexed track is denoted as $\mathcal{T}_m^l$, where l is used to denote the reference frame of the fuser which maintains the track and m is used as an index to uniquely identify different tracks. A track consists of a robot identifier $\mathcal{A}_r$, an estimate of the state vector of the corresponding robot $\mathbf{x}$, its covariance P, and a weight w. i.e., $\mathcal{F}^l \ni \mathcal{T}_m^l = \{\mathbf{x},\ P,\ w,\ \mathcal{A}_r\}$.

The robot identifier $\mathcal{A}_r$ is used to maintain the track-to-robot correspondence. A set of tracks which corresponds to the same robot provides a set of multiple estimates with Gaussian statistics. Existence of multiple solutions for the same robot that can be encountered in initialization and in unknown data correspondence scenarios will be explained in Chapter 6. Therefore, a subgroup of tracks corresponding to the same target robot is identified as a Gaussian mixture $Gm^{l,i} = \{\mathcal{T}_m^l : \mathcal{T}_m^l \ni \mathcal{A}_r = i\}$ with weights of the mixture components being w. The tracks are kept as decoupled states and necessary mechanisms are implemented in correction and fusion steps to main-

tain consistency of the estimates. Maintaining decoupled states allows the proposed approach to scale linearly with the number of robots.

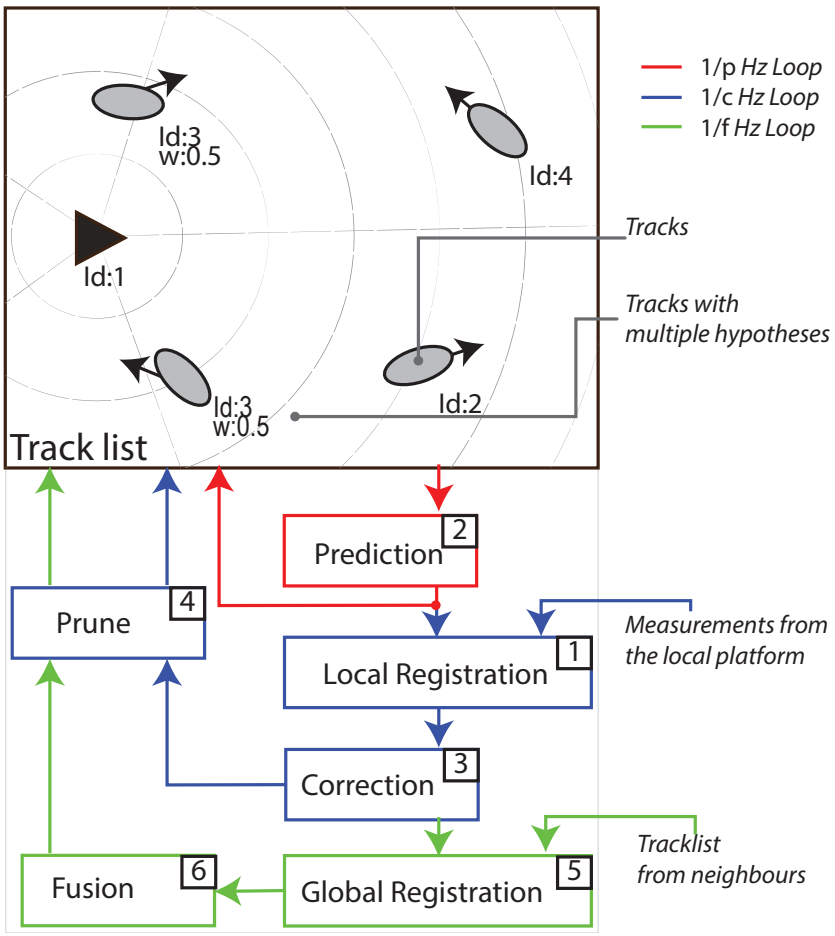

Figure 5.2: The proposed distributed localization framework. The prediction, correction and fusion operations are performed at different rates ($p < c < f$)

This work integrates an innovative state propagation scheme, a global registration scheme, and a consistent fusion scheme to the general distributed target tracking framework described in [58]. These non-trivial improvements are necessary to achieve a distributed multi-robot localization solution. These operations are performed by six different sub-modules as illustrated in Figure 5.2. In the following section, the functionality of each sub-module is discussed in detail in the order which they are enumerated in Figure 5.2.

5.3.1 Local Registration

The fuser $\mathcal{F}^l$ initializes a navigation frame at the location where the local robot initiates its mission. When $\mathcal{R}_l$ perceives another robot $\mathcal{R}_i$, it creates a new track corresponding to the identity of the measured robot with a weight of $P_B * \max(w \in Gm^{l,i})$. P_B is identified as the track birth probability which corresponds to the weight given to initialize the first track of $Gm^{l,i}$. Since the orientation of the perceived robot cannot be determined during initialization, the value for orientation is set randomly with a high value for initial covariance, to imitate a uniform distribution. This local initialization procedure is dynamic, where the registration routine constantly checks and initializes new tracks. The measurements that are not absorbed by any of the available tracks in the fuser for estimation are used to initialize new tracks.

5.3.2 Prediction

Following initialization, the tracks are propagated using the system model given by (5.5). The velocities of neighbouring robots are unknown until such time communication occurs. To support these unknown velocities, the system model is modified from the centralized version given in (5.1) to attain a constant velocity, turn rate model as given in (5.5).

$$\dot{\mathbf{x}}^{l,i} = \mathbf{f}_i(\mathbf{x}^{l,i}, \mathbf{u}, \boldsymbol{\epsilon})$$

$$\begin{bmatrix} \dot{\mathbf{p}}^{l,i} \\ \dot{\theta}^{l,i} \\ \dot{\mathbf{v}}^{i} \\ \dot{\omega}^{i} \end{bmatrix} = \begin{bmatrix} \mathbf{R}^{l,i}\ \mathbf{v}^{i} - \mathbf{v}^{l} - \boldsymbol{\omega}^{l} \times \mathbf{p}^{l,i} \\ \omega^{i} - \omega^{l} \\ 0 \\ 0 \end{bmatrix} + \begin{bmatrix} \boldsymbol{\epsilon}_{vl} + \boldsymbol{\epsilon}_{\omega l} \times \mathbf{p}^{l,i} \\ \epsilon_{\omega l} \\ \boldsymbol{\epsilon}_{\dot{\mathbf{v}}i} \\ \epsilon_{\dot{\omega}i} \end{bmatrix} \tag{5.5}$$

The state of each target robot is selected as $\mathbf{x}^{l,i} = (\mathbf{p}^{l,i\ \mathrm{T}},\ \theta^{l,i},\ \mathbf{v}^{i\ \mathrm{T}},\ \omega^{i})^{\mathsf{T}}$. Addi-

tionally, each robot propagates an estimate of its local velocity using its corresponding navigation frame $\{L*\}$. The state of frame $\{L*\}$ is selected as $\mathbf{x}^{l,l*} = (\mathbf{p}^{l*,l\ \mathrm{T}},\ \theta^{l*,l},\ \mathbf{v}^{l\ \mathrm{T}},\ \omega^{l})^{\mathsf{T}}$. The state and covariance are propagated using Kalman prediction equations.

5.3.3 Correction

The local measurements logged by the robots are used to perform the Kalman update. The local measurements are the measurements made with respect to frame $\{L\}$, which is same as the filter's frame of reference. As a result, in this decoupled form there is no requirement for any coordinate transformation, which in turn does not develop any measurement to state correlation. This is not the case if a globally fixed coordinate frame is considered as the reference frame of the filter (for example $\{L*\}$). In such a scenario, relative measurements are correlated between multiple tracks, resulting in inconsistent Kalman updates if a decoupled form is used. In order to handle measurement outliers, the correction step is preceded by a measurement gating operation with a gate probability of P_G.

The weight of each track is updated during the update step using the following track management rules:

1. If the track was not associated with any measurement, the track weight is updated with the track survival probability.

$$w = w(1 - P_D P_G) \tag{5.6}$$

2. If the track was associated with a measurement, it's updated with the measure-

ment likelihood.

$$w = wP_D\mathcal{N}(\mathbf{z}^{i,j}|(\mathbf{z}^{i,j} - \mathbf{y}^{i,j}), (HPH^{\mathsf{T}} + \acute{R}))/\lambda \tag{5.7}$$

3. If a measurement was not associated with any track, the local registration module will initialize a track with the birth probability.

5.3.4 Pruning

The pruning step normalizes the Gaussian mixture $Gm^{l,i}$ corresponding to each robot. The tracks having weights below the track kill probability P_K are removed. The Mahalanobis distance between two tracks in a Gaussian mixture is used to combine estimates that are similar.

Up to this step the framework only considered the locally available measurements for the estimation process. The observability study of the problem presented in Chapter 3 verified that localization using only the locally available set of information is observable given that the robots move with non-zero velocities and the transverse velocities of the robots are constrained (known to be zero). Therefore, incorporating the communicated information is necessary in this framework in order to improve the accuracy of the estimate and more importantly to handle the unobservable cases such as: scenarios where all robots in the network are stationary; robots are moving with non-zero transverse platform velocities; and the filter has converged to the incorrect local solution out of the two possible global minima derived in Chapter 3.

5.3.5 Global Registration

The robots communicate the tracks between them in an asynchronous manner in this distributed framework. Due to observability limitations of the problem, it is

Algorithm 1: Global track registration

Data: Local track set $\mathcal{T}^l = \{\mathbf{x},\ P,\ w,\ \mathcal{A}_r\}$ of the local robot
Communicated track sets $\{\mathcal{T}^i,\ \dots\}$ of all robots $\mathcal{R}_i$ which communicated during the current time step
Result: $\tilde{\mathcal{T}}^l$ the initialized solutions for $\mathcal{T}^l$
$\tilde{\mathcal{T}}^l = \mathcal{T}^l$
if *any* $\mathbf{x} \in \tilde{\mathcal{T}}^l_m$ *is not initialized* **then**
1. Find $\mathcal{T}^i$ which matches $\mathcal{A}_r \in \tilde{\mathcal{T}}^l_m$
2. RANSAC Binary registration of $\tilde{\mathcal{T}}^l$ and $\mathcal{T}^i$
$S = \varnothing$
while *iteration* $<$ *maximum iterations* **do**
2.1 Sample 4 tracks $\mathcal{T}^l_{\mathrm{v}1},\ \mathcal{T}^l_{\mathrm{v}2},\ \mathcal{T}^i_{\mathrm{v}3},\ \mathcal{T}^i_{\mathrm{v}4}$

$$\begin{aligned} &s.t.\quad \mathrm{v}_1 \neq \mathrm{v}_2\ ,\ \mathrm{v}_3 \neq \mathrm{v}_4 \\ &\mathcal{T}^l_{\mathrm{v}1} \ni A_r = \mathcal{T}^i_{\mathrm{v}3} \ni A_r,\ \mathcal{T}^l_{\mathrm{v}2} \ni A_r = \mathcal{T}^i_{\mathrm{v}4} \ni A_r\ , \\ &||\mathcal{T}^l_{\mathrm{v}1} \ni \mathbf{p} - \mathcal{T}^l_{\mathrm{v}2} \ni \mathbf{p}|| = ||\mathcal{T}^i_{\mathrm{v}3} \ni \mathbf{p} - \mathcal{T}^i_{\mathrm{v}4} \ni \mathbf{p}|| \end{aligned}$$

2.2 Initialize $\tilde{\mathcal{T}}^l_m$ using the correspondences

$$\begin{aligned} &i.e.\ \mathcal{T}^l_{\mathrm{v}1} \ni \mathbf{p} := \mathbf{p}_{\mathrm{v}1},\ \mathcal{T}^l_{\mathrm{v}2} \ni \mathbf{p} := \mathbf{p}_{\mathrm{v}2},\ \mathcal{T}^i_{\mathrm{v}3} \ni \mathbf{p} := \mathbf{p}_{\mathrm{v}3}, \\ &\mathcal{T}^i_{\mathrm{v}4} \ni \mathbf{p} := \mathbf{p}_{\mathrm{v}4},\ \mathbf{p}_{\mathrm{v}12} = \mathbf{p}_{\mathrm{v}2} - \mathbf{p}_{\mathrm{v}1},\ \mathbf{p}_{\mathrm{v}34} = \mathbf{p}_{\mathrm{v}4} - \mathbf{p}_{\mathrm{v}3} \\ &\mathrm{S}\leftarrow \tilde{\theta} = \arctan 2(y_{\mathrm{v}12}, x_{\mathrm{v}12}) - \mathrm{ATan2}(y_{\mathrm{v}34}, x_{\mathrm{v}34}) \\ &\mathrm{S}\leftarrow \tilde{\mathbf{p}} = \mathbf{p}_{\mathrm{v}2} - \mathbf{R}_{\tilde{\theta}}\mathbf{p}_{\mathrm{v}4} \end{aligned}$$

3. Compute subset of independent solutions in S with sufficient inliers
4. Update $\tilde{\mathcal{T}}^l_m$ with solutions in S

possible that none of the orientation estimates in $\mathcal{T}^{l,i}$ will be properly estimated during the time period leading up to the communication of tracks. In order to perform initialization of these tracks, this thesis proposes a binary state registration algorithm. This algorithm is derived from multi robot registration schemes presented in [32]. Each communicated track set $\mathcal{T}^i$ is considered along with the local track set $\mathcal{T}^l$ for the binary state registration operation. The track set is augmented prior to implementing the algorithm by introducing the origin of the transformation frames. i.e., a track with states $\mathbf{x} = \mathbf{0}$ is added to $\mathcal{T}^l$ and $\mathcal{T}^i$ with $\mathcal{A}_r$ set to l, i for each track respectively.

The algorithm presented in Table 1 first determines whether any estimate $\mathcal{T}^{l,i}_m$ corresponding to the communicating robot $\mathcal{R}_i$ requires initialization. This is per-

formed by comparing the covariance of its orientation estimate and proceeding to initialization if it's above a threshold, which was selected as 0.003 rad^2. In cases where robot $\mathcal{R}_i$ requires initialization, a RANSAC based correspondence scheme is performed. Although the tracks of both local and communicating robots are of known correspondence, the RANSAC correspondence handling scheme is necessary since the track list may include multiple hypotheses for the location of a robot occurring due to outliers in measurements and multiple global solutions possible for the local filters. The RANSAC based correspondence scheme additionally allows addressing cases of unknown data correspondence under the proposed framework.

From each track set two matching track index pairs are selected. Then the two pairs of matching vectors are used to generate a closed form solution for the relative pose of the communicating robot. Next, an inlier count is performed following standard RANSAC steps. A solution is selected if there are more than two inliers. This solution generation procedure is carried out until a predefined maximum number of iterations is reached, or all number of possible putative correspondences are considered. Therefore, the algorithm remains bounded in computation and the initialization routine is re-attempted in future communications in case of failure. The fusion scheme only requires an adjustment of the mean of the orientation of tracks, which was originally set to a random value by the local registration routine. The global registration routine proposed here effectively achieves this task.

This algorithm is first proposed in [32] to handle unknown correspondence using raw measurement communication. The modified approach proposed here is an efficient distributed implementation of the binary registration algorithm which is based on system states rather than raw measurements. This approach significantly reduced the communication demand.

5.3.6 Fusion

The state fusion scheme incorporates the communicated information to the current track set. The overall fusion procedure is performed as follows.

First, the communicated track set is transformed to the reference frame of the local robot. This process is also termed as *sensor registration*. The sensor registration routine can be summarized by the following equations:

$$\mathbf{z}_{eq} = \mathcal{T}^{l,i} \oplus \mathcal{T}^{i,j}$$

Navigation frame fusion :

$$\begin{aligned} &\text{if } j = i* \quad H = [\mathbf{0}_4\ I_4] \quad && \mathbf{z}_{eq} = H\mathbf{x}^{i,j} \\ &\qquad\qquad G = H && \acute{R}_{eq} = GP^{i,j}G^{\mathsf{T}} \end{aligned}$$

Mutual frame fusion :

$$\begin{aligned} &\text{if } j = l \quad H = [I_4\ \mathbf{0}_4] \quad && \mathbf{z}_{eq} = \ominus H\mathbf{x}^{i,j} \\ &\qquad\qquad G = \partial\mathbf{z}_{eq}/\partial\tilde{\mathbf{x}}^{i,l} && \acute{R}_{eq} = GP^{i,j}G^{\mathsf{T}} \end{aligned} \tag{5.8}$$

Indirect frame fusion :

$$\begin{aligned} &\text{if } j \neq l, i* \quad H = [I_4\ \mathbf{0}_4] \quad && \mathbf{z}_{eq} = H\mathbf{x}^{l,i} \oplus \mathbf{H}\mathbf{x}^{i,j} \\ &\qquad\qquad G = \partial\mathbf{z}_{eq}/\partial\tilde{\mathbf{x}}^{i,j} && \acute{R}_{eq} = P^{l,i} + GP^{i,j}G^{\mathsf{T}} \end{aligned}$$

$$\mathbf{x}^{l,i} \oplus \mathbf{x}^{i,j} = \begin{bmatrix} \mathbf{p}^{l,i} + \mathbf{R}_\theta^{i,j}\mathbf{p}^{i,j} \\ \theta^{l,i} + \theta^{i,j} \\ \mathbf{v}^{l,i} + \mathbf{R}_\theta^{i,j}\mathbf{v}^{i,j} \\ \omega^{l,i} + \omega^{i,j} \end{bmatrix} \quad \ominus\mathbf{x}^{i,l} = \begin{bmatrix} -(\mathbf{R}_\theta^{i,l})^{\mathsf{T}}\mathbf{p}^{i,l} \\ -\theta^{i,l} \\ -(\mathbf{R}_\theta^{i,l})^{\mathsf{T}}\mathbf{v}^{i,l} \\ -\omega^{i,l} \end{bmatrix}$$

where $\tilde{\mathbf{x}}$ is used to denote the error state corresponding to a state variable $\mathbf{x}$, and a mapping matrix H is used to select only the relevant variables of states which accumulate new locally measured information.

In the next step, the transformed set of communicated tracks (which is also re-

ferred to as equivalent measurements) is associated with individual tracks of the local track set. A gating procedure is incorporated to eliminate the equivalent measurements that have originated from inaccurate initialization. The final step performs an update of the local track set with its corresponding associated equivalent measurements.

The equivalent measurements cannot be directly used to perform a conventional Kalman update of the local track set. This is because the communicated tracks and local tracks become correlated soon after the first update, resulting in inconsistent updates thereafter. State de-correlation procedures are used in distributed tracking literature to overcome this problem [58]. State de-correlation is the process of removing any common information related to the two sets of tracks prior to fusion. For this purpose, each track separately propagates statistics for mean $\mathbf{x}_c$ and covariance P_c corresponding to the common information between the communicating robots. Common information only exists after the first communication, where during each subsequent communication $\mathbf{x}_c$ and P_c are replaced with the mean and covariance of the associated equivalent measurement. Using the additive property of the information form, the de-correlation of an equivalent measurement can be performed by

$$\begin{aligned} \acute{R}_{eq} &= (\acute{R}_{eq}^{-1} - P_{c,k|k-f}^{-1})^{-1} \\ \mathbf{z}_{eq} &= (\acute{R}_{eq} - P_{c,k|k-f})^{-1}(\acute{R}_{eq}^{-1}\mathbf{z}_{eq} - P_{c,k|k-f}^{-1}\mathbf{x}_{c,k|k-f}) \end{aligned} \tag{5.9}$$

Here the time index f corresponds to the time lapsed since the last communication. After de-correlation of an equivalent measurement, it can be used to perform a usual Kalman update. The state de-correlation procedure is only valid if the communication network topology of the robots remains static, and remains hierarchical without any feedback. Additionally, as pointed out in [58], this de-correlation procedure is ideally valid when no process noise is present.

In the proposed approach, a covariance intersection [102] based state fusion scheme is employed, in order to achieve a solution that is independent from the communication topology. CI is a conservative fusion scheme resulting in consistent updates which inherently assumes that the track and the associated measurements are correlated with an unknown cross correlation structure. CI does not require propagation of additional statistics for common information, which bounds the memory requirement to scale linearly.

$$\begin{aligned} w &= \text{argmin}_w(|wP^{-1} + (1-w)H^\intercal \acute{R}^{-1} H|^{-1})_{0\leq w\leq 1} \\ P &= P/w \qquad\qquad \acute{R} = \acute{R}/(1-w) \end{aligned} \tag{5.10}$$

The CI update scheme solves the optimization problem given by (5.10) and re-weights the state covariance and measurement covariance matrices using the scalar w. Then the re-weighted state covariance P and measurement noise covariance $\acute{R}$ are used to apply Kalman correction equations in order to realize the CI update. The weights of the tracks are updated similarly to a local correction scheme where the weight is multiplied by the likelihood of the equivalent measurement and likelihoods of tracks used for coordinate transformation.

This completes the proposed distributed multi-robot relative localization framework.

5.4 Results

The proposed framework was evaluated using several numerical simulations and an experimental dataset. The results validate four different aspects. 1) The global initialization capability, 2) Consistency of estimates, 3) Repeatability of results, 4) Validity of the method for experimental data. For the first three simulations, the stochas-

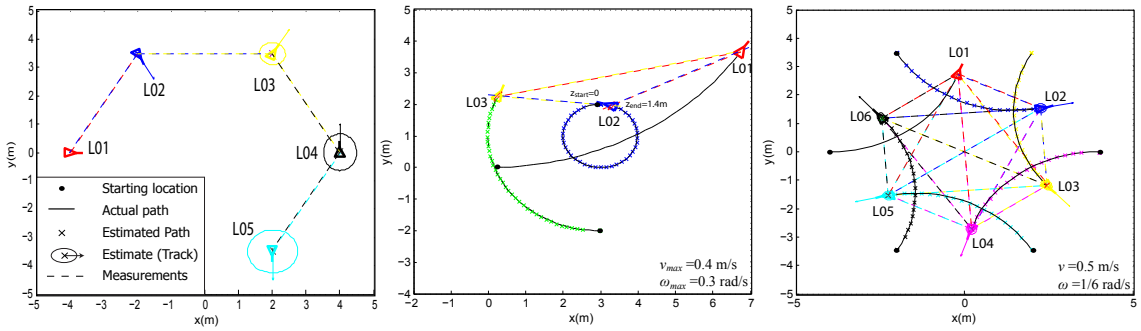

Figure 5.3: Robot configuration for the numerical tests. Left: Global initialization test, Middle: Consistency study, Right: Repeatability study

tic system model presented in equation (5.1) was used to simulate each robot in a predefined trajectory illustrated in Figure 5.3. The process noise values were set to $\sigma_{vx} = 0.01\text{m/s}$, $\sigma_{\omega} = 0.001\text{rad/s}$. To better simulate actual scenarios, the sensor models were simulated assuming polar forms with the corresponding range measurement and bearing measurement noise figures set to $\sigma_r = 0.01\text{m}$, $\sigma_{\alpha} = 0.002\text{rad}$, with detection probability $P_D = 0.9$. The centralized filter discussed in Section 5.2 was implemented for comparison purposes. The proposed distributed filter was implemented with parameters $P_G,\ P_B,\ P_K$ set to $0.9,\ 0.9,\ 0.001$.

5.4.1 Simulations - Global initialization

The observability of a target robot $\mathcal{R}_i$, relative to a local robot $\mathcal{R}_l$ is lost in the case where the robot network remains stationary. Therefore, a stationary robot network was selected as the scenario for validation of the global registration scheme. The multi-robot network consists of 5 robots arranged as illustrated in Figure 5.3. The sensing range of each robot was limited to 5m, to demonstrate hierarchical initialization that occurs as a result of this design. Each robot implements a fusing module with broadcast communication of its tracks at a rate of 1 Hz starting from 1.5s. Figure 5.4 illustrates the dynamic initialization of robots which were unseen by $L01$.

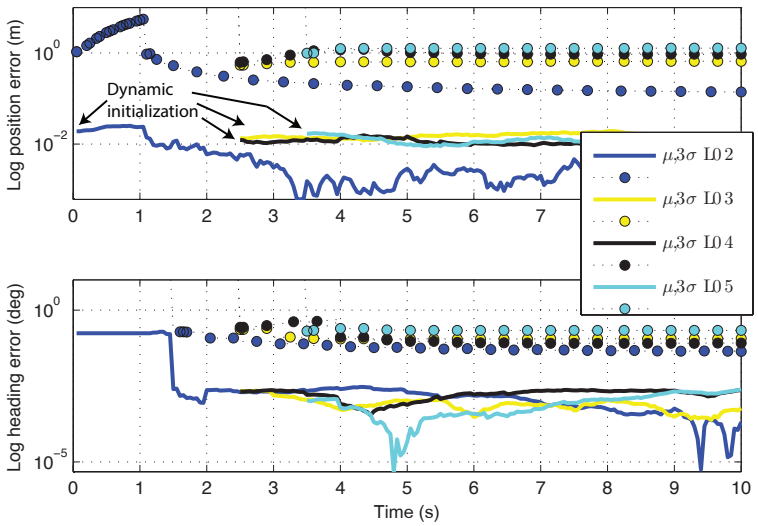

Figure 5.4: L01 Fuser delayed initialization by state communication and registration

Additionally, the mean and 3σ bound of position and heading estimate of each track maintained by $L01$ is presented. At 1.5 s, the orientation of the robot $L02$ is initialized. Similarly, in each fuser the corresponding orientations of locally observed robots are initialized. The proposed global registration module creates new tracks for each communicated fully initialized track. This results in fully initialized tracks for locally unseen robots to appear in the track set of $L01$ in a hierarchical manner.

5.4.2 Simulations - Consistency study

The second set of results presents the consistency of the proposed localization scheme. For this purpose, 3 robots were simulated along a trajectory as illustrated in Figure 5.3. No limitations on sensing range were imposed on this analysis. Robot $L02$ is given a velocity along z to simulate a 2.5D trajectory. A centralized multi-robot relative localization filter was implemented, to compare the consistency of results generated by the proposed distributed localization approach. The distributed filtering framework was implemented using both CI and State De-correlation (**SD**) based fusion schemes

for comparison purposes.

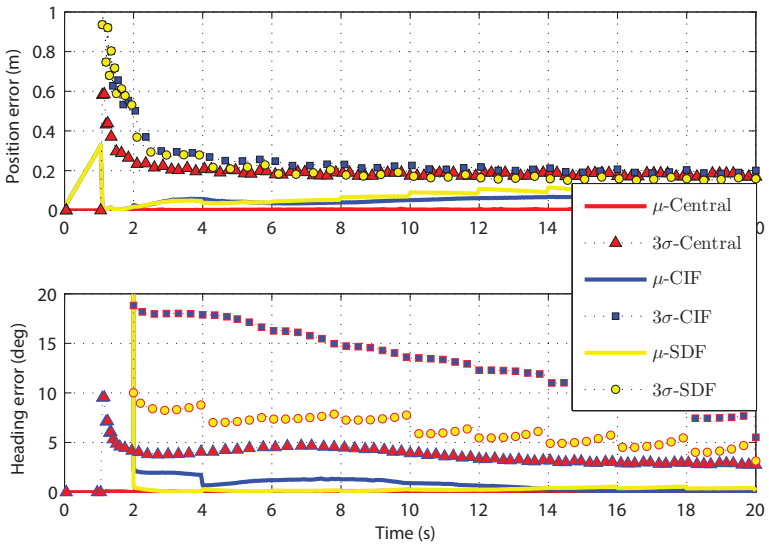

Figure 5.5: Consistency analysis for a hierarchical fusion case

Figure 5.5 illustrates the comparison of the centralized, distributed CI, and distributed SD based localization approaches for a hierarchically communicating set of robots. The communication was set to 0.5 Hz. The figure illustrates the localization results of $L02$ relative to $L01$, where both approaches were providing consistent estimates; i.e, the 3σ bounds of the distributed schemes were above those of a centralized filter.

Figure 5.6 presents the results for the same simulation setup with a different communication topology. Communication was set to broadcast with different rates for the three robots; i.e, 0.5 Hz, 1 Hz, and 0.3 Hz for robots $\mathcal{R}_1$, $\mathcal{R}_2$, and $\mathcal{R}_3$ in order. As illustrated, the distributed CI filtering strategy resulted in robust and consistent estimates. The distributed SD approach resulted in inconsistent estimates. The results justify the selection of a CI based fusion scheme in place of the SD based fusion scheme. By construction the CI approach scales linearly in terms of computational demand, supports asynchronous communication, and supports dynamically changing

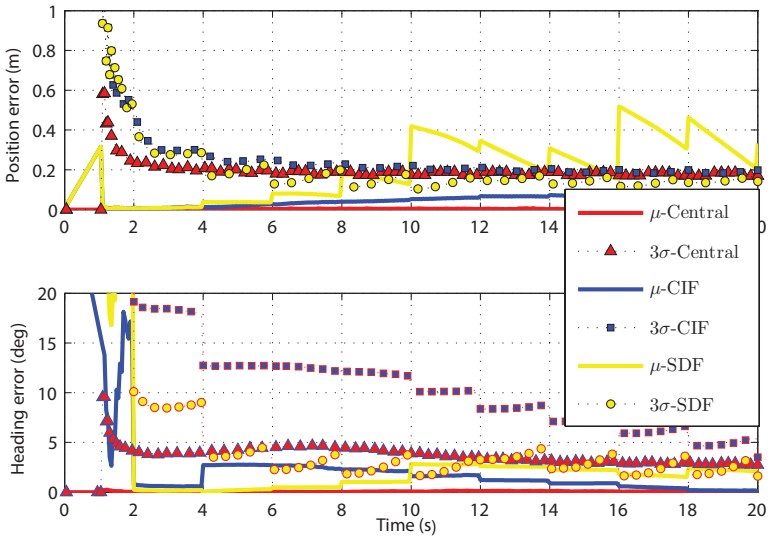

Figure 5.6: Consistency analysis for a multi-rate decentralized fusion case

network topologies.

5.4.3 Simulations - Repeatability study

The third result set presents the repeatability and robustness of the proposed approach with an increased number of robots. Figure 5.3 illustrates the trajectory of the 6 robots used for the simulation. Each robot implements a fuser with broadcast fusion at a constant rate of 2 Hz. A Monte Carlo analysis of 50 runs was performed with a stochastic simulation of the robots' system models and sensor models. Figure 5.7 presents the average results for 50 runs, where performance of both centralized and proposed distributed localization frameworks are presented. Table 5.1 presents the average localization accuracy of the relative pose of the robot network as estimated by $L01$. The average results only consider the estimation performance after convergence, which occurs around 2 seconds. All runs successfully localized robots with no inconsistency in estimates, verifying good repeatability of the method.

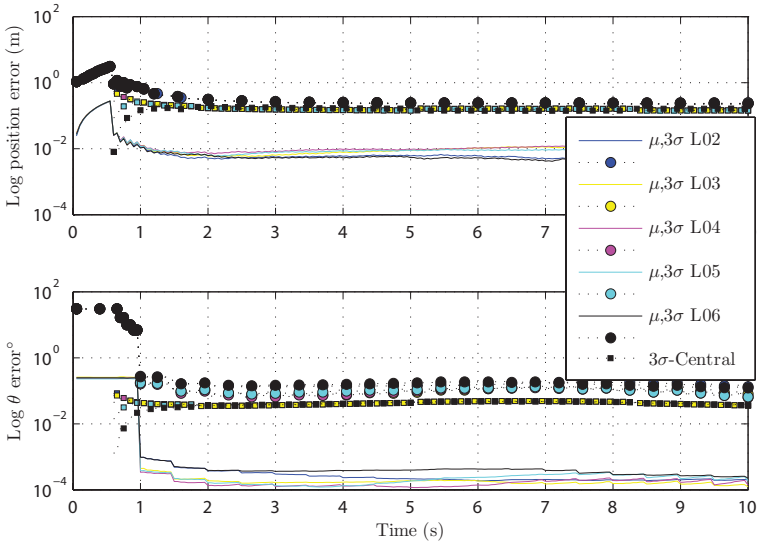

Figure 5.7: Average results of 50 Monte Carlo runs. Only the average estimation results of the fuser on L01 areshown.

Table 5.1: Summary of Monte Carlo average results

Robot	x error (mm)		y error (mm)		z error (mm)		θ error°	
	RMSE	3σ	RMSE	3σ	RMSE	3σ	RMSE	3σ
L02	0.79	139.5	0.38	166.4	0.0011	96.4	0.013	8.8
L03	1.20	146.3	0.54	158.9	0.0026	97.6	0.010	5.8
L04	1.05	166.8	1.04	140.8	0.0030	97.7	0.009	5.5
L05	0.59	135.3	1.15	166.0	0.0023	97.4	0.013	6.0
L06	0.33	145.5	0.75	160.9	0.0010	96.3	0.021	9.1

5.4.4 Experimental data set

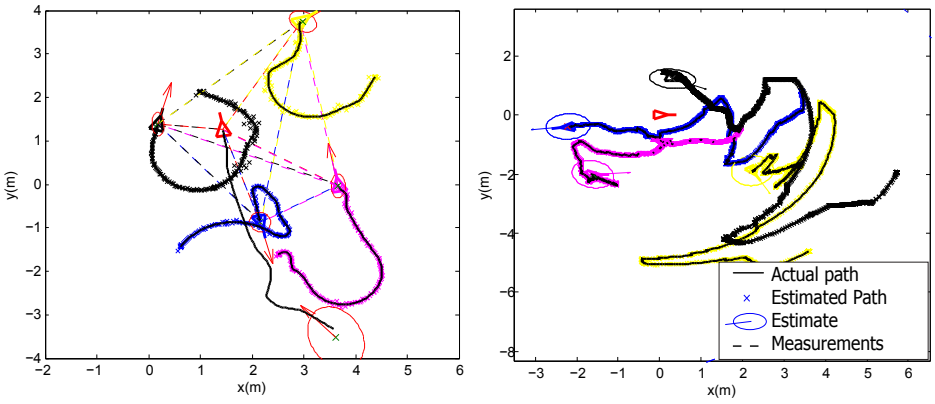

Figure 5.8: Robot trajectories and estimates for the experimental data set. Left: World frame, centralized estimates. Right: L01 frame, distributed estimates of fuser $L01$

The performance of the proposed distributed scheme was evaluated using a publicly available UTIAS multi-robot data set [36]. The multi-robot network consists of 5 robots. The odometry data from robots were used for the estimation. The ground truth data from the experiment were used to synthesize relative measurements and to validate the results. The actual relative measurements from the data set were not used to validate performance of the algorithm because there are numerous occlusions in the actual data which does not allow to appreciate the consistency of estimation which is achieved by this approach. This drawback of the dataset comes from the vision based relative measurement scheme used in the experiment which did not reproduce decent relative measurement sets for relative localization purposes. The landmark measurement data available in the data set were not used in these results since the objective is to validate the relative localization performance. The next chapter introduces a method to incorporate self localization with the proposed DRL approach with experimental validation using the data set of [36].

Each robot runs the proposed distributed fusion module. Figure 5.8 illustrates

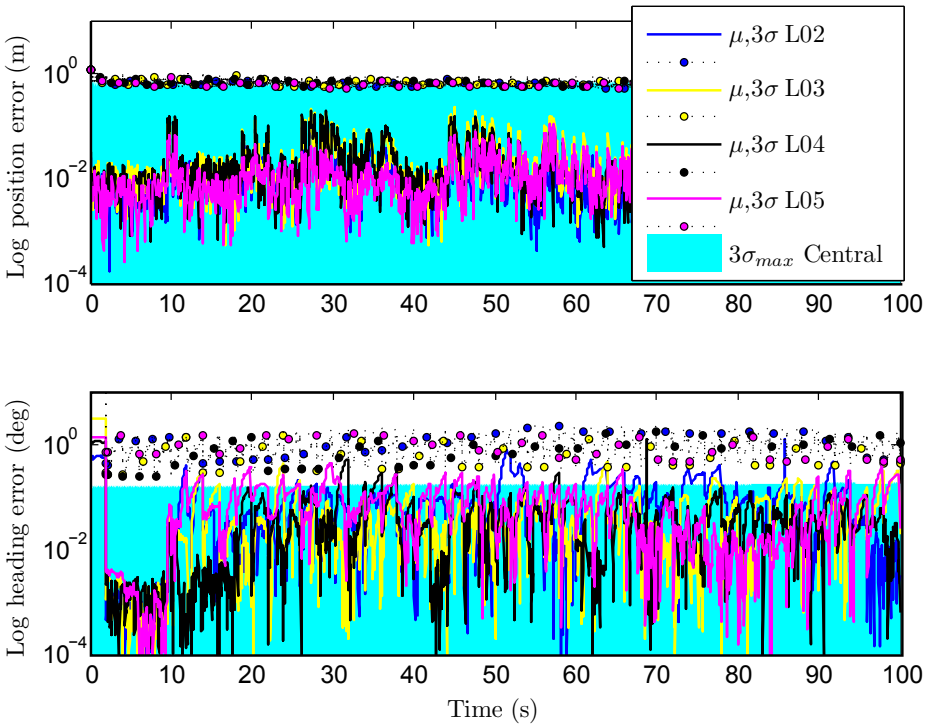

Figure 5.9: Consistency analysis using experimental data. Distributed estimates of fuser $L01$ compared with the centralized (shaded) estimates.

the trajectory of the robots and the estimated path by robot L01. The mean and covariance of estimates of each target robot as estimated by L01 are presented in Figure 5.10. The consistency of estimates was evaluated by comparing them with a centralized filter running on L01. The shaded area in Figure 5.9 illustrates the maximum 3σ value among all the robots using a centralized filter. This remains below the distributed estimate of the covariance for each robot, verifying the consistency of the proposed scheme. The following link (https://dl.dropboxusercontent.com/u/62036046/Thesis/Ch5_attachment.mp4) provides a video of the experimental results which validates the consistency of the proposed multi robot relative localization algorithm when implemented at 0.5Hz.

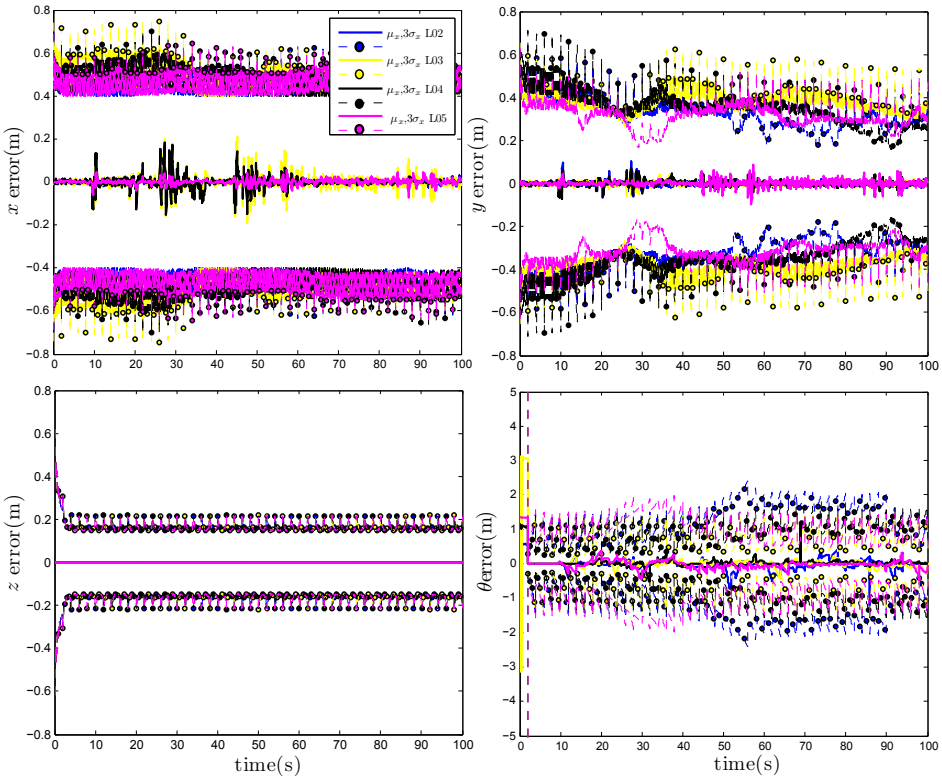

Figure 5.10: Mean and covariance of the states x, y, z and θ of the distributed fuser $L01$.

5.5 Conclusion

This chapter proposed a novel distributed multi-robot localization framework. The proposed approach is based on distributed target tracking frameworks and integrates a state propagation scheme, a global state registration scheme, and a CI based fusion scheme to address the specific problems related to multi-robot localization. The resulting design performs consistent estimation, scales linearly with the number of robots, and has no constraints in terms of network topology, rates, or scheduling of communication between robots. These features of the proposed scheme were validated by multiple experiments which simulate different scenarios. A repeatability study illustrates good localization performance and convergence properties of the design.

The following limitations of this work can be identified.

- The method assumes perfect data correspondence. This assumption is not applicable in some robotic sensing modalities which include laser scanners and vision based perception methods, where non distinct features are used for robot detection purposes. However, the proposed method is extensible to unknown data correspondence cases since the framework is based on the well established field of target tracking where proven data correspondence approaches are available. The next chapter details the integration of a data correspondence scheme to the proposed framework in order to address measurements with unknown origins.

- The proposed method is not readily applicable to range only and bearing only multi robot localization problems. This constitutes a potential research direction which would allow the use of range only beacons, and bearing based perception means such as cameras, for robot relative localization purposes in an efficient manner where communication is performed at low rates in order to support

practical bandwidth limitations.

- The proposed method does not complement theoretical performance bounds in terms of minimum rates that can be supported by the algorithm, limiting communication to achieve prescribed performance levels, and the effects of packet routing and communication delays on the approach.

Investigation into these aspects is a necessary future direction of this research work which would enable the proposed method to be applied as a general framework in designing distributed multi robot systems which complement communication, computational, and sensing limitations of platforms.

Chapter 6

Relative Localization of Heterogeneous Multi-Robot Systems

This chapter explains the experimental validation of the proposed distributed relative localization method under limitations related to heterogenous multi-robot systems. For this purpose, this chapter[1] develops two auxiliary modules: 1) a method of integrating self localization capability of robots with the proposed distributed relative localization approach; 2) a method to incorporate relative measurements which are acquired without data correspondence in the proposed DRL scheme. The performance of these two modules and the proposed DRL approach are validated using an experimental multi-robot system. The chapter also summarizes the technical details related to the mutli-robot system design which is used throughout the thesis for validation

[1] This chapter is based on the following publications of the author:

[*] O. De Silva, G. K. I. Mann, and R. G. Gosine, "An Efficient Distributed Data Correspondence Scheme for Multi-Robot Relative Localization," in Proceedings, *Moratuwa Engineering Research Conference (MERCon)*, IEEE, 2015.

of the proposed work.

6.1 Introduction

The previous chapter introduced a novel method for relative localization which does not require forced communication within the team during each measurement log. The method is capable of using conservative fusion schemes to achieve linearly scaling computational cost for an increasing number of robots. The proposed DRL method assumes that the robots are equipped with IRRM hardware which provides relative measurements with known data correspondence. However, in a typical heterogenous robot team there are many other information sources available to assist the relative localization problem.

It is possible to have SLAM filters implemented on capable robots of a heterogeneous team which allows the particular robot to localize itself with respect to a map. This is one reliable information source which provides the robot‘s location in the environment with respect to a frame of reference attached to its locally generated map. As a result, when multiple robots implement SLAM, the estimates of the location provided by SLAM will be registered in different reference frames. Therefore, a suitable method of incorporating SLAM estimates (or more generally self localization estimates) is necessary in order for a robot to make use of SLAM filters to improve the estimates given by the proposed DRL scheme.

A second source of information available to improve the estimates of the proposed DRL method is the environmental perception sensors attached to the robots, e.g. laser scanners and cameras. These sensors typically serve the SLAM filters for self localization purposes. However, these sensors are equally capable of perceiving the neighbouring robots often without any identification of whether it is a robot, a

moving object, or some object similar to a robot. I.e, there is no data correspondence. Therefore, these sensors can also be used to improve the estimates of the proposed DRL scheme if a suitable method for addressing the problem of data correspondence is established.

This chapter focuses on designing two modules, namely the self localization and DRL integration module, and the data correspondence module, which are necessary in realizing distributed relative localization in a typical heterogenous multi robot system. In order to incorporate SLAM or some form of self localization to the proposed DRL framework, this work proposes an approach where a global frame register is maintained in the same communication framework which compliments the proposed DRL scheme. This allows the robots in the team which implement SLAM to improve their awareness of neighbours even when the IRRM sensors are out of range.

In order to design the data correspondence module this work employs a likelihood based multiple hypothesis data association scheme commonly employed in target tracking [49]. The method allows to incorporate relative measurements logged by laser scanners and vision sensors to improve estimates of the DRL approach without compromising the efficient communication capability and the scaling capability established in the design. The two modules are validated using numerical simulations and experimental data sets. The chapter concludes with technical details related to implementation of the experimental test bed which was used to validate the methods proposed in this thesis.

6.2 Material and Methods

6.2.1 Integrating SLAM with DRL

Figure 6.1 illustrates the different estimates provided by the proposed DRL approach and SLAM filters running on robots. Recall the definitions of different frames introduced in Section 5.2. The body fixed frame of a robot $\mathcal{R}_l$ was denoted by $\{L\}$. The navigation frame which is the frame attached to the start location of the robot was denoted by $\{L^*\}$. The SLAM filter estimates the transformation from the navigation frame $\{L^*\}$ to body fixed frame $\{L\}$. In the previous chapter an estimate related to self localization of the robot was propagated using a separate track related to the navigation frame. i.e., $\mathcal{T}^{l,l*}$. Therefore, when SLAM is implemented on a robot, it is used as the filter that propagates the navigation frame track $\mathcal{T}^{l,l*}$. As a result, by enabling SLAM on a robot of the team, the particular robot is capable of propagating the navigation frame track with bounded estimate precision in an environment with sufficient features to support SLAM.

As illustrated in Figure 6.1, there can be many robots in the team having SLAM filters. However, the corresponding navigation frames of the robots which run SLAM will not be common to the whole team. As a result, a method should be in place so that each robot in the team is able to capture the transformations required to register the communicated information to a common frame. In the method proposed here each robot propagates a separate track collection termed the navigation frame register. This allows for each robot to store and update the navigation frame of its neighbours as necessary. Navigation frames related to two robots $\{L*\}$ and $\{I*\}$ are illustrated in Figure 6.1.

The proposed algorithm allows incorporating estimates of multiple robots running SLAM and DRL in the same communication framework and conservative fusion

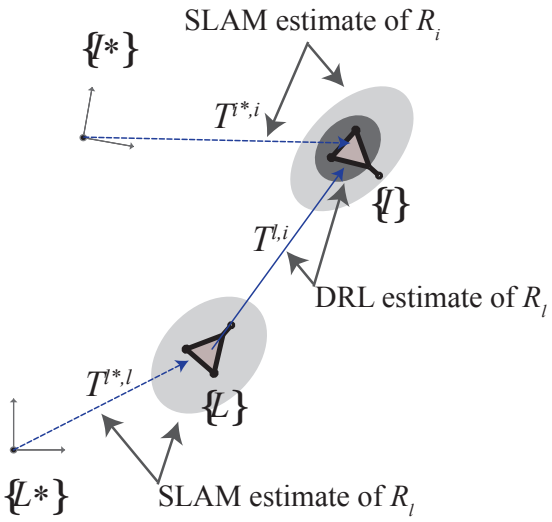

Figure 6.1: Estimates provided by SLAM running on robots and the proposed DRL approach running on robots

framework proposed in this thesis. Algorithm 2 details the steps involved in achieving this capability. The overall approach can be described in three main steps: 1) navigation frame initialization, 2) navigation frame correction, and c) platform frame correction.

6.2.1.1 Navigation frame initialization

Consider a local robot $\mathcal{R}_l$ and a communicating robot $\mathcal{R}_i$. The navigation frame related to the two robots will be different in a heterogenous robot team, since robots will not be able to establish the start location of each other in a general case. Therefore, the two robots need to communicate to establish the transformations related to navigation frames between the pair of robots. During the first instance of communication between the robots, the SLAM integration module checks and initializes the navigation frame of $\mathcal{R}_i$ in its navigation frame register $\mathcal{T}^{l*}$. For this purpose the navigation

Algorithm 2: Algorithm to combine SLAM estimate with the DRL estimates

Data: Local track set $\mathcal{T}^l = \{\mathbf{x},\ P,\ w,\ \mathcal{A}_r\}$ of the local robot
Communicated track sets $\{\mathcal{T}^i,\ \dots\}$ of all robots $\mathcal{R}_i$ which communicated during the current time step
Tracks of the Navigation frame register of the local robot $\mathcal{T}^{l*} = \{\mathbf{x},\ P,\ w,\ \mathcal{A}_r\}$
Result: $\mathcal{T}^l$ the updated estimates of the local tracks,
$\mathcal{T}^{l*}$ the updated estimates of the navigation frame tracks

for *each communicating* $\mathcal{R}_i$ **do**
  select $\mathbf{x}^{l*,l}, P^{l*,l} \in \mathcal{T}^{l*,l} \in \mathcal{T}^l$
  select $\mathbf{x}^{l,i}, P^{l,i} \in \mathcal{T}^{l,i} \in \mathcal{T}^l$
  select $\mathbf{x}^{i*,i}, P^{i*,i}, A_r^{i*,i} \in \mathcal{T}^{i*,i} \in \mathcal{T}^i$
  if *Track for* $\mathcal{R}_i$ *is not initialized in* $\mathcal{T}^{l*}$
  & *Track* $\mathcal{T}^{l,i} \in \mathcal{T}^l$ *is initialized* **then**
    1. Initialize the track of $\mathcal{R}_i$'s navigation frame in $\mathcal{R}_l$'s navigation frame register:
    $\mathbf{x}^{l*,i*} = \mathbf{x}^{l*,l} \oplus \mathbf{x}^{l,i} \ominus \mathbf{x}^{i*,i}$
    $P^{l*,i*} = P^{l*,l} + F_1 P^{l,i} F_1^T + F_2 P^{i*,i} F_2^T, \quad F_1 = \frac{\partial \mathbf{x}^{l*,i*}}{\partial \mathbf{x}^{l,i}},\ F_2 = \frac{\partial \mathbf{x}^{l*,i*}}{\partial \mathbf{x}^{i*,i}}$
    $A_r^{l*,i*} = A_r^{i*,i}$
    $\mathcal{T}^{l*} \leftarrow \mathcal{T}^{l*,i*} = \{\mathbf{x}^{l*,i*}, P^{l*,i*}, 1, A_r^{l*,i*}\}$
  else
    select $\mathbf{x}^{l*,i*}, P^{l*,i*} \in \mathcal{T}^{l*,i*} \in \mathcal{T}^{l*}$
    2. Perform navigation frame update
    $\mathbf{z}_{eq}^{l*,i*} = \mathbf{x}^{l*,l} \oplus \mathbf{x}^{l,i} \ominus \mathbf{x}^{i*,i}$
    $R_{eq}^{l*,i*} = P^{l*,l} + F_1 P^{l,i} F_1^T + F_2 P^{i*,i} F_2^T, \quad F_1 = \frac{\partial \mathbf{x}^{l*,i*}}{\partial \mathbf{x}^{l,i}},\ F_2 = \frac{\partial \mathbf{x}^{l*,i*}}{\partial \mathbf{x}^{i*,i}}$
    $\{\mathbf{x}^{l*,i*}, P^{l*,i*}\} \leftarrow$Covariance intersection of $\{\mathbf{x}^{l*,i*}, P^{l*,i*}\}$ and $\{\mathbf{z}_{eq}^{l*,i*}, R_{eq}^{l*,i*}\}$

    3. Perform platform frame update
    $\mathbf{z}_{eq}^{l,i} = \ominus \mathbf{x}^{l*,l} \oplus \mathbf{x}^{l*,i*} \oplus \mathbf{x}^{i*,i}$
    $R_{eq}^{l,i} = F_1 P^{l*,l} F_1^T + F_2 P^{l*,i*} F_2^T + F_3 P^{i*,i} F_3^T$
    $F_1 = \frac{\partial \mathbf{x}^{l,i}}{\partial \mathbf{x}^{l*,l}},\ F_2 = \frac{\partial \mathbf{x}^{l,i}}{\partial \mathbf{x}^{l*,i*}},\ F_3 = \frac{\partial \mathbf{x}^{l,i}}{\partial \mathbf{x}^{i*,i}}$
    $\{\mathbf{x}^{l,i}, P^{l,i}\} \leftarrow$Covariance intersection of $\{\mathbf{x}^{l,i}, P^{l,i}\}$ and $\{\mathbf{z}_{eq}^{l,i}, R_{eq}^{l,i}\}$

frame track $T^{i*,i}$ available in the communicated track list of R_i is utilized. Frame transformation and covariance propagation to frame $\{L*\}$ is performed to arrive at an estimate of the state $\mathbf{x}^{l*,i*}$ and covariance $P^{l*,i*}$ of the track used to concatenate the navigation frame register. This registration process is illustrated in Figure 6.2

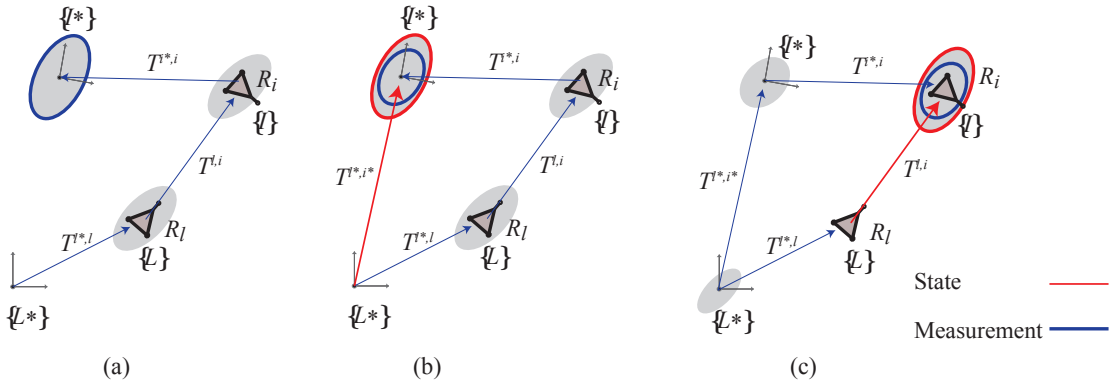

Figure 6.2: (a) Navigation frame initialization in track set $\mathcal{T}^{l*}$ (b) Navigation frame update in track set $\mathcal{T}^{l*}$ (c) Target frame update in track set $\mathcal{T}^{l}$

(a).

6.2.1.2 Navigation frame correction

Once the navigation frame of a communicating robot $\mathcal{R}_i$ is registered, this information can be used to perform updates of various frame estimates during subsequent communication. Figure 6.2 (b) illustrates one scenario of pose estimate improvement. In this case the estimate of the initialized navigation frame is updated using a conservative covariance intersection approach. For this purpose the transformation from frame $\{L*\}$ to $\{I*\}$ is estimated using the communicated track $\mathcal{T}^{i*,i} \in \mathcal{T}^{i}$ and the local tracks $\mathcal{T}^{l*,l}, \mathcal{T}^{l,i} \in \mathcal{T}^{l}$. Then this estimate is fused with $\mathcal{T}^{l*,i*}$, already available from the navigation frame register $\mathcal{T}^{l*}$.

6.2.1.3 Platform frame correction

During the platform frame update step, the estimate of each neighbouring robot available from the DRL framework is updated using the SLAM estimate. Figure

6.2 (c) illustrates one scenario of pose estimate improvement. For this purpose the transformation from frame $\{L\}$ to $\{I\}$ is estimated using the communicated track $\mathcal{T}^{i*,i} \in \mathcal{T}^{i}$, the track $\mathcal{T}^{l*,i*} \in \mathcal{T}^{i*}$ which is available in the navigation frame register, and the track $\mathcal{T}^{i*,l} \in \mathcal{T}^{l}$. Then this estimate is fused with the estimate of the platform frame $\mathcal{T}^{i,l}$ already available in the track set $\mathcal{T}^{l}$ generated by the DRL. These operation are performed for each communicating robot $\mathcal{R}_i$ which allows the generated tracks of the DRL approach to survive even when the relative measurements are not available due to field of view constraints.

The results section details the validation of the proposed SLAM integration algorithm using the UTIAS multi-robot localization dataset.

6.2.2 Data Correspondence module

The data correspondence module is used in the proposed DRL framework to make use of such measurements that are available with unknown data correspondence (e.g., laser scanners, vision sensors). The measurements generated by these sensors are denoted as $\mathbf{z}^{l,\dagger}$. The double superscript $l, \dagger$ denotes that that the relative measurement is made with respect to frame $\{L\}$ and the frame being measured is unknown. In order to accommodate these measurements, the following additions are made to the proposed DRL framework: 1) A multi hypothesis track management mechanism, and 2) a distributed track weight update mechanism. The multi hypothesis track management method allows maintaining all possible poses of a given robot based on the available measurements. Recall that each track is associated to a weight which maintains the likelihood of the particular track. The distributed weight update mechanism updates these track weights using the information from the communicated tracks of neighbours. This allows the improvement of the weight of the correct hypothesis for a given robot while diluting the unlikely estimates.

These two additions ensure that the maximum likelihood estimate for a given neighbouring robot's pose emerges from the overall DRL framework when it is introduced to measurements with unknown correspondences.

6.2.2.1 Multi hypothesis track management

The operations described here replace the track management operations performed following the correction module in Section 5.3.3. The track management operations are modified here to improve the overall approach for handling cases with unknown data correspondence. Consider a robot $\mathcal{R}_l$, the track $\mathcal{T}_m^{l,i}$ corresponding to m'th hypothesis of a target robot $\mathcal{R}_i$'s estimate, and the relative measurement $\mathbf{z}^{l,\dagger}$ taken by $\mathcal{R}_l$. The following track management rules are followed to realize a multi hypothesis data correspondence scheme:

1. If a track $\mathcal{T}_m^{l,i}$ is not associated to any relative measurement, the track weight $w \in \mathcal{T}_m^{l,i}$ is updated using the survival probability. I.e., $w = w(1-P_D P_G)$, where P_D is the probability of detection related to the sensor and P_G is the probability of the measurement being within the measurement gate.

2. If a track $\mathcal{T}_m^{l,i}$ is associated to a measurement $\mathbf{z}^{l,\dagger}$, the measurement $\mathbf{z}^{l,\dagger}$ is flagged as associated to the corresponding robot $\mathcal{R}_i$. Then the track $\mathcal{T}^{l,i}$ is updated using the measurement $\mathbf{z}^{l,\dagger}$ along with the track weight w which is updated using the measurement likelihood. I.e, $w = wP_D\mathcal{N}(\mathbf{z}^{l,\dagger}|(\mathbf{z}^{l,\dagger} - \mathbf{y}^{l,i}), (HPH^\intercal + \acute{R}))/\lambda$.

3. If a track $\mathcal{T}_m^{l,i}$ is associated to multiple measurements, all measurements are flagged as associated, and the nearest measurement is used to update the track. All remaining in gate measurements branch in to a new set of tracks where each is generated while updating the track $\mathcal{T}_m^{l,i}$ using the measurements $\mathbf{z}^{l,\dagger}$.

4. When a track is associated to several measurements, a new hypothesis termed as the "false alarm track " is also generated. This hypothesis considers the case that the in gate measurement is a false alarm in which case the weight is updated with the survival probability of $w = w(1 - P_D P_G)$.

5. The measurements which are associated to a track $\mathcal{T}_m^{l,i}$ of robot $\mathcal{R}_i$, are not considered with the tracks $\mathcal{T}_l^{l,i}, l \neq m$ of the same robot for further hypothesis generation.

6. If a measurement $\mathbf{z}^{l,\dagger}$ is not associated to any track (if the measurement is out of gate for all tracks), the measurement is used to initialize new tracks for each robot in the team. Hence for each out of gate measurement, N number of tracks will be initialized corresponding to each robot $\mathcal{R}_i$ in the team. This is because for a given measurement with unknown correspondence it is possible that the measurement is generated from any robot in the team.

An illustration of track formation for multitude of possible scenarios is given in Figure 6.3. In all the cases shown, all possible hypotheses are generated for estimation purposes using the track management policy described above. The pruning step ensures that the hypothesis count does not grow exponentially.

The weights of the tracks are only updated using the local likelihood measures in the track management policy given here. For cases where there are no measurements with known correspondence, these local likelihood updates only allow handling clutter and false alarms in measurements. In order to differentiate the correct hypothesis from the multiple tracks generated locally to each robot, it is necessary to communicate information between robots and achieve a distributed track weight update mechanism.

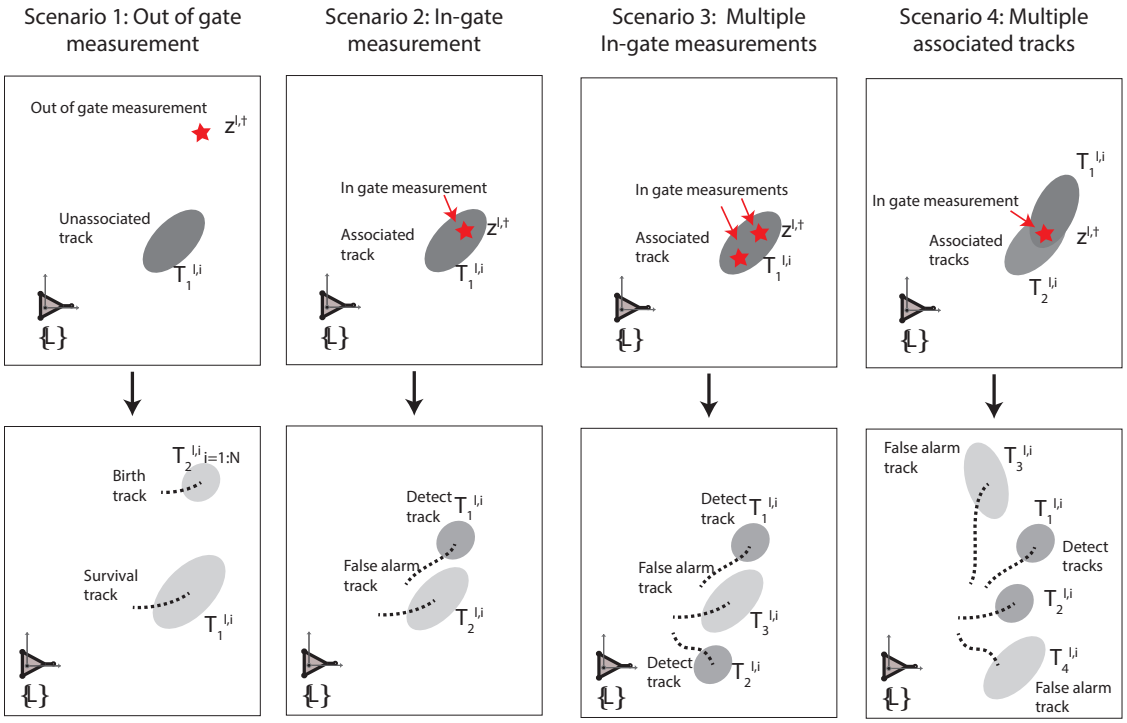

Figure 6.3: Tracks generated by the multi hypothesis track management policy for different scenarios.

6.2.2.2 Distributed track weight update

The distributed track weight update mechanism is acquired using the global registration module and the fusion module of the DRL framework. The global track registration module, as presented in Section 5.3.5, performs the necessary pose initialization of the robots by correcting the orientation of each track in cases where they have not been initialized. The ability to handle unknown data correspondence is already incorporated in Algorithm 1. Therefore, in terms of initialization no explicit modifications are necessary to handle measurements with unknown data correspondence.

The fusion module which follows the global registration module performs the sensor registration task and conservative fusion of the estimates. When there is known data correspondence of measurements, ideally there would be only one hypothesis for

a given neighbouring robot. However, in the case of unknown measurement correspondences there would be many hypotheses for a given robot. Therefore, the sensor registration approach is performed in a multi hypothesis sense. Following is a descriptive explanation of how the multi hypothesis registration scheme works.

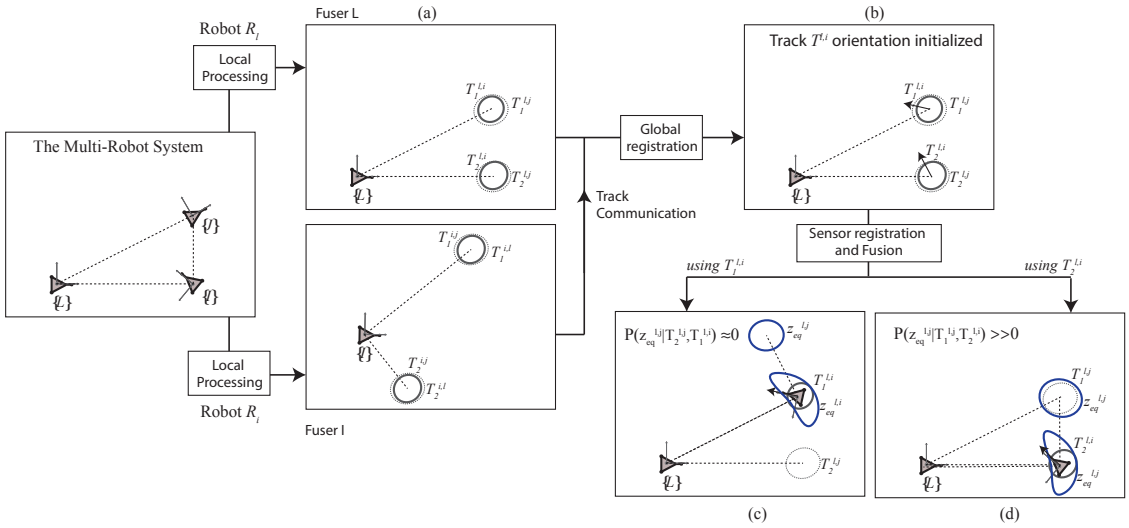

Figure 6.4: Multi hypothesis sensor registration example

Consider Figure 6.4(a) where a robot $\mathcal{R}_l$ has four tracks of two hypotheses each for robots $\mathcal{R}_i$ and $\mathcal{R}_j$. Consider the case where $\mathcal{R}_i$ communicates its track set to $\mathcal{R}_l$. The global registration module initializes the tracks in cases where the orientation of the tracks of $\mathcal{R}_l$ does not converge. Then the initialized tracks given in Figure 6.4(b) will be used to perform sensor registration as given by equation set (5.3.6). The sensor registration and fusion modules perform the following three operations: 1) navigation frame fusion, 2) mutual frame fusion, and 3) indirect frame fusion.

1. Navigation frame fusion updates the velocities of the local tracks using the communicated navigation frame tracks of each robot. Since the velocities of the platforms are known with measurement origin there is no requirement of explicitly handling data correspondence for this operation. After the DRL approach

converges to the tracks with correct data correspondences, SLAM integration module would further assist the data correspondence operation by weighting the tracks which are consistent with the self localization estimates.

2. Figure 6.4(c) and (d) illustrate the registration of the tracks related to $\mathcal{R}_i$ in $\mathcal{R}_l$ using two different hypothesis generated locally to $\mathcal{R}_l$. This operation where the robots use each other's tracks to perform fusion is termed mutual frame fusion. The weight update for mutual frame correction considers a likelihood based approach, where likelihood of the mutual measurement, and the likelihood based on the indirect frame registrations resulting from the hypothesis, are both used in the weight update process.

3. Then the corrected frame of $\mathcal{R}_i$ is used for the purpose of updating the tracks of $\mathcal{R}_j$. This is called an indirect frame fusion. The weights of the different hypotheses for $\mathcal{R}_j$ are updated using the likelihood calculated using the equivalent measurements.

The multi hypothesis data correspondence scheme is a distributed efficient implementation since it follows the same asynchronous communication and conservative fusion scheme which is designed in chapter 4. This data correspondence method is validated using multiple numerical simulations and an experimental data set in the results section.

6.2.3 The Experimental Setup

The experimental setup is designed using equipment available at the Intelligent Systems lab of Memorial University of Newfoundland, for system validation of the relative localization based navigation framework proposed in this thesis. The experimental setup consists of pioneer mobile robots, iRobot create platforms, and ARDrone 2.0

MAVs. As of June 2015, an OptiTrack motion capture system is used for the purposes of ground truth validation which is used in the experimental results presented in this chapter. Figure 6.5 illustrates the overview of the experimental setup used throughout the thesis. Details of each element of this setup is presented in the following sections.

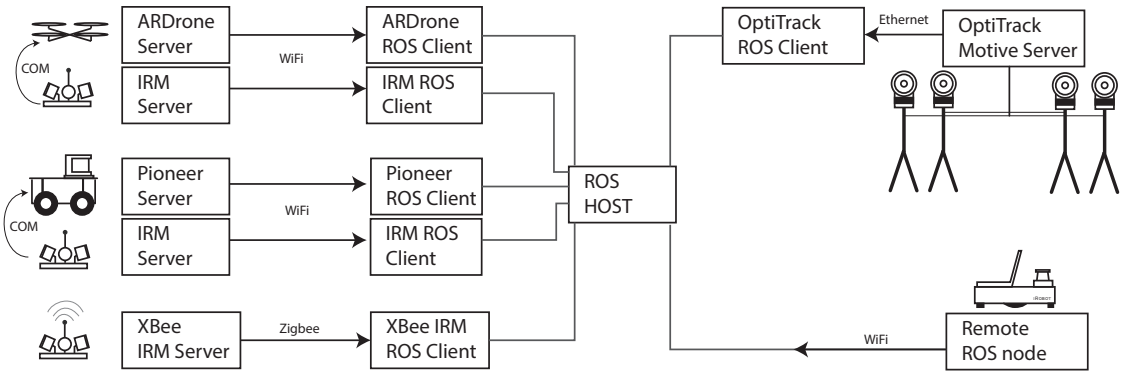

Figure 6.5: ROS enabled multi robot system used for experimental validation

6.2.3.1 The Pioneer robots

Pioneer P3-AT platforms from Adept are 4 wheel skid steer robot platforms. These robots are equipped with wheel encoders for odometry, sonar for obstacle avoidance, and laser scanners for mapping operations. The research resulted in development of the AriaClinetDriver ROS node and associated firmware which allows to realize the connectivity illustrated in Figure 6.5. All nodes that were developed are available in the following Github repository. https://github.com/sendtooscar.

For implementation of SLAM, the gmapping ROS node was used which implements SLAM using a Rao-Blackwellized particle filter.

6.2.3.2 The Relative localization sensor nodes

The sensor node developed as part of the thesis is ROS enabled. The sensor communicates over USB to an IRRM measurement server implemented on the attaching

platform. The attaching platform connects to the centralized supervisory controller through Wifi which implements a ROS node for communicating with the IRRM measurement server running on the robot. XBee based communication to the ROS system is also enabled where an XBee data server running on the micro controller of the sensor node communicates with the ROS IRRM measurement client node to stream measurement data to the ROS system.

6.2.3.3 ARDrone 2.0 robots

The AR Drone 2.0 MAV is used as the main aerial research platform in the multi robot system. To connect the platform to the ROS system the ARdrone autonomy stack developed by the Autonomy Lab of Simon Fraser university was used. The data of the platform velocities, images from the front and bottom cameras, and the estimates from the onboard AHRS are available as ROS topics.

For AHRS design experimentation and custom flight controller development, a custom firmware was developed for ARDrone 2.0 which implements an AHRS tuned using the methods proposed in this thesis.

6.2.3.4 Turtle bots

The turtle bot is a low cost mobile robot platform realized using a ROS enabled computer attached to the iRobot create platform. A Hokuyo UST-20LX laser scanner is attached to the platform to enable environmental sensing. The robot operates as a ROS remote host which publishes the robot's information and command signal through the Wifi network.

6.2.3.5 Laser and camera based relative measurements

The Laser scanners and cameras of the robot platforms serve as valuable sources for measuring the neighbouring robots. The laser scans are used to generate relative measurements using incremental scan matching and identifying moving objects in the map.

6.2.3.6 The ground truth validation system

Ground truth validation of the experiments is performed primarily using three methods in this thesis. For measurement system calibration a laser based ground truth validation was used. Prior to purchase of the Opti Track measurement system, an April tags based ground truth validation method was used to capture robot trajectories. For this purpose the Apriltags libraries were used to implement a minimal implementation for the ROS system. The experiments presented in this chapter are validated using an OptiTrack based ground truth validation system. For this purpose the ROS nodes available for OptiTrack Tracking tools software was modified in order to be compatible with the new OptiTrack Motive software which allowed to perform multiple object ground truth validation. Table 6.1 reports all the ROS nodes used as part of the thesis for designing the experimental system.

The overall system was used to validate the relative localization sensor, observability limitations, and RINCF filter for relative localization in Chapters 2, 3, and 4 respectively. In this chapter the system is used for validation of the overall DRL framework, SLAM integration approach and the data correspondence approach using mobile robots.

Table 6.1: ROS nodes used in the experimental testbed

ROS node	Author	Description
AriaClientDriver	IsLab	The driver node and the robot server to connect pioneer robots to a ROS system running on a remote machine.
RelocSensorDriver	IsLab	The driver node and the measurement server to connect an Arduino based relative measurement sensor node to a ROS system running on a remote machine.
AprilTagsMinimal	IsLab	A minimal ROS implementation for april tag system for ground truth validation of robots
IslabArdroneController	IsLab	A ROS enabled custom firmware for flight dynamic research and onboard navigation filter research for ARDrone 2.0
mocap_optitrack	Clearpath/ IsLab	A modified version of the mocap_optitrack node from Clear path Robotics to be compatible with the new data stream protocol of OptiTrack Motive software link to the above ROS nodes: https://github.com/sendtooscar/
ardrone_autonomy	Manni Monajjemi	The driver node to connect AR Drone 2.0 MAVs to a ROS system running on a remote machine. https://github.com/AutonomyLab/ardrone_autonomy
gmapping	Brian Gerkey	SLAM implementation available with the navigation stack of ROS http://wiki.ros.org/gmapping
urg_node	Chad Rockey	ROS driver node for Hokuyo laser scanners http://wiki.ros.org/urg_node

6.3 Results

6.3.1 SLAM integration method validation - UTIAS dataset

Validation of the SLAM integration method was performed using the UTIAS public multi robot localization dataset. Figure 6.6 illustrates the landmark locations of the environment and the path the robots traversed during the experiment. An EKF

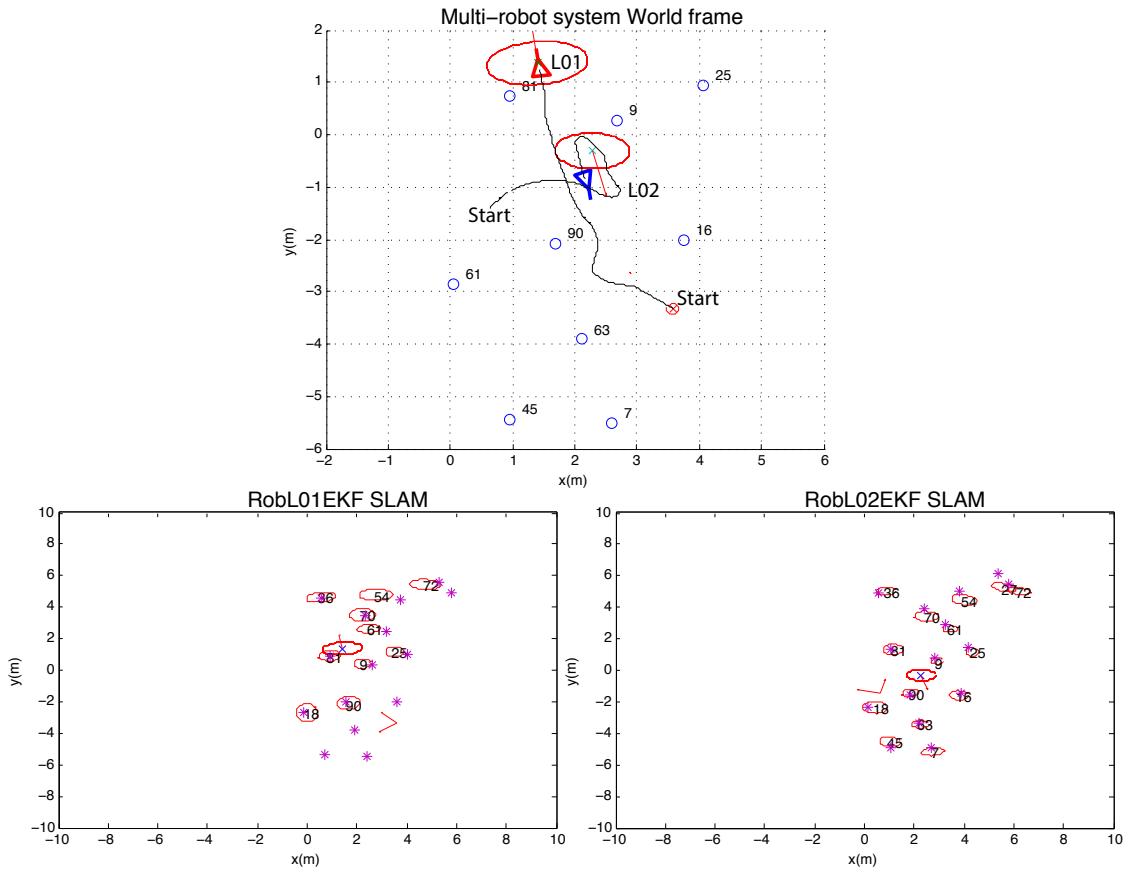

Figure 6.6: The path of the two robots and the locations of the landmarks

SLAM filter was used for self localization purposes which produced the 2 maps shown at the bottom of Figure 6.6. For implementing SLAM the actual odometer readings and the relative measurement readings of the landmarks were used. As a result of the rather noisy measurements of the iRobot create platforms, the localization filter requires higher sensor noise settings for consistent localization estimates using SLAM. The localization accuracy of the SLAM filters is presented in Figure 6.7.

The proposed DRL framework in chapter 5 is implemented to perform relative localization of the robot team. The experiment assumed a sensor which had a 180^o field of view limitation. Therefore, the IRRMs between the robots are not available during many instances of the experiment. Communication was implemented at 1 Hz

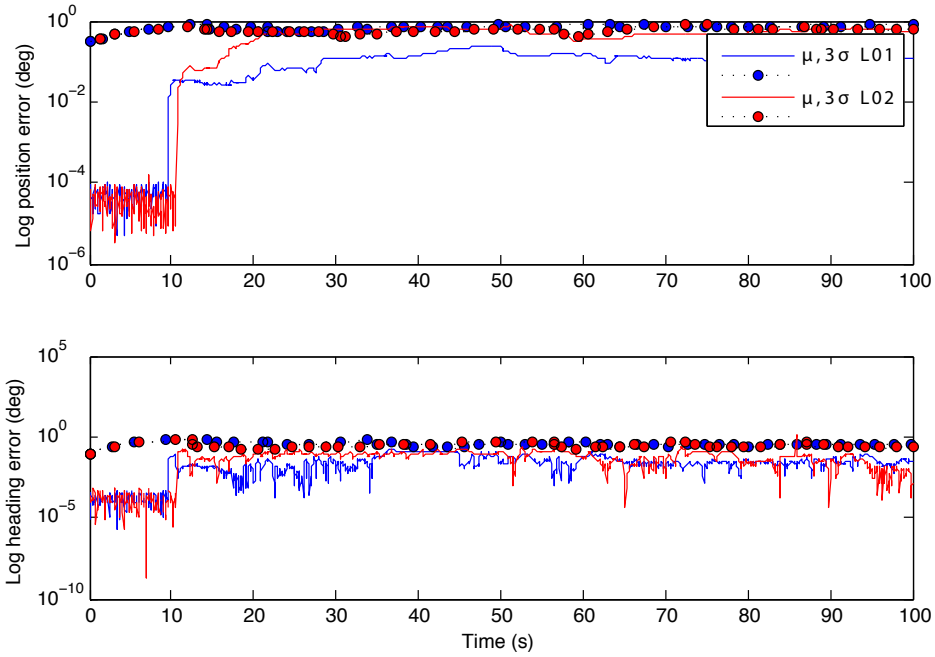

Figure 6.7: Errors of SLAM self localization of robots

to limit the communication rate. Upon the first few information exchanges between the robots, the DRL approach converges to a confident relative localization estimate. This occurs for Fuser 1 at around 2 seconds and for Fuser 2 at around 25 seconds. After convergence of the estimates the navigation frame register records the location of the navigation frame track related to each neighbouring robot. Then this is used for subsequent navigation frame estimate improvement and improvement of the target robot estimates when there are no relative measurements to sustain the tracks.

Figure 6.8 illustrates the navigation frame register and the track list corresponding to Fuser 1 and Fuser 2. Figure 6.9 illustrates the localization estimates achieved by the DRL design together with the SLAM integration approach. In the 10 second spans where relative measurements are non existent, shown in Figure 6.9, the navigation frame register allows incorporating the self localization estimates to the track, thereby limiting the growth of track which would otherwise cease to exist due to lack

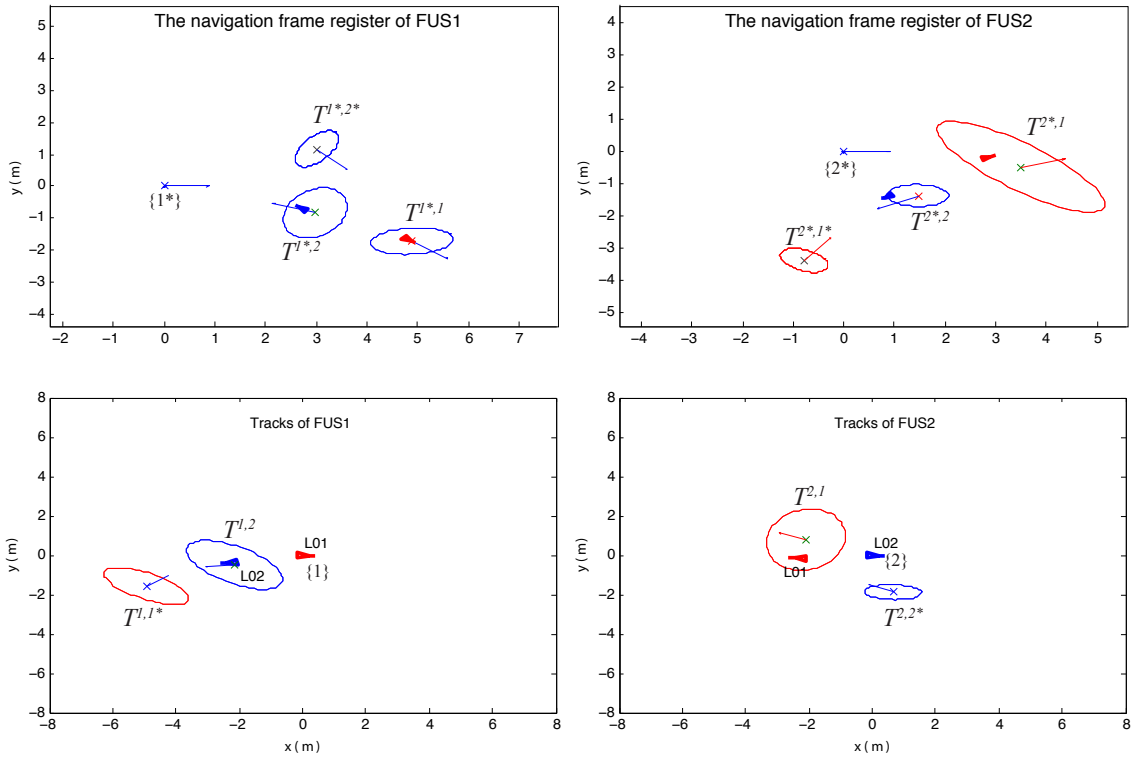

Figure 6.8: The navigation frame register and the track list of each Fuser

of relative measurements. Therefore this method would allow a fusing agent to estimate a neighbouring robot which has a fairly accurate odometer for short periods of non line of sight operation, and neighbouring robots with powerful SLAM filters for long periods of non line of sight operation.

6.3.2 Data correspondence approach validation - simulated dataset

Numerical simulations were performed to validate the data correspondence method introduced in this chapter. For this purpose a team of three robots was simulated to follow a path as shown in Figure 6.12. Robots $L01$ and $L02$ perform relative measurements of the team using laser scanners which generate measurements with unknown data correspondence. The Fusers communicate at a predefined rate of 2Hz. Robot

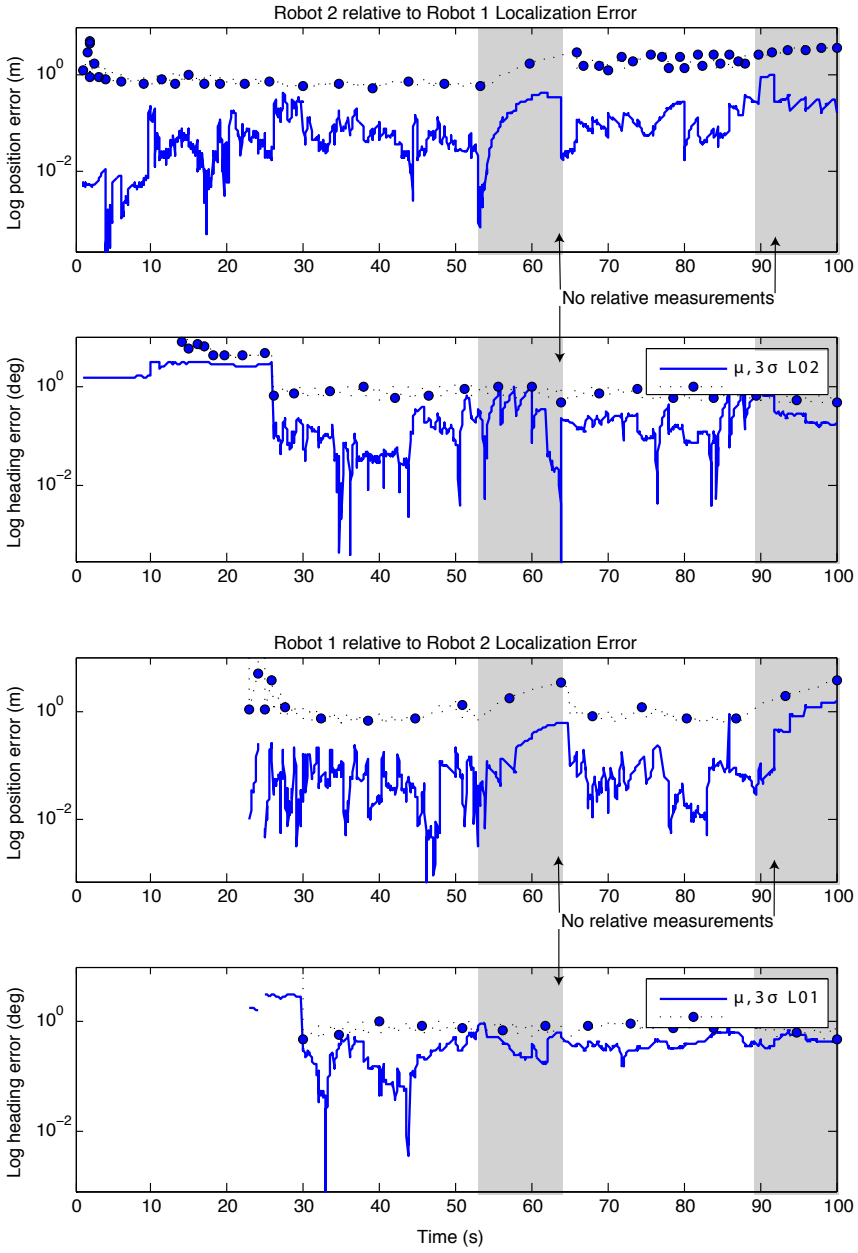

Figure 6.9: Localization errors of the DRL approach with the SLAM integration module. (Without SLAM integration the tracks do not survive during the periods of measurement loss shown in figure)

$P01$ does not take any relative measurements and communicates only its velocity data to be incorporated in the corresponding tracks at the set communication rate.

This particular configuration was selected for the experiment because it corresponds to a challenging scenario where the relative measurements do not have any correspondence information about the measured robot and the team does not have all agents performing relative measurements.

The DRL module was able to successfully converge to the correct track hypothesis as illustrated in Figure 6.12. The log position and heading errors related to relative localization are presented in Figure 6.11 which illustrates convergence after few information exchanges and consistent estimation of both the mean and covariance related to the pose estimates.

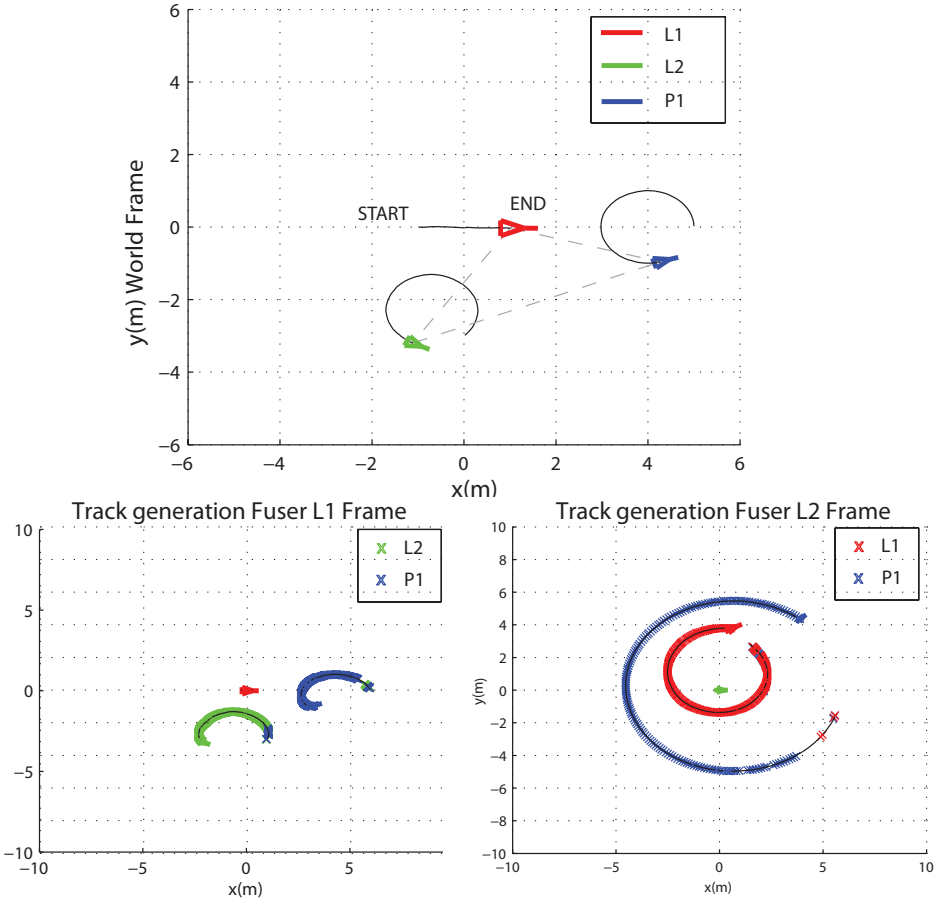

Figure 6.10: Top: The path of three robots used for simulation 1. Bottom: Estimates of the paths given by the DRL approach together with the data correspondence scheme

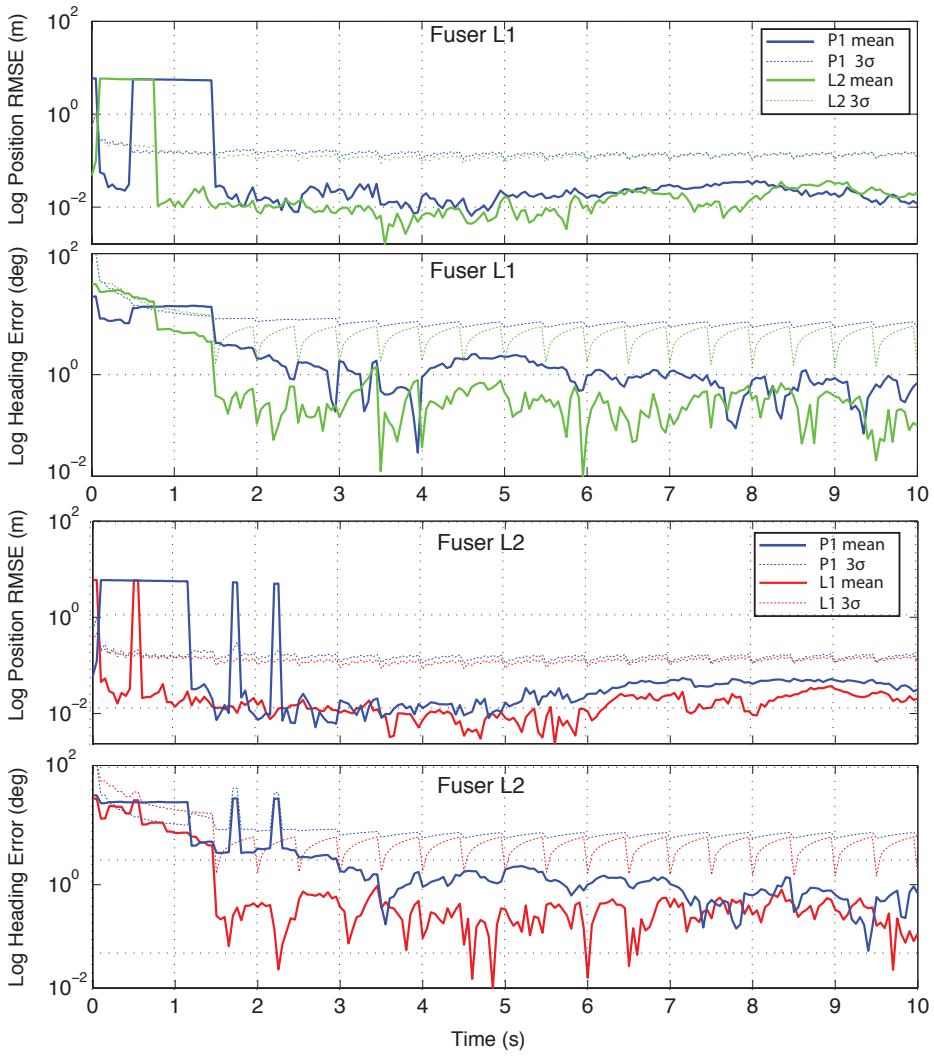

Figure 6.11: The localization errors of tracks generated by Fuser 1 and Fuser 2

In order to validate the robustness of the data correspondence approach, a Monte Carlo analysis was performed. For this purpose a team of 5 robots was simulated on a path as illustrated in Figure 6.12 . The simulation assumes a relative measurement sensor where range is measured with known correspondence and bearing is measured with unknown correspondence. These two types of measurements can be combined to form a set of possible cartesian relative position measurements with known correspondence for a given robot. This scenario was selected to validate the capability

of handling measurements with both known and unknown correspondences and the applicability of the method in a range of relative measurement scenarios.

25 Monte Carlo stochastic simulations were performed to obtain average localization estimates for the experimental scenario illustrated in Figure 6.12. Figure 6.13 illustrates the time history of the average number of confirmed tracks of each robot along with the RMS error of position and the orientation of the dominant hypothesis corresponding to each robot. The results validate the capability of the proposed architecture where it converges to the correct hypothesis corresponding to each robot's location with good reproducibility of results. The multimedia attachment presents experiments with increased clutter, 50% increased noise, and an increased number of 20 robots. In all experiments the proposed data correspondence approach was able to successfully initialize the robots in the network and track the robots while solving for unknown correspondences.

6.3.3 System validation - Experimental multi robot system of IS Lab

For experimental validation of the methods proposed in this thesis the multi-robot system of IS Lab was employed. For this purpose three ground robots were maneuvered along a trajectory in the capture volume of the available motion capture system. The objective of this experiment is to validate the distributed relative localization method and the ability of incorporating additional sensors such as laser scanners to the framework using the data correspondence approach proposed in this chapter. The robots use lasers as a means of measuring the neighbours with unknown correspondence. A range only measurement sensor is assumed, which measures the relative range between the robots with known correspondence. The lasers used in this study have a 180^0 field of view constraint which does not produce sufficient measurements to

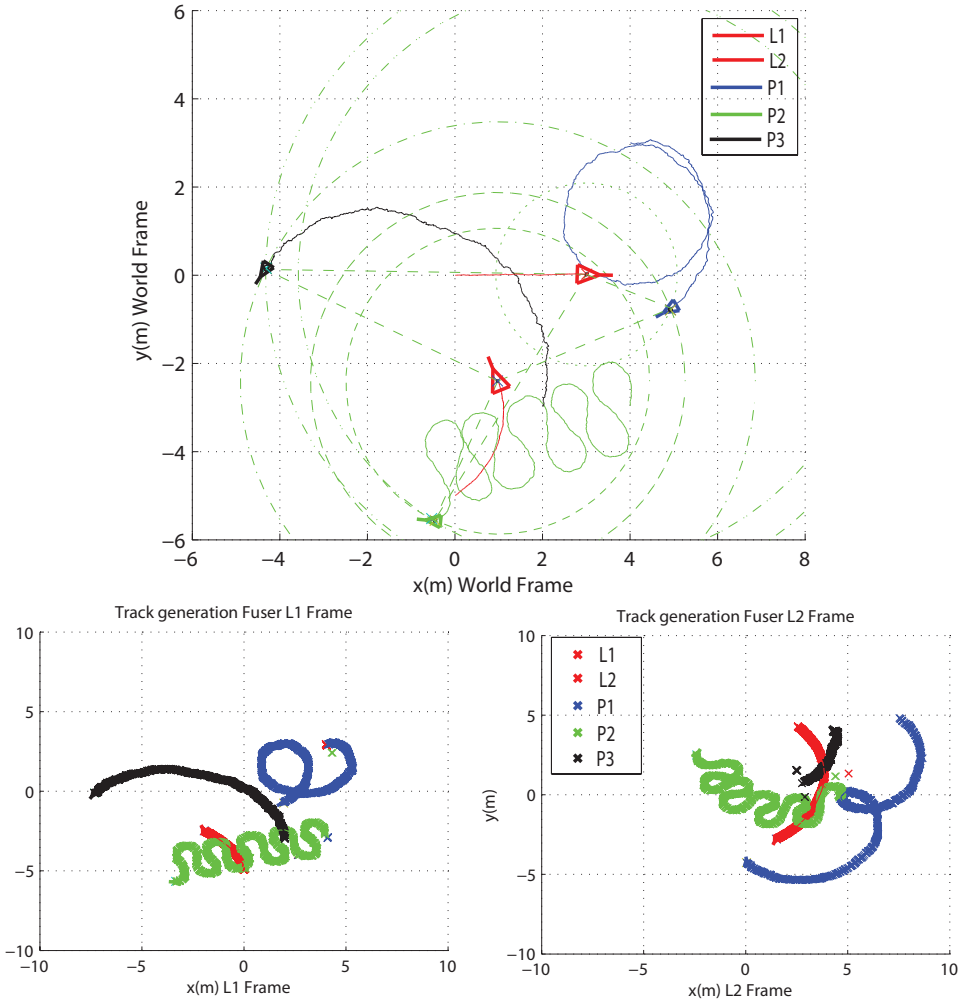

Figure 6.12: Top: The path of five robots used for simulation 2. Bottom: estimates of the trajectories given by the DRL approach together with the data correspondence scheme running on two Fusers L01 and L02

achieve sustained data correspondence using only the lasers. Each robot implements a fuser using the proposed DRL framework which runs at $10Hz$. The odometer readings of the robots were used for self localization. The robots communicate at 0.5Hz to perform the distributed estimation task.

Figure 6.14 illustrates the path traversed by the robots along with the final estimated trajectory achieved by the Fuser implemented on robot $L03$. Figure 6.15 illustrates the resulting estimates by each fuser implemented on $L01$, $L02$, and $L03$.

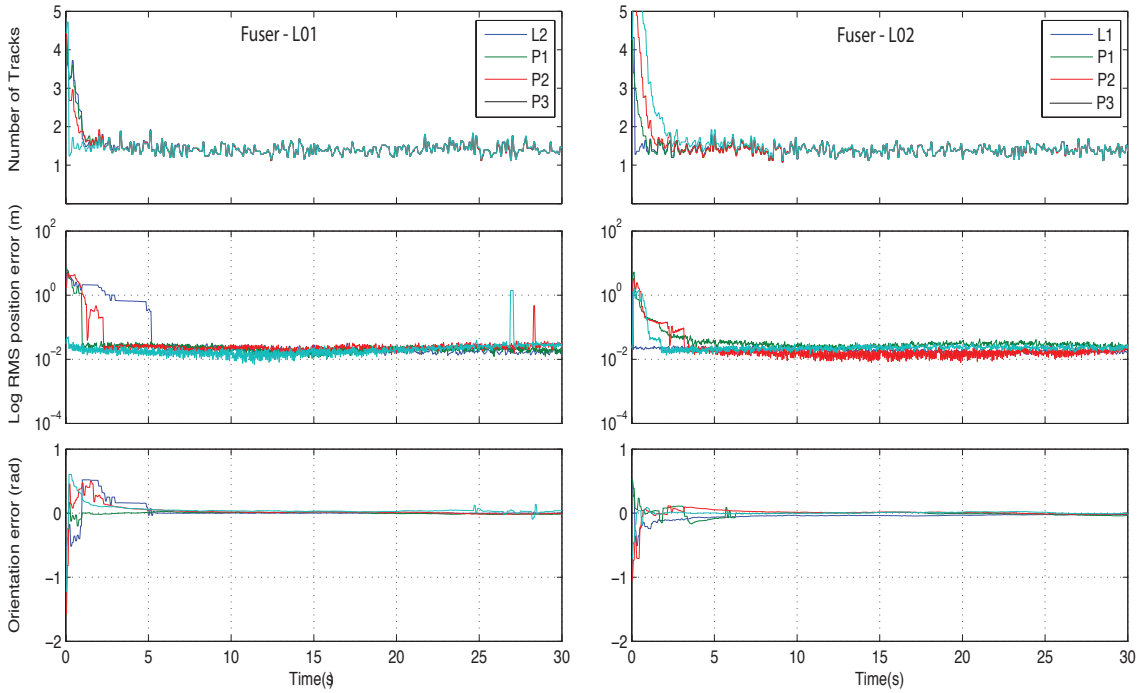

Figure 6.13: The estimates of position and heading averaged for 25 Monte Carlo runs of simulation 2.

The results validate the capability of the data correspondence module to solve for the unknown correspondences of the measurements where the robots were capable of localizing and identifying the neighbours in their field of view, as illustrated in the trajectory estimates given in Figure 6.15.

The estimation errors achieved by the Fuser on $L03$ are given in Figure 6.16, and Figure 6.17. It is important to note that the neighbours of robot $L03$ travel in its field of view which allowed Fuser 3 to perform sustained location estimation of the neighbours using both local and communicated tracks. Fusers on $L01$ and $L02$ do not achieve sustained localization estimates since the neighbouring robots traverse outside its field of view. These short periods of non line of sight operation of robots are effectively addressed by the method proposed in this chapter which allows to incorporate self localization estimates to the DRL framework. The multimedia attachment is found in this link: https://dl.dropboxusercontent.com/u/62036046/Thesis/

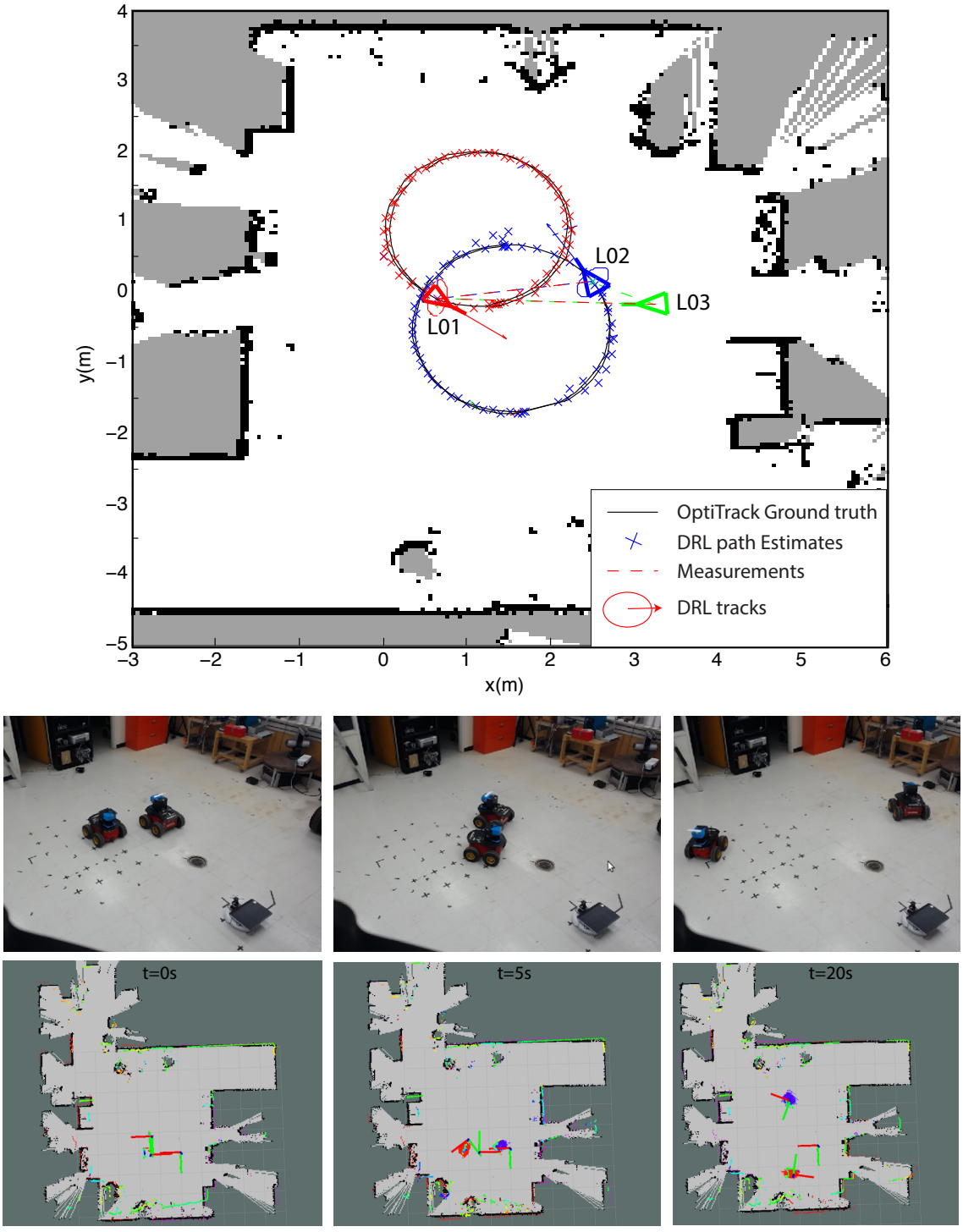

Figure 6.14: The path traversed by robots during the experiment and the estimated trajectory form the proposed DRL scheme.

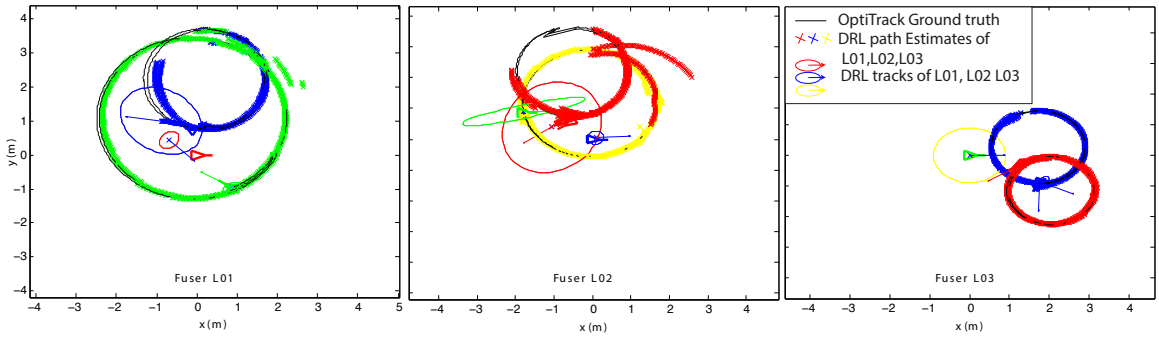

Figure 6.15: The relative localization estimates generated by each Fuser

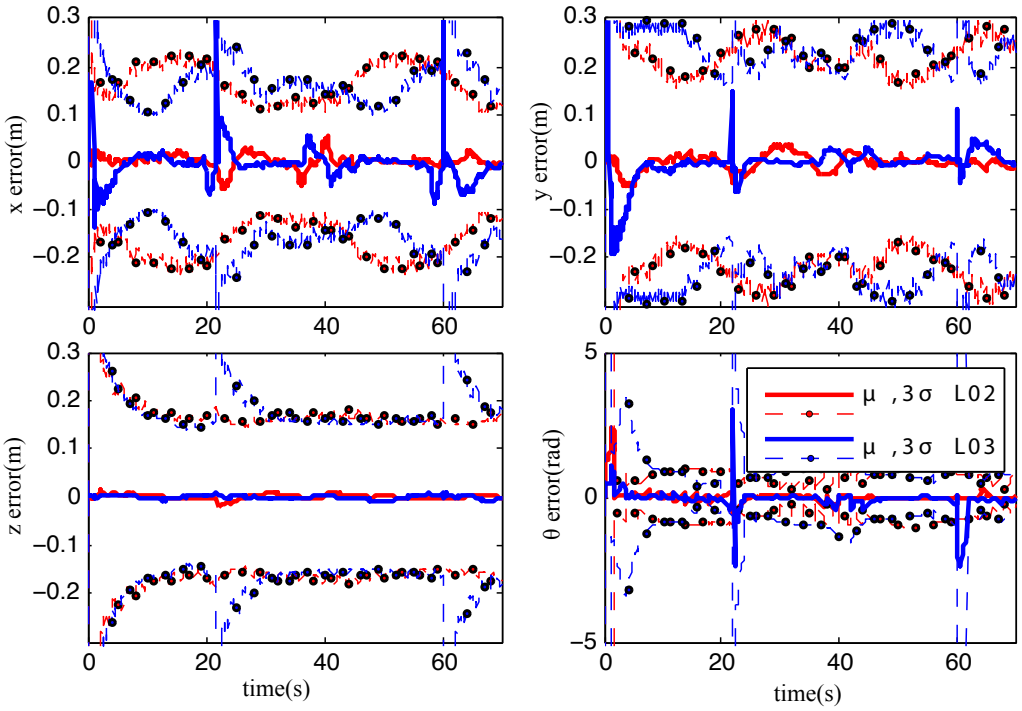

Figure 6.16: The path traversed by robots during the experiment and the estimated trajectory of the proposed DRL scheme.

Ch6_attachment.mp4 carries a descriptive video related to experiments detailed in this chapter. The video includes numerical simulations related to validation of the proposed two modules and a video of the experiment outlining the results achieved by the distributed relative localization method, data correspondence method, and the method proposed to incorporate self localization estimates to the framework.

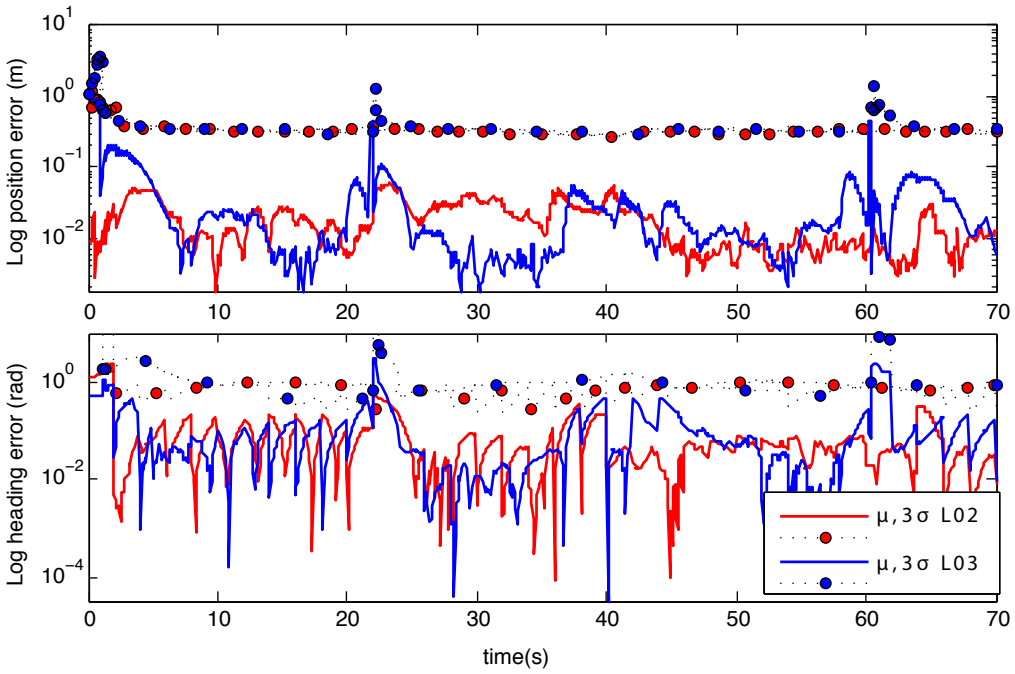

Figure 6.17: The path traversed by robots during the experiment and the estimated trajectory of the proposed DRL scheme.

6.4 Conclusion

This chapter presented the design and validation of two axillary modules required by the distributed relative localization method proposed in this thesis. This includes a method to incorporate self localization estimates to the proposed DRL framework, and a method to incorporate measurements with unknown data correspondence to the proposed DRL scheme. These modules were designed to operate in the same efficient communication and approximate fusion framework proposed in Chapter 5 of the thesis. The two approaches were validated using the UTIAS multi robot dataset and numerical simulations, where the designed method achieved consistent performance under multiple simulated scenarios. The results section also presents the validation of the overall DRL framework using multiple mobile robots equipped with laser scanners. The experiment validates the performance of the distributed relative localization

approach and the data correspondence approach, where accurate estimation of neighbouring robots was achieved when the neighbouring robots were in the field of view of a fuser. In a practical heterogenous robot mission, this field of view constraint can be minimized using the method proposed in this chapter which allows to incorporate self localization estimates in the DRL framework. This can effectively address short periods of non line of sight operation for less capable robots in the team which rely on odometers for self localization, while the more capable robots of a team can be tracked for much longer durations depending on the quality of their self localization estimates.

It is important to note that the case where all robots implement SLAM is an ideal situation which would effectively allow the robots to derive the relative poses without relying on any form of relative measurements. The significance of the DRL scheme is that it operates irrespective of the availability of SLAM and also that it services the robots which are not equipped with SLAM filters. Thus it serves as a team awareness module for heterogenous teams in order to support tasks such as formation control, and sense and avoidance. The method also allows attaining supervisory control of less capable platforms in a robot team by enabling a relative localization service for the less capable robots to operate in the vicinity of the fusers implementing SLAM.

Future work will attempt to further validate and improve the proposed localization framework for a multitude of scenarios including different measurement combinations, different rates of communication, and different levels of heterogeneity in the team. This would allow the distributed relative localization approach to mature as a sound method to serve the important function of providing localization estimates for formation control and supervisory control tasks of a heterogenous multi robot team.

Chapter 7

Conclusion and Outlook

The focus of this research study was to address the localization problem of a multi-robot system operating in GPS denied environments, using a relative localization-based navigation framework. Each element of this full framework was studied targeting an application towards a ground aerial multi-robot system. The research study formed three primary objectives:

1. Designing a scalable inter-robot relative measurement sensor for ground and MAV localization.

2. Designing a nonlinear filtering solution for relative localization.

3. Designing an efficient distributed relative localization method.

The research summary related to each objective is presented in the following sections.

7.1 Research summary based on Objective I

As the first objective this research study focused on designing an inter-robot relative measurement sensor applicable for ground and MAV localization. The research study

performed an extensive literature review on the available methods for relative sensing between robots. The outcome of this review indicated that the available solutions suffer from multiple drawbacks that make it difficult to implement those solutions as sensors for multi-robot studies. The strategy pursued by this study was an ultrasonic and vision based approach. This is motivated by the unprecedented performance that the two methods achieve individually in terms of range measurement and bearing measurement, respectively. The approach allowed better accuracies over the state of the art solution reported in [8], and allowed application of the sensor as a module to ground robots as well as aerial robots at a maximum rate of 10Hz. This was a considerable improvement over [8], which needed spherical array designs custom made for the robot to achieve this capability at a lower accuracy, and a higher power demand than the proposed approach. The proposed sensor was designed to be applicable in multi-robot domains using TDMA for hardware level measurement correspondence between robots and to coexist with other ultrasonic height measurement and obstacle avoidance modules of robots. The sensor was evaluated in a multi-robot setting with both ground and aerial robots, which validates its performance for practical multi-robot applications.

7.2 Research summary based on Objective II

The second objective was related to filtering of these measurements. Specifically, the relative localization problem faced by the robots and the design of nonlinear filters which are capable of addressing the filtering problem in an efficient manner were analysed. The absence of observability studies for relative localization under conditions of unknown velocities of platforms led this research to conduct a detailed analysis of the problem and establish theoretical limitations related to relative localization. The

necessary 2.5D simplifications of the filtering problem were established with filtering requirements relevant to the simplification. The theoretical analysis and limitations provided an excellent starting point for the filter designs pursued in this thesis.

Next, the research study developed the filters relevant to 2.5D relative localization. The focus was on exploiting the symmetry of the problem in the filter design approach and establishing optimal low cost filters which are applicable on the low level embedded controllers of the sensors. A novel steady state invariant EKF design approach was devised in this research study. Specifically three filters were designed using this approach: 1) a low cost steady state Invariant EKF for attitude reference systems, 2) a low cost steady state Invariant EKF for relative localization under known velocity conditions, 3) an invariant EKF design for relative localization for cases of unknown target platform velocities. The first two designs were complemented with a novel optimal method for tuning the parameters of the filters using noise parameters of the system, allowing the implementation of the filters on low cost embedded electronics. The third filter design is a stochastic filter which propagates the state and its covariance together, and hence is applicable in subsequent distributed filter implementations proposed in this work. The filter designs and observability limitations were experimentally evaluated to produce good validation of the proposed filters for low cost applications as well as for distributed implementations attempted in objective 3.

7.3 Research summary based on Objective III

The third objective of this research study was to develop a distributed method in order to perform the filtering operation in a multi-robot setting. The proposed method has the ability to address the communication constraints that are prevalent in the majority of available approaches, which extensively demand high bandwidth low la-

tency communication in the network. In order to address this problem, the research study proposed a method based on the well established distributed target tracking frameworks. The use of a target tracking framework in a multi-robot domain allows to perform communication at a prescribed low rate. This is a significant improvement that is otherwise not possible using almost all reported methods for distributed multi-robot localization. The study performed the necessary improvements to the distributed target tracking framework by establishing methods for consistent fusion of the estimates, performing initialization/recovery from unknown positions, performing sensor registration in a multi-robot setting, and achieving data correspondence in an efficient distributed manner.

Finally this study integrated the proposed method with already established SLAM filters running on some robots of the team. This integration allows a team of multiple robots to sense each other, localize each other, globally localize themselves using the knowledge of the network, and map the environment in a consistent manner, all achievable in an efficient distributed implementation where communication is only required at a preset low rate.

All these modules were validated as part of this research study. The research study revealed drawbacks and limitations of different elements of the overall system which are discussed in detail in Section 7.5.

7.4 Contributions

To summarize, this thesis made the following key contributions in relative localization of ground aerial systems, fulfilling all of the outlined research objectives.

1. Contributions from Objective I:

    (a) Hardware design of a novel scalable IRRM sensor network with sufficient

accuracy and range suitable for ground aerial systems operating in indoor environments.

(b) Experimental evaluation and optimization of the novel IRRM sensor design for UGV and MAV systems.

2. Contributions from Objective II:

(c) An observability analysis of the relative localization problem considering unknown platform velocities.

(d) A geometric nonlinear filter design for relative localization.

(e) An optimal gain tuning approach for low cost deterministic nonlinear filter designs related to relative localization.

3. Contributions from Objective III:

(f) A target tracking inspired distributed design for relative localization which supports asynchronous data communication and consistent estimation.

(g) A distributed data correspondence approach for multi-robot relative localization.

(h) A method to incorporate self localization filters running on robots with the proposed distributed relative localization framework.

This thesis lead to the following technical papers that report the contributions of the proposed work.

1. O. De Silva, G. K. I. Mann, and R. G. Gosine, "An Ultrasonic and Vision-Based Relative Positioning Sensor for Multirobot Localization," *IEEE Sensors Journal*, vol. 15, no. 3, pp. 1716-1726, 2015.

2. O. De Silva, G. K. I. Mann, and R. G. Gosine, "Efficient Distributed Multi-Robot Localization : A Target Tracking Inspired Design," in Proceedings, *IEEE International Conference on Robotics and Automation (ICRA)*, 2015.

3. O. De Silva, G. K. I. Mann, and R. G. Gosine, "An Efficient Distributed Data Correspondence Scheme for Multi-Robot Relative Localization," in Proceedings, *Moratuwa Engineering Research Conference (MERCON)*, IEEE, 2015.

4. O. De Silva, G. K. I. Mann, and R. G. Gosine, "Pairwise Observable Relative Localization in Ground Aerial Multi-Robot Networks," in Proceedings, *European Control Conference (ECC)*, IEEE, 2014, pp. 324-329.

5. O. De Silva, G. K. I. Mann, and R. G. Gosine, "Relative Localization with Symmetry Preserving Observers," in Proceedings, *Canadian Conference on Electrical and Computer Engineering (CCECE)*, IEEE, 2014.

6. O. De Silva, G. K. I. Mann, and R. G. Gosine, "Automated Tuning of the Nonlinear Complementary Filter for an Attitude Heading Reference Observer," in Proceedings, *IEEE Workshop on Robot Vision*, 2013, pp. 171-176.

7. O. De Silva, G. K. I. Mann, and R. G. Gosine, "Robot Operating System Based Relative Localization Test Bed," in Proceedings, *Newfoundland Electrical and Computer Engineering Conference*, 2013.

8. O. De Silva, G. K. I. Mann, and R. G. Gosine, "Multiple Wii-mote based 3D tracking system calibration," in Proceedings, *Newfoundland Electrical and Computer Engineering Conference*, 2012.

9. O. De Silva, G. K. I. Mann, and R. G. Gosine, "Development of a relative localization scheme for ground-aerial multi-robot systems," in Proceedings, *IEEE*

International Conference on Intelligent Robots and Systems (IROS), 2012, pp. 870-875.

Additionally the following completed papers are under review for publication:

10 O. De Silva, G. K. I. Mann, and R. G. Gosine, "Relative Localization of Robots with Steady State Invariant Extended Kalman Filtering," Under review in *IEEE Transactions on Control System Technology*, 2015.

11 O. De Silva, G. K. I. Mann, and R. G. Gosine, "The Right Invariant Nonlinear Complimentary Filter: A Low cost Optimal Design for Attitude Estimation" Under review, 2015.

7.5 Future research directions

The overall final design validated in this thesis constitutes a practical and theoretically sound solution to the problem of GPS denied relative localization of robots with many avenues for improvement through further research. The relative sensing module, filtering module, and the distributed localization module of the proposed approach can be developed further along three main avenues as discussed in the following sections.

7.5.1 Phase III design of the relative measurement sensor

The current design of the sensor requires improvements in terms of realizing omnidirectional sensing capability and operating in outdoor settings under direct sunlight conditions. These capabilities are necessary if the sensor is to be used in practical operations such as underground mines where better sensing volumes are required for

the robots to locate each other, or earthquake damaged buildings where the robots are required to operate in both indoor and outdoor environments under direct sunlight exposure of the sensing system.

The objective of the next major version of the sensor is to achieve a solution which has an extended field of view and which is capable of operating both in indoor and outdoor environments. The design is expected to combine the capability of robust camera based bearing estimation and ultrasonic array signal processing techniques. This research would address the following limitations related to the current iteration of the sensor.

- **Field of view limitations of the relative sensing module:** The vision based bearing measurement method of the proposed relative sensing module has a limited field of view in comparison to the omnidirectional reception capability of the acoustic modules of the sensor. Although a panning servo mechanism is implemented for improved field of view, this has poor performance in terms of speed and increases the power consumption of the sensor. In order to effectively address the field of view limitation of the design, the preferred approach is to establish better ultrasonic based bearing measurement capability and use a vision sensor only for improvement of the estimates in its field of view.

- **Outdoor application of the relative measurement sensor:** In the current form, the proposed relative sensor module is not applicable in outdoor settings. This is mainly due to the inability of the IR based vision sensor to operate under direct sunlight. A solution for this is not to rely on IR features for bearing measurement, and use passive visual feature detection with a standard CMOS camera for bearing measurement. However, the feature detection method employed should be kept elementary to meet the computational constraints of the sensor. Improving the ultrasonic bearing measurement capability pursued

as ongoing research work also contributes to enabling the system in outdoor settings, since ultrasonic modules are equally applicable for indoor and outdoor environments.

This design assumes the vision based passive feature detection modules are auxiliary sources for measurement improvement while ultrasonic modules provide both range and bearing measurements. This development is inspired and enabled by recent developments in omni-directional MEMS microphones [79] and surface mount ultrasonic sensors [80]. Other evolutionary improvements required for the sensor include, improving the signal to noise ratio under flight conditions and optimizing the design for weight and power consumption.

7.5.2 Design and implementation of estimators with dynamic constraints

The localization filters designed in this thesis are 2.5D designs which suit applications where low roll and pitch dynamics can be assumed. A full SE(3) formulation as presented in Appendix 1 would complement those applications where high velocity maneuvers are expected. This was not considered in the overall DRL design, in order to keep the formulation minimal and because the design did not consider the dynamic constraints of the platforms which would otherwise require a full SE(3) analysis. Recent work reported in [96, 97], has demonstrated the ability to use the dynamic model of MAVs to achieve better attitude filtering and velocity estimation. Filter development where the dynamics of the platform and couplings with pose filtering modules are considered presents important research directions desirable for nonlinear filter designs for relative localization. It is expected to investigate in to the full SE(3) design of the filter with dynamic constraints, which would ultimately allow the filter's application

over a wide range of aggressive trajectories and under different dynamic constraints of the attaching platforms. Other evolutionary developments that are required by the relative localization filter design includes theoretical proofs related to performance of the filters under non permanent trajectories, and incorporating dynamic constraints to the steady state versions of the filter.

7.5.3 Multi robot exploration and mapping based on distributed relative localization

The overall DRL framework proposed in this thesis requires experimentation in the field where the DRL method is applied in real life missions as the next step of the validation process. This research study would design and deploy an autonomous mapping system which is primarily based on relative localization estimates. The following limitations related to the current design of the DRL scheme would be addressed in realizing autonomous mapping using the robots.

- **Polar sensor models:** The overall heterogenous navigation framework is designed for a class of sensors; i.e., a robot network with relative position measurements. The filters of the framework do not translate well to polar parametrization. This is due to the difficulty of identifying the symmetries when a polar form is used, and the highly nonlinear characteristics of the polar form to cartesian mapping functions. However, cartesian parametrization of a sensor model is a good approximation of the relative position sensing technologies used by robots, under low noise conditions comparable to the levels experienced by the designed sensor. Thus under low noise conditions the framework can be used effectively when both range and bearing data are present, which is the case for the proposed autonomous mapping application. However, the method is not

readily applicable to range only and bearing only multi-robot localization problems. This is a potential research direction which would allow the use of range only beacons and bearing based perception means such as cameras to be addressed in an efficient manner where communication is performed at low rates, to support practical bandwidth limitations.

- **Theoretical performance bounds:** The distributed relative localization design presented in this thesis lacks theoretical performance bounds in terms of minimum rates that can be supported by the algorithm, limiting communication to achieving prescribed performance levels, and including the effects of packet routing and communication delays on the approach. These studies are valuable extensions to the proposed method which would provide performance guarantees of the system during the design process.

- **Non line of sight operation:** The current design of the DRL scheme does not explicitly posses capability of confining less capable robots of the team to an area which can be estimated using the DRL scheme. Therefore it is necessary to establish control laws for the less capable agents of a team, and improve navigation capability of the robots for short periods of non line of sight operation.

- **Validation of DRL for long period operation:** The experimental validation presented in this thesis is limited to operations which span a scale of few minutes. Hence the experimental work of the thesis does not fully represent timescales of practical missions which would span couple of hours. Therefore it is necessary to validate the performance of the methods for more representative operational periods by implementing a practical indoor mapping and exploration operation using the DRL framework as future work.

On site validation of the DRL scheme combined with suitable designs to overcome the said limitations can be considered as the overall goal of future research study.

The completed research study of this thesis contributes a necessary, theoretically valid, and experimentally validated body of work to the area of GPS denied localization of ground aerial systems. The research opens up many interesting elements of the overall system requiring further scientific research which is currently driving research efforts of the Intelligent Systems lab at Memorial university of Newfoundland. It is expected that this research would develop to achieve local field trials in the near future, where the algorithms, sensors, and distribution modules of this work operate in unison to attain a highly reliable and robust system applicable for real life missions involving autonomous ground and aerial robots.

Appendices

A Relative localization in SE(3) using Invariant Extended Kalman Filtering

This section provides the IEKF derivation for the relative localization problem in SE(3). The $S2 - Star$ configuration introduced in (3.15) is used for filter derivation since it constitutes the configuration which only considers the locally available measurements for localization purposes and allows communicated target platform quantities to be incorporated at low rates as measurements.

Step 1: Identify System Symmetries

Identifying symmetries of the system is the process of finding the actions on the states $\mathbf{x}$, inputs $\mathbf{u}$, and outputs $\mathbf{y}$, such that the system is *G-invariant*. Consider the system given by $S_2 - Star$ configuration in (3.15) with noises removed i.e. $\nu = 0$, $\mathbf{w} = 0$. For group $G = SE(3)$ define group actions on states $\varphi_g : G \times X \to X$, on input $\psi_g : G \times U \to U$, and on measurements $\rho_g : G \times Y \to Y$ as follows.

$$
\begin{aligned}
\varphi_g \begin{pmatrix} \mathbf{p} \\ \mathbf{R}_\theta \end{pmatrix} &= \begin{pmatrix} \mathbf{R}_{\theta_0}\mathbf{p} + \mathbf{p}_0 \\ \mathbf{R}_{\theta_0}\mathbf{R}_\theta \end{pmatrix} \\
\psi_g \begin{pmatrix} \mathbf{v}_l \\ \boldsymbol{\omega}_l \\ \mathbf{g}_l \end{pmatrix} &= \begin{pmatrix} \mathbf{R}_{\theta_0}\mathbf{v}_l - [\mathbf{R}_{\theta_0}\boldsymbol{\omega}_l]_\times \mathbf{p}_0 \\ \mathbf{R}_{\theta_0}\boldsymbol{\omega}_l \\ \mathbf{R}_{\theta_0}\mathbf{g}_l \end{pmatrix} \\
\rho_g \begin{pmatrix} \mathbf{y_p} \\ \mathbf{y_{gi}} \\ \mathbf{y_{vi}} \\ \mathbf{y}_{\omega\mathbf{i}} \end{pmatrix} &= \begin{pmatrix} \mathbf{R}_{\theta_0}\mathbf{y_p} + \mathbf{p}_0 \\ \mathbf{y_{gi}} \\ \mathbf{y_{vi}} \\ \mathbf{y}_{\omega\mathbf{i}} \end{pmatrix}
\end{aligned} \tag{1}
$$

Consider a group element $g_0 = (\mathbf{p}_0,\ \mathbf{R}_{\theta_0}) \in G$. Equation set (2) verifies that the system given by (3.15) is *G-invariant* under the group actions φ_g and ψ_g, i.e., $D\varphi_g \circ f(\mathbf{x}, \mathbf{u}) = f(\varphi_g(\mathbf{x}), \psi_g(\mathbf{u}))$.

$$
\begin{aligned}
&\tfrac{d}{dt}\varphi_g \begin{pmatrix} \mathbf{p} \\ \mathbf{R}_\theta \end{pmatrix} = \tfrac{d}{dt} \begin{pmatrix} \mathbf{R}_{\theta_0}\mathbf{p} + \mathbf{p}_0 \\ \mathbf{R}_{\theta_0}\mathbf{R}_\theta \end{pmatrix} = \begin{pmatrix} \mathbf{R}_{\theta_0}\dot{\mathbf{p}} \\ \mathbf{R}_{\theta_0}\dot{\mathbf{R}}_\theta \end{pmatrix} \\
&= \begin{pmatrix} \mathbf{R}_{\theta_0}(\mathbf{R}_\theta \mathbf{v}_i - \mathbf{v}_l - [\boldsymbol{\omega}_l]_\times \mathbf{p}) \\ \mathbf{R}_{\theta_0}\mathbf{R}_\theta [\boldsymbol{\omega}_i - \mathbf{R}_\theta^T \boldsymbol{\omega}_l]_\times \end{pmatrix} \\
&= \begin{pmatrix} \mathbf{R}_{\theta_0}\mathbf{R}_\theta \mathbf{v}_i - \Big(\mathbf{R}_{\theta_0}\mathbf{v}_l \\ -[\mathbf{R}_{\theta_0}\boldsymbol{\omega}_l]_\times \mathbf{p}_0 \Big) - [\mathbf{R}_{\theta_0}\boldsymbol{\omega}_l]_\times (\mathbf{R}_{\theta_0}\mathbf{p} + \mathbf{p}_0) \\ \mathbf{R}_{\theta_0} R_\theta [\boldsymbol{\omega}_i - \mathbf{R}_\theta^T \mathbf{R}_{\theta_0}^T \mathbf{R}_{\theta_0} \boldsymbol{\omega}_l]_\times \end{pmatrix} \\
&= \begin{pmatrix} \varphi_g(\mathbf{R}_\theta)\psi_g(\mathbf{v}_i) - \psi_g(\mathbf{v}_l) - [\psi_g(\boldsymbol{\omega}_l)]_\times \varphi_g(\mathbf{p}) \\ \varphi_g(\mathbf{R}_\theta)[\psi_g(\boldsymbol{\omega}_i) - \varphi_g(\mathbf{R}_\theta)^T \psi_g(\boldsymbol{\omega}_l)]_\times \end{pmatrix} \\
&\tfrac{d}{dt}\varphi_g \begin{pmatrix} \mathbf{v}_i \\ \boldsymbol{\omega}_i \end{pmatrix} = \tfrac{d}{dt} \begin{pmatrix} \mathbf{v}_i \\ \boldsymbol{\omega}_i \end{pmatrix} = \begin{pmatrix} \mathbf{0} \\ \mathbf{0} \end{pmatrix} \\
&\Rightarrow D\varphi_g \circ f(\mathbf{x}, \mathbf{u}) = f(\varphi_g(\mathbf{x}), \psi_g(\mathbf{u}))
\end{aligned} \tag{2}
$$

Here we used the rotational invariance of the cross product as part of the derivation process. i.e., $\mathbf{R}_{\theta_0}(\boldsymbol{\omega}_l \times \mathbf{p}) = \mathbf{R}_{\theta_0}\boldsymbol{\omega}_l \times \mathbf{R}_{\theta_0}\mathbf{p}$. The measurement model given by (3.15) is found to be *G-equivariant* under the group actions ρ_g, φ_g, ψ_g. i.e., $\rho_g(\mathbf{y}) = h(\varphi_g(\mathbf{x}), \psi_g(\mathbf{u}))$.

$$h(\varphi_g(\mathbf{x}), \psi_g(\mathbf{u})) = \begin{pmatrix} \mathbf{R}_{\theta_0}\mathbf{p} + \mathbf{p}_0 \\ \mathbf{R}_\theta^T \mathbf{R}_{\theta_0}^T \mathbf{R}_{\theta_0} \mathbf{g}_l \\ \mathbf{v}_i \\ \boldsymbol{\omega}_i \end{pmatrix} = \begin{pmatrix} \mathbf{R}_{\theta_0}\mathbf{y}_\mathbf{p} + \mathbf{p}_0 \\ \mathbf{y}_{gi} \\ \mathbf{y}_{vi} \\ \mathbf{y}_{\omega i} \end{pmatrix} \tag{3}$$
$$\Rightarrow \rho_g(\mathbf{y}) = h(\varphi_g(\mathbf{x}), \psi_g(\mathbf{u}))$$

Step 2: Identify Invariants

The moving frame is identified by solving the equation $\phi_g(\mathbf{x}) = e$ for $g := \gamma(\mathbf{x})$, where e is the group identity element.

$$\varphi_g \begin{pmatrix} \mathbf{p} \\ \theta \end{pmatrix} = \begin{pmatrix} \mathbf{R}_{\theta_0}\mathbf{p} + \mathbf{p}_0 \\ \mathbf{R}_{\theta_0}\mathbf{R}_\theta \end{pmatrix} = \begin{pmatrix} \mathbf{0} \\ \mathbf{I} \end{pmatrix}$$
$$\Rightarrow \gamma(\mathbf{x}) = (-\mathbf{R}_\theta^T \mathbf{p}, \mathbf{R}_\theta^T)$$

Then the set of invariants $\mathcal{I}(\hat{\mathbf{x}})$ is found by operating $\gamma(\hat{\mathbf{x}})$ on U and Y.

$$\begin{pmatrix} \mathcal{I}_{v_l} \\ \mathcal{I}_{\omega_l} \\ \mathcal{I}_{g_l} \end{pmatrix} = \psi_{\gamma(\hat{\mathbf{x}})} \begin{pmatrix} \mathbf{v}_l \\ \boldsymbol{\omega}_l \\ \mathbf{g}_l \end{pmatrix} = \begin{pmatrix} \mathbf{R}_{\hat{\theta}}^T \mathbf{v}_l + [\mathbf{R}_{\hat{\theta}}^T \boldsymbol{\omega}_l]_\times \mathbf{R}_{\hat{\theta}}^T \hat{\mathbf{p}} \\ \mathbf{R}_{\hat{\theta}}^T \boldsymbol{\omega}_l \\ \mathbf{R}_{\hat{\theta}}^T \mathbf{g}_l \end{pmatrix}$$

$$\mathcal{J}(\hat{\mathbf{x}}, \mathbf{u}) = \rho_{\gamma(\hat{\mathbf{x}})} \begin{pmatrix} \mathbf{y}_p \\ \mathbf{y}_{gi} \\ \mathbf{y}_{vi} \\ \mathbf{y}_{\omega i} \end{pmatrix} = \begin{pmatrix} \mathbf{R}_{\hat{\theta}}^T \mathbf{y}_p - \mathbf{R}_{\hat{\theta}}^T \hat{\mathbf{p}} \\ \mathbf{y}_{gi} \\ \mathbf{y}_{vi} \\ \mathbf{y}_{\omega i} \end{pmatrix}$$

The trajectories for which the invariants $\mathcal{I}$,$\mathcal{J}$ are constant are termed permanent trajectories.

The Invariant frame W is defined as the mapping of basis vectors ν_i of the tangent space $\mathcal{T}X$, by the smooth map $D\varphi_g$. The basis vectors $\nu_i = e_i$ for $T\mathbb{R}^3$ and $\nu_i = S(e_i)$ for $TSO(3)$, where e_i denotes the standard basis of $\mathbb{R}^3$. The invariant frame is found as follows.

$$W = \frac{d}{d\tau}\left(\varphi_{\gamma(\hat{x})^{-1}}(\nu_i\tau)\right)|_{\tau=0} = \begin{pmatrix} \mathbf{R}_{\hat{\theta}}e_i \\ \mathbf{R}_{\hat{\theta}}S(e_i) \\ e_i \\ e_i \end{pmatrix}$$

Step 3: Identify Invariant Error State Dynamics

The invariant observer for a general *G-invariant* system $\dot{x} = f(x,u)$, and a *G-equivariant* output $y = h(x,u)$, is given by *Theorem* 1 in reference [41]. It takes the following general form.

$$F(\hat{\mathbf{x}},\mathbf{u},\mathbf{y}) = f(\hat{\mathbf{x}},\mathbf{u}) + W(\hat{\mathbf{x}})L(\mathcal{I},\mathcal{E})\mathcal{E}(\hat{\mathbf{x}},\mathbf{u},\mathbf{y}) \tag{4}$$

The invariant error $\mathcal{E}$ is defined as $\mathcal{E} = \mathcal{J}(\hat{\mathbf{x}},\mathbf{y}) - \mathcal{J}(\hat{\mathbf{x}},h(\hat{\mathbf{x}},\mathbf{u}))$ and is found as follows.

$$\begin{aligned}\mathcal{E}(\hat{\mathbf{x}},\mathbf{u},\mathbf{y}) &= \rho_{\gamma(\hat{\mathbf{x}})}(h(\hat{\mathbf{x}})) - \rho_{\gamma(\hat{\mathbf{x}})}(\mathbf{y}) \\ &= \begin{pmatrix} \mathbf{R}_{\hat{\theta}}^T(\hat{\mathbf{p}} - \mathbf{y}_p) \\ \hat{\mathbf{g}}_\mathbf{i} - \mathbf{y}_{g_i} \\ \hat{\mathbf{v}}_\mathbf{i} - \mathbf{y}_{v_i} \\ \hat{\omega}_\mathbf{i} - \mathbf{y}_{\omega_i} \end{pmatrix}\end{aligned}$$

The invariant observer for the problem is obtained by substituting the invariant output

error and the invariant frame in (4).

$$\begin{pmatrix} \dot{\hat{\mathbf{p}}} \\ \dot{\mathbf{R}}_{\hat{\theta}} \\ \dot{\hat{\mathbf{v}}}_i \\ \dot{\hat{\boldsymbol{\omega}}}_i \end{pmatrix} = \begin{pmatrix} \mathbf{R}_{\hat{\theta}}\hat{\mathbf{v}}_i - \mathbf{v}_l - \boldsymbol{\omega}_l \times \hat{\mathbf{p}} \\ \mathbf{R}_{\hat{\theta}}[\hat{\boldsymbol{\omega}}_i - \mathbf{R}_{\hat{\theta}}^T\boldsymbol{\omega}_l]_\times \\ \mathbf{0} \\ \mathbf{0} \end{pmatrix} + \begin{pmatrix} \mathbf{R}_{\hat{\theta}}(L_p\mathcal{E}) \\ \mathbf{R}_{\hat{\theta}}S(L_\theta\mathcal{E}) \\ L_v\mathcal{E} \\ L_\omega\mathcal{E} \end{pmatrix} \tag{5}$$

The invariant estimation error η of the observer is defined as $\eta = \varphi_{\gamma(\hat{\mathbf{x}})}(\hat{\mathbf{x}}) - \varphi_{\gamma(\hat{\mathbf{x}})}(\mathbf{x})$. The invariant estimation error reads as

$$\begin{aligned} \eta &= \varphi_{\gamma(\hat{\mathbf{x}})}(\hat{\mathbf{x}}) - \varphi_{\gamma(\hat{\mathbf{x}})}(\mathbf{x}) \\ &= \begin{pmatrix} \mathbf{R}_{\hat{\theta}}^T(\hat{\mathbf{p}} - \mathbf{p}) \\ \mathbf{I}_3 - \mathbf{R}_{\hat{\theta}}^T\mathbf{R}_\theta \\ \hat{\mathbf{v}}_i - \mathbf{v}_i \\ \hat{\boldsymbol{\omega}}_i - \boldsymbol{\omega}_i \end{pmatrix} =: \begin{pmatrix} \eta_p \\ I - \mathbf{R}_{\eta_\theta}^T \\ \eta_{vi} \\ \eta_{\omega i} \end{pmatrix} \end{aligned}$$

In order to perform error state Kalman filtering, a stochastic model of the system should be deduced. The new stochastic model should also preserve the stochastic versions of *G-invariant* and *G-equivariant* definitions given by the following equations.

$$\begin{aligned} D\varphi_g \circ f(\mathbf{x}, \mathbf{u}, M(x)\mathbf{w}) &= f\Big(\varphi_g(\mathbf{x}), \psi_g(\mathbf{u}), M(\varphi_g(x))\mathbf{w}\Big) \\ \rho_g\Big(h(\mathbf{x}, \mathbf{u}, N(x)\nu)\Big) &= h\Big(\varphi_g(\mathbf{x}), \psi_g(\mathbf{u}), N(\phi_g(x))\nu\Big) \end{aligned} \tag{6}$$

The definitions given by (6) are satisfied when $M(x) = \mathbf{R}_\theta$ for $\mathbf{w}_p$, while all other noise terms remain unchanged. i.e., $M(x), N(x) = \mathbf{I}$ for $\mathbf{w}_\theta, \mathbf{w}_{vi}, \mathbf{w}_{\omega i}, \boldsymbol{\nu}_p, \boldsymbol{\nu}_{gi}, \boldsymbol{\nu}_{vi}$, and $\boldsymbol{\nu}_{\omega i}$.

Now the error state dynamics of the system is derived as a function of η. The

invariant output error $\mathcal{E}$ in terms of η reads

$$\begin{aligned}\mathcal{E}(\hat{\mathbf{x}},\mathbf{u},\mathbf{y}) &= \mathbf{R}_{\hat{\theta}}^T(\hat{\mathbf{p}}-\mathbf{y}_p)\\ &= \mathbf{R}_{\hat{\theta}}^T(\hat{\mathbf{p}}-\mathbf{p}-\mathbf{R}_\theta\boldsymbol{\nu}_p)\\ \Rightarrow \mathcal{E}(\eta,\nu) &= \eta_p - \mathbf{R}_{\eta_\theta}^T\boldsymbol{\nu}_p\end{aligned}$$

The other output error terms corresponding to $\mathbf{y}_{g_i}$, $\mathbf{y}_{v_i}$, $\mathbf{y}_{\omega_i}$, remain trivial. By differentiating the estimation error state, we have

$$\begin{pmatrix}\dot{\eta_p}\\ \dot{\mathbf{R}}_{\eta_\theta}\\ \dot{\eta_{vi}}\\ \dot{\eta_{\omega i}}\end{pmatrix} = \begin{pmatrix}\dot{\mathbf{R}}_{\hat{\theta}}^T(\hat{\mathbf{p}}-\mathbf{p})+\mathbf{R}_{\hat{\theta}}^T(\dot{\hat{\mathbf{p}}}-\dot{\mathbf{p}})\\ \dot{\mathbf{R}}_\theta^T\hat{\mathbf{R}}_\theta+\mathbf{R}_\theta^T\dot{\hat{\mathbf{R}}}_\theta\\ \dot{\hat{\mathbf{v}}}_i-\dot{\mathbf{v}}_i\\ \dot{\hat{\boldsymbol{\omega}}}_i-\dot{\boldsymbol{\omega}}_i\end{pmatrix}$$

By substituting the derivative terms and identifying $\dot{\mathbf{R}}_\theta^T = S(\mathbf{R}_\theta^T\boldsymbol{\omega}_l-\boldsymbol{\omega}_i-\mathbf{w}_\omega)\mathbf{R}_\theta^T$, $\dot{\mathbf{R}}_{\hat{\theta}}^T = S(\mathbf{R}_{\hat{\theta}}^T\boldsymbol{\omega}_l-\boldsymbol{\omega}_i-L_\theta\mathcal{E})\mathbf{R}_\theta^T$, we can derive the error state dynamics of the observer.

$$\begin{pmatrix}\dot{\eta_p}\\ \\ \dot{\mathbf{R}}_{\eta_\theta}\\ \dot{\eta_{vi}}\\ \dot{\eta_{\omega i}}\end{pmatrix} = \begin{pmatrix}S(-\hat{\boldsymbol{\omega}}_i+\eta_{\omega i})\eta_p+(I_3-\mathbf{R}_{\eta_\theta}^T)(\hat{\mathbf{v}}_i-\eta_{vi})\\ -S(L_\theta\mathcal{E})\eta_p-\mathbf{R}_{\eta_\theta}^T\mathbf{w}_v+L_p\mathcal{E}\\ \mathbf{R}_{\eta_\theta}S(\hat{\boldsymbol{\omega}}_i+L_\theta\mathcal{E})-S(\hat{\boldsymbol{\omega}}_i-\eta_{\omega_i}+\mathbf{w}_\omega)\mathbf{R}_{\eta_\theta}\\ L_{vi}\mathcal{E}-\mathbf{w}_{vi}\\ L_{\omega i}\mathcal{E}-\mathbf{w}_{\omega i}\end{pmatrix} \tag{7}$$

The symmetry preserving observer for the system is (5). The gains L should be designed such that the invariant error state system given by (7) is stable.

Step 4: Perform Error State Kalman Filtering

The gain design of the observer can be achieved using an error state extended Kalman filtering approach.

The nonlinear error state system is already found by equation (7). Next a lin-

earization is performed by applying the small signal assumption for the error states. i.e., $\eta = \delta\eta$. Linearizing the rotation error dynamics $\mathbf{R}_{\eta\theta}$ is difficult in its matrix form. This is converted to a vector form as follows. For small angles $\delta\eta_\theta$, the rotation matrix $\mathbf{R}_{\eta\theta}$ is simplified as $\mathbf{R}_{\delta\eta\theta} = I + [\delta\eta_\theta]_\times$. This approximation is applied to $\dot{\mathbf{R}}_{\eta\theta}$ in (7), and the second order error terms such as $[\delta\eta_{\omega i}]_\times[\delta\eta_\theta]_\times$, $[\mathbf{w}_\theta]_\times[\delta\eta_\theta]_\times$ are removed. By identifying that $[\delta\eta_\theta]_\times[\hat{\boldsymbol{\omega}}i]_\times - [\hat{\boldsymbol{\omega}}i]_\times[\delta\eta_\theta]_\times = [\delta\eta_\theta \times \hat{\boldsymbol{\omega}}i]_\times$, we get

$$\dot{\mathbf{R}}_{\delta\eta\theta} = [\dot{\delta\eta_\theta}]_\times = [\delta\eta_\theta \times \omega_i]_\times + [\delta\eta_{\omega i}]_\times - [\mathbf{w}_v]_\times + [L_\theta E]_\times$$

Using this expression, the error state dynamic system for $\delta\eta_\theta$ can be extracted.

$$\dot{\delta\eta_\theta} \quad = \delta\eta_\theta \times \boldsymbol{\omega}_i + \delta\eta_{\omega i} - \mathbf{w}_v + L_\theta E$$

Linearization of the error states $\eta_p,\ \eta_\theta,\ \eta_{vi},\ \eta_{\omega i}$, is performed by applying the small signal assumption and removing the resulting second order error terms. This results in a Linear Kalman like filter structure.

$$\begin{pmatrix} \dot{\delta\eta_p} \\ \dot{\delta\eta_\theta} \\ \dot{\delta\eta_{vi}} \\ \dot{\delta\eta_{\omega i}} \end{pmatrix} = (A - KC) \begin{pmatrix} \delta\eta_p \\ \delta\eta_\theta \\ \delta\eta_{vi} \\ \delta\eta_{\omega i} \end{pmatrix} - M \begin{pmatrix} \mathbf{w}_p \\ \mathbf{w}_\theta \\ \mathbf{w}_{vi} \\ \mathbf{w}_{\omega i} \end{pmatrix} + KN \begin{pmatrix} \nu_p \\ \nu_{gi} \\ \nu_{vi} \\ \nu_{\omega i} \end{pmatrix}$$

The A,C,K,M,N matrices are identified from this linearized system. This completes the design of the invariant Kalman filter for relative localization in 3D. The resulting

filter can be summarized as follows.

Initialization

$$\begin{aligned}\hat{\mathbf{x}} &= \begin{bmatrix}\mathbf{y}_p & \mathbf{I} & \mathbf{0} & \mathbf{0}\end{bmatrix}^T \\ P &= \mathrm{E}(\boldsymbol{\eta}\boldsymbol{\eta}^T) = \mathbf{I} \\ Q &= \mathrm{E}(\mathbf{w}\mathbf{w}^T) \\ R &= \mathrm{E}(\boldsymbol{\nu}\boldsymbol{\nu}^T)\end{aligned}$$

3D Observer

$$\begin{pmatrix}\dot{\hat{\mathbf{p}}} \\ \dot{\hat{\mathbf{R}}}_\theta \\ \dot{\hat{\mathbf{v}}}_i \\ \dot{\hat{\omega}}_i\end{pmatrix} = \underbrace{\begin{pmatrix}\mathbf{R}_{\hat{\theta}}\hat{\mathbf{v}}_i - \mathbf{v}_l - \boldsymbol{\omega}_l \times \hat{\mathbf{p}} \\ \mathbf{R}_{\hat{\theta}}[\hat{\boldsymbol{\omega}}_i - \mathbf{R}_{\hat{\theta}}^T\boldsymbol{\omega}_l]_\times \\ \mathbf{0} \\ \mathbf{0}\end{pmatrix}}_{\textit{State Prediction}} + \underbrace{\begin{pmatrix}\mathbf{R}_{\hat{\theta}}(L_p\mathcal{E}) \\ \mathbf{R}_{\hat{\theta}}S(L_\theta\mathcal{E}) \\ L_v\mathcal{E} \\ L_\omega\mathcal{E}\end{pmatrix}}_{\textit{State Correction}}$$

$$\textit{Innovation} \qquad \mathcal{E} = \begin{pmatrix}\mathbf{R}_{\hat{\theta}}^T(\hat{\mathbf{p}} - \mathbf{y}_p) \\ \hat{\mathbf{g}}_\mathbf{i} - \mathbf{y}_{g_i} \\ \hat{\mathbf{v}}_\mathbf{i} - \mathbf{y}_{v_i} \\ \hat{\boldsymbol{\omega}}_\mathbf{i} - \mathbf{y}_{\omega_i}\end{pmatrix}$$

$$\textit{Gain Matrix} \quad K = \begin{bmatrix}-L_p & -L_\theta & -L_{vi} & -L_\omega\end{bmatrix}^T$$

Covariance Prediction

$$\begin{aligned}A &= \begin{bmatrix}S(-\hat{\boldsymbol{\omega}}_i) & S(-\hat{\mathbf{v}}_i) & \mathbf{I} & \mathbf{0} \\ \mathbf{0} & S(-\hat{\boldsymbol{\omega}}_i) & \mathbf{0} & \mathbf{I} \\ \mathbf{0} & \mathbf{0} & \mathbf{0} & \mathbf{0} \\ \mathbf{0} & \mathbf{0} & \mathbf{0} & \mathbf{0}\end{bmatrix} \\ M &= \mathbf{I} \\ \dot{P} &= AP + PA^T + MQM^T\end{aligned}$$

Covariance Correction

$$\begin{aligned}C &= \begin{bmatrix}\mathbf{I} & \mathbf{0} & \mathbf{0} & \mathbf{0} \\ \mathbf{0} & S(\hat{\mathbf{R}}_\theta^\mathbf{T}\mathbf{g_l}) & \mathbf{0} & \mathbf{0} \\ \mathbf{0} & \mathbf{0} & \mathbf{I} & \mathbf{0} \\ \mathbf{0} & \mathbf{0} & \mathbf{0} & \mathbf{I}\end{bmatrix} \\ N &= \mathbf{I} \\ K &= PC^T(CPC^T + NRN^T)^{-1} \\ P &= (I - KC)P\end{aligned}$$

Bibliography

[1] A. Breitenmoser, L. Kneip, and R. Siegwart, "A Monocular Vision-based System for 6D Relative Robot Localization," in *IEEE/RSJ International Conference on Intelligent Robots and Systems*, pp. 79–85, 2011.

[2] B. Kim, M. Kaess, L. Fletcher, J. Leonard, A. Bachrach, N. Roy, and S. Teller, "Multiple Relative Pose Graphs for Robust Cooperative Mapping," in *IEEE International Conference on Robotics and Automation*, pp. 3185–3192, 2010.

[3] M. Achtelik, T. Zhang, K. Kühnlenz, and M. Buss, "Visual tracking and control of a quadcopter using a stereo camera system and inertial sensors," in *International Conference on Mechatronics and Automation*, pp. 2863–2869, Aug. 2009.

[4] K. E. Wenzel, A. Masselli, and A. Zell, "Visual Tracking and Following of a Quadrocopter by another Quadrocopter," in *IEEE/RSJ International Conference on Intelligent Robots and Systems*, pp. 4993–4998, 2012.

[5] F. Rivard, J. Bisson, F. Michaud, and D. Létourneau, "Ultrasonic relative positioning for multi-robot systems," in *IEEE International Conference on Robotics and Automation*, pp. 323–328, May 2008.

[6] J. Eckert, K. Koeker, P. Caliebe, F. Dressler, and R. German, "Self-localization capable mobile sensor nodes," in *IEEE International Conference on Technologies for Practical Robot Applications*, pp. 224–229, Ieee, Nov. 2009.

[7] J. Pugh, X. Raemy, C. Favre, and R. Falconi, "A Fast Onboard Relative Positioning Module for Multirobot Systems," *IEEE/ASME Transactions on Mechatronics*, vol. 14, no. 2, pp. 151–162, 2009.

[8] J. F. Roberts, T. Stirling, J.-C. Zufferey, and D. Floreano, "3-D relative positioning sensor for indoor flying robots," *Autonomous Robots*, vol. 33, pp. 5–20, Feb. 2012.

[9] B. Grocholsky, J. Keller, V. Kumar, and G. Pappas, "Cooperative Air and Ground Surveillance," *IEEE Robotics & Automation Magazine*, vol. 13, no. 3, pp. 16–26, 2006.

[10] N. Michael, S. Shen, K. Mohta, Y. Mulgaonkar, V. Kumar, K. Nagatani, Y. Okada, S. Kiribayashi, K. Otake, K. Yoshida, K. Ohno, E. Takeuchi, and S. Tadokoro, "Collaborative Mapping of an Earthquake-Damaged Building via Ground and Aerial Robots," *Journal of Field Robotics*, vol. 29, no. 5, pp. 832–841, 2012.

[11] S. Shen, N. Michael, and V. Kumar, "Autonomous Multi-Floor Indoor Navigation with a Computationally Constrained MAV," in *IEEE International Conference on Robotics and Automation*, pp. 20–25, 2011.

[12] S. Grzonka, G. Grisetti, and W. Burgard, "A Fully Autonomous Indoor Quadrotor," *IEEE Transactions on Robotics*, vol. 28, pp. 90–100, Feb. 2012.

[13] A. Bry, A. Bachrach, and N. Roy, "State estimation for aggressive flight in GPS-denied environments using onboard sensing," *2012 IEEE International Conference on Robotics and Automation*, pp. 1–8, May 2012.

[14] J. F. Roberts, *Enabling Collective Operation of Indoor Flying Robots*. PhD thesis, Swiss Federal Institute of Technology Lausanne, 2011.

[15] NSFRN, "NSERC Canada Field Robotics Network."

[16] T. Foote, "ROS Community Metrics Report," 2014.

[17] D. Fox, W. Burgard, H. Kruppa, and S. Thrun, "A Probabilistic Approach to Collaborative Multi-Robot Localization," *Autonomous Robots*, vol. 8, no. 3, pp. 325–344, 2000.

[18] A. Bachrach, S. Prentice, R. He, and N. Roy, "RANGE - Robust Autonomous Navigation in GPS-denied Environments," *Journal of Field Robotics*, vol. 28, no. 5, pp. 644–666, 2011.

[19] L. Heng, L. Meier, P. Tanskanen, F. Fraundorfer, and M. Pollefeys, "Autonomous Obstacle Avoidance and Maneuvering on a Vision-Guided MAV Using On-Board Processing," in *IEEE International Conference on Robotics and Automation*, pp. 2472–2477, 2011.

[20] H. Durrant-Whyte and T. Bailey, "Simultaneous Localization and Mapping : Part I," *IEEE Robotics & Automation Magazine*, vol. 13, no. 2, pp. 99–110, 2006.

[21] S. Grzonka, G. Grisetti, and W. Burgard, "Towards a navigation system for autonomous indoor flying," in *IEEE International Conference on Robotics and Automation*, pp. 2878–2883, 2009.

[22] M. Cognetti, P. Stegagno, A. Franchi, G. Oriolo, and H. H. Bülthoff, "3-D Mutual Localization with Anonymous Bearing Measurements," in *IEEE International Conference on Robotics and Automation*, no. 3, pp. 791 – 798, 2012.

[23] M. Achtelik, M. Achtelik, S. Weiss, and R. Siegwart, "Onboard IMU and Monocular Vision Based Control for MAVs in Unknown In- and Outdoor En-

vironments," in *IEEE International Conference on Robotics and Automation*, pp. 3056–3063, 2011.

[24] M. J. Milford, F. Schill, P. Corke, S. Member, and G. Wyeth, "Aerial SLAM with a Single Camera Using Visual Expectation," in *IEEE International Conference on Robotics and Automation*, pp. 2506–2512, 2011.

[25] J. Engel, J. Sturm, and D. Cremers, "Camera-Based Navigation of a Low-Cost Quadrocopter," in *IEEE/RSJ International Conference on Intelligent Robots and Systems*, pp. 2815–2821, 2012.

[26] V. Kumar and N. Michael, "Opportunities and challenges with autonomous micro aerial vehicles," *The International Journal of Robotics Research*, vol. 31, pp. 1279–1291, Aug. 2012.

[27] M. J. Barth, "Distributed Panoramic Sensing in Multiagent Robotics," 1994.

[28] K. Kat, H. Ishiguro, and M. Barth, "Identifying and Localizing Robots in a Multi-Robot System Environment," in *IEEE/RSJ International Conference on Intelligent Robots and Systems*, pp. 966–971, 1999.

[29] A. Howard, M. J. Matarić, and G. S. Sukhatme, "Putting the ' I ' in ' Team ': an Ego-Centric Approach to Cooperative Localization," in *IEEE International Conference on Robotics and Automation*, pp. 868–874, 2003.

[30] S. Zickler and M. Veloso, "RSS-Based Relative Localization and Tethering for Moving Robots in Unknown Environments," in *IEEE International Conference on Robotics and Automation*, pp. 5466–5471, 2010.

[31] A. Franchi, G. Oriolo, and P. Stegagno, "Probabilistic Mutual Localization in Multi-Agent Systems from Anonymous Position Measures," in *IEEE Conference on Decision and Control*, pp. 6534–6540, 2010.

[32] A. Franchi, G. Oriolo, and P. Stegagno, "Mutual localization in multi-robot systems using anonymous relative measurements," *The International Journal of Robotics Research*, vol. 32, pp. 1302–1322, Sept. 2013.

[33] P. Stegagno, M. Cognetti, L. Rosa, P. Peliti, and G. Oriolo, "Relative localization and identification in a heterogeneous multi-robot system," in *IEEE International Conference on Robotics and Automation*, pp. 1857–1864, Ieee, May 2013.

[34] A. I. Mourikis and S. I. Roumeliotis, "Performance Analysis of Multirobot Cooperative Localization," *IEEE Transactions on Robotics*, vol. 22, no. 4, pp. 666–681, 2006.

[35] N. Patwari, J. N. Ash, S. Kyperountas, A. O. Hero III, R. L. Moses, and N. S. Correal, "Locating the Nodes- Cooperative localization in wireless sensor networks," *IEEE Signal Processing Magazine*, vol. 22, no. 4, pp. 54–69, 2005.

[36] K. Y. Leung, Y. Halpern, T. D. Barfoot, and H. H. Liu, "The UTIAS multi-robot cooperative localization and mapping dataset," *The International Journal of Robotics Research*, vol. 30, pp. 969–974, Mar. 2011.

[37] W. Li, T. Zhang, and K. Kühnlenz, "A Vision-Guided Autonomous Quadrotor in An Air-Ground Multi-Robot System," in *IEEE International Conference on Robotics and Automation*, pp. 2980–2985, 2011.

[38] D. Fox, W. Burgard, and S. Thrun, "Active Markov localization for mobile robots," *Robotics and Autonomous Systems*, vol. 25, pp. 195–207, Nov. 1998.

[39] S. Roumeliotis and G. Bekey, "Distributed multirobot localization," *IEEE Transactions on Robotics and Automation*, vol. 18, pp. 781–795, Oct. 2002.

[40] J. L. Crassidis, F. L. Markley, and Y. Cheng, "Survey of Nonlinear Attitude Estimation Methods," *Journal of Guidance, Control, and Dynamics*, vol. 30, pp. 12–28, Jan. 2007.

[41] S. Bonnabel, P. Martin, and P. Rouchon, "Symmetry-Preserving Observers," *IEEE Transactions on Automatic Control*, vol. 53, no. 11, pp. 2514–2526, 2008.

[42] G. Baldwin, R. Mahony, J. Trumpf, T. Hamel, and T. Cheviron, "Complementary filter design on the Special Euclidean group SE(3)," in *European Control Conference*, pp. 3763–3770, 2007.

[43] R. Hermann and A. J. Krener, "Nonlinear Controllability and Observability," *IEEE Transactions on Automatic Control*, vol. 22, no. 5, pp. 728–740, 1977.

[44] F. Gustafsson and F. Gunnarsson, "Mobile Positioning Using Wireless Networks -Possibilities and fundamental limitations based on available wireless network measurements," *IEEE Signal Processing Magazine*, no. July 2005, pp. 41–53.

[45] Y. Dieudonn, "Deterministic Robot-Network Localization is Hard," *IEEE Transactions on Robotics*, vol. 26, no. 2, pp. 331–339, 2010.

[46] N. Trawny, X. S. Zhou, K. Zhou, and S. I. Roumeliotis, "Interrobot Transformations in 3-D," *IEEE Transactions on Robotics*, vol. 26, no. 2, pp. 226–243, 2010.

[47] A. Franchi, G. Oriolo, and P. Stegagno, "Mutual Localization in a Multi-Robot System with Anonymous Relative Position Measures," in *IEEE/RSJ Interna-*

tional Conference on Intelligent Robots and Systems, pp. 3974–3980, IEEE, 2009.

[48] A. Cristofaro, A. Renzaglia, and A. Martinelli, "Distributed Information Filters for MAV Cooperative Localization," in *Distributed Autonomous Robotic Systems*, pp. 133–146, Springer Berlin Heidelberg, 2013.

[49] S. Blackman and R. Popoli, *Design and Analysis of Modern Tracking Systems*. Artech House, 1999.

[50] J. Eckert, F. Dressler, and R. German, "Real-time indoor localization support for four-rotor flying robots using sensor nodes," in *2009 IEEE International Workshop on Robotic and Sensors Environments*, pp. 23–28, Ieee, Nov. 2009.

[51] J. Eckert, R. German, and F. Dressler, "ALF : An Autonomous Localization Framework for Self-Localization in Indoor Environments," in *International Conference on Distributed Computing in Sensor Systems and Workshops (DCOSS)*, 2011.

[52] J. R. Gonzalez and C. J. Bleakley, "High-Precision Robust Broadband Ultrasonic Location and Orientation Estimation," *IEEE Journal of Selected Topics in Signal Processing*, vol. 3, no. 5, pp. 832–844, 2009.

[53] A. Martinelli and R. Siegwart, "Observability Analysis for Mobile Robot Localization," in *IEEE/RSJ International Conference on Intelligent Robots and Systems*, pp. 1471–1476, 2005.

[54] R. Mahony, T. Hamel, and J.-M. Pflimlin, "Nonlinear Complementary Filters on the Special Orthogonal Group," *IEEE Transactions on Automatic Control*, vol. 53, pp. 1203–1218, June 2008.

[55] P. Martin and E. Sala, "Invariant Extended Kalman Filter : theory and application to a velocity-aided attitude estimation problem," in *IEEE Conference on Decision and Control*, pp. 1297–1304, 2009.

[56] S. Bonnabel, P. Martin, and P. Rouchon, "Non-Linear Symmetry-Preserving Observers on Lie Groups," *IEEE Transactions on Automatic Control*, vol. 54, no. 7, pp. 1709–1713, 2009.

[57] K. Y. K. Leung, S. Member, T. D. Barfoot, and H. H. T. Liu, "Decentralized Localization of Sparsely-Communicating Robot Networks : A Centralized-Equivalent Approach," *IEEE Transactions on Robotics*, vol. 26, no. 1, pp. 62–77, 2010.

[58] M. E. Liggins, C.-y. Chong, I. Kadar, M. G. Alford, V. Vannicola, and S. Thomopoulos, "Distributed Fusion Architectures and Algorithms for Target Tracking," *Proceedings of the IEEE*, vol. 85, no. 1, pp. 95–107, 1997.

[59] K.-c. Chang, C.-Y. Chong, and Y. Bar-shalom, "Joint Probabilistic Data Association in Distributed Sensor Networks," *IEEE Transactions on Automatic Control*, vol. AC-31, no. 10, pp. 889–897, 1986.

[60] D. B. Reid, "An Algorithm for Tracking Multiple Targets," *IEEE Transactions on Automatic Control*, vol. 24, pp. 843–854, Dec. 1979.

[61] O. De Silva, G. K. I. Mann, and R. G. Gosine, "Development of a relative localization scheme for ground-aerial multi-robot systems," in *IEEE/RSJ International Conference on Intelligent Robots and Systems*, pp. 870–875, 2012.

[62] O. De Silva, G. K. I. Mann, and R. G. Gosine, "An Ultrasonic and Vision-Based Relative Positioning Sensor for Multirobot Localization," *IEEE Sensors Journal*, vol. 15, no. 3, pp. 1716–1726, 2015.

[63] D. Scaramuzza, A. Martinelli, and R. Siegwart, "Precise Bearing Angle Measurement Based on Omnidirectional Conic Sensor and Defocusing," in *European Conference on Mobile Robots*, 2005.

[64] H. Wymeersch, J. Lien, and M. Z. Win, "Cooperative Localization in Wireless Networks," *Proceedings of the IEEE*, vol. 97, pp. 427–450, Feb. 2009.

[65] C. D. Marziani, J. Ureña, A. Hernández, J. J. García, F. J. Álvarez, A. Jiménez, M. C. Pérez, J. Manuel, V. Carrizo, J. Aparicio, and R. Alcoleas, "Simultaneous Round-Trip Time-of-Flight Acoustic Signals," *IEEE Sensors Journal*, vol. 12, no. 10, pp. 2931–2940, 2012.

[66] J. Eckert, R. German, and F. Dressler, "An Indoor Localization Framework for Four-Rotor Flying Robots Using Low-Power Sensor Nodes," *IEEE Transactions on Instrumentation and Measurement*, vol. 60, no. 2, pp. 336–344, 2011.

[67] J. Biswas and M. Veloso, "WiFi Localization and Navigation for Autonomous Indoor Mobile Robots," in *IEEE International Conference on Robotics and Automation*, pp. 4379–4384, 2010.

[68] N. Michael, D. Mellinger, Q. Lindsey, and V. Kumar, "The GRASP Multiple Micro-UAV Test Bed," *IEEE Robotics & Automation Magazine*, vol. 17, no. 3, pp. 56–65, 2010.

[69] W. Etter, P. Martin, and R. Mangaharam, "Cooperative Flight Guidance of Autonomous Unmanned Aerial Vehicles," in *The Second International Workshop on Networks of Cooperating Objects*, 2011.

[70] E. Olson, "AprilTag: A robust and flexible multi-purpose fiducial system," tech. rep., University of Michigan APRIL Laboratory, 2010.

[71] N. B. Priyantha, A. Chakraborty, and H. Balakrishnan, "The Cricket location-support system," in *Proceedings of the 6th annual international conference on mobile computing and networking*, vol. 2000, pp. 32–43, ACM Press, 2000.

[72] M. Hazas and A. Ward, "A Novel Broadband Ultrasonic Location System," in *UbiComp 2002: Ubiquitous Computing*, vol. 2498, pp. 264–280, Springer Berlin Heidelberg, 2002.

[73] J. C. Prieto, A. R. Jiménez, J. Guevara, J. L. Ealo, F. Seco, J. O. Roa, and F. Ramos, "Performance Evaluation of 3D-LOCUS Advanced Acoustic LPS," *IEEE Transactions on Instrumentation and Measurement*, vol. 58, no. 8, pp. 2385–2395, 2009.

[74] J. Ureña, A. Hernández, A. Jiménez, J. Villadangos, M. Mazo, J. García, J. García, F. Álvarez, C. De Marziani, and M. Pérez, "Advanced sensorial system for an acoustic LPS," *Microprocessors and Microsystems*, vol. 31, pp. 393–401, Sept. 2007.

[75] M. M. Saad, C. J. Bleakley, and S. Dobson, "Robust High-Accuracy Ultrasonic Range Measurement System," *IEEE Transactions on Instrumentation and Measurement*, vol. 60, no. 10, pp. 3334–3341, 2011.

[76] C. Medina, J. Segura, and A. de la Torre, "Accurate time synchronization of ultrasonic TOF measurements in IEEE 802.15.4 based wireless sensor networks," *Ad Hoc Networks*, vol. 11, pp. 442–452, Jan. 2013.

[77] J. Ramon, G. Hernandez, and C. J. Bleakley, "Low-Cost , Wideband Ultrasonic Transmitter and Receiver for Array Signal Processing Applications," *IEEE Sensors Journal*, vol. 11, no. 5, pp. 1284–1292, 2011.

[78] A. Yildiz, A. Akay, and Y. S. Akgul, "Wii Remote Calibration Using the Sensor Bar," in *IEEE Computer Society Conference on Computer Vision and Pattern Recognition Workshops*, pp. 7–12, 2011.

[79] Knowles Corporation, "Ultrasonic MEMS Microphones."

[80] Murata Electronics North America, "Open-Structure Ultrasonic Sensors."

[81] A. Martinelli, F. Pont, and R. Siegwart, "Multi-Robot Localization Using Relative Observations," in *IEEE International Conference on Robotics and Automation*, no. April, pp. 2797–2802, Ieee, 2005.

[82] F. L. Markley, "Attitude error representations for Kalman filtering," *Journal of guidance, control, and dynamics*, vol. 26, no. 2, pp. 311–317, 2003.

[83] S. Suksakulchai, S. Thongchai, D. Wilkes, and K. Kawamura, "Mobile robot localization using an electronic compass for corridor environment," in *IEEE International Conference on Systems, Man, and Cybernetics*, vol. 5, pp. 3354–3359, 2000.

[84] H.-J. von der Hardt, A. Philippe, D. Wolf, and M. Dufaut, "A method of mobile robot localisation by fusion of odometric and magnetometric data," *The International Journal of Advanced Manufacturing Technology*, vol. 9, no. 1, pp. 65–69, 1994.

[85] J. Farrell, *Aided navigation: GPS with high rate sensors*. McGraw-Hill New York, 2008.

[86] S. Thrun, W. Burgard, and D. Fox, *Probabilistic Robotics*. MIT Press, Cambridge, MA, 2005.

[87] G. L. Mariottini, F. Morbidi, D. Prattichizzo, G. J. Pappas, and K. Daniilidis, "Leader-Follower Formations : Uncalibrated Vision-Based Localization and Control," in *IEEE International Conference on Robotics and Automation*, pp. 10–14, 2007.

[88] S. Bonnabel, "Symmetries in Observer Design : Review of Some Recent Results and Applications to EKF-based SLAM," in *Robot Motion and Control*, ch. 1, pp. 3–15, Springer London, 2012.

[89] T. Hervier, S. Bonnabel, and F. Goulette, "Accurate 3D Maps from Depth Images and Motion Sensors via Nonlinear Kalman Filtering," in *IEEE/RSJ International Conference on Intelligent Robots and Systems*, pp. 5291–5297, 2012.

[90] M. Barczyk, S. Member, and A. F. Lynch, "Invariant Observer Design for a Helicopter UAV Aided Inertial Navigation System," *IEEE Transactions on Control Systems Technology*, vol. 21, no. 3, pp. 791–806, 2013.

[91] E. Lefferts, F. L. Markley, and M. D. Shuster, "Kalman filtering for spacecraft attitude estimation," *Journal of Guidance, Control, and Dynamics*, vol. 5, no. 5, pp. 417–429, 1982.

[92] W. Arnold and A. Laub, "Generalized eigenproblem algorithms and software for algebraic Riccati equations," *Proceedings of the IEEE*, vol. 72, no. 12, pp. 1746–1754, 1984.

[93] P. Martin and E. Salaün, "Design and implementation of a low-cost observer-based attitude and heading reference system," *Control Engineering Practice*, vol. 18, pp. 712–722, July 2010.

[94] L. Ljung, "Asymptotic Behavior of the Extended Kalman Filter as a Parameter Estimator for Linear Systems," *IEEE Transactions on Automatic Control*, vol. 24, no. 1, pp. 36–50, 1979.

[95] F. Markley, "Attitude Determination Using Vector Observations and the Singular Value Decomposition," *Journal of the Astronautical Sciences*, vol. 36, no. 3, pp. 245–258, 1988.

[96] D. Abeywardena, S. Kodagoda, G. Dissanayake, and R. Munasinghe, "Improved State Estimation in Quadrotor MAVs: A Novel Drift -Free Velocity Estimator," *IEEE Robotics & Automation Magazine*, no. December, pp. 32–39, 2013.

[97] R. C. Leishman, J. C. Macdonald Jr., R. W. Beard, and T. W. Mclain, "Quadrotors and Accelerometers: State Estimation with an Improved Dynamic Model," *IEEE Control Systems Magazine*, no. February, pp. 28–41, 2014.

[98] N. Karam, F. Chausse, R. Aufrère, and R. Chapuis, "Localization of a Group of Communicating Vehicles by State Exchange," in *IEEE/RSJ International Conference on Intelligent Robots and Systems*, pp. 519–524, Ieee, Oct. 2006.

[99] L. C. Carrillo-Arce, E. D. Nerurkar, J. L. Gordillo, and S. I. Roumeliotis, "Decentralized Multi-robot Cooperative Localization using Covariance Intersection," in *IEEE/RSJ International Conference on Intelligent Robots and Systems*, pp. 1412–1417, 2013.

[100] C.-C. Wang, C. Thorpe, S. Thrun, M. Hebert, and H. Durrant-Whyte, "Simultaneous Localization, Mapping and Moving Object Tracking," *The International Journal of Robotics Research*, vol. 26, pp. 889–916, Sept. 2007.

[101] R. Marchant, P. Guerrero, and J. Ruiz-del solar, "Cooperative Global Tracking Using Multiple Sensors," in *RoboCup 2012: Robot Soccer World Cup XVI*, pp. 310–321, 2013.

[102] S. Julier and J. K. Uhlmann, "General Decentralized Data Fusion with Covariance Intersection (CI)," in *Handbook of Multi Sensor Data Fusion*, no. Ci, pp. 12.1–12.25, 2001.